

# THE HIGH TIME RESOLUTION RADIO SKY

A THESIS SUBMITTED TO THE UNIVERSITY OF MANCHESTER FOR THE  
DEGREE OF DOCTOR OF PHILOSOPHY IN THE FACULTY OF  
ENGINEERING AND PHYSICAL SCIENCES

2013

BY

DAN PHILIP GRANT THORNTON  
SCHOOL OF PHYSICS AND ASTRONOMY

## The University of Manchester

ABSTRACT OF THESIS submitted by Dan Philip Grant Thornton  
for the Degree of Doctor of Philosophy and entitled  
“The High Time Resolution Radio Sky”  
September 2013

Pulsars are laboratories for extreme physics unachievable on Earth. As individual sources and possible orbital companions can be used to study magnetospheric, emission, and superfluid physics, general relativistic effects, and stellar and binary evolution. As populations they exhibit a wide range of sub-types, with parameters varying by many orders of magnitude signifying fundamental differences in their evolutionary history and potential uses. There are currently around 2200 known pulsars in the Milky Way, the Magellanic clouds, and globular clusters, most of which have been discovered with radio survey observations. These observations, as well as being suitable for detecting the repeating signals from pulsars, are well suited for identifying other transient astronomical radio bursts that last just a few milliseconds that either singular in nature, or rarely repeating.

Prior to the work of this thesis non-repeating radio transients at extragalactic distances had possibly been discovered, however with just one example status a real astronomical sources was in doubt. Finding more of these sources was a vital to proving they were real and to open up the universe for millisecond-duration radio astronomy.

The High Time Resolution Universe survey uses the multibeam receiver on the 64-m Parkes radio telescope to search the whole visible sky for pulsars and transients. The temporal and spectral resolution of the receiver and the digital back-end enable the detection of relatively faint, and distant radio sources. From the Parkes telescope a large portion of the Galactic plane can be seen, a rich hunting ground for radio pulsars of all types, while previously poorly surveyed regions away from the Galactic plane are also covered.

I have made a number of pulsar discoveries in the survey, including some rare systems. These include PSR J1226–6208, a possible double neutron star system in a remarkably circular orbit, PSR J1431–471 which is being eclipsed by its companion with each orbit, PSR J1729–2117 which is an unusual isolated recycled pulsar, and PSR J2322–2650 which has a companion of very low mass – just  $7 \times 10^{-4} M_{\odot}$ , amongst others. I begin this thesis with the study of these pulsars and discuss their histories. In addition, I demonstrate that optical observations of the companions to some of the newly discovered pulsars in the High Time Resolution Universe survey may result in a measurement of their age and that of the pulsar.

I have discovered five new extragalactic single radio bursts, confirming them as an astronomical population. These appear to occur frequently, with a rate of  $1.0_{-0.5}^{+0.6} \times 10^4 \text{ sky}^{-1} \text{ day}^{-1}$ . The sources are likely at cosmological distances – with redshifts between 0.45 and 1.45, making them more than half way to the Big Bang in the most distant case. This implies their luminosities must be enormous,  $10^{31}$  to  $10^{33}$  J emitted in just a few milliseconds. Their source is unknown but I present an analysis of the options. I also perform a population simulation of the bursts which demonstrates how their intrinsic spectrum could be measured, even for unlocalised FRBs: early indications are that the spectral index of FRBs  $< 0$ .

# Declaration

No portion of the work referred to in this thesis has been submitted in support of an application for another degree or qualification of this or any other university or other institution of learning.

Dan Philip Grant Thornton  
Department of Physics and Astronomy  
University of Manchester  
Jodrell Bank Centre for Astrophysics  
Alan Turing Building  
University of Manchester  
Manchester  
M13 9PL  
United Kingdom

# Copyright

Copyright in text of this thesis rests with the Author. Copies (by any process) either in full, or of extracts, may be made only in accordance with instructions given by the Author and lodged in the John Rylands University Library of Manchester. Details may be obtained from the Librarian. This page must form part of any such copies made. Further copies (by any process) of copies made in accordance with such instructions may not be made without the permission (in writing) of the Author. The ownership of any intellectual property rights which may be described in this thesis is vested in the University of Manchester, subject to any prior agreement to the contrary, and may not be made available for use by third parties without the written permission of the University, which will prescribe the terms and conditions of any such agreement. Further information on the conditions under which disclosures and exploitation may take place is available from the head of Department of Physics and Astronomy.

# Acknowledgements

During my PhD I have been lucky enough to work with some outstanding scientists and mentors. Not least my supervisor Ben Stappers whose support over the three years has been brilliant. Your guidance and help has been invaluable, thanks for giving me the opportunity to work on such great projects.

In the course of my work I have also worked and interacted with some talented scientists at Jodrell Bank, in no particular order, Andrew Lyne, Sir Francis Graham-Smith, Chris Jordan, Cees Bassa, Gemma Janssen, Patrick Weltevrede, Rob Ferdman, Mike Keith, Mark Purver, Cristobal Espinoza, Evan Keane, Sam Bates, Tom Hassall, Neil Young, Sotirios Sanidas, Kuo Liu, Phrudth Jaroenjittichai, Monika Obrocka, Rob Lyon, Sally Cooper, and Simon Rookyard. In differing proportions you've made the last three years funny, challenging, interesting, and above all enjoyable. To Ant Holloway and Bob Dickson, this PhD would have been next to impossible without your help and hard work.

The HITRUN collaboration, you gave me the opportunity to work on this excellent survey. Thanks to all of you, in particular Michael Kramer, Matthew Bailes, and Simon Johnston for helping me along the way. Thanks also to Andrea Possenti for showing me the ropes that first time at Parkes.

I have been lucky to spend several months observing with the Parkes radio telescope, where the staff and scientists have always looked after me, particularly John Sarkissian, a brilliant scientist who makes a visit to Parkes all the more interesting, and who doesn't mind the 5 am phone calls. Of course no PhD which uses Parkes should fail to acknowledge all the staff who work at the telescope - here's to another 50 years of pulsars, FRBs, and anything else which may pop up! Thanks also to my friends at the ATNF who took me to trivia and made being so far from home bearable, Shari Breen and Ryan Shannon, and the multitude of friendly people down under.

To the people who have supported me for so long, mum and dad. You were right, doing the hard subjects at school was the right thing to do! To Rosie and Miri, thanks for being such great sisters.

And finally to my Lucy, without you this would never have been possible, thank you for supporting me and being so patient with me. All those times when I said I couldn't do it, you kept me going. This one's for you. PB.

# Acronyms

<b>BPSR</b>	Berkeley-Parkes-Swinburne recorder
<b>ccSN</b>	Core-collapse supernova
<b>DFT</b>	Discrete Fourier transform
<b>DM</b>	Dispersion measure
<b>FFT</b>	Fast Fourier transform
<b>FPGA</b>	Field programmable gate array
<b>FRB</b>	Fast radio burst
<b>(SH)GRB</b>	(Short hard) Gamma-ray burst
<b>HPBW</b>	Half-power beam-width
<b>HTRU</b>	High time resolution universe [survey]
<b>H/LMXB</b>	High/Low mass x-ray binary
<b>IGM</b>	Intergalactic medium
<b>ISM</b>	Interstellar medium
<b>JBO</b>	Jodrell Bank Observatory
<b>MB</b>	Multibeam [receiver]
<b>MSP</b>	Millisecond pulsar
<b>MW</b>	Milky Way
<b>NS</b>	Neutron star
<b>DNS</b>	Double neutron star
<b>PMPS</b>	Parkes multibeam pulsar survey
<b>RFI</b>	Radio frequency interference
<b>RRAT</b>	Rotating radio transient
<b>SNR</b>	Signal to noise ratio
<b>UTC</b>	Coordinated universal time
<b>WD</b>	White dwarf

## Refereed publications

A population of fast radio bursts at cosmological distances

Thornton D., *et al.*

2013

Science, **341** 6141 pp. 53 – 56

The High Time Resolution Universe Pulsar Survey - VI. An artificial neural network and timing of 75 pulsars

Bates S., *et al.* incl. Thornton D.

2012

MNRAS, **427** pp. 1052 – 1065

The High Time Resolution Universe Pulsar Survey - VII. Discovery of five millisecond pulsars and the different luminosity properties of binary and isolated recycled pulsars

Burgay M., *et al.* incl. Thornton D.

2013

MNRAS, **433** p. 259

The High Time Resolution Universe Pulsar Survey - VIII. The Galactic millisecond pulsar population

Levin L., *et al.* incl. Thornton D.

2013

MNRAS, **434** p. 1387

# Contents

<b>1</b>	<b>Introduction</b>	<b>11</b>
1.1	Pulsars . . . . .	11
1.1.1	History . . . . .	11
1.1.2	Neutron stars . . . . .	12
1.1.3	Observing and timing pulsars . . . . .	17
1.1.4	Fundamental parameters . . . . .	20
1.1.5	Pulsar Families . . . . .	22
1.1.6	Why are pulsars interesting? . . . . .	27
1.2	Radio Transients . . . . .	32
1.2.1	Rotating Radio Transients . . . . .	32
1.2.2	Highly dispersed radio bursts . . . . .	33
<b>2</b>	<b>Searching and the High Time Resolution Universe survey</b>	<b>37</b>
2.1	Pulsar Searching . . . . .	37
2.1.1	Sensitivity . . . . .	38
2.1.2	Incoherent dedispersion . . . . .	39
2.1.3	The discrete Fourier transform . . . . .	43

---

2.1.4	Candidate filtering and generation . . . . .	47
2.2	Single pulse searching . . . . .	49
2.2.1	Matched filtering and wide pulses . . . . .	50
2.3	The High Time Resolution Universe south survey . . . . .	53
2.3.1	Hardware and data recording . . . . .	54
2.3.2	Survey regions . . . . .	57
2.3.3	Sensitivity . . . . .	58
2.3.4	RFI removal . . . . .	59
2.3.5	HTRU Fourier and single pulse searching . . . . .	60
2.3.6	Artificial neural network . . . . .	64
2.3.7	Human inspection . . . . .	68
2.3.8	Candidate follow-up . . . . .	69
2.3.9	Single pulse searching in the HTRU survey . . . . .	70
<b>3</b>	<b>Discovery of five recycled pulsars in the High Time Resolution Universe survey</b>	<b>77</b>
3.1	Introduction . . . . .	78
3.2	Discovery and Timing . . . . .	78
3.3	Results . . . . .	80
3.3.1	PSR J1227–6208 . . . . .	84
3.3.2	PSR J1405–4656 . . . . .	89
3.3.3	PSR J1431–4715 . . . . .	90
3.3.4	PSR J1653–2054 . . . . .	94
3.3.5	PSR J1729–2117 . . . . .	94

---

3.4	Possibility of optical detection of binary MSP companions discovered in the HTRU survey . . . . .	96
3.5	Discussion . . . . .	99
<b>4</b>	<b>Binary pulsars - two extreme cases</b>	<b>102</b>
4.1	PSR J2322–2650 . . . . .	103
4.1.1	Spin characteristics . . . . .	105
4.1.2	Orbital characteristics . . . . .	105
4.2	PSR J1837–0832 . . . . .	109
<b>5</b>	<b>A Population of Fast Radio Bursts at Cosmological Distances</b>	<b>111</b>
5.1	Introduction . . . . .	112
5.2	Pulse fitting . . . . .	112
5.2.1	FRB 110220 . . . . .	115
5.2.2	FRB 110703 . . . . .	117
5.3	Interpretation . . . . .	117
5.3.1	Combining dispersive regions . . . . .	118
5.3.2	Dispersion and scattering sources . . . . .	121
5.4	Non-dispersed origins . . . . .	123
5.5	Energetics . . . . .	124
5.6	Fast Radio Burst rate . . . . .	125
5.7	FRB locations . . . . .	128
5.8	Possible sources . . . . .	129

---

<b>6</b>	<b>FRBs: burst profiles, population, and source</b>	<b>131</b>
6.1	Introduction . . . . .	131
6.2	FRB 121002 . . . . .	133
6.2.1	Distance . . . . .	135
6.2.2	Burst profile . . . . .	136
6.3	An FRB population simulation . . . . .	142
6.3.1	Spatial distribution . . . . .	142
6.3.2	Dispersive delay contributions . . . . .	144
6.3.3	Luminosity . . . . .	146
6.3.4	Burst broadening effects . . . . .	147
6.3.5	Detectability . . . . .	148
6.3.6	HTRU detectability and the Galactic plane . . . . .	149
6.3.7	The effect of the Galactic plane . . . . .	150
6.3.8	The simulation and the known FRB sample . . . . .	151
6.3.9	The effect of $\gamma < 0$ . . . . .	152
6.3.10	Inferred redshift accuracy . . . . .	153
6.4	FRBs and SGR giant flares . . . . .	156
6.4.1	SGRs, AXPs, and magnetars . . . . .	156
6.4.2	SGR giant flares . . . . .	156
6.4.3	Could FRBs be associated with SGR giant flares? . . . . .	158
<b>7</b>	<b>The High Time Resolution Universe Survey high Galactic-latitude survey - Status</b>	<b>162</b>

---

7.1	Survey status . . . . .	163
7.2	Pulsars . . . . .	165
7.2.1	Normal pulsars . . . . .	165
7.2.2	Recycled pulsars . . . . .	165
7.3	Fast Radio Bursts . . . . .	167
<b>8</b>	<b>Conclusions</b>	<b>168</b>
8.1	The High Time Resolution Universe survey . . . . .	168
8.1.1	Pulsars . . . . .	169
8.1.2	Fast Radio Bursts . . . . .	170

# List of Tables

1.1	Pulsar Families - the key attributes . . . . .	24
2.1	The HTRU south survey parameters . . . . .	58
2.2	The HTRU artificial neural net heuristics . . . . .	67
3.1	MSP observing systems . . . . .	79
3.2	Parameters for five pulsar discoveries . . . . .	83
3.3	Known double neutron star systems . . . . .	85
3.4	Optical magnitudes for HTRU MSPs . . . . .	98
3.5	Optical magnitudes for HTRU MSPs with $\tau_{c,10}$ . . . . .	99
4.1	Parameters for two new pulsar binary systems . . . . .	104
5.1	The fast radio burst parameters . . . . .	127
6.1	Parameters for FRB 121002 . . . . .	135

# List of Figures

1.1	Neutron star cross section . . . . .	14
1.2	The lighthouse model . . . . .	16
1.3	The $P - \dot{P}$ diagram . . . . .	23
1.4	Orbital decay of PSR J1913+16 . . . . .	29
1.5	<i>Hellings and Downs</i> correlation curve . . . . .	30
1.6	Mass constraints for the double pulsar system PSR J0737–3039 . . . . .	31
1.7	Dynamic spectrum of the “Lorimer burst” . . . . .	35
2.1	Incoherent dedispersion . . . . .	41
2.2	Fourier power spectrum, $P(k)$ . . . . .	46
2.3	Time-series folding . . . . .	48
2.4	Pulse profile vs. DM waterfall plot . . . . .	50
2.5	An unfiltered and matched-filtered single pulse . . . . .	51
2.6	Comparison of power-of-two and integer boxcar widths . . . . .	52
2.7	Boxcar filtering of a test pulse - power-of-two sample widths . . . . .	53
2.8	Multibeam receiver pointing tessellation on the sky . . . . .	55
2.9	The HTRU South survey regions . . . . .	57

---

2.10	HTRU survey region sensitivity plots . . . . .	59
2.11	HTRU survey high-latitude computing cluster processing schematic . . . . .	61
2.12	HTRU survey high-latitude processing node schematic . . . . .	62
2.13	HTRU survey pulsar candidate - PSR J2322–2650 . . . . .	64
2.14	An ANN layering schematic . . . . .	65
2.15	Pulsar candidate - noise . . . . .	68
2.16	Pulsar candidate - RFI . . . . .	69
2.17	Threshold-exceeding Gaussian noise samples . . . . .	71
2.18	Single pulse sensitivity - the HTRU survey . . . . .	73
2.19	Single pulse candidate - a strong single pulse . . . . .	75
2.20	HTRU survey single pulse candidate - RFI . . . . .	76
3.1	A recycled pulsar $P - \dot{P}$ diagram . . . . .	80
3.2	Multi-frequency MSP pulse profiles . . . . .	82
3.3	PSR J1227–6208 $M_c$ and $\sin(i)$ constraint from Shapiro delay . . . . .	87
3.4	The orbital phase residuals with Shapiro delay signatures . . . . .	88
3.5	Residual TOAs for PSR J1431–4715 . . . . .	91
3.6	A schematic of the binary MSP PSR J1431–4715 . . . . .	93
3.7	$P_{\text{orb}}$ against $M_c$ for HTRU MSPs . . . . .	100
4.1	Probability of planet-like companion mass . . . . .	106
4.2	PSR J2322–2650 pulse times of arrival . . . . .	107
4.3	Mass - maximum radius relation for PSRs J2322–2650 and J1719–1438 . . . . .	108

5.1	Fast Radio Burst profiles . . . . .	113
5.2	Dynamic spectrum of FRB 110220 . . . . .	114
5.3	$\chi^2$ plot of $\alpha$ and $\beta$ for FRB 110220 . . . . .	116
5.4	Observed dispersive delay as a function of redshift . . . . .	121
5.5	DM vs. $ b $ for known pulsars and FRBs . . . . .	122
5.6	SNR across the observing band for four FRBs . . . . .	125
6.1	Single and double Gaussian fit to FRB 121002 . . . . .	137
6.2	Double Gaussian fits to four subbands of FRB 121002 . . . . .	139
6.3	Frequency dependence of parameters describing the two Gaussian components of FRB 121002 . . . . .	140
6.4	True redshift, $z_t$ , distribution of simulated FRBs . . . . .	144
6.5	$DM_{\text{obs}}$ plotted against detected SNR - scattering and no scattering . . . . .	149
6.6	A histogram of rates for $DM_{\text{obs}}$ for $ b  < 15^\circ$ and $ b  > 15^\circ$ . . . . .	150
6.7	A histogram of $DM_{\text{obs}}$ with known FRBs . . . . .	151
6.8	A histogram of $\overline{DM}_{\text{obs}}$ . . . . .	152
6.9	The effect of $\gamma < 0$ on $\overline{DM}_{\text{obs}}$ . . . . .	153
6.10	Inferred redshift, $z_i$ , as a function of true redshift, $z_t$ . . . . .	154
6.11	Gamma-ray counts of a giant flare from SGR 1806–20 . . . . .	157
7.1	A projection of the high-latitude HTRU survey . . . . .	164
7.2	$P$ against DM of new high-latitude pulsars . . . . .	166

# Chapter 1

## Introduction

This thesis is about astrophysical phenomena that use and require the highest time-resolution observations possible. These observations enable the discovery of things which change on similar timescales. In lower resolution observations they are simply indistinguishable from the noise. A historical example is the serendipitous discovery of repeating pulsed radio sources - pulsars - which occurred when temporal filters were removed from the telescope. This suddenly gave the astronomer access to radio signals which varied on a timescale of seconds to milliseconds.

The hardware and software for observing and searching for pulsars has become increasingly sensitive during the years since their discovery, and is also now well suited for searching for highly dispersed single and irregularly repeating radio transients. The detection and study of these types of events is in its infancy and is expected to be an exciting new avenue for radio astronomy - not to mention an opportunity for millisecond transient radio astronomers to break the confines of the Milky Way and its vicinity.

### 1.1 Pulsars

#### 1.1.1 History

The first pulsar was discovered by chance at Cambridge in 1968 by Jocelyn Bell and Anthony Hewish using a newly constructed transit radio telescope (Hewish et al., 1968). They were using the telescope to monitor the sky for interplanetary scintillation of distant ra-

dio sources when the unexpected repeating pulses were first noticed. These first pulsar pulses were so bright they were found via identification of single pulses in the raw detected voltages induced in the telescope.

They eventually correctly attributed the pulses as being associated with the dense rotating core left after a supernova explosion - a neutron star (NS) - which had been predicted some years earlier (Baade & Zwicky, 1934). Just prior to Bell and Hewish's discovery it was predicted that a rotating NS could produce electromagnetic radiation, and that this may be a source of power in the Crab nebula (Pacini, 1967) - a remnant from a supernova recorded in 1054 AD. The first source discovered is now designated PSR B1919+21; indicating its position in right ascension and declination. These objects were named *pulsars* and before long many more were discovered (Pilkington et al., 1968).

The existence of NSs was postulated when Chandrasekhar predicted that a White Dwarf (WD) star would collapse if its mass,  $M_{\text{WD}} \gtrsim 1.4M_{\odot}$  (Chandrasekhar, 1931). This occurs when the mass is sufficiently high that the outward electron degeneracy pressure that prevents the WD from collapsing is insufficient to prevent further gravitational collapse. Oppenheimer & Volkoff (1939) were the first to evaluate an equation of state (mass as a function of radius) for a NS and found it is comprised largely of neutrons and is supported against further collapse by *neutron* degeneracy pressure. A typical NS has collapsed to a radius of around 10 km, forming an extremely dense object ( $\rho_{\text{NS}} \sim 10^{17} \text{ kg m}^{-3}$ ).

### 1.1.2 Neutron stars

A massive star ( $M_{\text{star}} \approx 8 - 10 M_{\odot}$ ) can progressively fuse increasingly heavy elements, until iron is formed in the hottest, densest part of the star - the core. Further fusion reactions to form elements heavier than iron are not energetically favourable and fusion ceases in the core. This halt results in a reduction of the outward radiation pressure from fusion and the core collapses under gravity. This collapse causes high pressure, sufficient to force together iron nuclei, resulting in inverse beta decay,



where the electrons and protons of the iron atoms are converted to neutrons and neutrinos. The neutrinos have a sufficiently small collisional cross-section that they escape the supernova without interacting, leaving a core of almost pure neutrons. The outer layers of the

star in turn fall towards the core causing an increase in pressure and a shock wave, which causes fusion in the outer layers of the star to proceed, forming heavier elements, in turn causing the star to explode. The ejected outer layers form the supernova remnant. The bare degenerate stellar core is composed mainly of neutrons (see Figure 1.1) - this is a *neutron star*. This whole process is called a core-collapse or type II supernova.

A NS is supported against further gravitational collapse by *neutron degeneracy pressure*. If the remnant mass is larger than the Oppenheimer-Volkov limit ( $1.5 - 3 M_{\odot}$ ) there is no stable solution to the equation of state and collapse to a black hole may occur (Oppenheimer & Volkoff, 1939). For a lower core mass electron degeneracy pressure is not overcome, and instead a WD is formed (which is supported by electron degeneracy pressure). For a more detailed discussion of NS equations of state see Lattimer & Prakash (2001) and Lattimer & Prakash (2004).

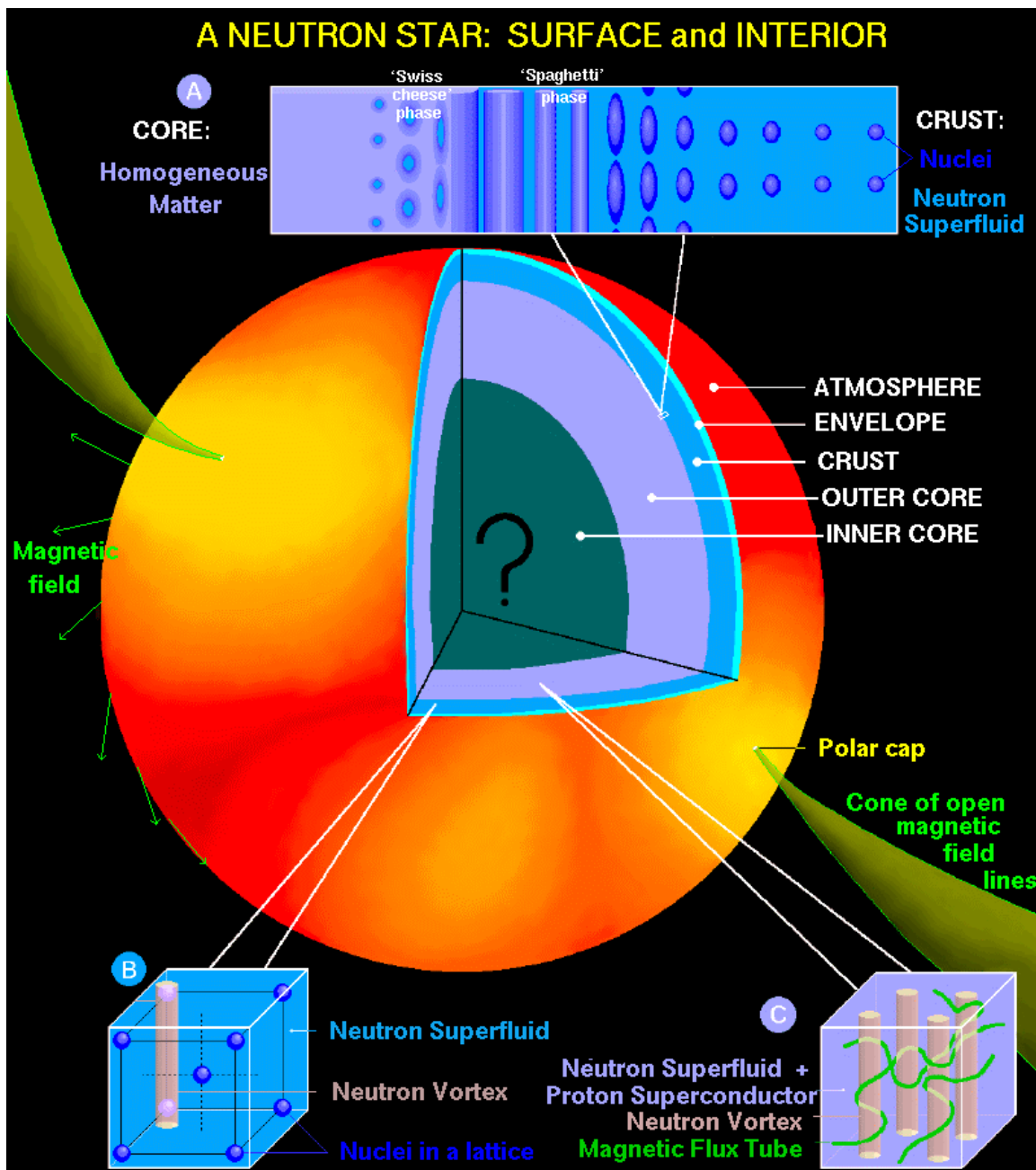


**Figure 1.1** – A cut-away schematic of a neutron star indicating the different components which make up the overall structure. Methods to probe the equation of state include studying “glitches” in spin period which may be due to the unpinning of vortices in the superfluid core region from the neutron star crust. (Baym & Pines (1971); Alpar et al. (1981)). Figure from Dany Page (<http://www.astroscu.unam.mx/neutrones/NS-Picture/NS-Picture.html>).

The NS retains approximately  $1.4 M_{\odot}$  of the mass of the progenitor star - the Chandrasekhar mass (Chandrasekhar, 1931). After collapse the NS has a typical radius  $\sim 10$  km,

contrasting with typical stellar radii of  $\sim 7 \times 10^5$  km. This dramatic reduction in size, but not mass, leaves the NS extremely dense. The NS also conserves the angular momentum of the core, resulting in a faster rotation rate than the progenitor. The slowest radio pulsar, PSR J2144–3933, has a spin period,  $P = 8.51$  s (Young, Manchester & Johnston, 1999), while the fastest, PSR J1748–2446ad, has  $P = 0.00139$  s, although this spin period is not the period at birth (Hessels et al., 2006). See Section 1.1.5 and Chapter 3 for more details.

Magnetic flux is also conserved during collapse: the field lines are closer together in the NS and consequently the field strength is many orders of magnitude greater than a typical stellar surface magnetic field strength. A young pulsar has a dipolar magnetic field with a typical magnitude of  $10^{10} - 10^{14}$  G at the surface. It is this extreme magnetic field which is responsible for the radio pulses.

### The Lighthouse Model

The strong magnetic field of the NS is predominantly dipolar in configuration and co-rotates with the NS. The magnetosphere is filled with a plasma of charged material. As the distance from the NS increases the speed of the co-rotating magnetosphere increases, the plasma is trapped in the magnetosphere and co-rotates with it. Of course, the plasma may not move faster than the speed of light. The radius at which the co-rotation speed equals the speed of light defines the *light cylinder* (see Figure 1.2). There are then two types of dipolar magnetic field line from the NS. First, there are those that are able to close to the opposite pole within the light cylinder, these are the *closed field lines*. Second, there are those field lines which cross the light cylinder and therefore cannot close to the opposite pole, these are the *open field lines*.

Because the NS is rotating and has a magnetic field, an electric field is created which is proportional to  $v \times B$ , where  $B$  is the magnetic vector field, and  $v$  is velocity of the magnetic field. The electric field is perpendicular to the surface of the NS, and causes a voltage difference at the surface (a voltage gap). In some scenarios incoming high-energy particles, for example cosmic rays, cause pair production in the gap, these pairs fill the magnetosphere with charged particles. These charged particles build up to cause an electrostatic field, which reduces the voltage drop at the surface to zero (Goldreich & Julian, 1969). However, at the magnetic polar caps, where the open field lines originate, the charged particles produced in the voltage gap do not generate the electrostatic field, instead they stream along the open fields and escape the magnetosphere. Because the open field lines are bent (see Figure 1.2) these charged particles are accelerated. The accelerating charged particles

emit radio waves tangentially to the open field lines, and radio emission is beamed in the direction of the magnetic field lines at the point of emission. This depletion of charged particles leaves a voltage drop at the polar caps which again causes pair production from incoming high-energy particles, it is this pair production that provides the charged particles which cause persistent radio emission.

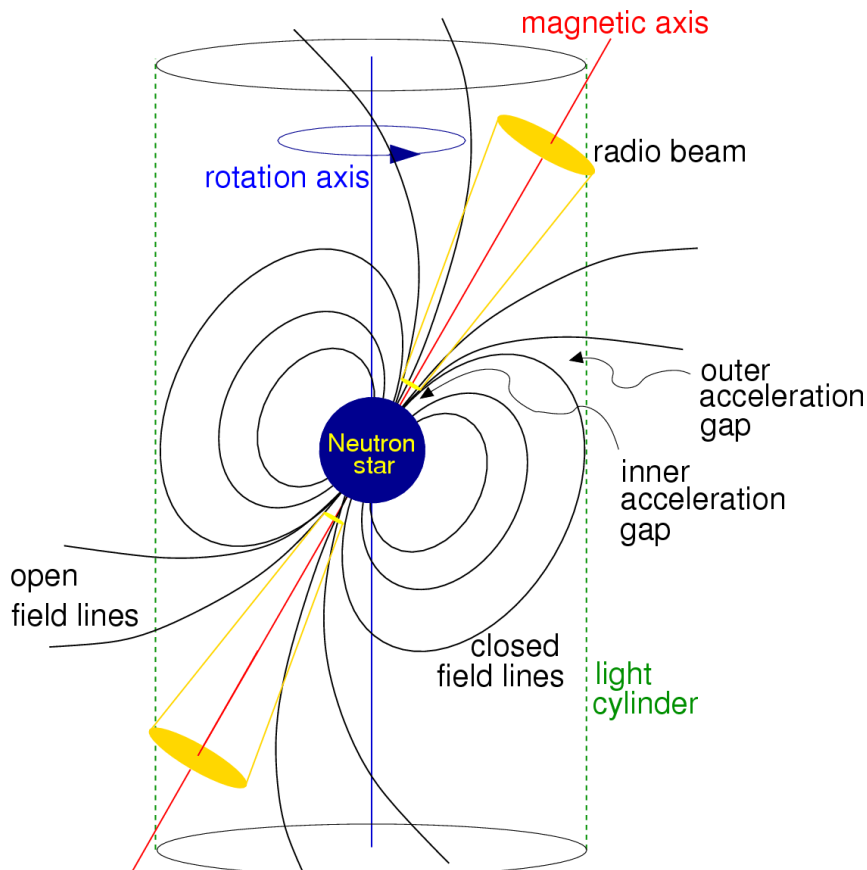


**Figure 1.2** – A schematic showing the lighthouse model. There is a co-rotating plasma with the magnetic field lines of the pulsar. The light cylinder is shown, with the open and closed field lines. Note the misalignment of magnetic and rotational axes. The inner and outer acceleration gaps are voltages generated via charge depletion. For the inner gap this is charges streaming along the open field lines; for the outer gap the depletion is from charges (of only one sign) escaping. It is thought that the outer acceleration gap may be the source of the gamma-ray emission seen in some pulsars (Cheng, Ho & Ruderman, 1986). Not to scale. Figure from Lorimer & Kramer (2005).

With each rotation of the pulsar the radio emission from one or, if the angle between magnetic and spin axes is large enough, both magnetic poles may be detected at the Earth.

Although the pulsar is in general emitting constantly, the radio emission from the poles is only detected when the beam is actually pointing to the Earth. Hence, the pulsar appears to “pulse” once per rotation, much like a lighthouse.

While the majority of pulsar observing takes place at radio frequencies ( $\sim 10$ 's MHz – 10's GHz) some pulsars are detectable in other frequency regimes. A handful of pulsars are detectable at optical wavelengths (e.g. the Crab pulsar, Cocke, Disney & Taylor 1969), while many more are detectable via their high energy emission (e.g. Abdo et al. 2010). The Fermi gamma-ray satellite has detected a total of 125 pulsars at the time of writing, these are mostly young pulsars on the  $P - \dot{P}$  diagram (Figure 1.3) with gamma-ray pulsations also detected for some millisecond pulsars (Abdo et al. 2009; Espinoza et al. 2013; see Section 1.1.5).

### 1.1.3 Observing and timing pulsars

Each pulse of radio energy corresponds to a single rotation of the pulsar. By measuring the Times Of Arrival of the pulses (TOAs) the apparent rotation rate of the pulsar as a function of time is measured, and then modelled (with a *timing solution*). The aim of the timing solution is to predict the TOAs for future pulses. Before a timing solution can be made however the pulsar must first be observed a number of times and TOA measurements made. The precision with which a TOA can be measured means there are systematic effects unrelated to the pulsar imprinted in the TOAs. There are several processing steps required to correct for these, and to generate an accurate TOA.

#### Barycentric Correction

The precision with which we can measure TOAs is sufficiently high that the Earth's motion around the Sun, and the Earth's rotation must be taken into account. This process is called barycentric correction and involves changing the observed TOA to what it would be if the observatory were located at the Solar System Barycentre (SSB), which is approximately the location of the Sun. A commonly used solar system ephemeris, which describes the motion of the Sun and planets, is the DE414 ephemeris from NASA JPL<sup>1</sup>. Using this ephemeris to calculate the position of the telescope relative to the SSB for the observation time, the difference in light travel time can be accounted for in the TOA. This forms an inertial

---

<sup>1</sup><http://ssd.jpl.nasa.gov/?ephemerides>

reference frame and stable location from which to “observe” the pulsar and to do long term timing from.

## Dispersion

Astronomical electromagnetic signals are affected by ionised intervening material between the source and the Earth; one of the main consequences is pulse dispersion. This needs to be corrected for, but also provides an opportunity to study the intervening ionised material.

Dispersion occurs because electromagnetic waves traversing an ionised medium experience a frequency dependent change in group velocity. The interstellar medium (ISM) is ionised by the ultra-violet emission of massive stars and supernovae. For continuous astrophysical signals dispersion is not observable, however for short time-scale pulsed emission, like pulsars, dispersion of the signal becomes important and measurable. In general, dispersion results in broadband, temporally narrow pulses at the pulsar being smeared in time at the observer.

For small electron densities,  $n_e \approx 0.03 \text{ cm}^{-3}$ , typical of the ISM (Ables & Manchester, 1976),

$$v_g^2 = c^2 \left( 1 - \frac{n_e e^2}{2\pi m_e \nu^2} \right), \quad (1.2)$$

where  $v_g$  is the group velocity of the radiation,  $m_e$  and  $e$  are the electron mass and charge respectively, and  $\nu$  is the propagating wave frequency. This means that the light travel time over a distance  $L$  is

$$T = \int_0^L \frac{dl}{v_g} = \frac{L}{c} + \frac{e^2 \int_0^L n_e dl}{2\pi m_e c \nu^2}. \quad (1.3)$$

These two terms are the light travel time in a vacuum plus the additional delay introduced by the frequency dependent group velocity of the waves. In this way the dispersion measure DM is defined as

$$\text{DM} = \int_0^L n_e dl \quad (1.4)$$

For DM in conventional units of  $\text{cm}^{-3} \text{ pc}$  the delay between pulse arrival time at infinite frequency and frequency (in MHz)  $\nu$  is given by

$$\delta t = 4.150 \times 10^3 \frac{\text{DM}}{\nu^2} \text{ s.} \quad (1.5)$$

The dispersion effect results in a quadratic drift in arrival time of a pulse across an observing band with observing frequency: the pulse energy at lower frequency is delayed relative to the pulse energy at higher frequency. Because dispersion spreads pulses in time it must be reversed to maximise the significance of a pulse measurement.

As the DM is the integrated column density of free electrons along the line of sight to the pulsar (see Equation 1.1.3), an estimated average density allows the inference of a distance. In practice, a model of the Galactic electron density is usually used for estimating the distance to a pulsar (Cordes & Lazio, 2002). Conversely, a pulsar with a known distance, for example from a parallax measurement, can be used to calculate the mean electron density along the line of sight.

The effect described here is only valid when there is no redshift, and the frequency of the pulsed radiation is the same at the source and observer. For cosmological distances dispersion is affected significantly by redshift (see Chapter 5).

## Residuals

When observing pulsars, one of the aims is to build a model that can predict the spin of the pulsar and thus future TOAs. There is a multitude of reasons why the pulse period will change with time, including but not limited to, position, proper motion, orbital motion, general relativistic effects, and eclipses. These phenomena are modelled in a timing solution for a particular pulsar. With such a model and a set of observations, the timing residuals,  $R$ , are calculated as

$$R = \text{TOA}_{\text{obs}} - \text{TOA}_{\text{m}} \quad (1.6)$$

where  $\text{TOA}_{\text{obs}}$  is the corresponding observed TOA, and  $\text{TOA}_{\text{m}}$  is the model prediction. A good timing solution results in  $R$  which are Gaussian distributed noise; the rms of this noise is then a measure of the timing stability of a pulsar, or of the limitations of the instrumentation. Once a timing model has been generated the residuals may be used to detect other phenomena, for example correlating multiple pulsars' residuals simultaneously to look for gravitational wave signatures (see Section 1.1.6).

### 1.1.4 Fundamental parameters

The rotation of pulsars is usually extremely stable and predictable. The most common term attributable to the pulsar is an increasing pulse period,  $\dot{P}$ , indicating that they are slowing down and losing energy. Pulsars lose energy in a number of ways including through dipole radiation, radio emission, and gravitational wave emission. A pulsar may be approximated as a dipole magnet and will therefore lose energy via the emission of electromagnetic waves at its spin frequency (magnetic dipole radiation). With typical rotation frequencies of 1 – 700 Hz we are not able to measure this radiation directly as it cannot propagate through the ionised ISM. Based on assuming that the slow down of a pulsar's spin rate is due to the emission of magnetic dipole radiation, and using a best known value for the NS moment of inertia, the rate of energy loss,  $\dot{E}$ , can be derived from its slowdown. The energy,  $E_{\text{rot}}$ , of a rotating sphere is given by

$$E_{\text{rot}} = I\Omega^2, \quad (1.7)$$

and

$$\frac{dE_{\text{rot}}}{dt} = -I\Omega\dot{\Omega}, \quad (1.8)$$

where  $I$  is the moment of inertia and  $\Omega = \frac{2\pi}{P}$  is the rotational angular frequency. In terms of measured  $P$  and  $\dot{P}$ ,  $\dot{E}_{\text{rot}}$  is therefore described as

$$\dot{E}_{\text{rot}} = \frac{dE_{\text{rot}}}{dt} = -\frac{4\pi^2 I \dot{P}}{P^3}. \quad (1.9)$$

This is found to far exceed the energy lost via radio emission as measured by the pulsar

luminosity. The energy loss is therefore likely dominated by the dipole radiation and a wind of particles streaming away from the pulsar.

By equating the calculated  $\dot{E}_{\text{rot}}$  to the energy lost by a rotating dipole  $\dot{E}_{\text{dip}}$ , the magnetic field strength at the surface  $B_{\text{surf}}$  of the NS can be approximated. The energy radiated by a magnetic dipole of moment  $\mathbf{m}$  is given by

$$\dot{E}_{\text{dip}} = \frac{2}{3c^3} |\mathbf{m}|^2 \Omega^4 \sin^2 \alpha, \quad (1.10)$$

where  $c$  is the speed of light and  $\alpha$  is the angle between the rotational and magnetic axes. Approximating the dipolar magnetic field strength,  $B \approx \frac{|\mathbf{m}|}{r^3}$ , it is found that

$$B_{\text{surf}} = \left( \frac{3c^3}{8\pi^2} \frac{I}{R^6 \sin^2 \alpha} P \dot{P} \right)^{\frac{1}{2}}, \quad (1.11)$$

where  $R$  is the radius of the pulsar. Taking canonical values of  $\alpha = 90^\circ$  (an orthogonal rotator),  $I = 10^{45} \text{ g cm}^2$ , and  $R = 10 \text{ km}$  we find that a useful approximation to the *surface* dipole magnetic field is

$$B_{\text{surf}} \approx 3.2 \times 10^{19} (P \dot{P})^{\frac{1}{2}} \text{ G}. \quad (1.12)$$

This is an order of magnitude approximation as  $I$  and  $R$  are not well known and  $\alpha$  is usually unknown for a given system.  $B_{\text{surf}}$  is however a useful parameter which differs by many orders of magnitude between types of pulsar (see Figure 1.3).

Given an observed spin-period,  $P$ , now and a period derivative  $\dot{P}$  we can calculate the age of the pulsar. How long has it been slowing down in order to reach its current spin period? To calculate this we express change of rotation with time as

$$\dot{\Omega} = -\frac{2|\mathbf{m}|^2 \sin^2 \alpha}{3Ic^3} \Omega^3 \quad (1.13)$$

By generalising Equation 1.13 to be for a power law  $n$  such that  $\dot{P} \propto KP^{2-n}$  where  $P = 2\pi/\Omega$  and integrating, the age of the pulsar is found to be

$$T = \frac{P}{(n-1)\dot{P}} \left( 1 - \left( \frac{P_0}{P} \right)^{n-1} \right), \quad (1.14)$$

where  $P_0$  is the spin period of the pulsar at birth. Assuming that the pulsar has slowed significantly since birth  $P \gg P_0$  and that the spin down *can* be approximated as solely due to dipole radiation ( $n = 3$ ) then the *characteristic age*,  $\tau_c$ , is given by

$$\tau_c = \frac{P}{2\dot{P}}. \quad (1.15)$$

The characteristic age is an approximation because the birth period of a pulsar is usually unknown. In cases when the pulsar has an associated supernova remnant and a measured velocity then a second measure of the time since the supernova, and hence the age of the pulsar, is possible (e.g. Kramer et al. 2003b). This is limited to the youngest pulsars as supernova remnants may only survive for  $\sim 10^4$  yrs whereas pulsar lifetimes may be  $> 10^7$  yrs (Frail, Goss & Whiteoak, 1994).

### 1.1.5 Pulsar Families

Given that a measurement of  $P$  and  $\dot{P}$  provide so much insight into a pulsar's properties, a plot of  $\dot{P}$  against  $P$  illustrates the wide range of the known pulsar population (see Figure 1.3). Also apparent from the  $P - \dot{P}$  diagram are the many sub-classes of pulsar. The many orders of magnitude difference in their properties points to fundamental differences in origin and/or evolution.

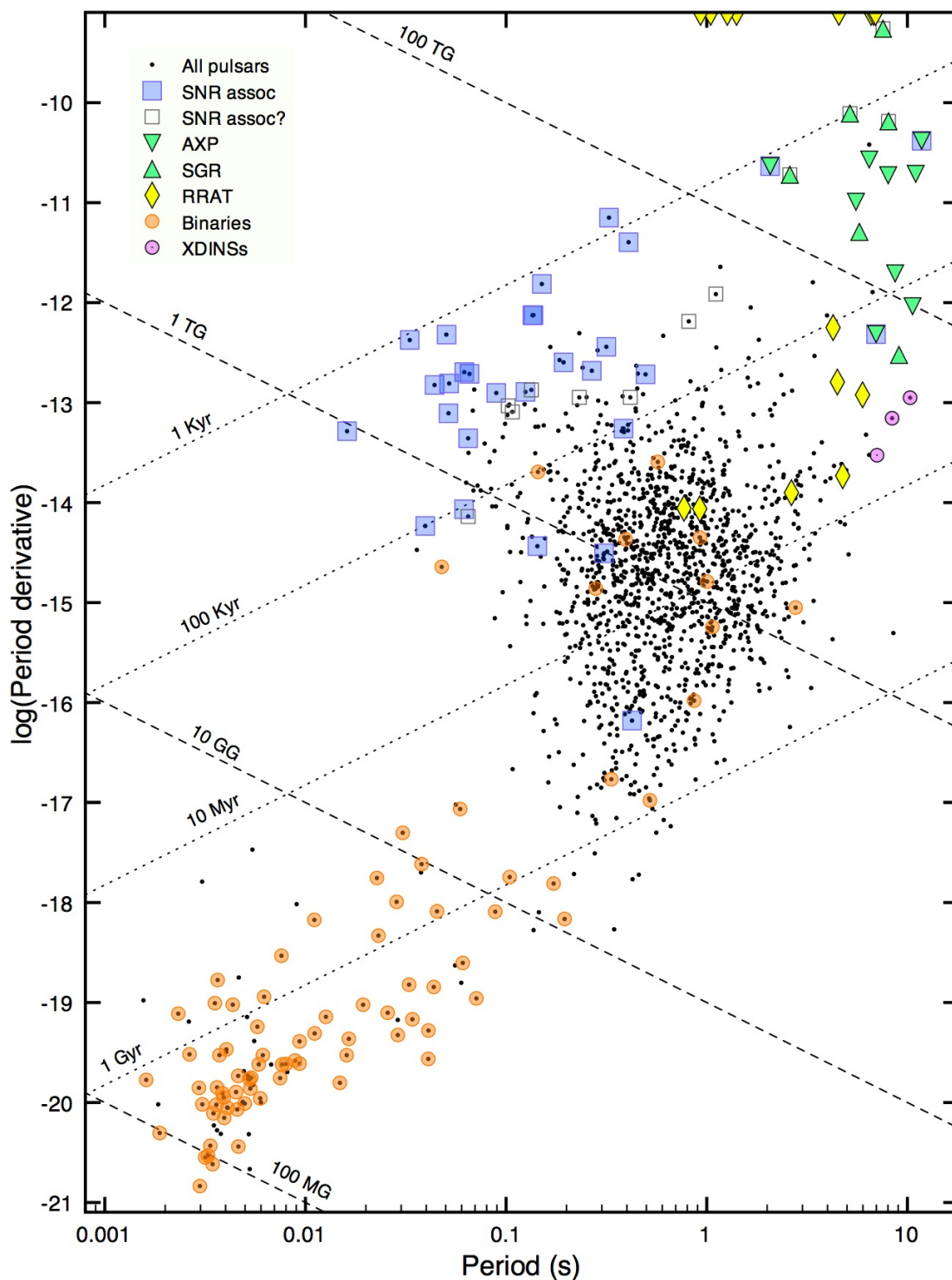


**Figure 1.3** – This is a logarithmic plot of  $\dot{P}$  against  $P$ . Lines of constant surface magnetic field strength and characteristic age are plotted (see Section 1.1.4). See text for descriptions of some of the sub-families shown here. Figure from Cristobal Espinoza.

There are many types of pulsar, however this thesis is concerned largely with the *normal* and *recycled* pulsars. X-ray binaries will also be discussed as they are thought to be the precursors to recycled pulsars (Bhattacharya & van den Heuvel, 1991). Some of the key attributes of these families are outlined in Table 1.1.

	$P$ (s)	$\dot{P}$	$B_{\text{surf}}$ (G)	$\tau_c$ (yr.)	Binary?
Normal	0.3–6	$10^{-16}$ – $10^{-14}$	$\sim 10^{11}$ – $10^{13}$	$\sim 10^7$	1%
Recycled	$< 30^{-3}$	$10^{-21}$ – $10^{-18}$	$\sim 10^8$ – $10^{10}$	$\sim 10^9$	$\sim 80\%$

**Table 1.1** – Table showing some of the key parameters for different pulsar families. Note the larger characteristic ages of recycled pulsars and the large proportion of recycled pulsars in binary systems.

### Normal Pulsars

Normal pulsars are found on the right of the  $P - \dot{P}$  diagram and have spin periods of around 0.1 – 4 s; they make up the majority of known pulsars. As can be seen in Figure 1.3 the youngest normal pulsars often have supernova remnant associations, which as previously mentioned, can provide an indication of their true age.

Normal pulsars are located throughout the Galaxy concentrated at low Galactic latitudes. This proximity to the Galactic plane is thought to be because this is where NS progenitors - massive stars - reside. Although normal pulsars are high-velocity objects (with typical velocities of  $450 \pm 90 \text{ km s}^{-1}$ ; Lyne & Lorimer 1994) they are not observable as pulsars for sufficient time for their velocities to carry them far from the Galactic plane. These high velocities are generated by an asymmetric kinematic kick during the ccSN. The rarity of normal pulsars in binary systems is also explained by this kick, which along with the sudden mass loss from system from the system during ccSN makes orbital disruption likely (Hills, 1983).

One of the interesting things about young normal pulsars in particular is they sometimes exhibit glitches. A glitch is a sudden increase in the spin-period followed by a slow return to normal spin-down (e.g. Espinoza et al. 2011). It is thought that perhaps glitches are

caused by changes in configuration of superfluid vortices in the interior of the NS, and as such are a probe of the NS equation of state (Anderson & Itoh, 1975; Alpar et al., 1984). Normal pulsars are not discussed in detail as this thesis concentrates on recycled pulsars and transients.

## Recycled pulsars

The pulsars to the bottom left of the  $P - \dot{P}$  diagram, with smaller values of  $P$  and  $\dot{P}$  form a distinct group. These pulsars have much lower magnetic field strengths and higher characteristic ages than the normal pulsars (see Table 1.1). They are more likely to have an orbital companion, with 80% of recycled pulsars found in binary systems, compared to just 1% of normal pulsars. This prevalence of binary systems provides a clue to their formation.

The progenitors of NSs are massive stars (or WDs); a large fraction of which are found in binary systems (Lada, 2006). The more massive of the two stars will have a shorter lifetime and, if sufficiently massive, undergo core collapse supernova (ccSN) first (see Section 1.1.2). The remnant of the stellar core may form a NS, which in turn could be a detectable pulsar. The fact that most observed normal pulsars are isolated implies that their progenitor's original stellar binary disrupted during this first ccSN. Pulsars that remain gravitationally bound to their companion post-ccSN may then be further affected by the evolution of the companion.

Recycled pulsars are thought to have undergone a *spin-up* phase in their history. Spin-up involves the accretion of material from an orbiting companion onto the NS (Alpar et al., 1982). This accretion begins when the companion/donor star ages and expands, filling its *Roche lobe*<sup>2</sup>. At this stage material from the edge of the donor can fall freely into an accretion disk surrounding the NS, frictional heating of material in this disk can produce persistent x-ray emission. At the Alfvén radius this material moves along the open magnetic field lines of the NS onto the polar regions, producing pulsed x-ray emission. This mass transfer increases the angular momentum of the NS and its spin-period decreases. Accretion also appears to decrease the surface magnetic field strength of the pulsar by several orders of magnitude, which in turn reduces the  $\dot{P}$  of the pulsar, although it is unclear how this field strength reduction takes place.

During the spin-up phase the systems are thought to be observed as an x-ray binary

---

<sup>2</sup>The Roche lobe is the gravitational potential equilibrium surface located between the two centres of mass in a binary system.

as the material is heated upon accretion to the NS magnetic poles emitting x-rays. These *x-ray binaries* are thought to be separable into two broad types: High and Low Mass X-ray Binaries (HMXB and LMXB respectively) (Bhattacharya & van den Heuvel, 1991). This nomenclature describes the mass of the donor star with LMXBs having  $M_{\text{donor}} = 1 - 8 M_{\odot}$  and HMXB having  $M_{\text{donor}} > 10 M_{\odot}$ .

This evolutionary link between x-ray binaries and recycled pulsars was strengthened with the discovery of SAX J1808.4–3658, an x-ray binary exhibiting periodic intensity fluctuations with a period of 2.4 ms (Wijnands & van der Klis, 1998). More recently the observation of x-ray emission modulated by both the pulsar spin period and the binary period in PSR J1023+0038, which is now observed to emit radio pulsations, further strengthens the spin-up model of recycled pulsar formation (Archibald et al., 2010).

HMXBs have a donor sufficiently massive to undergo ccSN, providing a strong kinematic kick to the system (Lyne & Lorimer, 1994). This kick and the mass loss during ccSN from the companion could either disrupt the binary totally or impart a significant eccentricity to the orbit (e.g. Chaurasia & Bailes 2005). What remains is therefore either an eccentric Double Neutron Star (DNS) system, for example PSR B1913+16 (Hulse & Taylor, 1975) and PSR J0737–3039 (Burgay et al., 2003; Lyne et al., 2004), or two isolated NSs. In both cases, one NS has undergone a spin-up phase while the other is a normal NS (either of which may be observable as a pulsar). The accretion and spin-up phase in a HMXB is unstable and relatively short-lived lasting around  $10^5$  years (Tauris & van den Heuvel, 2003). This means that relatively little angular momentum is transferred and the final spin period of the recycled pulsar,  $P \sim 10^{-2}$  s. Mildly recycled pulsars are expected to form one of the NSs in a DNS systems (the other would be a normal pulsar, which may not live long enough to be observed). These pulsars are referred to as *mildly recycled*.

LMXBs are formed when the companion to the NS has insufficient mass to undergo a ccSN. The companion instead reaches the end of its life as a red giant star with the expulsion of the outer layers, leaving a degenerate core supported by electron degeneracy pressure – a White Dwarf (WD). The long lived ( $\sim 10^7$  years) period of stable mass transfer means the pulsar can be spun-up to periods,  $P \lesssim 10$  ms with extremely low  $\dot{P}$ , and consequently (relatively!) low inferred surface magnetic field strength (Tauris & van den Heuvel, 2003). Tidal forces during the accretion phase also act to circularise any orbital eccentricity induced during the first ccSN (Bhattacharya & van den Heuvel, 1991). The LMXB mass transfer stage does not culminate in a second ccSN as the companion is not sufficiently massive, so no further eccentricity is induced. This explains why Galactic field MSP-WD binaries usually have a low orbital eccentricity ( $e < 10^{-3}$ ) (Phinney, 1992). The pulsars

thought to have evolved in these systems are called the fully recycled pulsars, or *Millisecond Pulsars* (MSPs).

The fact that most recycled pulsars are found in binaries is in agreement with the spin-up evolution scenario, however 20% of recycled pulsars in the Galactic field are isolated<sup>3</sup>. There are two broad scenarios to explain isolated recycled pulsars; the first is disruption of the orbit during the companion ccSN as the HMXB phase comes to an end; the second is that the pulsar has destroyed its companion through ablation by its pulsar wind (Ruderman, Shaham & Tavani, 1989). Systems currently undergoing ablation are so-called *Black Widow* systems (Fruchter, Stinebring & Taylor, 1988), these consist of an MSP with a ultra-low mass companion ( $M_c \sim 10^{-2} M_\odot$ ). In black widow systems the radio pulses from the pulsar are observed to be eclipsed by ionised material surrounding the companion when the pulsar passes behind the companion (superior conjunction) and, if the orbital inclination is favourable, eclipsed by the companion itself (e.g. PSR B1957+20; Fruchter, Stinebring & Taylor 1988). These eclipsing regions have sizes that are a significant fraction of the orbital separation, and often the material may not be gravitationally bound to the companion, therefore possibly requiring replenishment (e.g. Stappers et al. 1996).

As well as black widow systems there are so-called *Redback* systems which have a more massive ( $M_c \sim 10^{-1} M_\odot$ ) companion, often seen to be non-degenerate in optical studies (Roberts, 2011). These systems have been observed to have Roche lobe filling factors of 0.1 – 0.4, and as such are possibly an intermediate stage between x-ray binaries and Galactic field MSP binary systems (Breton et al., 2013). The timescale for total ablation of the companion is however too long to explain the observed number of isolated MSPs (Eichler & Levinson, 1988; Stappers et al., 1996).

The close links in the stellar evolution of the two bodies in a MSP-WD binary means that one may be used to study the other. It is known that recycled pulsar characteristic ages are unreliable (Tauris, 2012). This unreliability comes from assumptions about the spin-down evolution and the birth period of the pulsar (the spin period when accretion ceases in the recycled case). A WD companion to a recycled pulsar can provide another measure of the system age, and therefore of the pulsar (see Chapter 3).

---

<sup>3</sup>MSPs in Globular Clusters (GCs) are not considered here because of their significantly different environments (primarily the high stellar density increasing the chances of dynamical interaction)

### 1.1.6 Why are pulsars interesting?

Pulsars and their surroundings are some of the most remarkable astrophysical environments we know of, combine this with often stable rotation rates (particularly of MSPs), and pulsars constitute a laboratory for extreme physics unachievable on Earth. The study of extreme gravitational, quantum, electromagnetic, and stellar physics are all possible. In combination, pulsar populations and distributions can be used to study Galactic physics.

There are currently nearly  $\sim 2200$  known pulsars and this is increasing by  $\sim 100$  per year (Lorimer, 2010). Lorimer also states that this rate is expected to grow in the future as more powerful instruments and telescopes become available, for example LOFAR, the LOW Frequency ARray (van Leeuwen & Stappers, 2010), ASKAP, the Australian Square Kilometer Array Pathfinder (Johnston et al., 2007; Stairs et al., 2011), MeerKAT (B. Stappers, *private communication*) and the SKA, the Square Kilometer Array (e.g. Smits et al. 2009).

Of great interest are pulsars in orbital systems with another body, particularly those where general relativistic effects can be measured. In addition *clean* orbital systems - those with no ongoing mass transfer or mass loss - are important targets. Finding more pulsars in binary systems with another NS (e.g. Champion et al. 2004) or, even more excitingly, two observable pulsars orbiting one another (like PSR J0737–3039A/B system; Burgay et al. 2003; Lyne et al. 2004), is an important goal. The conclusion of this “wish list” of systems would be a pulsar in a close orbit with a black hole which could provide excellent tests of gravity, stellar dynamics and evolution, and is a current goal of pulsar searching (Faucher-Giguère & Loeb, 2011). Some examples of how pulsars are being used follow.

Gravitational waves are “ripples” in spacetime, caused by accelerating massive bodies, predicted by general relativity. Accelerating masses lose energy via this mechanism, with measurable consequences. PSR B1913+16 is a  $P = 59$  ms pulsar in a  $7^{\text{hr}}45^{\text{min}}$  binary orbit with another NS (not seen as a pulsar). Timing measurements enabled determination of a changing epoch of periastron. This measurement was in excellent agreement with the prediction from general relativity (see Figure 1.4): this constitutes the first, indirect evidence for the existence of gravitational waves (Taylor & Weisberg, 1982).

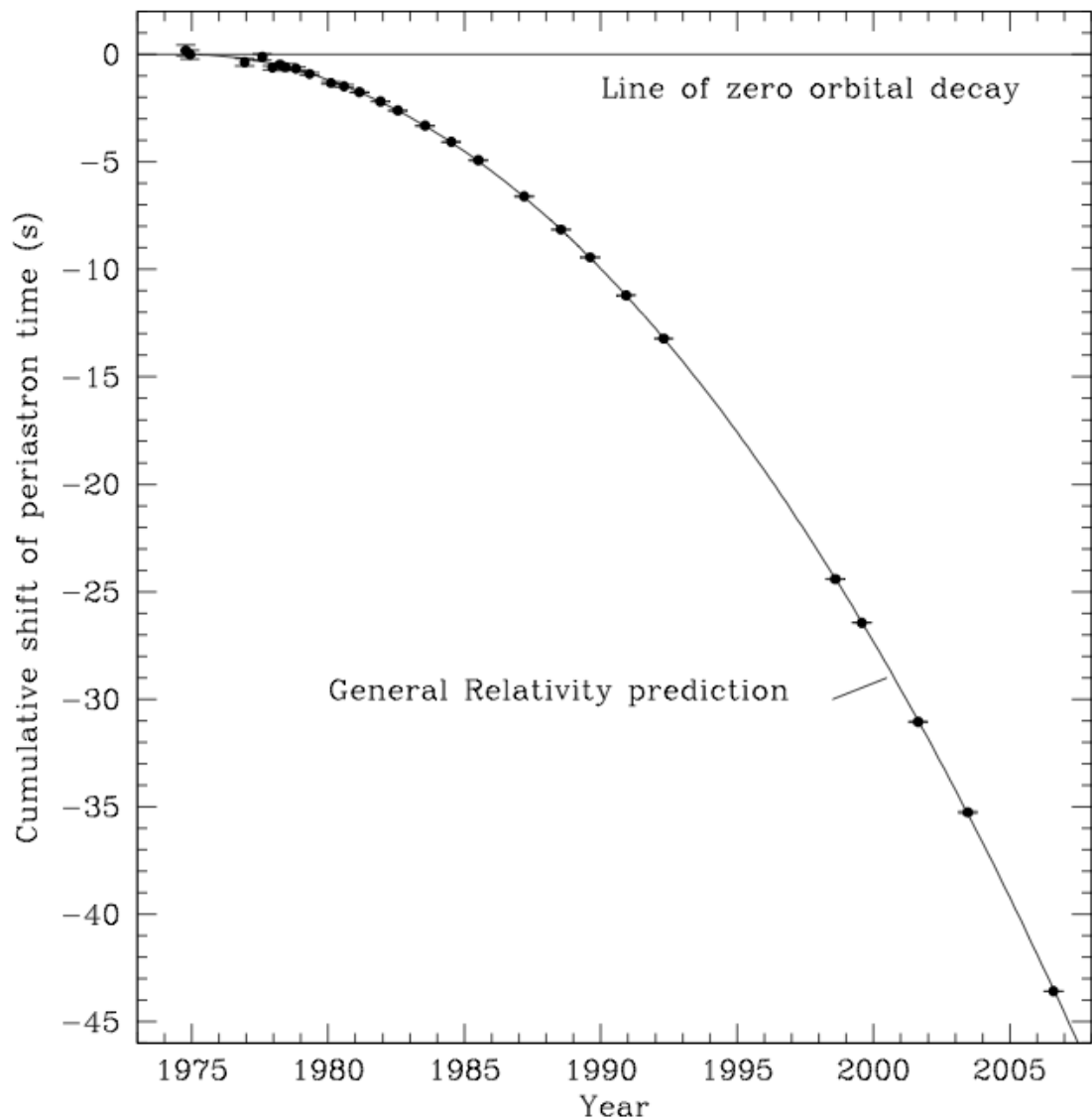


**Figure 1.4** – Orbital decay for the PSR B1913+16 system. The straight line indicates zero orbital decay and the curved line is the general relativistic prediction which predicts extremely closely the measurements. Figure from Weisberg, Nice & Taylor (2010).

As a gravitational wave passes a pulsar and the Earth, unmodelled variation in the timing residuals is induced. In the timing residuals of a single pulsar it is not possible to distinguish variation due to gravitational waves. A gravitational wave signal, however, produces timing residuals with a quadrupolar correlation between different pulsars, see Figure 1.5 (Hellings & Downs, 1983). By correlating timing residuals between a number of pairs of pulsars a gravitational wave signal can be separated from other uncorrelated effects (Ro-

mani, 1989; Foster, 1990). The high accuracy of TOA determination of some MSPs (often sub  $\mu\text{s}$ ), combined with stable long term timing (timing residuals with rms  $< 100$  ns over baselines of several years) (Verbiest et al., 2009) mean they can be used as accurate clocks and are suited for use in the the search for gravitational waves.

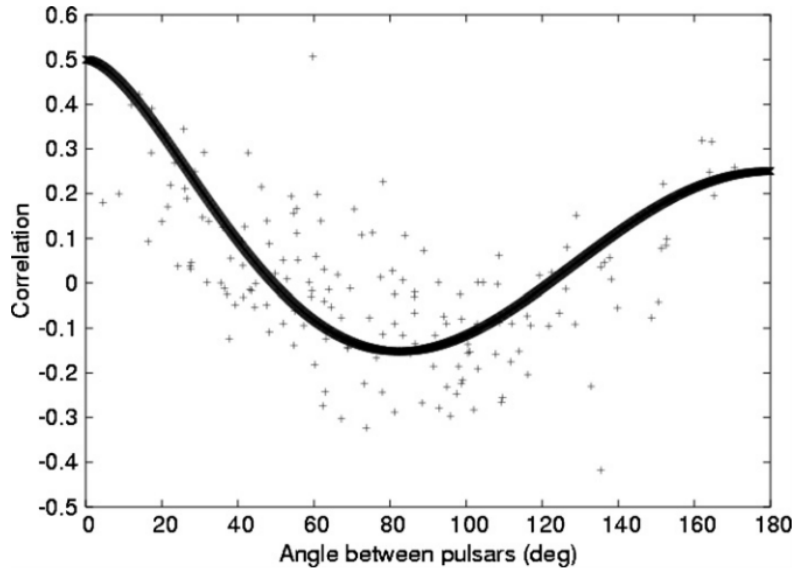


**Figure 1.5** – The simulated correlation in timing residuals (the points) between pairs of pulsars separated by angle  $\theta$ , the line indicates the theoretical correlation curve for an isotropic gravitational wave background (Hobbs et al., 2010).

Groups of MSPs are being observed and timed in an effort to detect and measure gravitational waves. These experiments are called Pulsar Timing Arrays (PTAs). The observing baseline of PTAs is  $\sim$  years, and they are therefore most sensitive to gravitational waves in the nHz regime. At these frequencies, the likely source of gravitational waves is a background from many supermassive black hole binaries in the centre of galaxies (Sesana, Vecchio & Volonteri, 2009). This is complementary to Earth-based gravitational wave detector experiments like LIGO, the Laser Interferometer Gravitational-Wave Observatory (Abbott et al., 2009), Virgo (Acernese et al., 2006) which are most sensitive in the mHz to kHz regime.

The three main PTA projects - the European PTA (EPTA), the Parkes PTA (PPTA), and the North American Nanohertz Observatory for Gravitational waves (NANOGrav) - are ongoing in their pulsar timing and analysis (Manchester et al., 2013; Jenet et al., 2009). Recent results have placed limits on gravitational wave backgrounds from different sources (e.g. van Haasteren et al. 2011; Sanidas, Battye & Stappers 2012). In the future, a corre-

---

lation between timing residuals as shown in the Figure 1.5 will form the detection. It is predicted that a gravitational wave detection may be made in the next decade using PTAs (Sesana, 2013).

A further example of what can be achieved with relativistic pulsar binaries is the double pulsar system PSR J0737–3039. Kramer et al. (2006b) measured the post-Keplerian (PK) parameters (relativistic corrections to the non-relativistic Keplerian orbital case) of the system to accurately constrain both pulsar masses. Their results are shown in Figure 1.6.

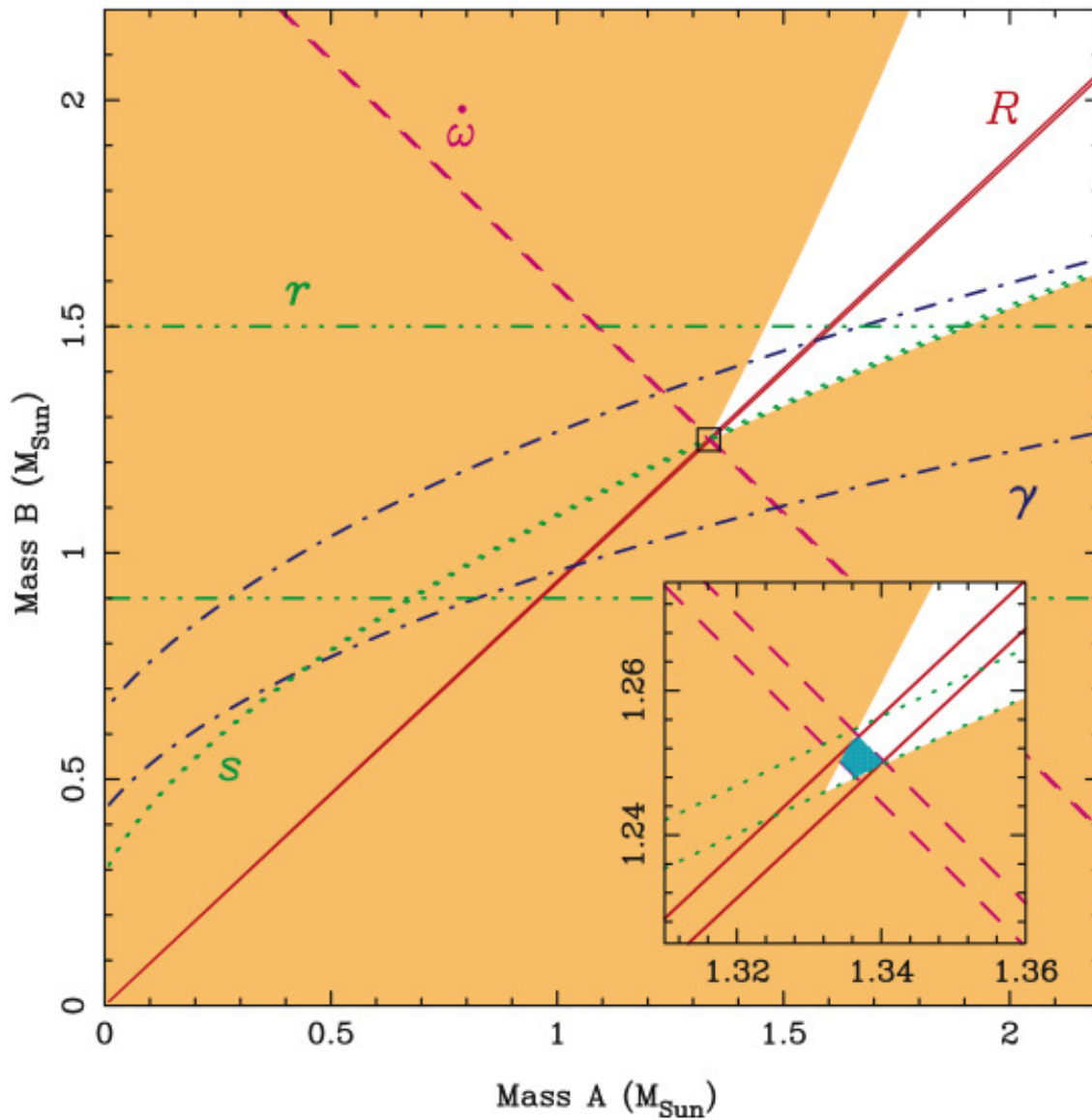


**Figure 1.6** – A plot of the mass of the pulsar A against the mass of pulsar B; a “mass-mass” plot. The orange shaded regions are forbidden by Keplerian the Keplerian mass functions of both pulsars (see Chapter 3), and the various constraints from each PK parameter are shown. The subplot is an enlarged plot of the region indicated by the square around the tightest constrained region. Note that there are consistent values for  $m_A$  and  $m_B$  which satisfy all constraints (grey region of inset).  $r$  and  $s$  describe the magnitude and shape of the Shapiro delay,  $\dot{\omega}$  is the advance of periastron,  $\gamma$  is the gravitational redshift, and  $R$  is mass ratio  $\frac{m_A}{m_B}$ . Figure from Lyne et al. (2004). This system provides the most accurate test of relativistic gravity yet known.

Finding bright MSPs (with sub  $\mu\text{s}$  TOAs and low rms of residuals) to incorporate in to PTAs is an important goal of pulsar searching. In addition, there are many other interesting possible sources to discover in a high time resolution radio survey. For example eclips-

ing Black Widow and Redback systems (Bates et al., 2011), double neutron star systems (Champion et al., 2004), pulsars with planetary mass orbital companions (Bailes et al., 2011), and radio-loud magnetars (Levin et al., 2010). This is why we search for pulsars.

## 1.2 Radio Transients

The high temporal and spectral resolution instrumentation developed for studying pulsars also lends itself to detecting other transient radio signals. These radio transients may either be from NSs or some other source class entirely. In the context of this thesis radio transients mean narrow ( $\sim$  ms) pulses or bursts of radio waves which may or may not repeat.

### 1.2.1 Rotating Radio Transients

McLaughlin et al. (2006) found many single bright pulses in the survey data from the Parkes Multibeam Pulsar Survey (PMPS; Manchester et al. 2001). These pulses were observed to repeat in the same direction with the same DM and were named *Rotating Radio Transients* (RRATs). RRAT pulses however did not repeat regularly, like those of pulsars, and were more easily detectable as single isolated pulses than as a repeating signal (see Chapter 2). Consequently, RRAT pulses have typical flux densities considerably higher (peak flux density  $S_{\nu, \text{peak}} \sim 10^2 - 10^3$  mJy) than single pulses from pulsars discovered in recent surveys ( $S_{\nu, \text{peak}} \sim$  mJy).

With this in mind Keane et al. (2011) define an RRAT as

*[...] a repeating radio source, with underlying periodicity, which is more significantly detectable via its single pulses than in periodicity searches*

This broad definition means that whether a radio pulsar is classed as a RRAT depends on its detectability, and therefore the instrumentation used. The equivalence of radio pulsars and RRATs, except for the method of highest SNR detection, is also implied.

The difficulty in detecting RRATs implies a very large undetected population; the implied supernova rate for the Galaxy is insufficient to support such a large population (Keane & Kramer, 2008). Either, the population is overestimated, a distinct possibility for extrap-

ulations from a small number of known sources; or RRATs are somehow evolutionarily linked to other families of pulsars (Keane et al., 2011).

When observed regularly over a long period of time, the time of arrival of each RRAT pulse was measured. Underlying periodicities of 0.1 – 7.7 seconds were found, periods typical of pulsars, if somewhat slow. Measurements of period derivative,  $\dot{P}$  have also been made (e.g. Keane et al. 2011): RRATs’ position in the  $P - \dot{P}$  diagram is near to that of magnetars, with some among the normal pulsars (see Figure 1.3).

The high brightness temperature of the radio emission from pulsars and RRATs indicates that the emission mechanism must be coherent. For a coherent mechanism to be causing the emission, the emitting region must be causally connected. The size of the coherent emission region is therefore defined by the light travel time across it, and consequently the observed pulse width provides an upper limit on this size. Typical observed pulse widths of several milliseconds for RRATs indicate the emission region size must be  $\lesssim 300$  km, smaller than typical white dwarf radii, another indication this is pulsar-type radio emission.

### 1.2.2 Highly dispersed radio bursts

As well as RRATs, some single bursts have been observed. One of these was found to have an anomalously high DMs, compared to maximum DM that the MW may impart to the signal. These bursts have never been observed to repeat, possibly indicative of an origin in a cataclysmic event. This would make these bursts entirely different from pulsars and RRATs whose pulses are an artefact of rotation. The first of these was discovered in a radio (1.4 GHz) survey of the Magellanic clouds using the 64-m Parkes radio telescope (Manchester et al., 2006; Lorimer et al., 2007); it has since been referred to as the “Lorimer burst” (LB; see Figure 1.7). The LB occurred on the 24th July 2001 with a simultaneous detection made in three beams of the 13-beam receiver (Lorimer et al., 2007).

With a variety of techniques, including pulsar measurements, the approximate 3-dimensional mapping and modelling of ionized material in the Milky Way has been possible (Cordes & Lazio, 2002). By using this map we can approximate the maximum DM that a source located in the Galaxy could have as function of position on the sky. The LB had a dispersion measure,  $DM = 375 \text{ cm}^{-3} \text{ pc}$ ; much greater than the model Galactic contribution in the source’s direction,  $DM_{\text{MW}} = 25 \text{ cm}^{-3} \text{ pc}$ . The direction of the LB was approximately  $3^\circ$  from the center of the small Magellanic cloud (SMC). The highest DM of any known pulsar attributed to the SMC is  $DM_{\text{SMC}} = 205 \text{ cm}^{-3} \text{ pc}$ ; which itself is atypically high because of

a known intervening ionised HII region (Manchester et al., 2006). This disparity between what may be attributed to the “local” environment (the Galaxy and the SMC) and measured DM implied another source of dispersion: possibly the inter-*galactic* medium (IGM).

The IGM is thought to have a much lower free electron density than the Milky Way. The amount of dispersion per unit distance is consequently much lower for the IGM, and a given DM in the IGM corresponds to a much greater distance than the same DM in the MW (Inoue, 2004). In the case of the LB, the co-moving distance to the source would therefore be  $\sim 500$  Mpc. These kind of bursts would therefore be of cosmological significance in their ability to measure the ionisation state of the IGM and the universe.

In the years after the discovery of the LB there was much controversy as to whether it was indeed of astronomical origin as no other similar events were found. In addition to the lack of similar signals, swept-frequency pulses of Radio Frequency Interference (RFI) called *peryttons* have been identified in observations using the 64-m Parkes telescope. It has been suggested that some parameters (particularly the “dispersive” delay across the observing band) of the LB closely match those of peryttons and that the LB may be a peryton (Burke-Spolaor et al., 2011a; Bagchi, Nieves & McLaughlin, 2012)

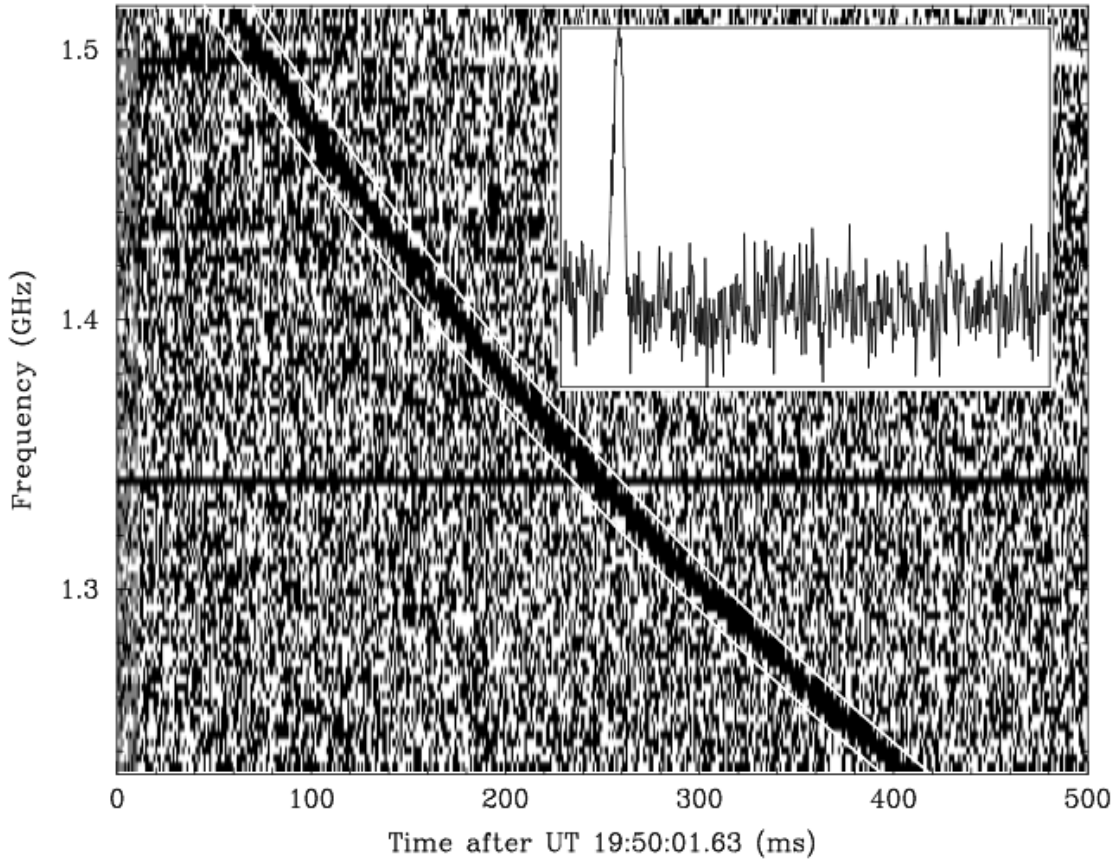


**Figure 1.7** – The dynamic spectrum of the LB in one of the receiver beams which did not saturate. The dispersive sweep with frequency, across the observing band is apparent. The white lines bounding the pulse follow the theoretical dispersion law (see Equation 1.1.3 and Chapter 2). The inset burst shape is obtained by correcting this dispersive sweep before summing all the channels together. Figure from Lorimer et al. (2007).

The uncertain status of the LB continued until Keane et al. (2012) presented a second similar burst with an anomalously high dispersion measure,  $DM = 746 \text{ cm}^{-3} \text{ pc}$ . However, this burst occurred in a direction that was separated by just  $4^\circ$  from the Galactic plane; a line of sight that passes through more, denser ionised ISM. The maximum Galactic DM contribution is therefore a significant fraction of the measured value,  $DM_{\text{Milky Way}} = 553 \text{ cm}^{-3} \text{ pc}$ . It has been shown there is significant uncertainty in the NE2001 model used for Galactic dispersion (Gaensler et al., 2008; Deller et al., 2009) and it is possible that the KB is of Galactic origin.

Large scale surveys of the radio sky provide an opportunity to find more of these bursts. Surveys away from the Galactic plane may be particularly important; if these bursts are

---

extragalactic then there will be no preferred direction for the sources with regards to the Milky Way. Dispersion from the Milky Way is simply a foreground whose effect is at a minimum when looking away from the Galactic plane. Therefore, for a given DM limit of a survey, bursts can have a greater contribution to their DM in directions away from the Galactic plane, and consequently be further away. While the rate of these bursts appears to be high, the field of view of a typical radio telescope is small, meaning a lot of observing time (several weeks to months with a Parkes size telescope) is required before their detection would be expected. Consequently, as much as possible time on sky is required, large pulsar surveys currently best achieve this goal.

# Chapter 2

## Searching and the High Time Resolution Universe survey

### 2.1 Pulsar Searching

Finding new pulsars has become an increasingly complex task. The first pulsars were found by detecting single pulses in the sampled power signal from the focus of a radio telescope, even without correcting for propagation effects which may have affected the pulsar signal (Hewish et al., 1968). This was only possible for the brightest and nearby pulsars. In its most basic form modern searches for pulsars rely on maximising the signal to noise ratio (SNR) by correcting for propagation effects and integrating multiple pulses. This requires knowledge of the periodicity of the pulsar the pulse period,  $P$ , and the dispersion measure, DM, which quantifies the amount of dispersion during propagation (see Section 1.1.3). The most basic pulsar searching equates to a blind search over these two parameters.

Pulsars usually emit across a broad frequency range from 10s of MHz upto 10s GHz and are therefore searched for with receivers with the widest possible bandwidths. In searches for radio pulsars the data is a sampling of the voltages induced by radio frequency electromagnetic radiation. The wide observing band is split into sub-bands or channels enabling the partial correction of the effects of the ionised interstellar medium (see section 2.1.2). The voltages are squared to form the power in each channel is integrated for the sampling period and the value is digitised. This sampling period defines the temporal resolution of the data, limiting the narrowest pulses and shortest spin period it is possible to detect. Most radio-pulsar search data therefore consists of a 2-dimensional array of samples where  $n_{\text{chan}}$

channels are sampled every  $t_{\text{samp}}$  seconds; this format is called *filterbank* data.

In addition to searching for repeating signals, so-called Fourier searching, there is *single pulse searching*. Single pulse searching is different from Fourier searching in that the repetition rate, if there is one, is not useful in improving sensitivity. While any repetition of single pulses may not be useful in aiding detectability in searching, it can be useful if found in a more detailed analysis both for the nature of the source, and also for proving it is a truly astronomical signal. Single pulses are as narrow, or even narrower, than a pulsar pulse, and dispersed. A survey can be sensitive both to periodic pulses from pulsars and single pulses of radio waves with the same telescope, receiver, and processing hardware. Pulsar survey filterbank data is therefore also suitable for searching for non-periodic pulses.

### 2.1.1 Sensitivity

The sensitivity of a survey for radio pulsars can be quantified by the amount of radio power required to give a certain pulse SNR. The standard radiometer equation describes the radio flux density required for a certain noise temperature. For pulsars the power measured is varying relative to the unpulsed background and the radiometer equation is modified by a term which describes the pulsed nature of the source. The radiometer equation quantifies the minimum detectable flux density,  $S_{\text{min}}$  as

$$S_{\text{min}} = \frac{\sigma\beta(T_{\text{sys}} + T_{\text{sky}})}{G\sqrt{n_p B \tau_{\text{obs}}}} \sqrt{\frac{W_{\text{obs}}}{P - W_{\text{obs}}}} \quad (2.1)$$

where  $T_{\text{sys}}$  and  $T_{\text{sky}}$  are the system and sky noise temperatures respectively,  $\beta = 1.07$  is a factor from digitisation (Kouwenhoven & Voûte, 2001),  $G$  is the system gain,  $n_p$  is the number of summed polarisations (usually two orthogonal polarisations are combined to form Stokes' intensity, I),  $B$  is the observing bandwidth,  $\tau_{\text{obs}}$  is the observation time,  $\sigma$  is minimum acceptable signal-to-noise ratio,  $P$  is the pulse period, and  $W_{\text{obs}}$  is the observed width of the pulses. For pulsed sources  $W_{\text{obs}} < P$  where  $W_{\text{obs}}$  incorporates the intrinsic width of the pulses, instrumental effects, and effects which broaden a pulse travelling through ionised space (see Equation 2.4).

### 2.1.2 Incoherent dedispersion

The group velocity of radio waves is affected by free electrons along the line of sight, leading to dispersion. This *dispersion* is manifest when a pulse of radio waves travels through the interstellar space, which contains free electrons and thus affects the propagation of astronomical radio pulses. Dispersion induces a delay in pulse time of arrival for a given radio frequency that is proportional to  $\nu^{-2}$ . A pulse therefore arrives earlier at the observer at higher frequencies and a pulse that is temporally narrow at the source is spread in time at the observer. In order to maximise a survey's sensitivity it is necessary to correct for the dispersive effect of the ionised interstellar medium (ISM). The presence and magnitude of this dispersive effect will also form an important tool in identifying and classifying astronomical sources. A more detailed discussion of dispersion is included in Chapter 1.

The amount of dispersion which has taken place for a source is quantified by its dispersion measure, DM. When searching for new pulsars and single pulses their DM is unknown at the time of searching and a range of test values must be used. Using a test value,  $DM_{\text{test}}$ , the relative time shifts between channels are calculated (see Equation 2.2) such that pulses from a source with  $DM = DM_{\text{test}}$  would have a maximal SNR.

Because interfering radio sources are located on the Earth or are orbiting satellites (Radio Frequency Interference - RFI), their signals will not have travelled long distances through ionised material. This means that such signals will not be dispersed (although some can mimic the frequency sweep of dispersion; Burke-Spolaor et al. (2011a)). Consequently, RFI often has a maximum SNR when  $DM_{\text{test}} = 0 \text{ cm}^{-3} \text{ pc}$ . At this DM the channels are simply averaged together with no delays applied. This so-called *zero-DM* time-series is a useful tool for distinguishing RFI and truly astronomical sources, and always forms the lower limit of  $DM_{\text{test}}$ .

The maximum value for  $DM_{\text{test}}$ ,  $DM_{\text{max}}$ , depends on the maximum DM expected for the sources of interest, and the regions they are located in; for example, the highest DM for a known source is  $1650 \text{ cm}^{-3} \text{ pc}$  for PSR J1754–2900 (Eatough et al., 2013; Shannon & Johnston, 2013). PSR J1754–2900 is a magnetar separated in angle from the Galactic center by just  $3''$ , an exceptionally highly dispersive region (Deneva, Cordes & Lazio, 2009). For pulsars located in the Milky Way, with a line of sight separated from the Galactic center by  $\gtrsim 1^\circ$ ,  $DM \lesssim 1000 \text{ cm}^{-3} \text{ pc}$  (Manchester et al., 2005).

To correct for this dispersive effect in filterbank data, *incoherent dedispersion* is applied. During incoherent dedispersion the samples for each channel are shifted in time

relative to the other channels (see Figure 2.1). Usually the low frequencies are shifted relative to the highest frequency by the delays,

$$\delta t_i = 4.150 \times 10^3 \text{ DM}_{\text{test}} (\nu_{\text{ref}}^{-2} - \nu_i^{-2}) \text{ s}, \quad (2.2)$$

where  $\nu_{\text{ref}}$  is the central frequency of a reference channel (usually the highest frequency channel) and  $\nu_i$  is the central frequency of channel  $i$  to which  $\delta t_i$  is applied (see figure 2.1). For  $\delta t_i$  in seconds,  $\nu_{\text{ref}}$  and  $\nu_i$  are both measured in MHz, and DM is measured in conventional units of  $\text{cm}^{-3} \text{ pc}$ . Because filterbank data is channelised and detected, there will always be some residual delay within a sample which is unresolved and can not be corrected for (see Figure 2.1).

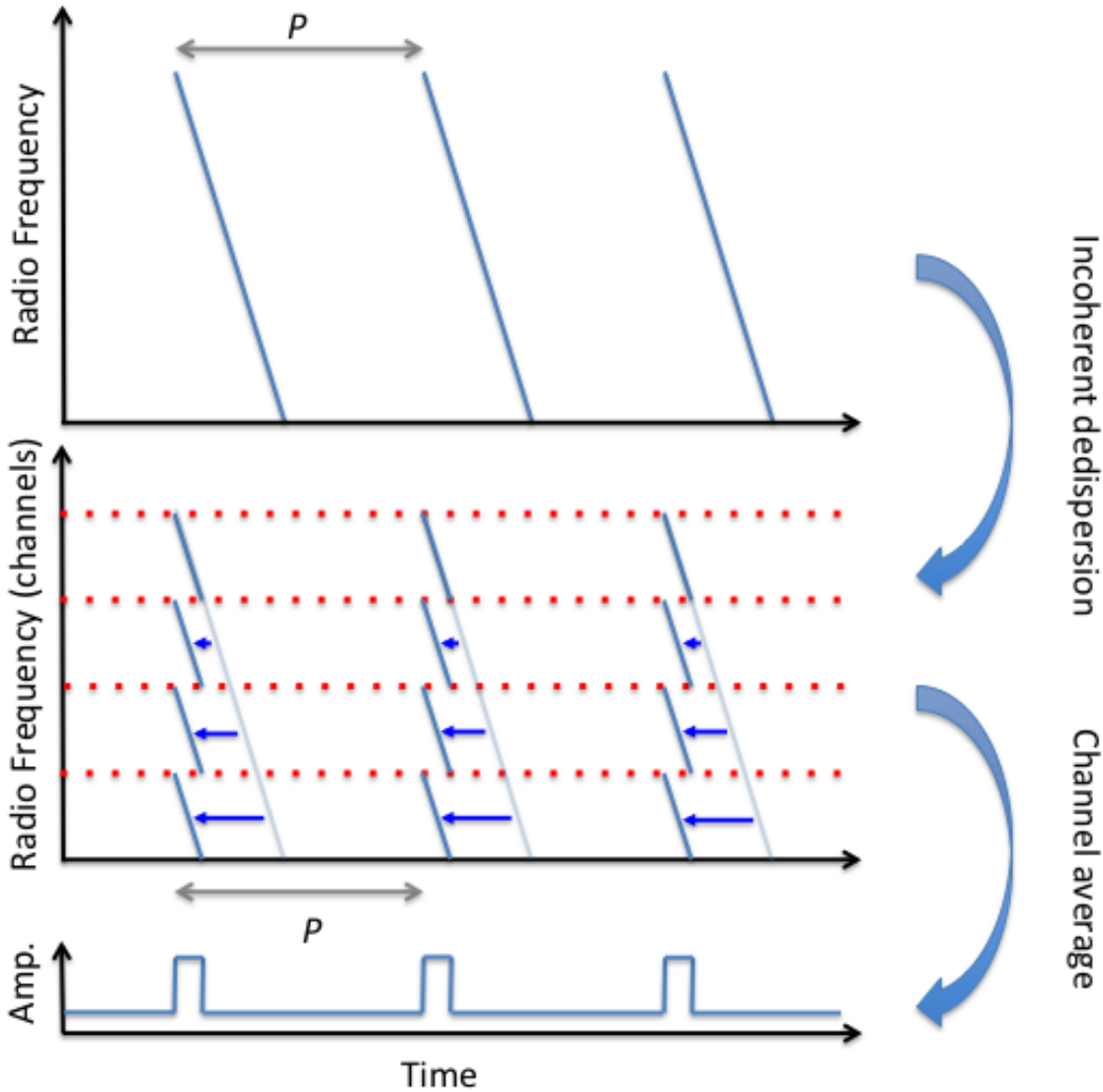


**Figure 2.1** – A schematic overview of the incoherent dedispersion process. The time shifts applied to the channels are calculated using Equation 2.2 before averaging all channels to form the 1-dimensional time-series shown at the bottom. Note the dispersive smearing which remains within a single channel (see Equation 2.3) which cannot be corrected for with incoherent dedispersion.

In filterbank data, a dispersed signal is smeared within a channel. This smearing is due to the finite width of the frequency channel and is largest in the lowest frequency channel. The uncorrected dispersive smear within a single channel is,

$$\delta t_{\text{chan}} = 8.3 \times 10^3 \left( \frac{\text{DM}}{\text{cm}^{-3} \text{ pc}} \right) \left( \frac{\Delta \nu_i}{\text{MHz}} \right) \left( \frac{\nu_i}{\text{MHz}} \right)^{-3} \text{ s} \quad (2.3)$$

where  $\Delta\nu_i$  is the channel bandwidth and  $\nu_i$  is the channel frequency, both in MHz. This spreading can smear out pulses from short period, high-DM pulsars and limits the DM –  $P$  phase space we are able to detect pulsars in. For example, if the lowest frequency channel has  $\delta t_{\text{chan}} > P$  then pulses are completely smeared out and correspond to non-pulsed emission in pulsar search data.

As can be seen in Equation 2.1, the sensitivity to pulsed signals depends on the apparent duty cycle  $W_{\text{obs}}/P$ ; and hence the narrower the pulse the easier it is to detect. As discussed above some smearing of the pulses is caused by residual dispersive smearing within a channel, and the finite sampling period of the data, and therefore such instrumental smearing should be minimised. The observed temporal width,  $W_{\text{obs}}$ , of a pulse is given by

$$W_{\text{obs}} = (W_{\text{int}}^2 + W_{\text{DM}}^2 + W_{\text{scatt}}^2 + W_{\text{samp}}^2)^{1/2}, \quad (2.4)$$

where  $W_{\text{int}}$ ,  $W_{\text{DM}}$ ,  $W_{\text{scatt}}$ , and  $W_{\text{samp}}$  are the intrinsic, dispersive, scattering and sampling widths respectively. Here  $W_{\text{DM}}$  is given by

$$W_{\text{DM}} = 8.3 \times 10^3 \left( \frac{|\Delta\text{DM}|}{\text{cm}^{-3} \text{ pc}} \right) \left( \frac{B_{\text{total}}}{\text{MHz}} \right) \left( \frac{\nu}{\text{MHz}} \right)^{-3} \text{ s} \quad (2.5)$$

where  $\Delta\text{DM}$  is the offset of the true source DM from the closest test value  $\text{DM}_{\text{test}}$ ,  $B_{\text{total}}$  is the total observing bandwidth, and  $\nu_{\text{MHz}}$  is the central frequency of the observing band, both measured in MHz. To minimise  $W_{\text{DM}}$  a DM step size,  $\text{DM}_{\text{step}}$ , is calculated by equating  $W_{\text{DM}}$  to the sampling time,  $t_{\text{samp}}$ . This corresponds to choosing a  $\text{DM}_{\text{step}}$  such that smearing due to  $|\Delta\text{DM}|$  is never greater than  $t_{\text{samp}}$ . This step size is given by

$$|\Delta\text{DM}| = \text{DM}_{\text{step}} = 1.205 \times 10^{-7} \left( \frac{t_{\text{samp}}}{\mu\text{s}} \right) \left( \frac{\nu}{\text{MHz}} \right)^3 \left( \frac{B_{\text{total}}}{\text{MHz}} \right)^{-1} \text{ cm}^{-3} \text{ pc}. \quad (2.6)$$

This step size is used until the total delay across the band is equal to  $n_{\text{chan}} \times t_{\text{samp}}$ ; the DM at this point is called the *diagonal* DM. For higher DM values, pulse smearing is greater than  $t_{\text{samp}}$ , thus unavoidably reducing the effective temporal resolution. When the diagonal DM is reached, consecutive samples (the number defined by the dispersive smear across one channel) are averaged together. Increasing  $t_{\text{samp}}$  in this way also doubles  $\text{DM}_{\text{step}}$ .

Dedispersion to DM values greater than the diagonal DM are easier to compute as the temporal resolution has decreased and hence there are fewer samples to shift. The next diagonal DM can be reached multiple times before  $DM_{\max}$  is reached. This whole process corresponds to progressive downsampling of the data, with values of  $DM_{\text{test}}$  that are not evenly spaced.

Once the delays have been applied, the samples from each channel are averaged. This forms a 1-dimensional time-series for each value of  $DM_{\text{test}}$ . Hence, if there had been a series of dispersed pulses in the filterbank data then the dedispersion process corrects for those delays (to the limits discussed above) and the SNR of those pulses will be maximal in one of the time-series. The searching of the time-series for constant amplitude periodic signals is considered below; followed by the searching of the same time-series for single or multiple non-periodic bright events.

### 2.1.3 The discrete Fourier transform

The time-series are a regularly sampled continuous time-domain data stream to be searched for periodic signals. This is a task generally more easily performed in the frequency domain when the pulsed signal shows only moderate amplitude modulation (McLaughlin & Cordes, 2003). The conversion from time to frequency domain is done using the Fourier transform. Because the signal is sampled and not continuous, the *discrete Fourier transform* (DFT) is used. The DFT represents a regularly sampled time-domain signal as a summation of complex exponentials - *Fourier components* - at a range of frequencies. The amplitude and phase of each Fourier component corresponds to the relative contribution to the time-series from a complex exponential of the corresponding frequency. DFT algorithms calculate the set of complex Fourier components for a time-series, forming a Fourier spectrum. The Fourier components,  $A(k)$ , for a time-series of  $N$  points,  $t_j$ , are given by

$$A(k) = \sum_{j=0}^{N-1} t_j e^{2\pi i j k / N}, \quad (2.7)$$

where  $i = \sqrt{-1}$ . The corresponding frequency,  $\nu_A(k)$ , for each component  $A(k)$  is given by

$$\nu_A(k) = \frac{k}{N t_{\text{samp}}}. \quad (2.8)$$

The relative phases and amplitudes of  $A(k)$  indicate the spectral content of the time-series. If there is a continuous signal from a pulsar with repeat frequency  $1/P$ , then the Fourier component corresponding to  $\nu_A(k) = 1/P$  will have a large amplitude. The DFT provides a method of detecting weak, repeating single pulses in a time-series.

A computer implementation of equation 2.7 requires  $O(N^2)$  arithmetic operations where  $N$  is the number of samples in the time-series. For pulsar searches long transforms are required ( $N = \tau_{\text{obs}}/t_{\text{samp}} \sim 10^6 - 10^9$  and DFTs can be slow. The fast Fourier transform (FFT) is an important implementation of the DFT which results in  $O(N \log N)$  operations. Methods of simplification, separation, and redundancy can reduce this further; for example the Cooley-Tukey algorithm (Cooley & Tukey, 1965). Modern implementations of these algorithms often optimise the method to the problem type or size, or to the computer's architecture, changing memory access patterns or sub-dividing a larger FFT. The FFTW library is a widely used example (Frigo & Johnson, 2005).

Each complex Fourier component represents both the phase and amplitude of that Fourier frequency. In search observations the absolute phase is unimportant and the total power of each Fourier component is calculated. The power spectrum,  $P(k)$ , is formed as

$$P(k) = (\text{Re}(A(k))^2 + \text{Im}(A(k))^2)^{\frac{1}{2}}. \quad (2.9)$$

Because the time-series is discretely sampled, so is the Fourier and power spectrum. It is likely that a real pulsar spin frequency will not fall exactly on the central frequency of a Fourier component. The result is spectral leakage of power from the closest Fourier component to the true pulse frequency into adjacent components. The best case scenario is a true spin frequency falling exactly at the centre frequency of a spectral bin; the worst case is a spin frequency falling on the edge of a spectral bin. The relative power in the latter case is 63.7% relative to the best case; this effect is mitigated as much as possible before any detections are attempted (Ransom, Eikenberry & Middleditch, 2002).

There are two common ways to counteract this loss of sensitivity. The first is to pad the time-series with zeros, effectively increasing the spectral resolution of the Fourier spectrum (see Equation 2.8) without adding any information. This reduces the spectral width of each Fourier component, and reduces spectral leakage; although this process does increase the computation time. Historically this was often used with FFT algorithms which required power-of-two-length time-series for computing; modern FFT algorithms seldom have this

requirement.

A second method compares a spectral bin with its neighbours, effectively restoring power spread over two bins into a single bin. The equation describing the replacement values for  $P(k)$  is as follows

$$P(k) = \max. \left( \frac{|A(k-1) + A(k)|^2}{2}; |A(k)|^2; \frac{|A(k) + A(k+1)|^2}{2} \right). \quad (2.10)$$

Either of these processes should be carried out prior to searching for significant peaks in the power spectrum.

In the ideal case the noise in the signal coming into, and from, the telescope and instrumentation would be *white noise*. White noise is power randomly and evenly distributed across the power spectrum - that is the mean and rms of the values in a sub-set of the power spectrum is the same as for all other sub-sets. The instrumentation and data acquisition systems often impart slow ( $\sim$  seconds) variation in the baseline of the time-series. RFI with a slow repeat rate (like radar) may be present in the time-series. These effects result in power in the low frequency bins of the spectrum and the noise is not white but *red*. This low-frequency power is not astrophysically meaningful, but could impede detection of long period pulsars. In order to minimise this loss of sensitivity, the power spectrum is split into narrow contiguous sections, each of which is corrected for the mean and rms of the section. This flattens the spectrum minimising the detrimental effects of red noise. A useful consequence of this red noise removal is that  $P(k)$  is scaled such that it is directly interpretable as the SNR (see Figure 2.2).

If pulsar pulse profiles were sinusoidal then a single Fourier component would contain all the power from that signal. Pulse shapes are however typically narrower than the pulse period with duty cycles  $\frac{W_{\text{obs}}}{P} \approx 5\%$  and have complex, non-sinusoidal, shapes. The Fourier transform of a signal of this type results in reduced power in the spectral bin corresponding to the *actual* pulse frequency (the fundamental), with the remaining power distributed across integer harmonics. In other words, if the pulse frequency is  $\nu_p$  then power may also be detected at  $2\nu_p$ ,  $3\nu_p$ ,  $4\nu_p$ , etc. (see Figure 2.2). This may mean a peak at the fundamental frequency falls below an applied threshold. To restore power to the fundamental Fourier component the spectrum is stretched by a factor of two and added to the original spectrum. In this way the power at  $\nu_p$  and  $2\nu_p$  are summed. Power is expected to be spread into approximately  $\frac{P}{W_{\text{obs}}}$  harmonics and the process is repeated, usually 5 or 6 times, to

add in these higher harmonics; process is also repeated for the odd-numbered harmonics. Harmonic summing is performed on the complex Fourier amplitudes as the *relative* phase between harmonics is predictable and can be corrected. Each harmonically summed power spectrum is searched for peaks via application of a threshold. It is expected that a pulsar signal that has power spread to higher harmonics because of a narrow pulse profile will increase in SNR with addition of higher harmonics. The SNR of the signal will increase until it is noise that is being added. SNR as a function of the number of summed harmonics can therefore be used both to identify possible pulsar signals, and also to estimate the width of the pulse.

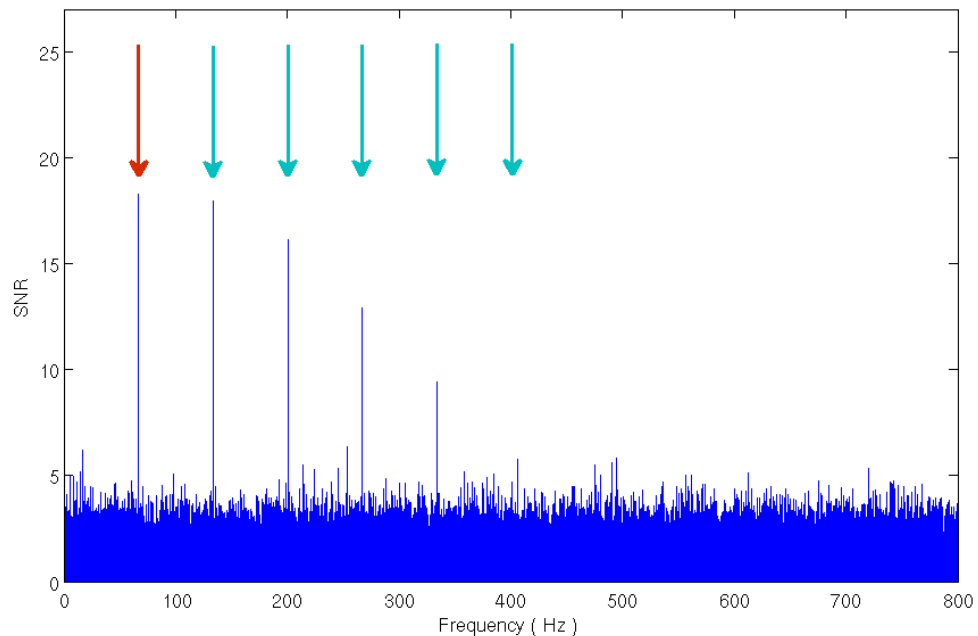


**Figure 2.2** – The Fourier power spectrum of a simulated 14.8 ms pulsar with 20% duty cycle and a Gaussian shaped pulse profile. The observation is 280 seconds long with  $t_{\text{samp}} = 64\mu\text{secs}$ ; the power spectrum has been truncated to show Fourier frequencies below 800 Hz only and scaled such that the values constitute the SNR. The position of the fundamental pulsar spin frequency (red arrow) and its higher harmonics (grey lines) are indicated.

Simple threshold detection of a power spectrum is used to identify significantly detected pulsed signals, and a series of candidate spin frequencies is produced. These candidates are designated by the frequency of the Fourier bin, and  $DM_{\text{test}}$  for the time-series. Given that  $P = \frac{1}{\nu_A}$  a candidate periodic source can be represented by a  $(P, DM)$  pair of values.

### 2.1.4 Candidate filtering and generation

Some pulsed signals may be visible in the time-series with adjacent  $DM_{\text{test}}$  values, where the increased apparent pulse width due to  $|\Delta DM|$  (Equation 2.5) is not sufficient to make it undetectable. The first stage of candidate reduction is therefore to combine closely matched DM and  $P$  values that could be the same candidate detected in multiple time-series.

The application of a simple threshold can also falsely identify a peak at a harmonic as a fundamental. To further reduce the number of candidates, those with harmonically related  $P$  values are combined to a single candidate. The fundamental period assigned to the candidate is that which is most significantly detected in the combined candidates.

For each reduced candidate the filterbank data is *folded* with the candidate period and dedispersed at the candidate DM (see Figure 2.3). The filterbank data consists of a time-series for  $n_{\text{chan}}$  frequency channels. During folding each of these time-series is divided into sections in time with a duration equal to the pulse period. These sections are then further grouped into contiguous groups of channels and summed to form a number of subbands ( $< n_{\text{chan}}$ ). This process is usually performed for a number of sections (sub-integrations or subints) each corresponding to a fraction of the total search observation. The result is a data cube of pulse profiles for each subint and each subband.

The subints and subbands preserve some spectral and temporal resolution, and as such the candidate period and DM can be further optimised. This resolution also allows some characteristics of the signal to be easily accessible, without having to store the large filterbank files.

The SNR of the folded pulse profile can be maximised with incremental changes to  $P$  and DM about the nominal values (derived from the power spectra). If the folding period exactly matched the true period of the pulsar then the pulse phase for each subint would be the same. The maximum resolution of this period is however defined by the Fourier component spacing. By making incremental changes to this original period the change in pulse phase for each subint is calculated and applied to the subint profiles. These profiles are again summed and the SNR calculated. By maximising the pulse profile SNR it is possible to optimise the period to a greater accuracy than the Fourier component spacing would otherwise allow.

An incorrect DM will cause the pulses to appear at a slightly different phase in each subband. An incremental change in DM is used to calculate the relative phase shifts of

the pulse profile in the subbands prior to summing the profiles together and calculating the profile SNR. By correcting for incremental changes in the DM about the  $DM_{\text{test}}$  value to maximise the pulse profile SNR then the DM is optimised to a higher resolution than the relatively course searched DM steps would otherwise allow.

These optimised values for  $P$  and DM are stored in a *candidate file*. This file also contains the folded data and spectral SNR in adjacent DM trials. Candidate files may then be used to generate a human viewable representation of the candidate, or may undergo further filtration (see Section 2.3.6).

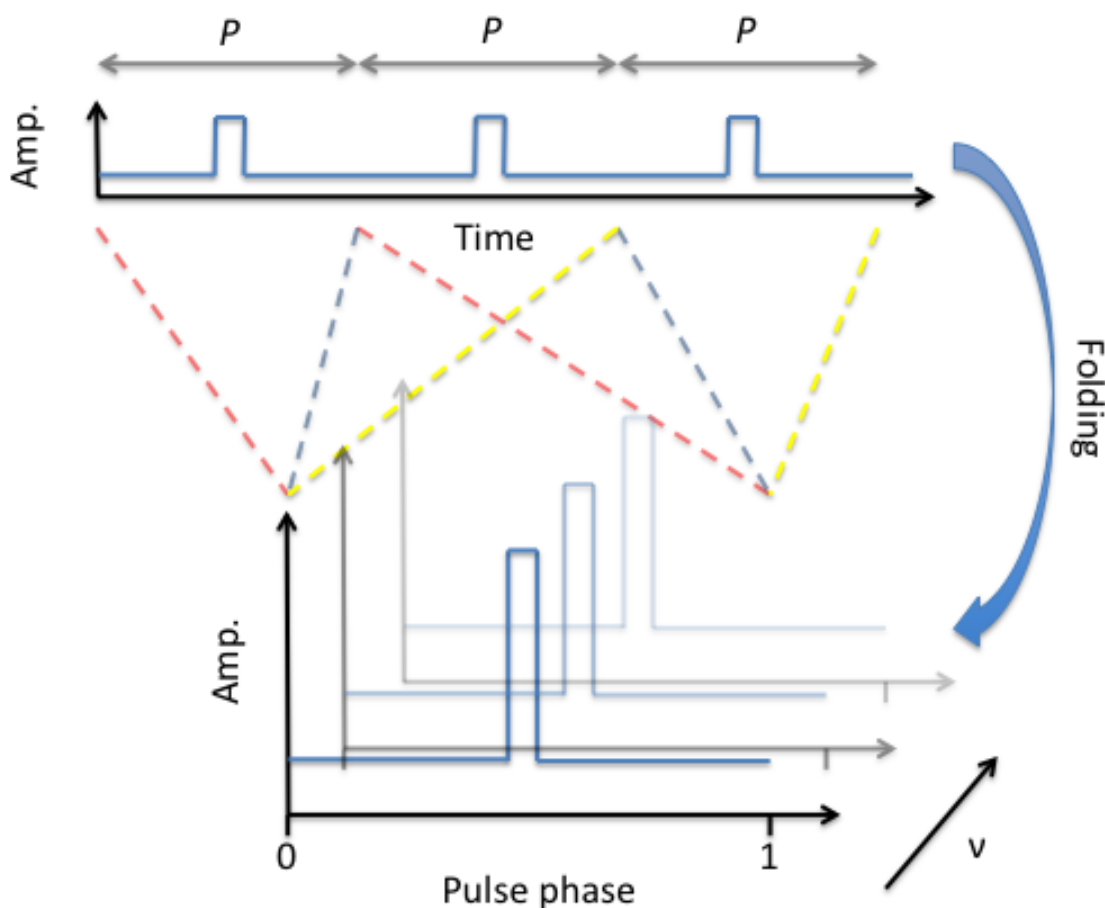


**Figure 2.3** – The pulse periods shown in a time-series are each added together to form a plot of amplitude against pulse phase (a pulse profile). Each pair of coloured dotted lines indicates the addition of a section of time-series equal in length to the pulse period. For illustrative purposes three subbands are shown.

## 2.2 Single pulse searching

The Fourier searching described above enable identification of periodic sources where a single pulse would likely be impossible to detect in the time-series. Single pulses where their periodicity is not helpful in this regard on the other can also be detected in the time-series. If they do repeat, like rotating radio transients (RRATs), then this repetition does not aid their detection via Fourier techniques. These single pulses must therefore be detected directly via peaks in the dedispersed time-series. Consequently the flux density of single pulses must be significantly higher than the mean flux density of a single pulsar pulse, in order to be detected in a given survey.

Single pulses (from pulsars or otherwise) are dispersed, and the wide observing band means that they can be identified by the distinctive dispersion delay. Indeed, the presence and removal of dispersion is key in detecting and identifying single pulses from an astronomical source. The spectral and temporal resolution in a typical pulsar survey provides sensitivity to pulses from 10s of  $\mu\text{s}$  to 10s of ms wide, with sensitivity falling for wider (and hence higher DM) pulses.

The processing for single pulse detection is the same as for the Fourier analysis up to and including the generation of the dedispersed time-series for values of  $\text{DM}_{\text{test}}$ . These 1-dimensional time-series (see Section 2.1.2) are searched for peaks exceeding a SNR threshold. For computational efficiency this is done during dedispersion while the data is in the Random Access Memory (RAM). Similarly to pulsar searching, the SNR of *a priori* undetected pulses is strongly affected by  $\text{DM}_{\text{test}}$ . A pulse will be detected with the highest SNR when  $\text{DM}_{\text{test}}$  is closest to the source's true DM. Like a pulsar signal, a single pulse could be detected at lower significance in adjacent DM trials (see Figure 2.4).

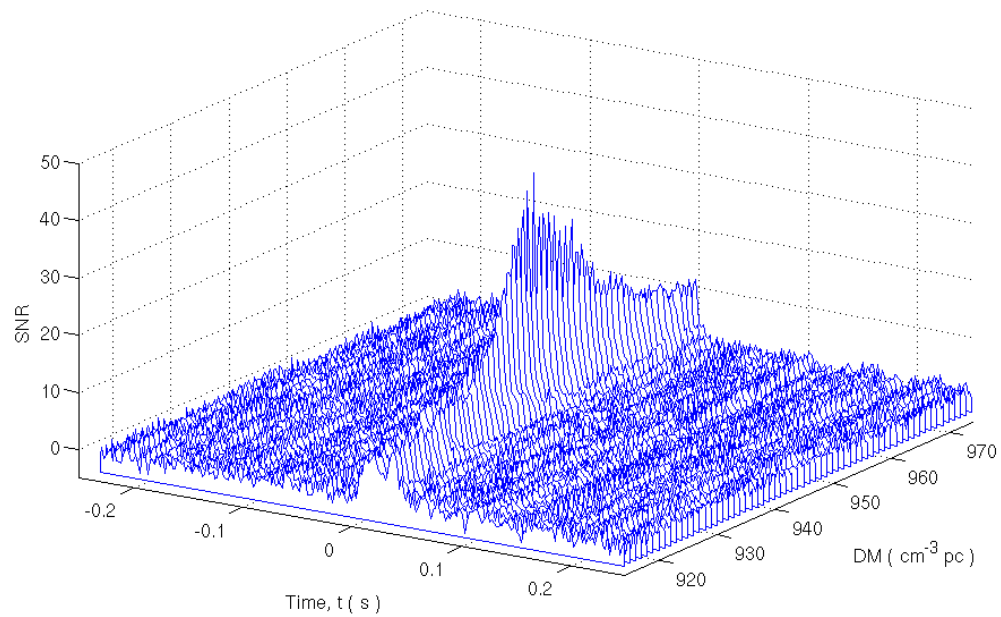


**Figure 2.4** – A waterfall plot of a dedispersed bright single pulse as a function of DM. The height and SNR of the pulse decreases when the DM is further from the true value ( $DM_{\text{pulse}} = 944.38 \text{ cm}^{-3} \text{ pc}$ ). See Chapter 5 for more information on this pulse, FRB 110220.

### 2.2.1 Matched filtering and wide pulses

Pulsar and RRAT pulses are usually considerably wider than one sample of search data ( $t_{\text{samp, typical}} = 64 \mu\text{s}$ ). To optimally detect these wide pulses adjacent time-series samples are summed together to increase the SNR - this is called *matched filtering*. The simplest matched filter shape (boxcar filter) corresponds to each of the samples having an equal weight in the summation. The width of the filter corresponds to the number of samples combined. After each filtering step the resultant time-series is searched for significant peaks (see Figure 2.5).

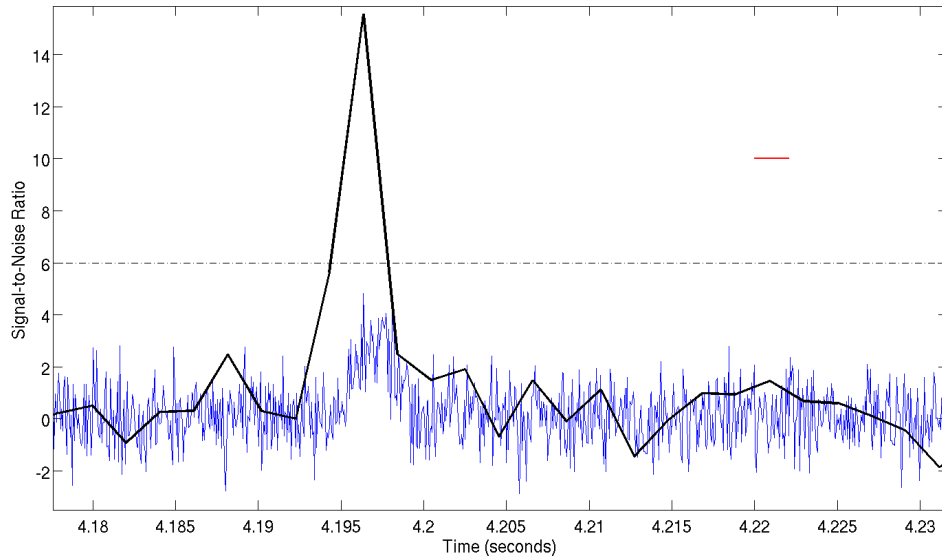


**Figure 2.5** – An example of an unfiltered time-series (blue) containing a wide single pulse (located at  $t \approx 4.197$  secs); the same time-series filtered (black) with a boxcar of width  $2^5 \times t_{\text{samp}} = 2.048$  ms (indicated by the red horizontal line). It is apparent that a typical  $6\sigma$  thresholding (indicated by the dash-dot line) of the unfiltered time-series would not detect the pulse, however with boxcar matched filtering it is detected. Note that the pulse width is not equal to the boxcar width.

A wide pulse's SNR will peak when the time-series is filtered with a boxcar which most closely matches its true width. While it is unlikely that a boxcar width will exactly match the true width, if the pulse width is within the range of boxcar widths then there will be an increase in SNR (see Figure 2.6) which follows a characteristic shape for a Gaussian pulse shape (see Figure 2.7). The single-pulse SNR as a function of boxcar width can also be a useful diagnostic in identifying single pulse candidates.

In real single-pulse searching the time-series is processed in sections, where these sections are usually a power-of-two number of samples in length. Boxcar widths which are a power-of-two are then simple to implement and correspond to progressive summing of pairs of adjacent samples. Using boxcar filters of power-of-two widths reduces the amount of processing required with little sensitivity loss (see Figure 2.6). The number of time-series to be searched falls by a factor of 56 for a maximum boxcar width of  $2^9$  samples when compared to boxcar filters with an integer number of samples up to same the maximum filter width.

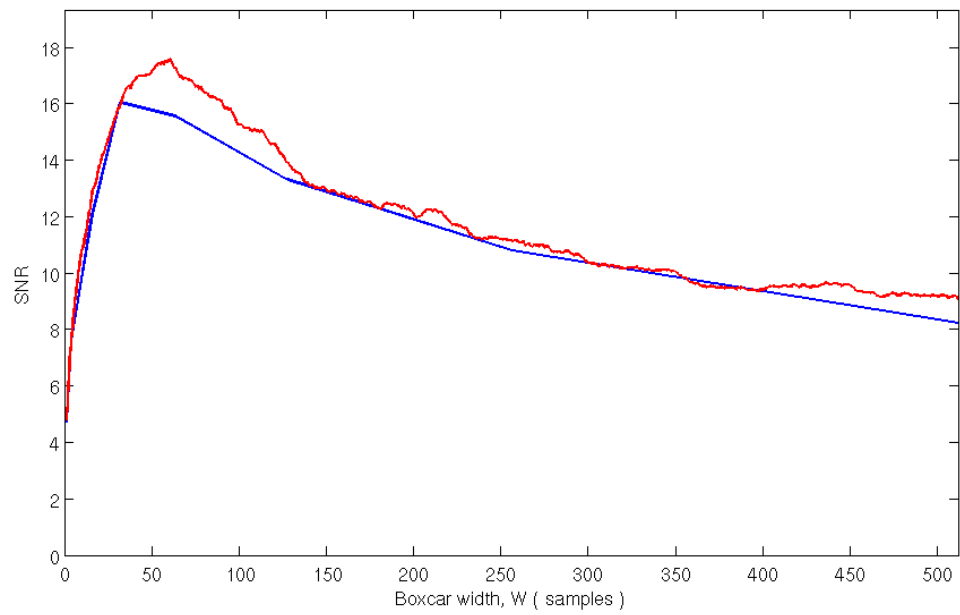


**Figure 2.6** – A comparison of the SNR of a test pulse when using power-of-two boxcar widths (blue) or an integer number of samples (red). There is only a small reduction in SNR when using the faster and easier to implement power-of-two filters.

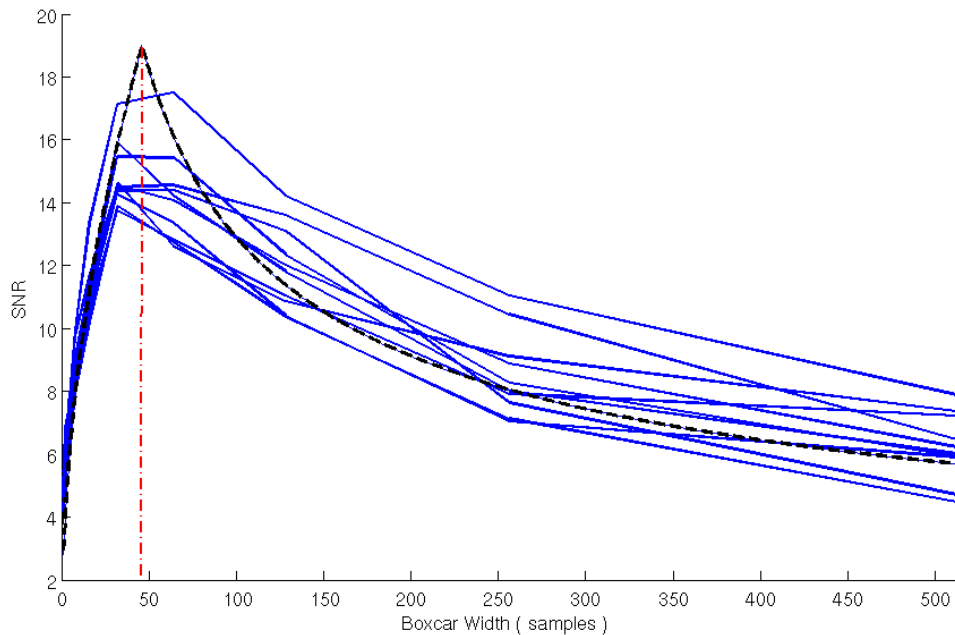


**Figure 2.7** – The SNR vs boxcar filter width is shown for the pulse considered in Figure 2.6) where boxcar filters were created with power-of-two sample widths. The true half-power width of the pulse does not match exactly any of the boxcar widths and is marked by the dashed-dotted line. Ten independent realisations of additive Gaussian noise are shown (blue). The theoretical SNR as a function of filter width of McLaughlin & Cordes (2003) is also shown (black dashed).

Because multiple time-series for a sequence of DM values are generated on the same processing computer, the candidate information from each is available at the same time. Multiple candidates corresponding to the same pulse seen in time-series corresponding to multiple values of  $DM_{\text{test}}$  are reduced down to leave a single candidate. SNR as a function of DM is then stored as part of a single pulse candidate and again helps to distinguish real pulses from noise and RFI (see Figures 2.19 and 2.20).

## 2.3 The High Time Resolution Universe south survey

The location of pulsars is *a priori* unknown, although typically surveys in and close to the Galactic plane and in Globular Clusters have proven particularly fruitful. Normal pulsars have ages and velocities which indicate they have not lived long enough to move far from their birth locations, and are therefore found close to where their progenitors existed. Pulsar progenitors are massive O and B type stars and they are predominantly located in the

Galactic plane. On the other hand Millisecond Pulsars (MSPs) generally have lower velocities than normal pulsars. MSPs are however considerably older than normal pulsars and are visible for sufficient time that they may move further from the Galactic plane. Consequently, MSPs have a larger scale height above the Galactic plane (Toscano et al., 1999). To maximise the number of discoveries the longest and most sensitive survey observations are centred around the Galactic plane. The Parkes radio telescope's Southern Hemisphere location means it can observe the majority of the Galactic plane and the Galactic center.

The previously most prolific Galactic plane survey (in terms of number of discoveries) was the Parkes Multibeam Pulsar Survey (PMPS) (Manchester et al., 2001); which searched within  $|b| < 5^\circ$  and discovered around 1000 new pulsars (e.g. Lyne et al. 2000; Morris et al. 2002; Kramer et al. 2003a; Faulkner et al. 2004; Hobbs et al. 2004; Faulkner et al. 2005; Manchester et al. 2005; Lorimer et al. 2006; Knispel et al. 2013). The PMPS used the 21-cm *multibeam* (MB) receiver (Staveley-Smith et al., 1996) with an analogue filterbank back-end to channelise the observing band into  $96 \times 3$  MHz channels; the sampling time was  $250 \mu\text{s}$  with 1-bit samples. The same receiver has been used for a succession of pulsar surveys from Parkes for different regions of the sky (e.g. Edwards et al. 2001a; Jacoby et al. 2006; Manchester et al. 2006; Burgay et al. 2006). Some of these surveys have extended the PMPS by increasing the range of Galactic latitudes slightly while still concentrating on the Galactic plane: Edwards et al. (2001a) surveyed  $5^\circ < |b| < 15^\circ$ . Other surveys have surveyed a region extending to high Galactic latitudes to explicitly search for MSPs: Burgay et al. (2006) surveyed to  $|b| < 60^\circ$  but only within  $220^\circ < l < 260^\circ$ .

### 2.3.1 Hardware and data recording

The MB receiver has 13 dual polarisation feeds at the primary focus of the 64-m Parkes radio dish. The beam pattern is a central beam and two hexagonal rings around the central axis (see Figure 2.8). This means each telescope pointing corresponds to 13 simultaneous, independent, dual-polarisation beams on the sky. Pointing schedules are created such that this pattern tessellates to fully cover the sky at the half-power beam-width (see Figure 2.8). Use of the MB receiver therefore increases the survey speed by factor of 13 compared to a single beam receiver.

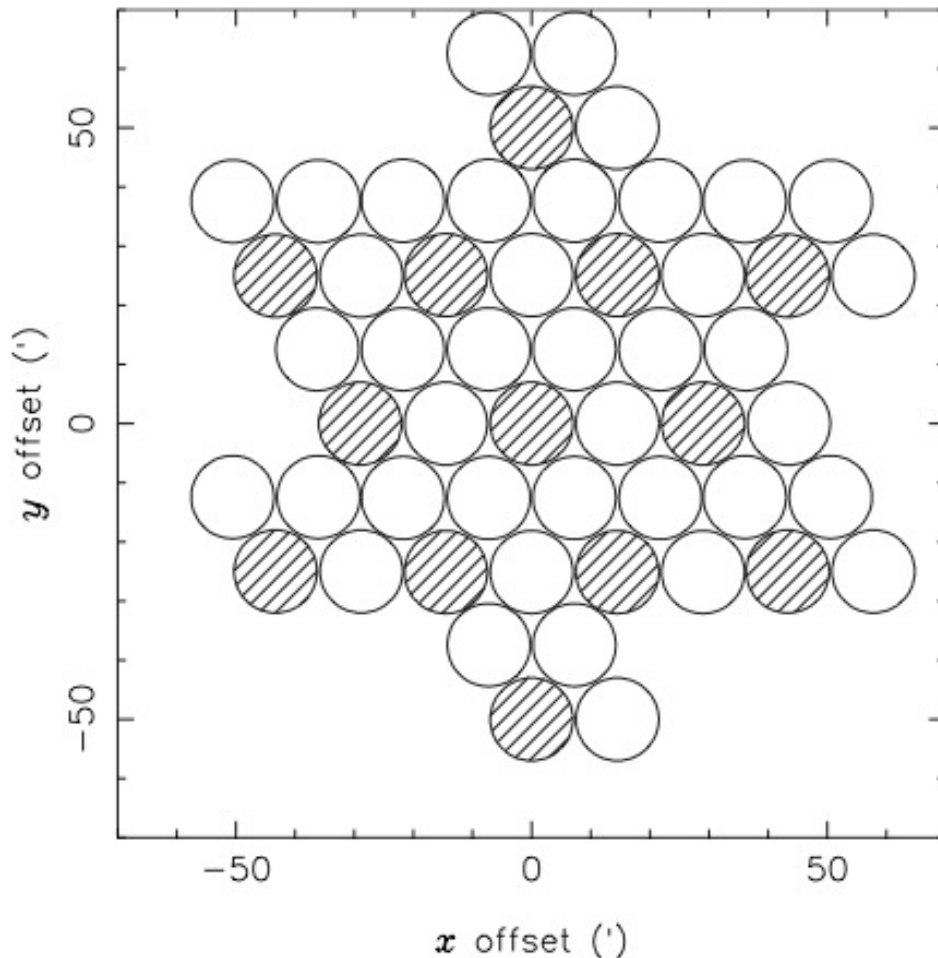


**Figure 2.8** – The combined beams of four telescope pointings, tessellated to show full sky coverage, are shown; 13 beams from a single telescope pointing are shaded (Edwards et al., 2001b).

Since the observations of the PMPS, the technology incorporated in the back-end, which samples and records the signal, has progressed significantly; in particular, cheaper electronic components and computer technology now allow digital rather than analogue filterbanks to channelise the observing band, enabling higher resolution data to be recorded. The digital back-end used in the HTRU survey is the Berkeley-Princeton-Swinburne Recorder (BPSR). BPSR is a digital filterbank with Interconnect Break-Out Board (IBOB) Field Programmable Gate Arrays (FPGAs) performing the channelisation after analogue-to-digital conversion of the baseband signal. A compute cluster is used for final polarisation summing and conversion to 2 bits. Recently BPSR has been replaced by HIPSUR, a new reconfigurable digital back-end at Parkes. HIPSUR uses more powerful Reconfigurable Open

Architecture Computing Hardware (ROACH) FPGAs for the channelisation. The HIPSR compute cluster uses Graphical Processing Units (GPUs) as well as CPUs for higher level processing.

Each beam of the MB receiver consists of two signals from two orthogonal polarisations. These 26 feeds are downconverted from  $\nu = 1.18 \rightarrow 1.58$  GHz to  $\nu = 0 \rightarrow 0.4$  GHz. The baseband signals are then digitally Nyquist sampled (i.e.  $\nu_{\text{samp}} = 800$  MHz) at 8 bits before passing to the FPGAs of BPSR. The FPGAs then split the signal into  $1024 \times 0.390625$  MHz channels. The baseband samples from each polarisation and each channel are accumulated for 25 samples and detected, giving a sample integration time of  $t_{\text{samp}} = 64 \mu\text{sec}$ , represented by a 32-bit number. These samples are further grouped into 10-second blocks and scaled according to the mean and standard deviation in the block. Finally, the two polarisation pairs for each  $64 \mu\text{sec}$  sample for each channel and each beam are summed and scaled to a 2-bit number to reduce the quantity of data to be stored; this takes place on the compute cluster, these samples are then written to disk as filterbank data. The data are written to tape at Parkes, all data is also transferred electronically to Swinburne University of Technology, Melbourne, where it is again written to tape. Upon completion of writing two full copies to tape the data are deleted from the compute cluster.

BPSR has a shorter sampling time and narrower channels than the PMPS analogue back-end ( $250 \mu\text{s}$  and 3 MHz for the PMPS respectively). This improves the sensitivity of the HTRU south survey to narrow-pulse, short-period, high-DM pulsars. In addition, 2-bit sampling improves dynamic range and resilience to RFI.

### 2.3.2 Survey regions

The HTRU south survey is split into three different parts, the low-, mid- and high-Galactic latitude regions (see Table 2.1 and Figure 2.9). The HTRU survey began in 2008, with 100% of the mid- and low-latitude, and 76% of the high-latitude survey observed to-date.

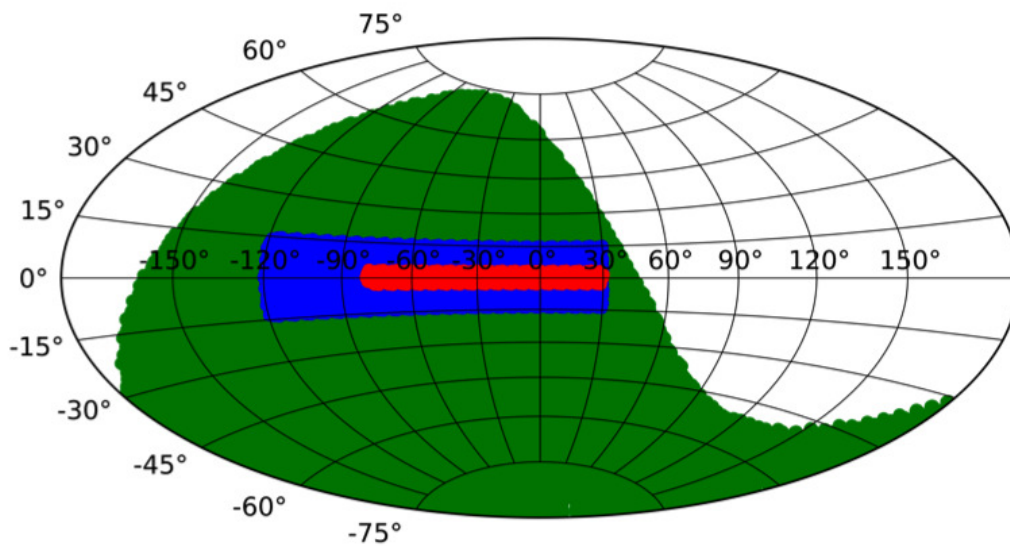


**Figure 2.9** – An Aitoff projection of the Galactic regions covered by the HTRU southern survey. Red is low-, blue is mid- and green is high-latitude. The high-latitude survey is approximately the visible sky using the Parkes 64-m radio telescope.

The three survey regions were designed with different goals. The low-latitude survey has pointings twice the length of the PMPS, and with the improved temporal and spectral resolution aims to detect faint, high-DM, fast pulsars undetectable in the PMPS. The mid-latitude survey extends the PMPS region; while the pointings are shorter than for the PMPS the limiting flux density is still lower for a large region of parameter space, particularly MSPs (see Figure 2.10). The short (270 s) pointings of the high-latitude survey aim to provide a “snapshot” of the high time resolution radio sky at  $1.1 < \nu < 1.5$  GHz which is visible with the 64-m Parkes. One of the aims of the high-latitude survey is to look for highly dispersed narrow pulses originating from outside the Galaxy.

Survey	High	Mid	Low
Region	$\delta_{eq} < +10$	$240^\circ < l < 30^\circ$ $ b  < 15^\circ$	$280^\circ < l < 30^\circ$ $ b  < 3.5^\circ$
$\tau_{\text{obs}}$	270	540	4300
$N_{\text{beams, total}}$	443287	95056	15990
$t_{\text{samp}}(\mu\text{s})$	64	64	64
$B_{\text{total}}(\text{MHz})$	400	400	400
$B_{\text{chan}}(\text{MHz})$	0.390625	0.390625	0.390625
$n_{\text{chan}}$	1024	1024	1024
Data Length (samples)	$10^{22}$	$10^{23}$	$10^{26}$
Data per Beam (GB)	$\sim 1$	$\sim 2$	$\sim 16$
Total Data (TB)	435	190	250

**Table 2.1** – Search parameters for the three sections of the HTRU south survey (Keith et al., 2010).

### 2.3.3 Sensitivity

The radiometer equation (Equation 2.1) quantifies how an increased total bandwidth and integration time lowers the limiting flux density of a survey. Observing bandwidth is limited by the receiver, or by the data rates which can be processed and stored. A compromise must be made between sensitivity and time required for the survey to determine the integration time,  $\tau_{\text{obs}}$ . Different regions of the sky also have different effects on the observations. In the direction of the Galactic plane there is an increase in the electron column density that affects both the DM and scattering. Also, there is a greater abundance of synchrotron emission in the direction of the Galactic plane which affects the sky temperature. In the low-latitude region  $T_{\text{sky}}$  has a mean of 7.5 K, compared to 2.5 K and 1.0 K for the mid- and high-latitude areas respectively (at  $\nu = 1.4$  GHz). The minimum detectable flux densities for the three HTRU survey regions, and for the PMPS, are shown in Figure 2.10.

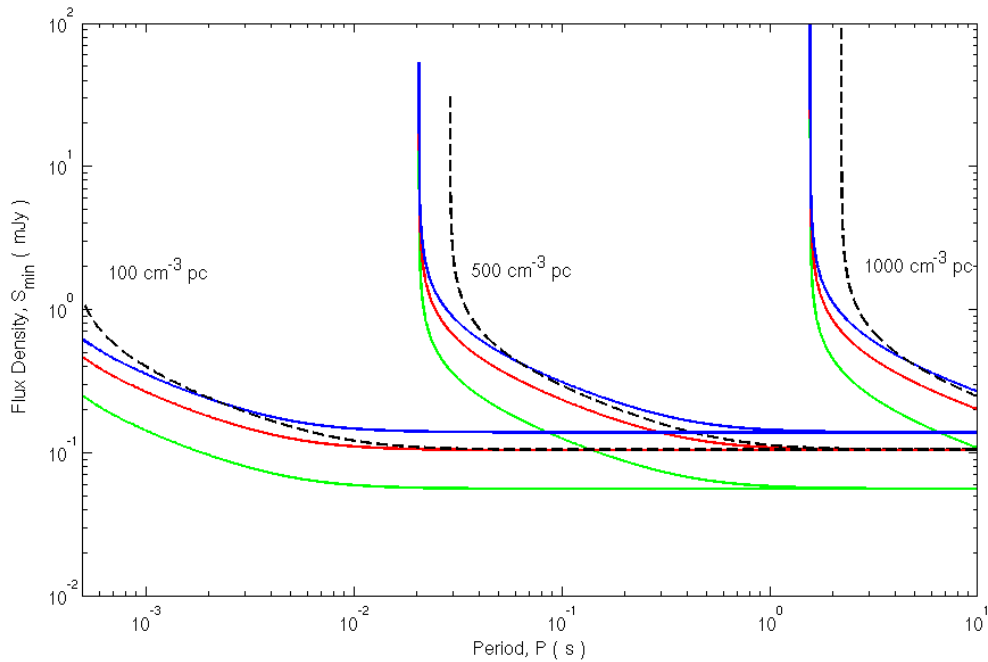


**Figure 2.10** – Minimum detectable flux density as a function of pulse period for a pulsar at  $DM = 100, 500, 1000 \text{ cm}^{-3} \text{ pc}$  in the three HTRU survey regions (low-, mid-, high-latitude regions are shown with the green, red, and blue lines respectively). The limiting flux densities were calculated using a minimum detectable SNR of 9, and the mean sky temperature of each region. For comparison the sensitivity of the PMPS is also shown (dashed black lines).

### 2.3.4 RFI removal

There is considerable RFI in the vicinity of Parkes. This includes satellite RFI ( $\nu_{\text{RFI}} = 1.525 - 1.559 \text{ GHz}$ ). There is a hardware filter in place to remove this part of the observing band. Once all channels with RFI are nulled in the data, the typical total useful bandwidth is approximately  $0.340 \text{ GHz}$ . There is also dynamic RFI that is sometimes present. It is of course necessary to mitigate for this in each observation as much as possible to maximise sensitivity to pulsars and single pulses. While pulsars and single pulses are narrow, the presence of RFI at the very least raises the noise floor of the observation, requiring a higher flux density of the source for a given SNR.

The most extreme form of RFI rejection is intervention by the observer. Because of the digital flexibility of BPSR the observer is able to see the band-pass (the relative power in each channel across the observing band), the zero-DM time-series and a DFT of the time-series in close-to real time. The observer can then identify periods of wide-band RFI,

which it would be difficult or impossible to excise, and they can choose to abandon the observation. As the RFI is often direction dependent the observer may either be able to observe a section of the survey with the telescope at a different azimuth and elevation, or try to confirm previous candidates from the survey.

The HTRU survey maintains a list of channels within the observing band that always contain RFI. These narrow regions of the band are not included in any searching of the data. This includes the channels which are blocked by a hardware filter to cut out satellite RFI at the top of the band. More subtle forms of RFI excision are performed on the filterbank data prior to any searching. The first is that each channel of the filterbank data is searched for periodicities with a DFT. Any channels found with any signal with  $\text{SNR} > 15$  are not included in further processing. The SNR in just a single channel of a pulsar would be considerably lower.

In addition to channel rejection, the zero-DM time-series is searched for bright peaks ( $\text{SNR} > 5$ ). If found, the corresponding samples in all channels are replaced with random values indistinguishable from the noise in the observation. In this way non-dispersed bursts of radiation should be removed. In addition to zero-DM bursts, this effectively removes bright low-DM pulses, where  $\text{DM} < 0.12 \left( \frac{w}{64\mu\text{s}} \right) \text{ cm}^{-3}\text{pc}$ .

### 2.3.5 HTRU Fourier and single pulse searching

HTRU search data arrives at Jodrell Bank on LTO-4 tapes, each of which stores approximately 800 GB of data. The data are transferred from these tapes onto temporary hard disk storage ready for processing. The searching, candidate generation, and sifting are all performed on the *Hydra* computing cluster at Jodrell Bank (see Figure 2.11). Hydra is comprised of a *head node* and tens of *processing nodes*. A processing node carries out the pulsar and single pulse searching and writes the results to a network location (see Figure 2.12).

All telescope pointings, corresponding to a set of 13 simultaneously observed beams, are independent of every other pointing. For the high-latitude survey the storage capacity of a processing node is large enough to store 13 completely searched beams (including raw data, intermediate data, and final candidates). In processing the high-latitude survey, observation times (UTCs) are used to group beams from the same pointing (which have the same UTC). A processing node then Fourier domain and single pulse searches all 13 beams in turn.

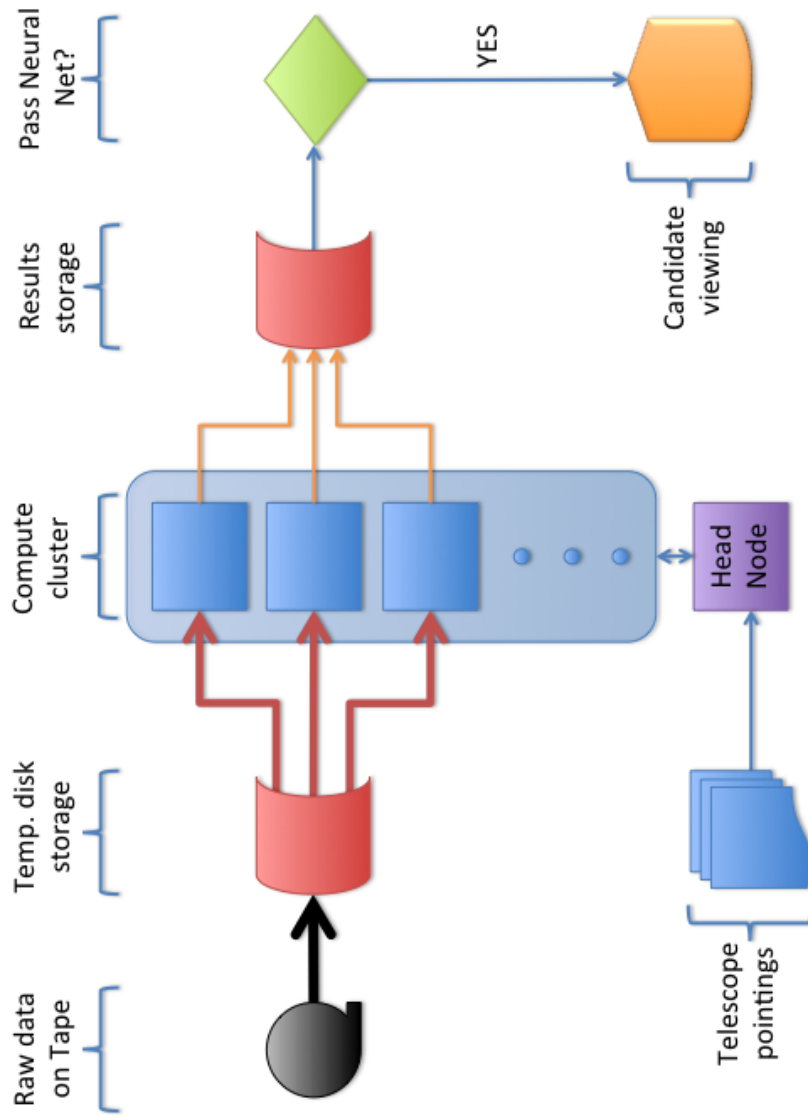


**Figure 2.11** – A schematic showing computing cluster level searching of the HTRU high-latitude survey.

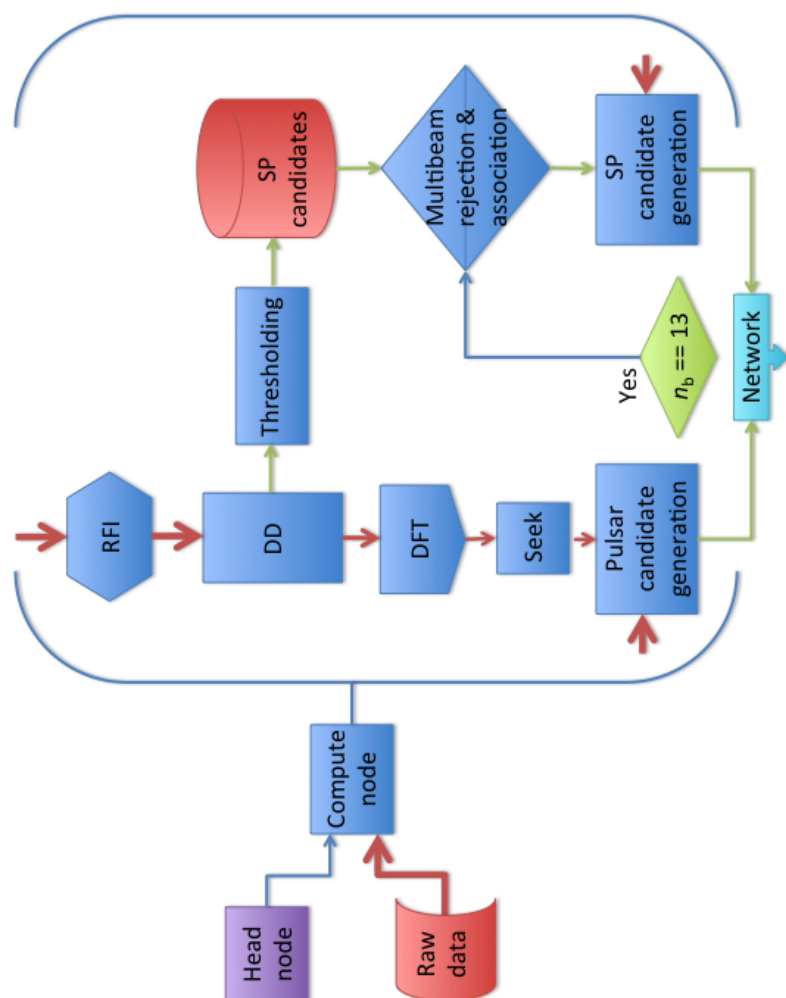


**Figure 2.12** – A processing node level schematic showing the different stages of Fourier domain and single pulse searching for the HTRU high-latitude survey. RFI: RFI rejection; DD: dedispersion; DFT: Fourier transform spectra; Seek: detecting and grouping periodicities in the power spectra.

### HTRU search details

The data are dedispersed to 1436  $DM_{\text{test}}$  values between 0 and  $2000 \text{ cm}^{-3} \text{ pc}$ ; the maximum value is chosen to be sensitive to the highest DM pulsars in the Galaxy. In addition to high-DM pulsars this upper limit for  $DM_{\text{test}}$  has enabled the discovery of highly dispersed extragalactic single pulses (see Chapters 5 and 6).

The time-series are Fourier transformed, harmonically folded, and threshold searched using the program `seek` which uses the FFTW library to perform the real-to-complex DFT (Frigo & Johnson, 2005). The output from `seek` is a list of pulse periods, the number of harmonic folds, the DM, and the SNR of each candidate dispersed periodic signal. As discussed in Section 2.1.3, these may be related harmonically or at similar DMs, in which case they may be the same signal independently discovered in multiple time-series. `ph-best` aims to combine these multiples, limiting the total number of candidates to 100 per beam.

Each candidate is a repeating signal which the software has identified: there has been no analysis of the signal and its properties except its presence in the Fourier spectrum. Each candidate is therefore further refined by using `dspsr` (Hotan, van Straten & Manchester, 2004) to fold the raw data at the period indicated by the Fourier spectrum, preserving 16 subbands and 32 subints. A fine search in  $P$  and DM is then performed on this folded data to optimise the SNR of the pulse profile. This SNR can then complement, and be compared to, the SNR from the DFT power spectrum. The folded data are included in the final candidate file (along with the optimised parameters) for human inspection. The final so-called *phcx* candidate files are an `xml` format containing the necessary data to produce a candidate plot like Figure 2.13. `xml` is chosen as the flexibility and accessibility of the data format provide the opportunity for further filtration and sorting of candidates.

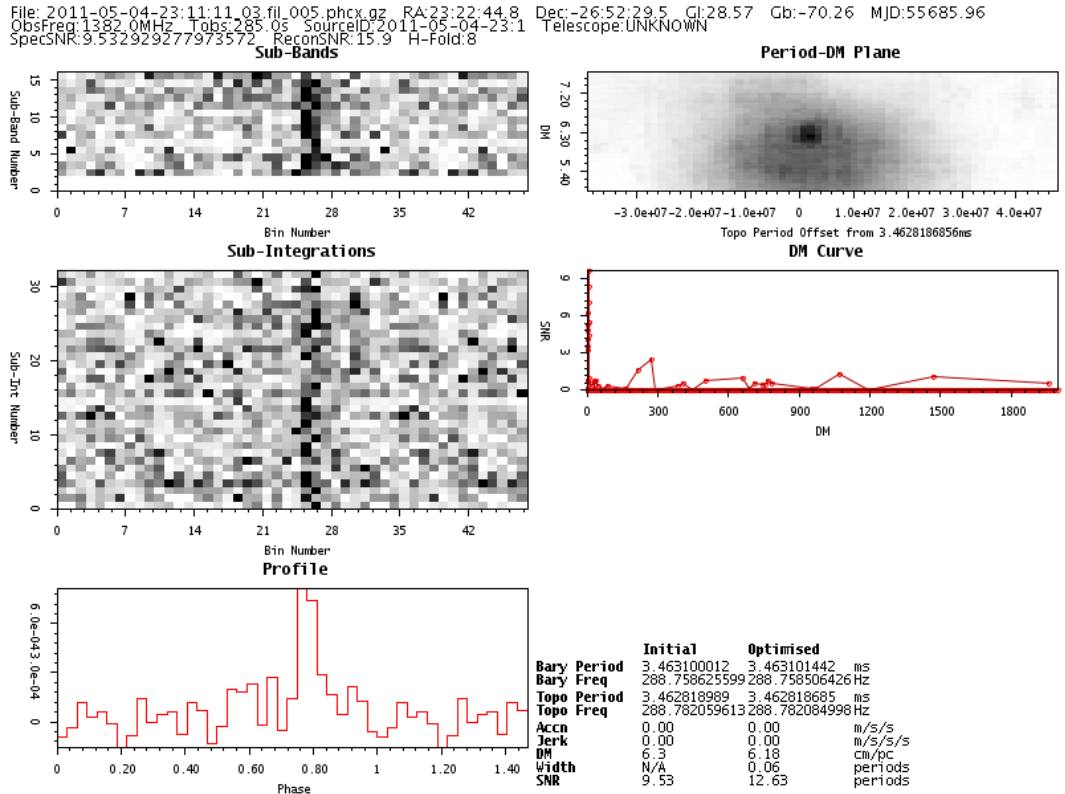


**Figure 2.13** – A candidate from the HTRU survey showing the initial and optimised parameters. The folded data are shown, including the fully averaged pulse profile (lower left) and the pulse profile in each subint and subband (top- and middle-left grayscale). Also shown is the amplitude spectrum SNR as a function of  $DM_{\text{test}}$ , and a *bullseye* plot (grayscale top-right) pulse profile SNR as a function of  $P$  and  $DM$  is shown from `pdmp`. Note that this candidate appears to be detected across the observing band, and is “on” for the duration of the observation. This candidate was confirmed as a real MSP - PSR J2322–2650. See Chapter 4 for more information.

The number of pulsar candidates from the HTRU survey is enormous; 100 candidates from each beam gives  $\sim 5 \times 10^7$  candidates for the high-latitude survey alone. For a single user to look at all these would take over one year assuming one second to look at each candidate 24 hours a day; not a feasible undertaking. An artificial neural network is therefore used to attempt to isolate the best candidates for human inspection.

### 2.3.6 Artificial neural network

An artificial neural network (ANN) is a machine learning pattern recognition technique which aims to categorise datasets. The ANN condenses an input vector of numbers de-

scribing a candidate, via a series of weighted summations, into an output vector whose values indicate membership of a set.

In the pulsar ANN the *input layer* is a vector of heuristics which describe a candidate (see Table 2.2). In general, an ANN has a number of *hidden layers*, each with any number of elements (defined at the time the net is constructed), which are connected to all the elements of the preceding layer (the input layer or another hidden layer). Finally an output layer, formed of just two elements, provides a simple indication of candidate category. A pulsar ANN attempts to separate candidates into two categories - *pulsar* and *not pulsar* - hence the two elements in the output layer (see Figure 2.14). In general, increasing the number of hidden layers allows an ANN to reproduce more complex behaviour; for the HTRU survey a single hidden layer is found to be sufficient.

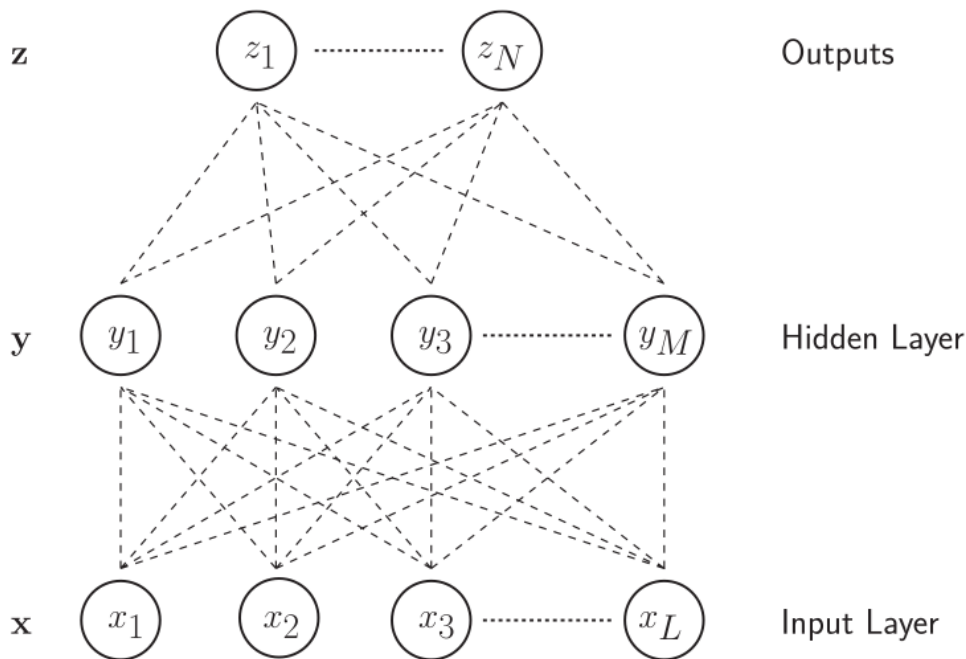


**Figure 2.14** – A schematic showing a generalised configuration of an ANN, each dotted line implies a “neural connection” and weight, the “neurons” (represented as circles) calculate the weighted sum of their inputs and produce an output value from an activation function. The information flow in this schematic is from bottom to top. Figure from Bates et al. (2012).

Each connection between neurons corresponds to a weight, and each neuron calculates the weighted sum of connections going into it. Each neuron then calculates an output value to pass-on using an *activation function*. The *logistic sigmoid function* is commonly used as activation function because it can reproduce linear or non-linear behaviour depending on

its input.

ANNs must be *trained* - that is, the weights between neurons must be set for maximal success in classification of a training set. The training set is a set of candidates where both the input and output layers are defined. A user has to pre-classify the training set and set the output layer accordingly (*pulsar* = 1 *not pulsar* = 0 for a true pulsar and vice-versa for an RFI/noise candidate). Initially, the weights are set randomly and the outputs calculated. A method of back propagation is then used iteratively to modify these weights such that the output layer tends towards correctly classifying as much as possible of the training set. A second set of candidates, also pre-classified, is used for verification purposes.

The HTRU survey uses the Stuttgart Neural Network Simulator (SNNS<sup>1</sup>). There are 22 numbers used to describe a candidate (outlined in Table 2.2); these 22 numbers form the input layer. The single hidden layer also has 22 *neurons*. The output layer has two neurons (*pulsar* and *not pulsar*) whose values indicate whether the input heuristics were from a pulsar candidate.

---

<sup>1</sup><http://www.ra.cs.uni-tuebingen.de/SNNS/>

Score Number	Description
1	Best Period, $P$
2	Best DM
3	Best SNR
4	Pulse Width, $W_{\text{obs}}$
5	$\chi^2$ value of pulse profile and sin curve
6	$\chi^2$ value of pulse profile and $\sin^2$ curve
7	$\chi^2$ value of pulse profile and Gaussian fit
8	Full-width half-maximum of Gaussian fit
9	$\chi^2$ value of pulse profile and two Gaussians fit
10	Mean full-width half-maximum of two Gaussians fit
11	Offset of profile histogram from zero
12	max.(profile histogram)/max.(fitted Gaussian)
13	Offset of score 11 and profile <i>gradient</i> histogram
14	$\text{SNR}_{\text{data}}/\sqrt{(P - W_{\text{obs}})/\bar{W}}$
15	$\text{SNR}_{\text{fit}}/\sqrt{(P - W_{\text{obs}})/\bar{W}}$
16	abs.(DM <sub>fit</sub> - DM <sub>best</sub> )
17	$\chi^2$ value of DM-SNR curve fit
18	RMS of the position of peaks in all sub-bands
19	Average of correlation coefficients for all pairs of sub-bands
20	Sum of correlation coefficients for all pairs of sub-bands
21	Number of peaks in pulse profile
22	Area under pulse profile after mean subtraction

**Table 2.2** – ANN heuristics for the HTRU survey processing at Jodrell Bank Centre for Astrophysics (Bates et al., 2012).

Once the net has been trained, it is applied to all pulsar candidates from the HTRU survey. The output scores are stored and those candidates with *pulsar* >0.5 and *not pulsar* <0.5 are inspected by a human. This filtering routinely reduces the number for human

inspection by a factor  $\sim 100$ . The ANN used at JBO is able to identify 85% of pulsars ( $P > 10$  ms) and 65% of MSPs ( $P < 10$  ms) (Bates et al., 2012). The ANN provides a useful first look at the data but it is also important to look at other high-SNR candidates with plausible  $P$  and DM values, particularly those with  $P < 10$  ms. Regardless of ANN scores, all candidates are stored on disk and themselves form a derivative dataset to mine for pulsars with new techniques.

### 2.3.7 Human inspection

The final stage of candidate selection is human inspection. Currently in the HTRU survey this is done for those that are scored highly by the ANN and for high-SNR MSP candidates. There are three basic categories of classification from human inspection - noise, RFI, or candidate pulsar. The amount of data is such that noise fluctuations will sometimes result in candidates which exceed the SNR threshold (see Figure 2.15).

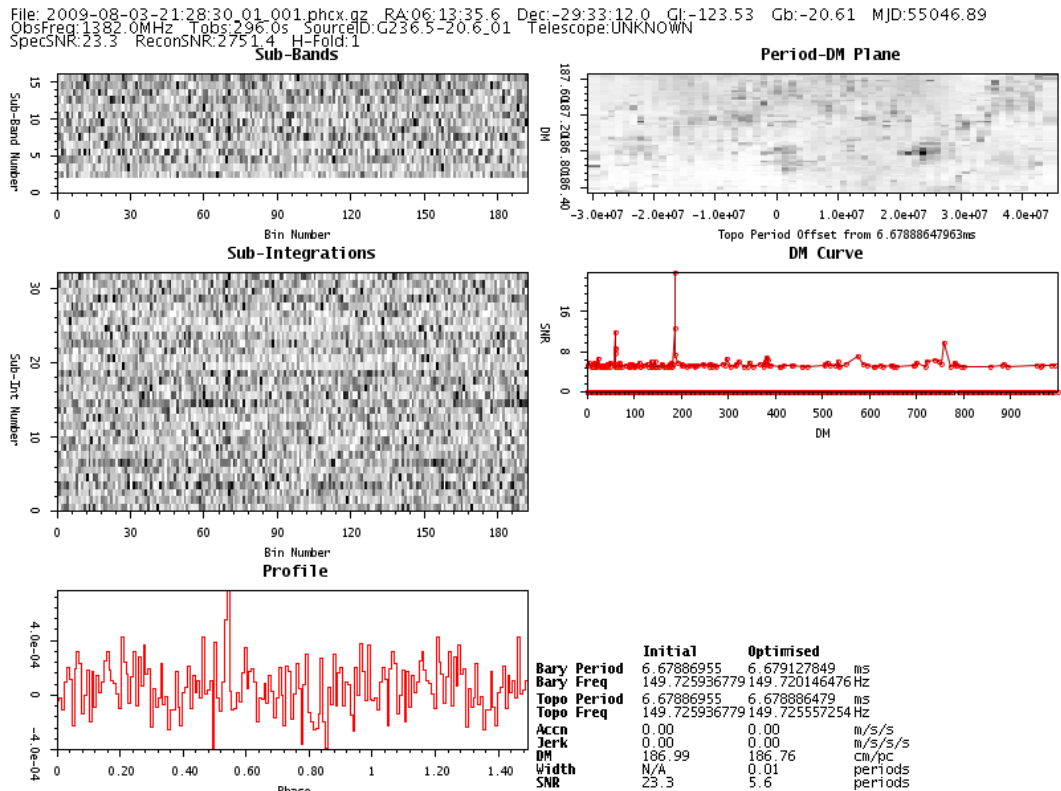


**Figure 2.15** – A noise candidate from the HTRU survey. While the spectral SNR is 23 the *optimised* SNR (from folding) has fallen to 5.6. There is also no discernible broadband or persistent emission, and the peak of the folded profile consists of just a single sample, again indicative of noise.

RFI candidates are usually easy to distinguish in the candidate plots. Often the signal is narrowband: the signal bandwidth is smaller than the total observing bandwidth. This is a typical feature of some types of RFI and thus candidates of this type are easily rejected. Similarly, the folded profile subbands shown in the candidate plot means that the user can tell if the pulsar was detected throughout the observation; temporally narrow signals are also typical of RFI. The user must however be mindful of intermittent pulsars which may switch “on” or “off” during an observation however (Kramer et al., 2006a).

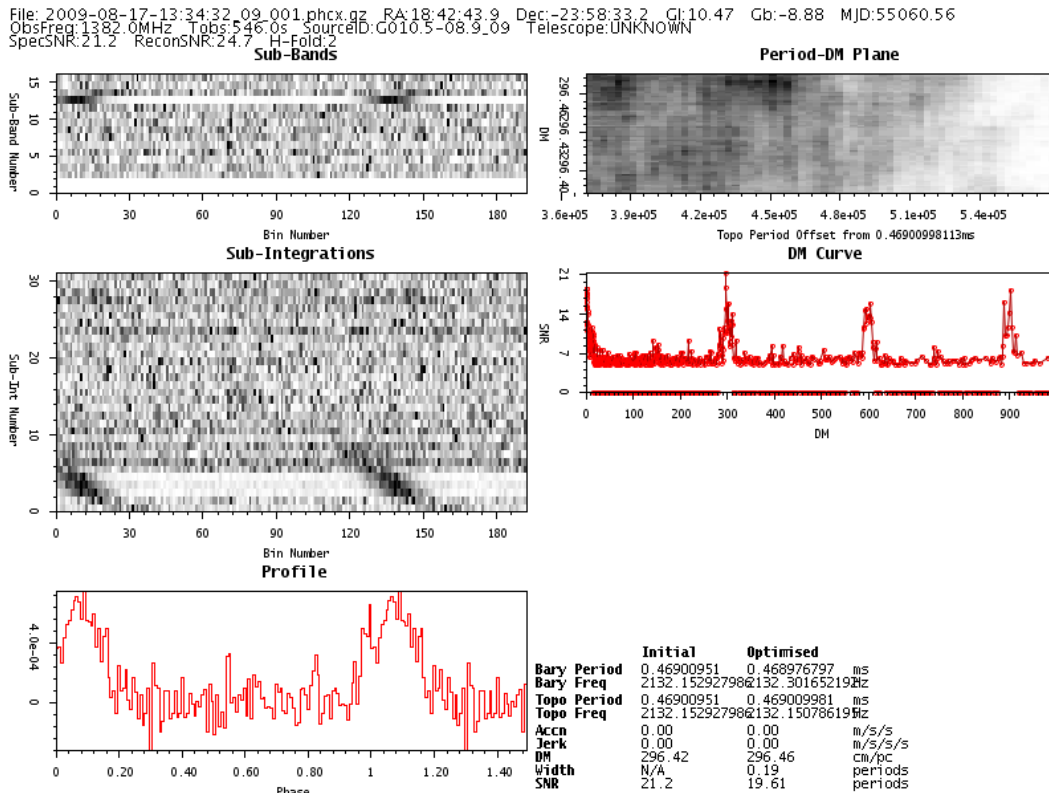


**Figure 2.16** – A candidate from the HTRU survey which is an example of RFI. This candidate shows detected pulsations across only a small fraction of the observing band, and only during a small fraction of the total integration time, strongly indicative of RFI. In addition,  $P = 0.47$  ms would be dispersed within a channel to greater than the pulse period at a DM of  $296 \text{ cm}^{-3} \text{ pc}$  - this can not have been a truly dispersed signal. The higher “harmonics” of  $\text{DM} = 296 \text{ cm}^{-3} \text{ pc}$  in the DM-SNR plot are due to the pulse wrapping over an integer number of pulse periods.

### 2.3.8 Candidate follow-up

When a strong pulsar candidate is identified (e.g. Figure 2.13) it is followed-up with a confirmation observation. For MSPs this consists of a search observation at the position of the centre of the beam in which the candidate was detected. The data is folded at the

optimised period of the candidate, and is corrected for the candidate DM. `pdmp` is used to optimise these nominal values and the observer checks for the detection of the pulsar. MSPs are often found in binaries and the apparent pulse period could be significantly different from the original search period due to orbital Doppler shifting. If the pulsar is not apparent then the data are dedispersed and searched for periodicity in the power spectrum. For normal pulsars the data is folded during the observation at the nominal pulse period; `pdmp`'s incremental changes are then able to directly optimise  $P$  and DM.

If confirmed, the new pulsar will be *gridded*. Gridding is a series of 5 observations, one at the position of the centre of the confirmation beam, and four equally spaced single beam pointings, separated by a half-power beam-width, from this nominal position. The SNR of any detections in these five beams is then used to constrain the position. The newly confirmed pulsar is then assigned the best position from gridding, which is then refined via long-term timing.

Confirmation and gridding observations are taken with the Parkes 64-m radio telescope, unless the candidate is at Decl.  $\gtrsim -30^\circ$  where the 76-m Lovell telescope at Jodrell Bank may be used. The ongoing timing of HTRU pulsar discoveries then continues from the same observatory.

### 2.3.9 Single pulse searching in the HTRU survey

The HTRU survey search pipeline uses the dedispersion routine `dedisperse_all`. For computing efficiency the single pulse search is performed by `dedisperse_all` on the time-series while they are still in the Random Access Memory (RAM) of the computer.

In addition to searching the full temporal resolution time-series ( $t_{\text{samp}} = 64 \mu \text{secs}$ ), each is searched after boxcar matched filtering. In the HTRU survey  $2^n$  adjacent samples are summed, where  $n = 0 - 9$ , greatly improving sensitivity to bursts with widths up to 32 ms.

A SNR threshold for single pulses is necessary to keep the number of candidates at a manageable level. Following the calculations of Burke-Spolaor et al. (2011b) the number of independent trials,  $N_t$ , (possible locations for a single pulse) in an observation is

$$N_t = N_{\text{DM}} \sum_{i=0}^{N_{\text{BC}}} \frac{N_{\text{samp}}}{2^i} \quad (2.11)$$

where  $N_{\text{DM}}$  is the number of DM trials,  $N_{\text{BC}}$  is the number of matched-filter widths used, and  $N_{\text{samp}}$  is the number of samples in a each dedispersed time-series. The error function can then be used to find the number of Gaussian distributed statistical noise samples,  $N_{\text{noise}}$ , which would exceed a certain SNR threshold,  $\text{SNR}_{\text{threshold}}$ . For a single beam of the high-latitude HTRU survey  $N_{\text{DM}} = 1436$ ,  $N_{\text{BC}} = 9$ , and  $N_{\text{samp}} = 4.2 \times 10^6$  (see Figure 2.17).

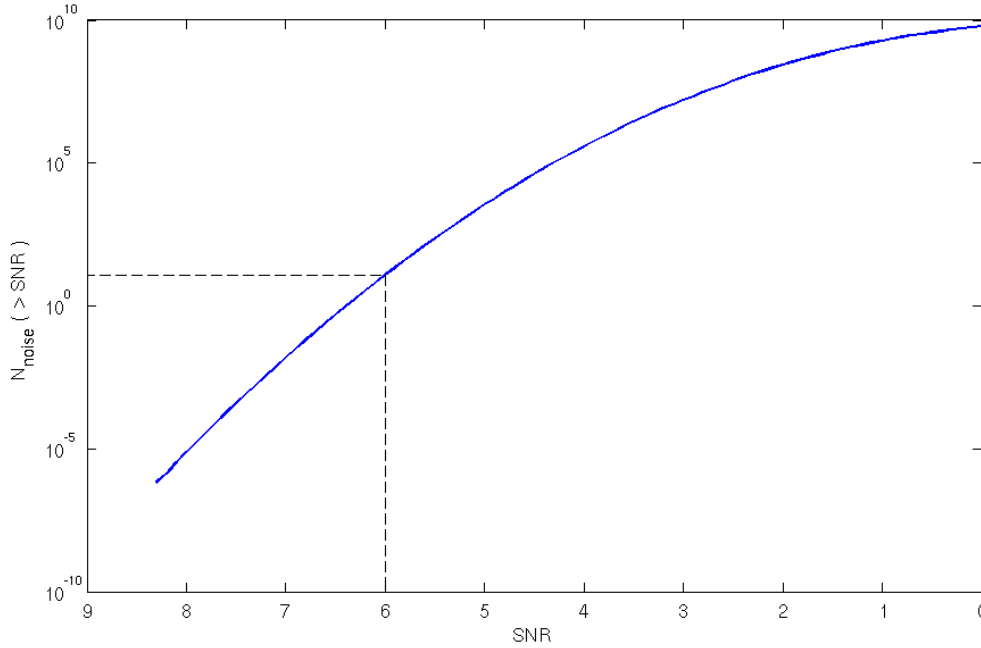


**Figure 2.17** – The number of Gaussian noise samples which will exceed a given SNR threshold in a HTRU high-latitude beam. The chosen SNR limit is shown with the black dashed line.

The  $\text{SNR}_{\text{threshold}}$  is chosen to minimise the number noise candidates while not rejecting real candidates. For  $\text{SNR}_{\text{threshold}} = 6$  then  $N_{\text{noise}} \approx 12$ . To reduce this number, other characteristics not expected of noise can be exploited. Of course, real broadband single pulses have non-Gaussian statistics and may appear in multiple DM and boxcar-width trials - this property is also used to reject statistical fluctuations. In the case of the HTRU survey,  $\text{SNR}_{\text{threshold}} = 6$  was therefore chosen as a suitable threshold after inspection of candidates.

Dispersion is not expected in terrestrial signals, which commonly have a peak in SNR when  $\text{DM}_{\text{test}} \approx 0 \text{ cm}^{-3} \text{ pc}$ . By restricting candidates to those with a peak SNR at  $\text{DM}_{\text{test}} > \text{DM}_{\text{cut}}$  the number of non-dispersed RFI candidates, which would otherwise pass for human inspection, is greatly reduced. In the HTRU survey this threshold is set to  $\text{DM}_{\text{cut}} = 3 \text{ cm}^{-3} \text{ pc}$ .

## Sensitivity

It is useful to consider how sensitive the HTRU survey is to single pulses, particularly as a function of DM. The ability to evaluate this will become important when considering populations of bursts and their DMs. A modified version of the radiometer equation for single pulses is used to calculate the peak intrinsic flux density a source would need to have in order to be detected in the HTRU single pulse search pipeline. In the case of single pulses, it is the observed width of the pulse,  $W_{\text{obs}}$ , which is important to its detectability.  $W_{\text{obs}}$  is defined as

$$W_{\text{obs}} = (W_{\text{int}}^2 + W_{\text{scatt}}^2 + W_{\text{DM}}^2 + W_{\text{samp}}^2 + W_{\text{channel}}^2)^{1/2}, \quad (2.12)$$

where  $W_{\text{int}}$  is the intrinsic width of the burst,  $W_{\text{DM}}$  is the width induced due to  $\text{DM}_{\text{test}}$  not being an exact match to the sources true DM,  $W_{\text{scatt}}$  is an increased observed width of a pulse imparted during propagation,  $W_{\text{channel}}$  is the dispersive smearing within a single channel, and  $W_{\text{samp}}$  is smearing of a pulse due to the finite sampling time of the signal.  $\tau_{\text{channel}}$  is calculated from system parameters to be

$$\tau_{\text{channel}} = 8.3 \times 10^3 \text{ secs} \left( \frac{\text{DM}}{\text{cm}^{-3}\text{pc}} \right) \left( \frac{\nu_{\text{mid}}}{\text{MHz}} \right)^{-3} \left( \frac{B_{\text{chan}}}{\text{MHz}} \right), \quad (2.13)$$

where  $\nu_{\text{mid}}$  is the central frequency of the observing band, and  $B_{\text{chan}}$  is the channel bandwidth. Scattering is more complicated; within the Galaxy there is an empirical relation found by Bhat et al. (2004) which relates the scattering timescale,  $W_{\text{scatt}}$ , to the DM. The relation was derived from multi-frequency measurements of pulsars throughout the Milky Way and as such it may not be applicable to propagation through the ionised intergalactic medium. There is also a spread of at least two orders of magnitude in  $W_{\text{scatt}}$  for a given DM: in calculating the required peak flux density of a burst to be detected in the HTRU data, a spread of one order of magnitude on  $W_{\text{scatt}}$  either side of the Bhat et al. (2004) relation is used (see Figure 2.18). The limiting peak flux density  $S_{\text{peak}}$ , for a burst is defined as

$$S_{\text{peak}} = \frac{\sigma \beta (T_{\text{sys}} + T_{\text{sky}})}{G \sqrt{n_p B W_{\text{obs}}}}, \quad (2.14)$$

where  $\sigma = 9$  is the minimum acceptable signal to noise ratio,  $\beta = 1.07$  is a factor from

digitisation (Kouwenhoven & Voûte, 2001),  $T_{\text{sys}}$  and  $T_{\text{sky}}$  are the system and sky temperatures respectively,  $G = 0.735 \text{ Jy K}^{-1}$  is the telescope gain, and  $B = 340 \text{ MHz}$  is the total useful observing bandwidth.

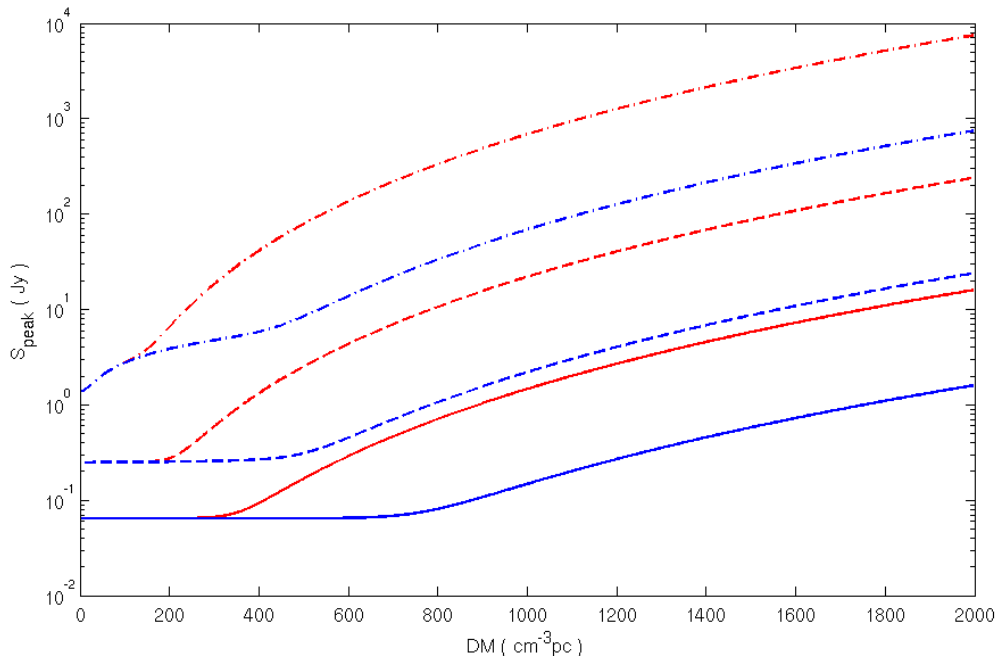


**Figure 2.18** – The minimum peak flux density of a single burst as a function of DM.  $S_{\text{peak}}$  is peak flux density a single pulse must have in order to be detected with an SNR of 9 in the HTRU survey. The intrinsic widths are shown; dashed-dotted lines correspond to  $W_{\text{int}} = 64 \mu\text{s}$  (the raw sampling rate), dashed lines to  $W_{\text{int}} = 2 \text{ ms}$ , and solid lines to  $W_{\text{int}} = 30 \text{ ms}$ . The blue lines correspond to a degree of scattering a factor of ten lower than the Bhat et al. (2004) scattering model, and the red lines a factor of 10 higher.

For  $\text{DM} \gtrsim 500 \text{ cm}^{-3} \text{ pc}$  the apparent pulse width is dominated by scattering. As a burst appears wider it becomes harder to detect; this calculation suggests that scattering is detrimental to the detectability of high-DM bursts. In order for a  $W_{\text{int}} = 2 \text{ ms}$  single pulse to have the same SNR when  $\text{DM} = 1000 \text{ cm}^{-3} \text{ pc}$  as when  $\text{DM} = 500 \text{ cm}^{-3} \text{ pc}$  its peak flux density would have to be approximately a factor of 10 higher, even in the low scattering regime shown in Figure 2.18.

The data from each of the 13 beams of the multibeam receiver are available on the same processing node so it is possible to take advantage of the fact that many single pulse sources of RFI often appear simultaneously in multiple beams (Burke-Spolaor et al., 2011a). This happens because the source is not in any of the beams at all but almost certainly in the direction of the horizon (the 64-m Parkes radio dish cannot point to the horizon). The RFI

are therefore likely in a sidelobe of the beam patterns of the receiver or in the near-field. The sources of RFI are instead extremely bright and arrive at the feed horns over the edge of the dish. When all 13 beams of a pointing have been processed we can combine the single pulse candidates, and reject any which are temporally associated and appear in  $> 9$  beams.

A number of heuristics and sections of reduced data are included in a single pulse candidate file. High SNR single-pulse candidate files include the dedispersed time-series around the pulse position in all 13 beams, the time-series in which the single pulse has the highest SNR, the time-series with  $DM_{\text{test}}$  value one step above and below, and the zero-DM time-series. The single pulse SNR as a function of boxcar matched filter width and of DM is included, as is small section of non-dedispersed filterbank data centred on the pulse (see Figure 2.19). All these diagnostics allow human inspection to quickly identify potentially interesting candidates.

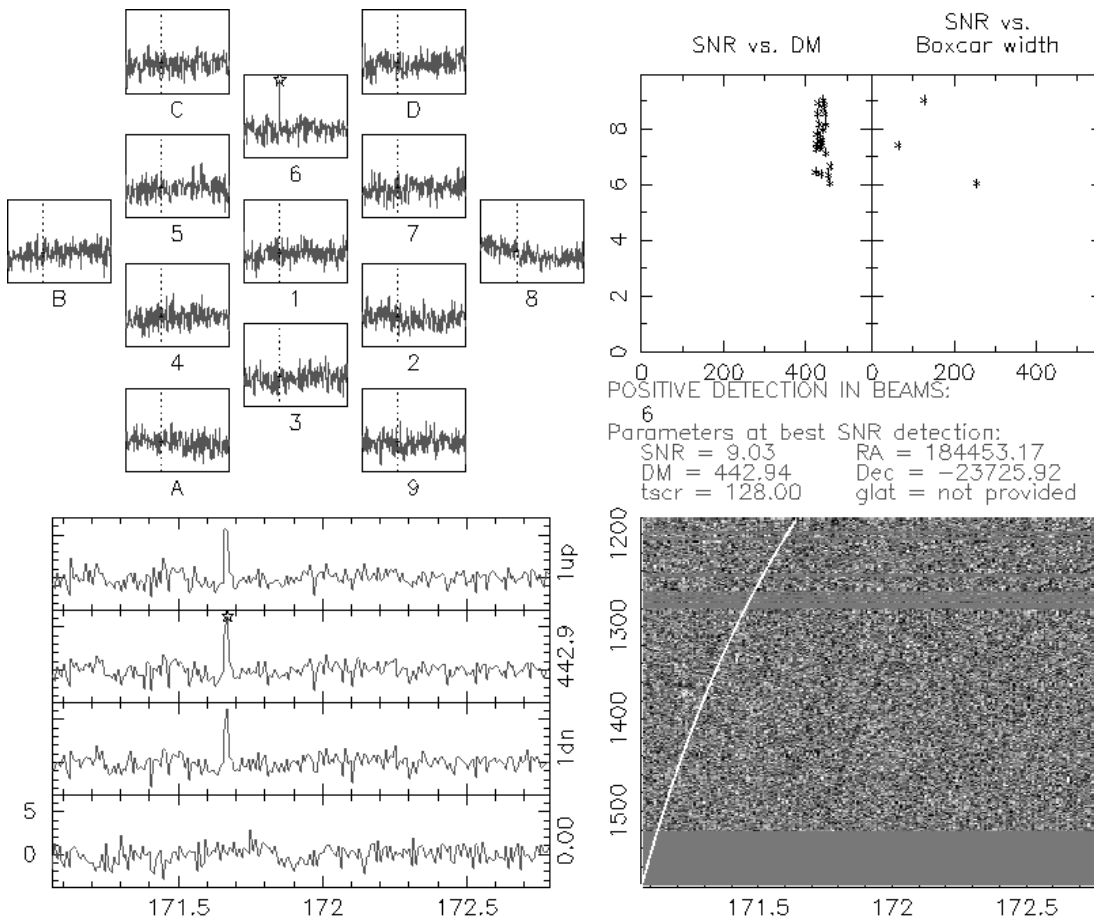


**Figure 2.19** – A single pulse candidate from PSR J1843–0211. The dedispersed time-series (dedispersed with the DM which gives the highest pulse) for all 13 beams of the receiver are shown (top left), the dedispersed time-series and one DM step above and below, the zero-DM timeseries shown (bottom left). The non-dedispersed section of filterbank data (bottom right) is overlaid with the dispersive sweep expected of pulse with  $DM_{\text{test}}$  (white line). In the top right the SNR as a function of  $DM_{\text{test}}$  and of boxcar matched filter width are shown. Basic parameters of the pulse (SNR, DM, best matched filter width, Right Ascension and Declination) are also shown. In this case the dispersed sweep of the pulse is visible across the band as well as in the dedispersed time-series (only in beam #6). Note that the pulse is not seen in any of the other beams of the receiver, or in the zero-DM time-series.

A large proportion of single pulse RFI is caused by bright, narrowband, short timescale bursts of radiation. These are sufficiently bright in a single part of the band that the receiver saturates. This causes the gain to fall across the *full* observing band. The result is a narrowband pulse where the levels across the rest of the band are depressed. At  $DM = 0 \text{ cm}^{-3} \text{ pc}$  the average of the channels at this sample may be zero or negative and does not look like RFI, where a peak in the zero-DM time-series would be expected. However, when dedispersed however the average is often positive, resulting in an apparent dispersed detection

(e.g. Figure 2.20). Human inspection allows the quick rejection of the majority of RFI, including this type which can pass the RFI rejection.

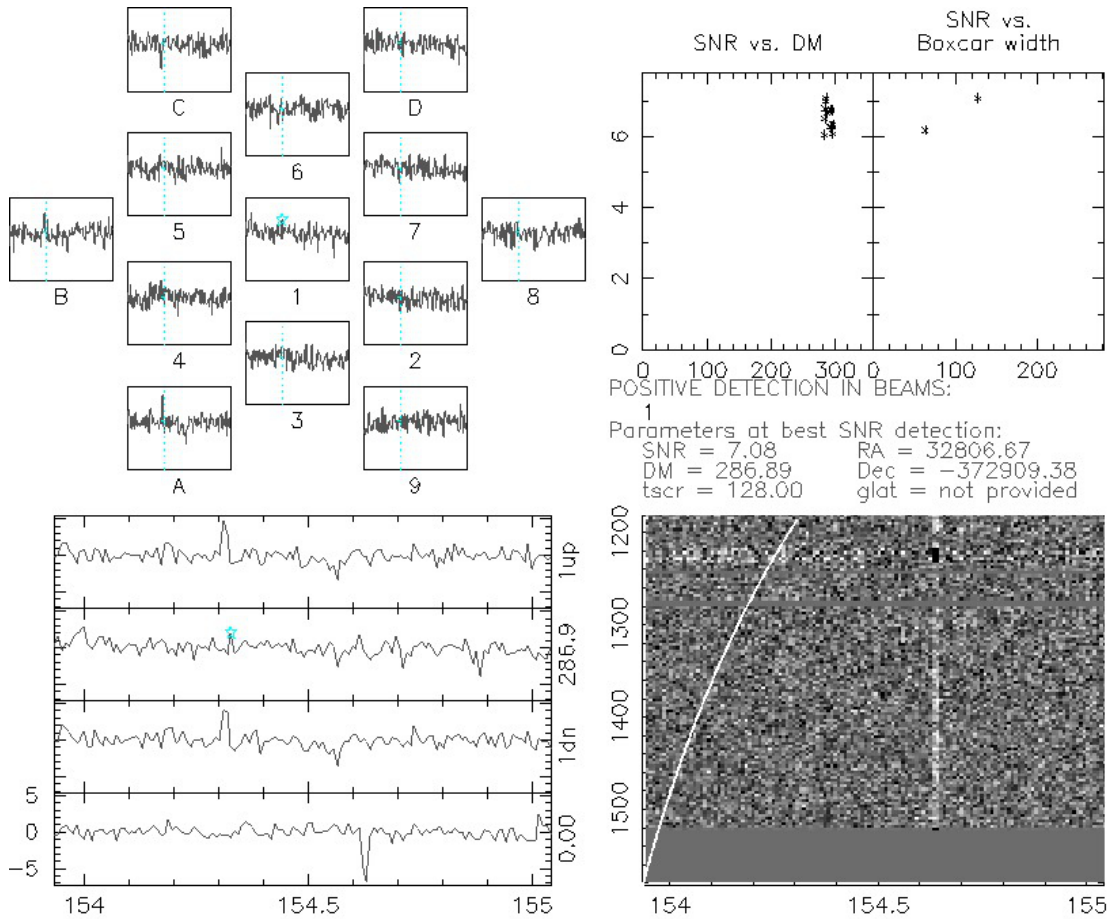


**Figure 2.20** – A single pulse RFI candidate showing a narrowband pulse which has saturated the receiver. The zero-DM timeseries shows no significant detection but the dedispersed timeseries do.

An `xml` candidate format for the single pulse candidates, similar to the `phcx` pulsar candidates, has been developed, enabling future searching and narrowing of the candidate repository. An implementation of an ANN, when a sufficient training set has been developed, may also prove useful.

## Chapter 3

# Discovery of five recycled pulsars in the High Time Resolution Universe survey

This chapter is based on a paper in preparation entitled “The High Time Resolution Universe survey: Discovery of 5 Millisecond Pulsars & the optical detectability of white dwarf companions”

D. Thornton, M. Bailes, C. Bassa, S. Bates, N. D. R. Bhat, M. Burgay, S. Burke-Spolaor, D. J. Champion, N. D’Amico, A. Jameson, S. Johnston, M. J. Keith, M. Kramer, L. Levin, A. Lyne, S. Milia, C. Ng, A. Possenti, B. Stappers, W. van Straten

In this chapter five partially and fully recycled pulsars discovered in the HTRU survey are presented and analysed. Their spin periods range from 2.01 ms to 66.29 ms, and three are in binary systems with companions that are most likely to be white dwarfs, one is in an orbit with either a heavy white dwarf or another neutron star, and one, which we conclude is a member of the growing class of disrupted binary pulsars, is isolated. Given the exciting possibility of testing evolutionary and gravitational theory through the study of pulsar-white dwarf binaries, I analyse the probability of an optical detection of the white dwarf companions to pulsars in the HTRU survey sample.

### 3.1 Introduction

The progenitors of neutron stars are massive stars ( $M = 8 - 10 M_{\odot}$ ); a large fraction of which are found in binary systems (Lada, 2006). The more massive of the two stars will have a shorter lifetime and, if sufficiently massive, undergo a core collapse supernova (ccSN) first (see Section 1). The remnant of the stellar core may form a neutron star (NS), which in turn could be a detectable pulsar. The fact that most of the normal pulsars observed are isolated implies that the majority of massive stellar binaries disrupt during the first ccSN. Pulsars that remain gravitationally bound to their companion post-ccSN may then have their evolution affected by the companion, possibly recycling them (Alpar et al., 1982). The recycling - or *spin-up* stage - shortens the spin-period and reduces the surface magnetic field strength, in turn allowing them to be detectable as radio pulsars for billions of years. See Chapter 1 for a more detailed discussion of the pulsar recycling process.

### 3.2 Discovery and Timing

The five pulsars presented here were discovered in the HTRU survey for pulsars and transients (Keith et al., 2010). Survey observations are made with the 64-metre Parkes radio telescope using the 13-beam 21 cm multibeam receiver. Each beam's half-power beamwidth is approximately 14 arcminutes. The 13 simultaneous beams enable rapid coverage of the sky compared to a single beam system. The survey has an observing band centred at 1352 MHz and has a useful bandwidth of 340 MHz. The HTRU survey is split into 3 areas: the low-, mid- and high-Galactic latitude regions. The discoveries presented here are from the mid-latitude region which is centred on the Galactic plane and has pointings of 540 seconds in duration. The region covers  $-120^{\circ} < l < +30^{\circ}$  and  $-15^{\circ} < b < +15^{\circ}$  in Galactic coordinates. See Chapter 2 for a more detailed discussion of the HTRU survey.

The data were processed using the Fourier transform based pulsar search pipeline described in Chapter 2 and Keith et al. (2010). The discoveries described here were initially identified using an artificial neural network (ANN) which aims to highlight the best candidates from the survey for human inspection (Bates et al., 2012; Eatough et al., 2010). After inspection, confirmation observations are taken at the sky positions of the survey beams deemed to contain the best candidates. These confirmations are performed with the 64-m Parkes dish or the 76-m Lovell Telescope at Jodrell Bank. Four of the five pulsars presented here, PSRs J1227–6208, J1405–4656, J1431–4715, and J1653–2054, are in orbit with a

**Table 3.1** – Observing system details for the timing observations made as part of this work. Note the specifications for the Lovell Telescope take into account the removal, as standard, of a section of the observing bandwidth due to contamination by RFI.

Telescope	Centre Freq. (GHz)	BW (GHz)	$n_{\text{chan}}$	$\langle\tau_{\text{obs}}\rangle$ (s)
Parkes 64-m	0.732	0.064	512	900
	1.369	0.256	1024	600
	3.094	1.024	1024	900
Lovell 76-m	1.524	0.384	768	1800

binary companion, while one, PSR J1729–2117, is isolated.

As well as being independently discovered in the mid-latitude region of the HTRU survey PSR J1227–6208 was also identified by two separate groups in the Parkes Multibeam Pulsar Survey (PMPS) (Mickaliger et al., 2012; Knispel et al., 2013). The PMPS discoveries happened around 10 years after the survey was completed and are illustrative of large pulsar surveys providing the opportunity to discover new pulsars with increasing computing power and new techniques many years after the data was recorded. All observations, timing, and analysis of PSR J1227–6208 presented here are independent work.

Once confirmed, the new pulsars were timed regularly with digital filterbank (DFB) backend systems; PSRs J1653–2054 and J1729–2117 with the 76-m Lovell telescope at Jodrell Bank Observatory (JBO) and PSRs J1431–4715, J1405–4656, and J1227–6208 with the 64-m radio telescope at Parkes (see Table 3.1). The pulsars timed with the Lovell telescope were observed approximately once per week, whereas those observed using the Parkes radio telescope were observed more sporadically, while maintaining phase coherence, with one case of an approximately 80 day gap between observations.

Each observation resulted in a pulse time-of-arrival (TOA) measurement. The temporal variation of these TOAs is then modelled by a series of astrometric, spin, and, if necessary, orbital parameters. This model is modified and fit by comparison with further TOA observations (described in Lorimer & Kramer 2005). Parameters were fitted using the TEMPO2 software package (Hobbs, Edwards & Manchester, 2006) using the DE 414 solar system ephemeris from JPL for barycentric correction<sup>1</sup>. The best fit parameters for the five pulsars are provided in Table 3.2.

<sup>1</sup><http://ssd.jpl.nasa.gov/?ephemerides>

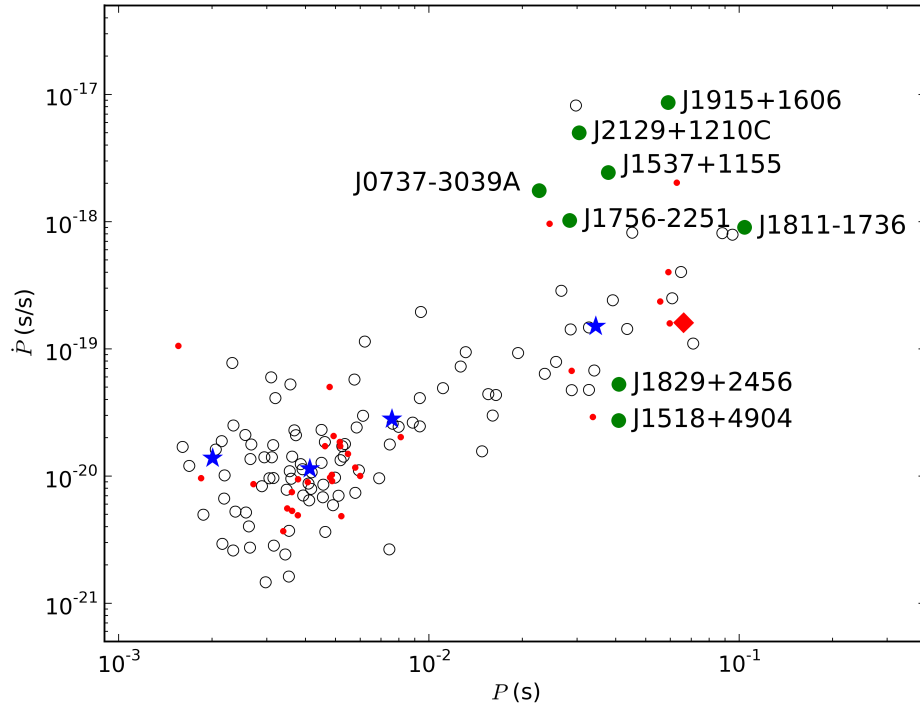


**Figure 3.1** – A plot of pulse period derivative  $\dot{P}$  against pulse period  $P$ . Pulsars in binaries are represented as open circles, isolated pulsars as red round points, DNS systems as green circles (see Table 3.3), the four newly discovered pulsar binaries are plotted as stars, and the isolated pulsar, PSR J1729–2117, as a large diamond (see Table 3.2). Only Galactic pulsars with  $P < 100$  ms and  $\dot{P} < 10^{-16}$  and DNS systems are shown.

### 3.3 Results

The pulse periods for the systems range from 2.01 ms (PSR J1431–4715), placing it among the 20 fastest spinning pulsars, and 66.29 ms (PSR J1729–2117), one of the longer periods for a recycled pulsar (Manchester et al., 2005). While the five pulsars do not represent any fundamentally new type, together they comprise systems from across the range of known recycled pulsar and binary types (see Figure 3.1). PSR J1729–2117, does not exhibit any detectable periodic variation of the apparent pulse period that would be indicative of a binary companion, making it one of just two isolated recycled pulsars in the HTRU survey to date; an interesting dearth when compared to previously known recycled pulsars, which is discussed in Burgay et al. (2013).

To determine the masses of the companion in binary pulsar systems the orbital period,  $P_{\text{orb}}$ , and the projected semi-major axis of the pulsar’s orbit,  $a_p \sin(i)$  are measured. These

two quantities are related via the *mass function* (Equation 3.1). The mass function for a range of inclinations can be used to derive a companion mass range; particularly a lower mass limit. In all calculations a canonical pulsar mass,  $M_p = 1.4 M_\odot$  is used; although it should be noted there is mounting evidence for pulsars more massive than  $1.4 M_\odot$  (e.g. Demorest et al. 2010; van Kerkwijk, Breton & Kulkarni 2011; Antoniadis et al. 2013). The ability to measure the pulsar mass is one of the reasons for detailed measurements of binary systems. It would be interesting, for instance, to determine if heavier pulsars have shorter spin periods, perhaps due to the mass accreted during spin-up (e.g. Jacoby et al. 2005). For Keplerian orbits the mass function relates these quantities to  $M_c$  and  $M_p$ , the mass of the companion and pulsar respectively:

$$\frac{(M_c \sin i)^3}{(M_p + M_c)^2} = \frac{4\pi^2 (a_p \sin i)^3}{G P_{\text{orb}}^2} M_\odot. \quad (3.1)$$

For a given inclination,  $i$ , a companion mass  $M_c$  can be determined. If the orbit is viewed edge-on ( $i = 90^\circ$ )  $M_c$  is the minimum companion mass,  $i = 60^\circ$  corresponds to the median companion mass, and a maximum mass,  $M_{c, \text{max}}$ , is defined such that for randomly inclined orbits the probability  $(M_c > M_{c, \text{max}}) < 0.05$  (see Table 3.2).

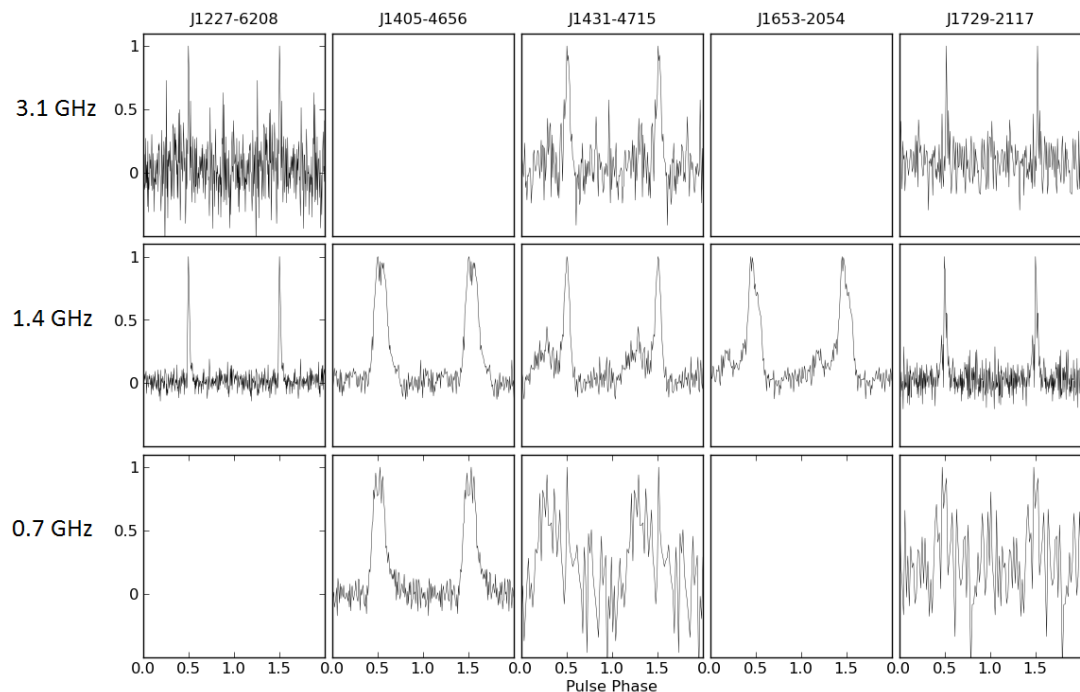


**Figure 3.2** – Typical pulse profiles are shown for the five recycled pulsars discussed in this chapter. The top, middle, and bottom rows correspond to 3.1 GHz, 1.4 GHz, and 0.732 GHz respectively. Blank plots correspond to non-detections. The observing times are given in Table 3.1). All observations are taken with the 64-m Parkes radio telescope, except for the 1.4 GHz observations and timing of PSRs J1653–2054 and J1729–2117, which use the 76-m Lovell telescope at Jodrell Bank.

Parameter	PSR J1227–6208	PSR J1405–4656	PSR J1431–4715	PSR J1653–2054	PSR J1729–2117
Right Ascension (J2000)	12:27:00.444(3)	14:05:51.4241(5)	14:31:44.6145(5)	16:53:31.014(1)	17:29:10.812(2)
Declination (J2000)	–62:08:43.81(1)	–46:56:02.296(6)	–47:15:27.64(1)	–20:54:55.3(1)	–21:17:26.3(5)
Galactic Longitude (°)	+300.08	+315.90	+320.05	+359.96	+4.49
Galactic Latitude (°)	+0.59	+14.05	+12.25	+14.26	+7.22
Discovery S/N	11.2	125.0	12.0	11.5	13.7
Offset from survey beam (°)	0.1	0.05	0.03	0.04	0.08
TOA Range (MJD)	55901–56331	55667–56331	55756–56022	55646–56332	55529–56334
$P$ (ms)	34.527834648(2)	7.60220343250(9)	2.011953440(1)	4.1129145284650(2)	66.2929002985(1)
$\dot{P}$ ( $\times 10^{-20}$ )	15(1)	2.81(3)	1.38(4)	1.14(1)	16(1)
DM ( $\text{cm}^{-3}$ pc)	362.6	13.89	59.4	56.52	34.9
$S_{1.4\text{GHz}}$ (mJy)	0.22	0.92	0.73	0.16	0.20
DM Distance, $d$ (kpc)	8.32	0.580	1.533	1.626	1.091
$L_{1.4\text{GHz}}$ (mJy kpc <sup>2</sup> )	15.2	0.3	1.7	0.4	0.02
$\tau_c$ (G.yr)	3.6	4.2	3.3	5.6	6.2
$B_{\text{surf}}$ (Gauss)	$2.3 \times 10^9$	$4.6 \times 10^8$	$2.2 \times 10^8$	$2.2 \times 10^9$	$3.3 \times 10^9$
$B_{\text{lc}}$ (Gauss)	$9.4 \times 10^1$	$8.4 \times 10^2$	$1.0 \times 10^5$	$1.8 \times 10^3$	$2.7 \times 10^1$
$\dot{E}$ (erg s <sup>−1</sup> )	$1.4 \times 10^{34}$	$2.5 \times 10^{33}$	$4.8 \times 10^{33}$	$6.4 \times 10^{33}$	$2.2 \times 10^{31}$
$\dot{E}/d^2$ (erg kpc <sup>−2</sup> s <sup>−1</sup> )	$2.0 \times 10^{30}$	$7.5 \times 10^{33}$	$2.0 \times 10^{33}$	$2.4 \times 10^{33}$	$1.9 \times 10^{31}$
$\dot{P}_{\text{Shk}}$ ( $\times 10^{-20}$ )	0.32	1.0	0.1	0.2	4.7
$P_{\text{orb}}$ (d)	6.72101336(4)	8.95641983(9)	0.449739151(1)	1.22681523(1)	–
$a \sin i$ (lt s)	23.20062(1)	6.567651(8)	0.550113(1)	0.688856(5)	–
$T_{\text{asc}}$ (MJD)	55991.1937916(8)	55692.739369(2)	55746.1047702(2)	55584.728429(3)	–
$e_1$	$5.22(1) \times 10^{-4}$	$6(2) \times 10^{-6}$	$1.52(3) \times 10^{-4}$	$< 2 \times 10^{-5}$	–
$e_2$	$1.028(1) \times 10^{-3}$	$3(2) \times 10^{-6}$	$-2.8(4) \times 10^{-5}$	$3(1) \times 10^{-5}$	–
$e$	$1.1153(1) \times 10^{-3}$	$7(2) \times 10^{-6}$	$< 1.7(8) \times 10^{-5}$	$< 10^{-5}$	–
$\omega$ (°)	26.95(7)	60(15)	–	–	–
$M_{\text{comp,min}}$ ( $M_{\odot}$ )	1.29	0.20	0.127	0.080	–
$M_{\text{comp,med}}$ ( $M_{\odot}$ )	1.60	0.25	0.148	0.093	–
$M_{\text{comp,max}}$ ( $M_{\odot}$ )	12.45	0.87	0.471	0.281	–
RMS of fit ( $\mu\text{s}$ )	106.8	30.0	36.4	27.9	195

Table 3.2 – See below

**Table 3.2** - The measured and calculated parameters for the presented pulsar systems. Where required a canonical pulsar mass of  $1.4 M_{\odot}$  has been used. The maximum companion mass  $M_{c, \text{max}}$  is the 95% confidence level limit which is at an inclination of  $i = 18^{\circ}$ . The NE2001 model of Galactic electron density (Cordes & Lazio, 2002) has been used to infer distance from the dispersion measure.  $\dot{P}_{\text{Shk}}$  is the apparent spin period derivative caused by the proper motion of the pulsar, this value is the maximum  $\dot{P}$  expected for a nominal MSP velocity of  $85 \text{ km s}^{-1}$  at the distance calculated from the dispersion measure (Toscano et al., 1999). None of the four binary systems have a highly eccentric orbit; because of this the ELL1 binary timing model was used (suitable for low- $e$  orbits) which uses

the Laplace-Lagrange parameters  $\epsilon_1$  and  $\epsilon_2$  (Lange et al., 2001).

### 3.3.1 PSR J1227–6208

PSR J1227–6208 has measured values of  $P$  and  $\dot{P}$  that place it in a region of the  $P - \dot{P}$  diagram where mildly recycled pulsars are found (see Figure 3.1). This is consistent with it having been spun-up during unstable, short lived mass transfer in an HMXB spin-up phase (see Section 1.1.5).

It has an orbital eccentricity,  $e = 1.153(1) \times 10^{-3}$ , a period  $P_{\text{orb}} = 6.72$  days, and a projected semi-major axis,  $a_p \sin(i) = 23.2$  ls. Using Equation 3.1 and assuming  $M_p = 1.4 M_\odot$ , this leads to a minimum companion mass of  $M_{c, \text{min}} = 1.29 M_\odot$  if the system is viewed edge-on. The low eccentricity and high minimum companion mass are unusual: there are only 3 other systems known with  $e < 0.1$  and  $M_{c, \text{min}} > 1.0 M_\odot$ .

PSR J1227–6208 is similar to other so-called Intermediate Mass Binary Pulsars (IMBPs); for example PSR J1435–6100 (Camilo et al., 2001) and PSR J2222–0137 (Boyles et al., 2013). PSR J1227–6208’s spin parameters are also similar to PSR J0609+2130 - an isolated pulsar thought to be the result of an HMXB which disrupted during the second ccSN (Lorimer et al., 2004). In an IMBP it is thought the companion was not sufficiently massive to undergo a ccSN, resulting instead in the formation of a heavy CO or ONeMg WD. The minimum mass for the companion to PSR J1227–6208 is common for ONeMg WDs, which have a mass range around  $1.1 - 1.3 M_\odot$  (Tauris, Langer & Kramer, 2012). This is however the *minimum* mass the companion may have: it is already close to the upper limit of ONeMg WDs, and to the Chandrasekhar mass limit. If the system was not edge-on then the companion mass would be higher and inconsistent with a heavy WD, indeed the median companion mass  $M_{c, \text{med}} = 1.60 M_\odot$  (see Table 3.3.1).

For an inclination  $i < 71^\circ$ ,  $M_c \gtrsim 1.4 M_\odot$ , the companion may be a second NS and PSR J1227–6208 would be part of a DNS. Unseen as a pulsar in the survey observation, the second NS would have formed from a massive progenitor ( $8 - 10 M_\odot$ ), and the system would have evolved through an HMXB phase, hence the partially recycled pulsar. Comparing to known DNS systems the eccentricity ( $e = 1.153(1) \times 10^{-3}$ ) would be unusually low; see Table 3.3). The formation of DNS systems with such a small eccentricity appears to be unlikely (Chaurasia & Bailes, 2005) and as such the eccentricity is the only characteristic of PSR J1227–6208 which suggests it is not a DNS system. The simulations of Dewi, Podsiadlowski & Pols (2005) and Chaurasia & Bailes (2005) do however appear to

**Table 3.3** – Basic orbital and spin parameters for known DNS systems. Also included are the same parameters for PSR J1227–6208.

Pulsar	Spin period	Orbital period	Projected semi-major axis	Eccentricity,	Companion mass
	$P$ (ms)	$P_{\text{orb}}$ (d)	$a_p \sin i$ (ls)	$e$	$M_{c, \text{min}}$ ( $M_{\odot}$ )
J0737–3039	22.69	0.102	1.415	0.088	1.250
J1518+4904	40.93	8.634	20.044	0.249	> 0.83
B1534+12	37.90	0.420	3.729	0.273	1.34
J1756–2251	28.46	0.319	2.756	0.180	1.18
J1811–1736	104.18	18.779	34.783	0.828	> 0.87
J1829+2456	41.00	1.176	7.236	0.139	> 1.22
B1913+16	59.03	0.322	2.341	0.617	1.38
B2127+11C	30.52	0.335	2.518	0.681	1.354
J1227–6208	35.52	6.721	23.200	0.001	> 1.29

suggest that such low-eccentricity DNS systems *could* exist because of the possibility of very small ccSN kinematic kicks, although they would be extremely rare. Low-eccentricity DNS systems, however, would not lose energy via gravitational wave emission as quickly as eccentric systems, and consequently will survive longer before merging.

With  $\text{DM} = 362.6 \text{ cm}^{-3} \text{ pc}$  PSR J1227–6208 appears to be located at a large distance of 8.3 kpc. This would make an optical detection of a WD companion extremely difficult. Consequently, the best chance of measuring the masses in the system could come from the measurement of post-Keplerian parameters.

### Periastron advance

While the eccentricity of the orbit of PSR J1227–6208 is small, it is measurable, and is significantly higher than is typical for systems which have likely evolved through an LMXB phase (Phinney, 1992). It is possible to predict relativistic changes to the orbit due to general relativity. These changes are quantified by the post-Keplerian parameters and are largest for eccentric orbits. One of the easiest to measure is a changing longitude of periastron,

$$\dot{\omega} = 3T_{\odot}^{2/3} \left( \frac{P_{\text{orb}}}{2\pi} \right)^{-5/3} \frac{1}{1 - e^2} (M_p + M_c)^{2/3} \text{ rad s}^{-1}, \quad (3.2)$$

where  $T_{\odot} = \text{GM}_{\odot}/c^3$ ,  $P_{\text{orb}}$  is the orbital period,  $e$  is the orbital eccentricity, and  $M_c$  and  $M_p$  are the companion and pulsar masses respectively. A measured  $\dot{\omega}$  constitutes a measure-

ment of the combined masses,  $M_c + M_p$  and consequently constrains the companion mass. The prediction of Equation 3.2 is  $\dot{\omega} = 0.63 \text{ deg yr}^{-1}$  for the PSR J1227–6208 system; to date no significant measurement of  $\dot{\omega}$  has been possible.

### Shapiro delay

The radio pulses from a pulsar in a binary system are delayed as they cross the gravitational potential of the companion; this phenomenon is called *Shapiro delay* (Shapiro, 1964). The electromagnetic radiation takes a curved path around the companion, this bent path then corresponds to a longer travel time, and delays in the pulse TOAs may be observed. The magnitude of the delay depends on the relative position of the line-of-sight to the pulsar and the companion's gravitational potential, which is orbital phase dependent. The pulses take the longest path around the deepest part of the companion's potential when the pulsar is at superior conjunction (orbital phase,  $\Phi = 0.25$ ). The magnitude of the observed delay also depends on the viewing angle of the orbit. For a given companion mass the delay is maximal for an orbital system viewed edge-on ( $i = 90^\circ$ ).

The Shapiro delay,  $\Delta_S$ , is quantified by two post-Keplerian parameters, the *range*,  $r$ , and the *shape*,  $s$ . For low-eccentricity systems

$$\Delta_S(\Phi) = -2r \ln(1 - s \sin \Phi), \quad (3.3)$$

where  $\Phi$  is the orbital phase (where  $\Phi = 0$  is the ascending node),  $r = T_\odot M_c$  and  $s = \sin i$ . The Shapiro delay is the same for every orbit of the system and so when the TOA residuals are folded modulo- $P_{\text{orb}}$  a characteristic shape in the timing residuals may be measured. The orbital phase,  $\Phi$ , dependence of this delay is given by Equation 3.3.

An observing program was undertaken using the 64-m Parkes radio telescope to obtain TOAs across the orbit. A global timing solution was made (as given in Table 3.2), from which the astrometric and spin parameters were fixed. These TOAs were then fit for all the orbital parameters ( $P_{\text{orb}}$ ,  $T_{\text{asc}}$ ,  $a_p \sin(i)$ ,  $\epsilon_1$  and  $\epsilon_2$ ) with fixed values of  $M_c$  and  $\sin(i)$ . The reduced- $\chi^2$  ( $\chi_{\text{red}}^2$ ) goodness-of-fit statistic was then calculated for each pair of  $M_c$  and  $\sin(i)$  values (see Figure 3.3). The results of these fits indicate that large sections of  $M_c - \sin(i)$  are still possible, however preferred values appear to be at high inclination angles. For a companion mass of  $M_c = 1.29 M_\odot$  and  $i = 90^\circ$  then  $\chi_{\text{red}}^2 = 3.8$ ; while for  $M_c = 1.4 M_\odot$  and  $i = 71^\circ$  then  $\chi_{\text{red}}^2 = 1.3$ . This suggests that the binary may be a DNS system with

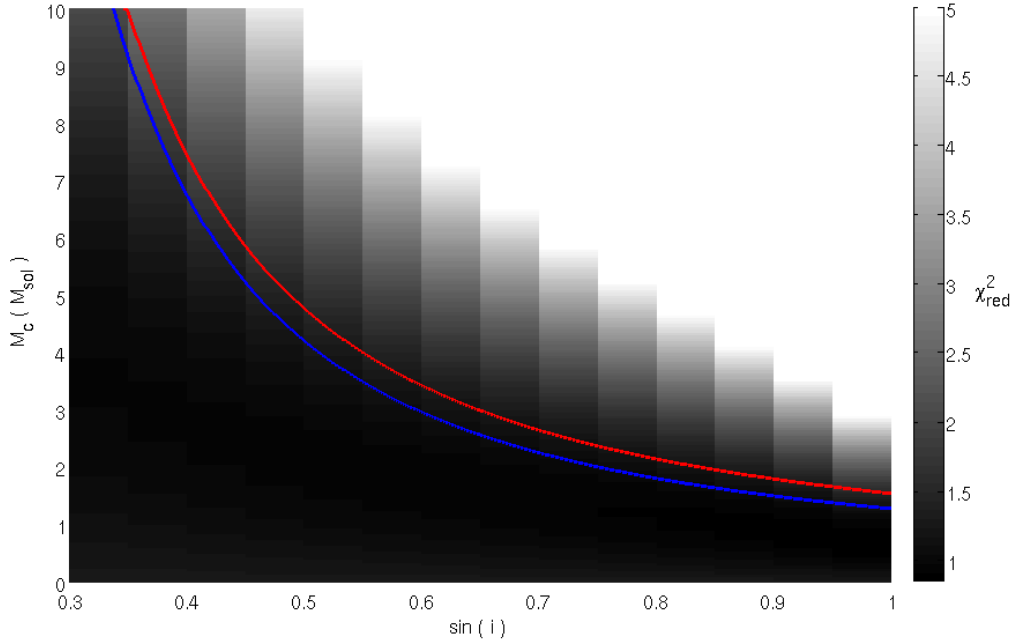


**Figure 3.3** – The  $\chi_{\text{red}}^2$  values calculated for a series of  $M_c$  and  $\sin(i)$  values. All  $\chi_{\text{red}}^2 > 5$  were set to be equal to 5 for sensible scaling. The constraints of a Keplerian orbit from pulsar timing with a  $1.4 M_{\odot}$  pulsar (blue) and for a  $2.0 M_{\odot}$  pulsar (red) are also shown (see Equation 3.1). For a pulsar of these masses or between then the true values will lie on or between these lines.

$i \approx 71^\circ$ . There is however little change in  $\chi_{\text{red}}^2$  along either the  $M_p = 1.4 M_{\odot}$  or the  $M_p = 2.0 M_{\odot}$  Keplerian relationships defined by the mass function (Equation 3.1).

Figure 3.4 shows that the density of observations around superior conjunction ( $\Phi = 0.25$ ) is high enough that if the system were edge-on with a  $M_c = 1.29 M_{\odot}$  companion then a measurable Shapiro delay would likely have been observed. Of course the lack of a Shapiro delay signal is consistent with a more massive companion. It is however important to note that some of the Shapiro delay may have been absorbed into the other timing parameters.

PSR J1227–6208 has a single narrow pulse at an observing frequency of 1.4 GHz, at 3.1 GHz a similarly narrow peak is detected. We have not yet made a detection at 0.732 GHz. The pulse profile appears to be approximately 3.2 times wider at 1.4 GHz than at 3.1 GHz. If this trend were due to scattering, and thus has a strong frequency dependence ( $\propto \nu^{-4}$  then the the profile width at 0.732 GHz would be approximately 2 ms. This time would not exceed the pulse period, consequently scattering would not be the reason that PSR J1227–6208 is not detected at 0.732 GHz.

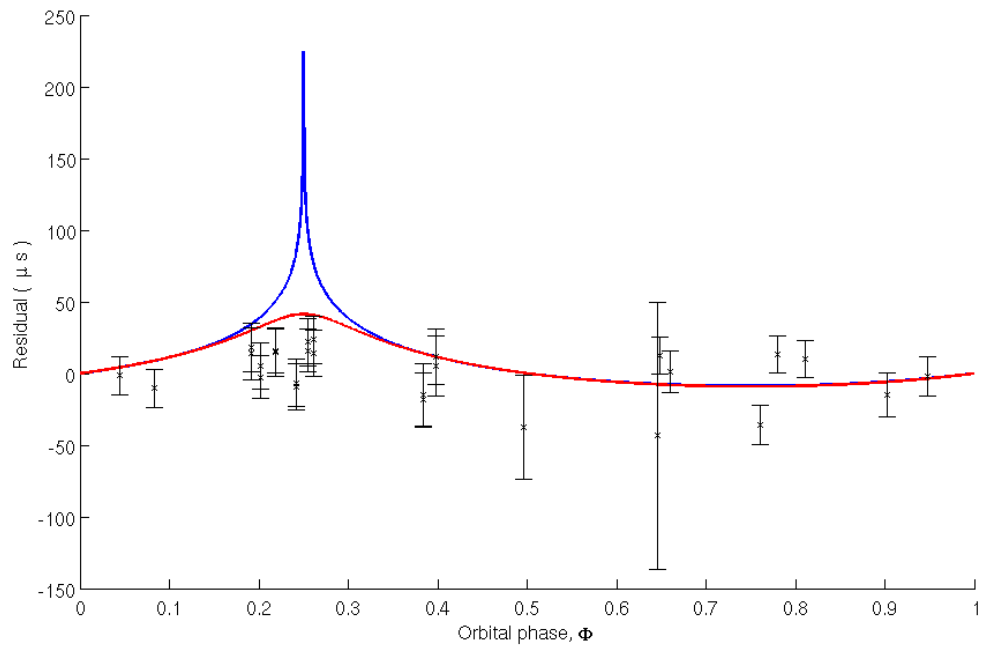


**Figure 3.4** – The residuals from the best fit global timing model for PSR J1227–6208 are shown plotted against orbital phase (these residuals have not had any Shapiro delay contribution taken into account). In blue is the expected Shapiro delay for  $M_c = 1.29 M_\odot$  and  $i = 90^\circ$ ; in red is the Shapiro delay for  $M_c = 1.4 M_\odot$  and  $i = 71^\circ$ , both are shown for  $M_p = 1.4 M_\odot$ .

### 3.3.2 PSR J1405–4656

The spin period,  $P = 7.6$  ms, and period derivative,  $\dot{P} = 2.81 \times 10^{-20}$ , of PSR J1405–4656 are typical of fully recycled MSPs (see Figure 3.1), and are indicative of it having undergone spin-up in a LMXB phase. The measured value of  $\dot{P}$  can be affected in a number of ways, one of these is the Shklovskii effect which is caused by a pulsar moving in the plane of the sky. This motion causes an apparent period derivative,  $\dot{P}_{\text{Shk}}$ . In the case of PSR J1405–4656 this contribution would be around 35% of the total measured, for a typical MSP velocity of  $v = 85$  km s<sup>-1</sup> (Toscano et al., 1999). Consequently the  $\dot{P}$  measured may not be totally intrinsic, and there is likely a contribution from the Shklovskii effect. This presence of a Shklovskii effect of this magnitude does not, however, change any of the conclusions about this MSP’s evolutionary history.

The flux density of PSR J1405–4656 varies significantly between observations. For instance, the survey observation had a SNR of 125 in 600 seconds whereas during timing there are many occasions when it was not detected in 1000 seconds. This is attributable to interstellar scintillation, which is caused by fluctuations in the density of the ionised material along the line of sight, which leads to ever-changing multipath propagation and results in the radio waves constructively and destructively interfering. For a distant pulsar a single fluctuation has relatively little effect, however for nearby pulsars a single fluctuation has a proportionately larger effect. The scintillation bandwidth for this source at 1.4 GHz is around 400 MHz (Cordes & Lazio, 2002), this would mean that with the observing band of the timing system (see Table 3.1) we would not expect to be able to discern individual scintles within the band - this is indeed the case. Because of the distance dependence of scintillation it is usually most pronounced in relatively nearby pulsars (Stinebring et al., 2000). PSR J1405–4656, with  $\text{DM} = 13.89$  cm<sup>-3</sup> pc and  $d = 0.580$  kpc, falls into this category. There is no discernible broadening of the pulse profile which may be attributed to scattering between the 1.4 GHz and 0.732 GHz pulse profiles. This is to be expected for such a low DM pulsar (Bhat et al., 2004).

### 3.3.3 PSR J1431–4715

PSR J1431–4715 has the 14th shortest spin period of all known pulsars ( $P = 2.01$  ms), and also a small spin-period derivative ( $\dot{P} = -1.38 \times 10^{-20}$  s s<sup>-1</sup>). These values place PSR J1431–4715 firmly amongst the fully recycled MSPs in the bottom left of the  $P - \dot{P}$  diagram (see Figure 3.1). The pulsar also exhibits significant, unmodelled, orbital-phase,

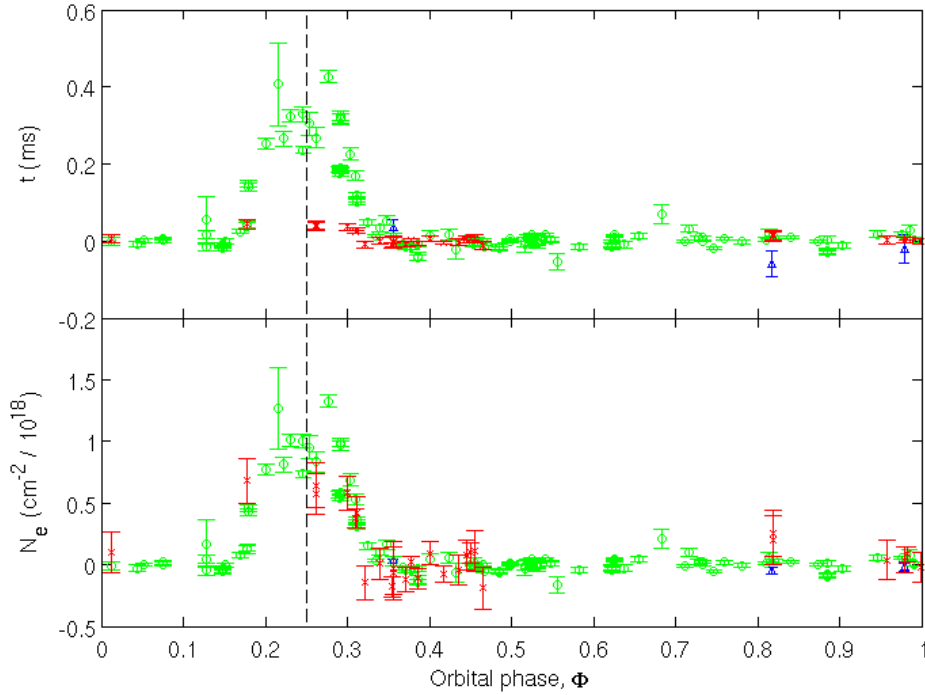


**Figure 3.5** – The top panel shows the timing residuals for PSR J1431–4715 which are folded modulo- $P_{\text{orb}}$ . The excess residuals which are not described by the timing model are centred around superior conjunction,  $\Phi = 0.25$  (indicated by the dashed line). The lower panel shows the same delays converted to an electron column density within the eclipsing region. In both panels there are observations at three frequencies; 1.4 GHz (green), 0.732 GHz (blue), 3.1 GHz (red).

$\Phi$ , dependent delays in the pulse TOAs. By plotting the TOAs modulo- $P_{\text{orb}}$  these excess delays are seen to occur around superior conjunction ( $\Phi = 0.25$ ), when the pulsar is directly behind the companion (see Figure 3.5). They can be explained by an orbital phase dependent DM, with a period of excess DM lasting approximately 10% of the orbital period. This excess DM is attributed to the passage of the radio pulses through ionised material surrounding the companion (see Figure 3.6). The timing model described in Table 3.2 was generated by excluding TOAs which are obviously associated with the eclipse region,  $0.1 < \Phi < 0.4$ .

Multi-frequency observations (see Figure 3.2) indicate the eclipse duration depends on observing frequency, with the 3.1 GHz observations showing a somewhat shorter eclipse than at 1.4 GHz. The lower frequency observations (centred on 0.732 GHz) have not re-

sulted in a positive detection to date across the eclipse region (see Figure 3.5). We can convert from the residual from the best fit timing model to the corresponding excess DM using Equation 2.2. By approximating the depth of the eclipsing region as being equal to  $R_{\text{ecl}}$  the free-electron column density along the line of sight can be calculated (see Figure 3.5). The magnitude of the column density is similar to other eclipsing systems; for example PSR J2051–0827 (Stappers et al., 1996) and PSR J1731–1847 (Bates et al., 2011).

Using multiple observations during different eclipses we find that there appear to be significantly different TOAs at the same orbital phase within the eclipse region. The TOAs were measured during observations which were separated by several months, that is  $\sim 10^2$  orbital periods. As such, the amount or density of dispersive material must be variable on this timescale. The width of the eclipsing region appears to be constant, suggesting it is the free electron density which is variable as opposed to depth of the eclipsing region.

By using the measured semi-major axis of the pulsar orbit,  $a_p$ , around the centre of mass (in the edge-on,  $i = 90^\circ$  case) the orbital separation for a circular system,  $A$ , is given by

$$A = a_p (1 + q), \quad (3.4)$$

where the mass ratio,  $q = M_p/M_c$ . Given that the eclipse duration is  $\approx 10\%$  of the orbital period then the physical size of the eclipsing region  $R_{\text{ecl}} = a_c/10$  where  $a_c$  is the semi-major axis of the companion orbit. Note that this is the size of the region which lies parallel to the line in the sky corresponding to the eclipse.

From the orbital separation and the mass ratio we determine the approximate distance of the Roche lobe from the companion,  $R_L$ , using

$$R_L = \frac{0.49Aq^{2/3}}{0.6q^{2/3} + \ln(1 + q^{1/3})}, \quad (3.5)$$

from Eggleton (1983). In this case  $R_L = 0.6 R_\odot$ , about half the size of  $R_{\text{ecl}} = 1.3 R_\odot$  (see Figure 3.6). A significant amount of the material in the eclipsing region is therefore further than  $R_L$  from the centre of the companion. Material which is close to the Roche lobe can easily be removed by a relativistic pulsar wind (Breton et al., 2013). This would mean some eclipsing material was not gravitationally bound to the companion and must therefore be being continually replenished (Stappers et al., 1996). This ablation of the companion may

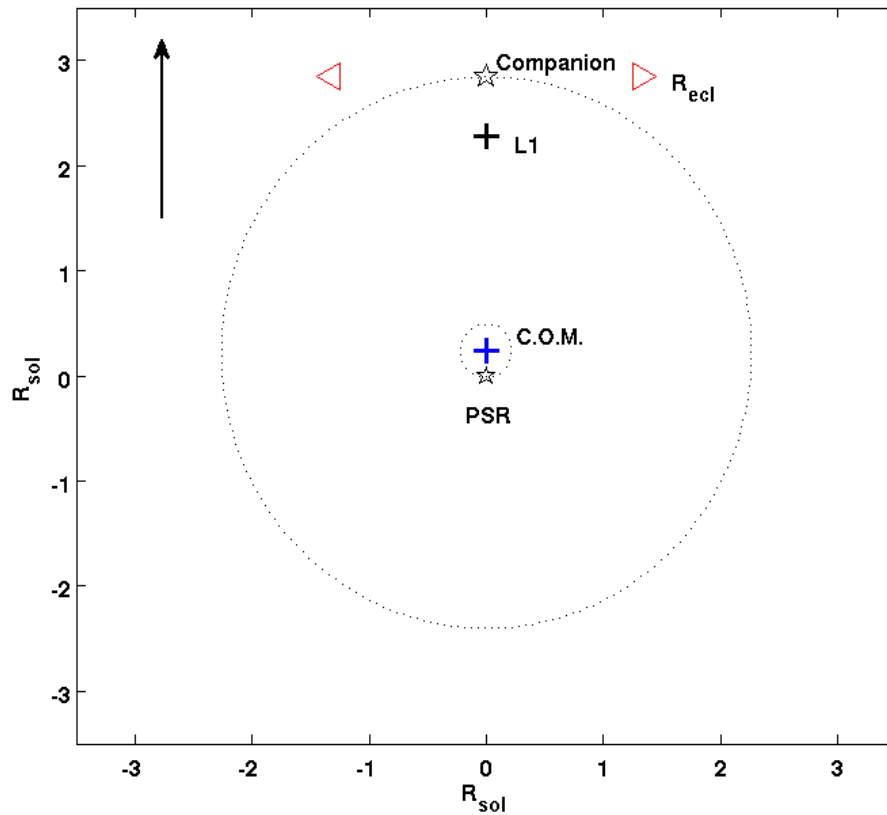


**Figure 3.6** – A to-scale top-down diagram of the PSR J1431–4715 system for  $i = 90^\circ$ . The red triangles indicate the extent of the eclipse region in the orbital plane, the black + symbol marks the position of the inner Lagrange (L1) point, the companion and pulsar are marked as stars, the centre-of-mass of the system is marked by the blue + symbol with the orbits of the pulsar and companion shown as the large dotted circles. The black arrow indicates the line of sight towards the Earth. The relative positions of the companion and pulsar are as they would be at superior conjunction,  $\Phi = 0.25$ .

result in the isolated MSPs which are observed.

Observations of PSR J1431–4715 at multiple frequencies reveal significant pulse profile evolution with observing frequency. At 1.4 GHz the pulse profile is double peaked, with a smaller and wider leading component, the profile at 3.1 GHz is similar although the leading component appears to be weaker. At 0.732 GHz (observed away from superior conjunction) the weaker trailing component at 1.4 GHz and 3.1 GHz has become the larger of the two. Pulse profile evolution has also been measured in other eclipsing systems, such as the PSR J2215+5135 system (Hessels et al., 2011).

### 3.3.4 PSR J1653–2054

PSR J1653–2054 is a fully recycled MSP with  $P = 4.129$  ms and  $\dot{P} = 1.14 \times 10^{-20}$ . The minimum mass of the companion to PSR J1653–2054 is just  $0.093 M_{\odot}$ , placing it between typical black widow and redback systems. The measurement of  $\dot{E}/A^2 \sim 3.7 \times 10^{31}$  ergs s<sup>-1</sup> ls<sup>-2</sup> is however somewhat lower than for the redback and black widow systems (and PSR J1431–4715). It is therefore possible the incident pulsar spin-down energy at the surface of the companion is too low to bloat the companion, and that therefore there are no eclipses. The orbital period is also at least a factor of two longer than known Galactic redback and black widow systems (Roberts, 2011). The wide orbit means that means that a possible ionised region subtends a smaller angle from the pulsar, and eclipses are less likely to be seen. If the orbit is not being viewed edge-on then the companion mass would be higher, for instance, if  $i < 25^{\circ}$  then  $M_c > 0.2 M_{\odot}$ , a typical He WD mass.

### 3.3.5 PSR J1729–2117

The spin period of PSR J1729–2117,  $P = 66.29$  ms, would not be too unusual for a young normal pulsar. However, the measured period derivative,  $\dot{P} = 1.6 \times 10^{-19}$ , places it amongst the mildly recycled pulsars in the  $P - \dot{P}$  diagram. PSR J1729–2117 has the correspondingly large characteristic age and low surface magnetic field strength of a pulsar which has undergone a spin-up phase (see Figure 3.1), it is an isolated pulsar. However, in order to have been recycled it must have had a binary companion, which it has now lost.

This system has very similar spin parameters to PSR J0609+2130 (Lorimer et al., 2004) and PSR J2235+1506 (Camilo, Nice & Taylor, 1993). Camilo, Nice & Taylor (1993) suggest that PSR J2235+1506 was spun-up in a HMXB system in which the second ccSN resulted in the disruption of the binary. The long spin period of PSR J1729–2117 is characteristic of a HMXB phase where mass transfer is relatively short-lived and unstable and this binary disruption may be the reason that PSR J1729–2117 no longer has a companion.

If this were the case then PSR J1729–2117 might be expected to have a high velocity (Bailes, 1989), and as the system is relatively close (the inferred distance from the NE2001 model is  $d = 1.09$  kpc), the proper motion should be measurable. However PSR J1729–2117 is separated from the ecliptic by just  $1.9^{\circ}$ , making accurate position measurements difficult and similarly the proper motion. Incidentally, this is the reason for the relatively large uncertainty on the declination of this system (see Table 3.2). Consequently

---

no significant proper motion measurement can yet be made from pulsar timing. This system may, however, be a good target for a VLBI parallax measurement and subsequent proper motion measurement.

### 3.4 Possibility of optical detection of binary MSP companions discovered in the HTRU survey

As discussed above the binary companion to a pulsar can have a significant effect on its evolution and properties. For those pulsars with probable low-mass WD companions, the WD can provide a way to determine the age, and masses in the system if it is detectable. One of the main ways that WDs can be used is to measure their age. How can the age of a WD be estimated? While WDs are not very luminous objects, they are degenerate and therefore cool extremely slowly. By modelling WD temperature as a function of mass it is possible to determine approximate *cooling curves* which gives the predicted temperature of a WD as a function of time for a given mass (and atmosphere, which can have a significant effect on the cooling). Temperature measurements of WDs can be made with optical observations (for example Bassa, van Kerkwijk & Kulkarni 2003, 2006), which then indicate their position on the cooling curve, from which the age of the WD can be approximated.

In addition to age determination, the prospect of a photometric and spectroscopic measurement of these companions gives an opportunity to measure and constrain theories of gravity (e.g. Freire et al. 2012). For example, measurement of the Doppler shift of WD spectral lines means that, in combination with proper motion measurements, the 3-d velocity of a system can be determined. With this, the intrinsic spin-down of the pulsar and any orbital decay can be determined with the removal of kinematic effects. Freire et al. also show how pulsar-WD systems are the best known systems to test alternate theories of gravity, which predict quadrupolar gravitational radiation for binaries in which the two bodies have significantly different binding energies, as a NS and a WD do. These and other tests of general relativity are otherwise only possible with measurement of post-Keplerian parameters from pulsar timing, usually only measurable for highly relativistic systems like eccentric DNSs (e.g. Kramer et al. 2006b).

Here we present the calculations necessary to determine which, if any, of the 17 MSPs with likely WD companions so far discovered in the HTRU survey may be suitable for an optical observation campaign. There are two questions, is the WD likely optically detectable in colour filters? and will spectroscopic measurements be possible? Detection typically requires an apparent magnitude  $\lesssim 24$  for observations with an 8-m class telescope. It may then be possible to make a spectroscopic measurement to measure the WD spectrum and also any orbital modulation; it is estimated that this would require an apparent magnitude  $\lesssim 23$ . With spectroscopy it may be possible to measure Balmer lines from the WD atmosphere; the presence of these lines can also constrain the surface gravity of

the WD and consequently its mass (e.g. van Kerkwijk, Bergeron & Kulkarni 1996). In addition, a measurable orbitally-modulated radial velocity enables the ratio of the pulsar and WD masses to be determined, breaking the mass function degeneracy.

We use model predictions for the absolute magnitude of pure hydrogen and pure helium atmosphere WDs (HWD and HeWD, respectively) as a function of age (Holberg & Bergeron, 2006; Kowalski & Saumon, 2006; Tremblay, Bergeron & Gianninas, 2011; Bergeron et al., 2011). We estimate the age of the WD as being equal to the spin-down age of the companion MSP. As MSP spin-down ages may not be reliable (Lorimer et al., 1995a; Tauris, 2012), and evidence suggests that WD cooling ages are significantly lower than spin-down ages, the calculations were repeated with  $\tau_{c, 10} = \tau_c/10$ .

In order to calculate the apparent magnitude of a HWD or HeWD from an absolute magnitude, an estimate of distance is required in order to determine the amount of Galactic extinction along the line of sight. We use distances derived from the NE2001 model for the measured pulsar DM (Cordes & Lazio, 2002) and a model of Galactic extinction that takes into account the spiral structure (Amôres & Lépine, 2005). This model provides the extinction in the V-band,  $A_v$ , as a function of depth into the Galaxy. The relations of Schlegel, Finkbeiner & Davis (1998) are used to convert  $A_v$  to the extinction in a particular filter. Table 3.4 provides the apparent magnitudes for HWD and HeWD in the common U, B, V, and R filters, and the values for the lower characteristic age are given in Table 3.5.

Name	$g_1(^{\circ})$	$g_2(^{\circ})$	DM(pc.cm <sup>-3</sup> )	$d_{\text{HTRU}}(\text{kpc})$	$\tau_c(\text{Gyrs})$	$M_{\text{min}}$	$A_v(\text{mag.})$	$U_{\text{H}}$	$B_{\text{H}}$	$V_{\text{H}}$	$R_{\text{H}}$	$U_{\text{He}}$	$B_{\text{He}}$	$V_{\text{He}}$	$R_{\text{He}}$	Ref.
J1017-7156	+291.6	-11.4	94.2	2.8	14.3	0.193	0.263	34	32	30	29	32	31	29	28	(Keith et al., 2010)
J1125-3825	+291.9	+2.6	124.8	2.6	0.8	0.269	1.765	27	27	26	26	27	27	26	26	(Bates et al., 2011)
J1337-6423	+307.9	-0.0	260.3	4.7	0.8	0.798	3.008	30	29	28	28	30	29	28	28	(Keith et al., 2010)
J1405-4656	+315.9	+14.1	13.9	0.6	4.3	0.215	0.885	29	28	26	25	30	29	26	25	this chapter
J1431-4715	+320.0	+12.3	59.4	1.6	2.3	0.127	2.290	31	29	28	26	31	30	28	27	this chapter
J1431-5740	+316.0	+2.7	131.5	2.6	10.2	0.160	2.821	38	35	32	31	36	34	32	30	(Burgay et al., 2013)
J1446-4701	+322.5	+11.4	55.8	1.5	3.4	0.019	2.422	33	31	29	27	35	33	30	28	(Keith et al., 2010)
J1502-6752	+314.8	-7.9	151.8	4.2	1.5	0.022	1.044	29	29	28	27	29	29	28	27	(Keith et al., 2010)
J1543-5149	+327.9	+2.5	50.9	2.4	2.0	0.228	4.413	34	33	30	29	35	33	30	29	(Keith et al., 2010)
J1545-4550	+331.9	+7.0	68.4	2.1	1.1	0.157	2.580	29	29	27	26	29	28	27	26	(Burgay et al., 2013)
J1653-2054	+380.0	+14.3	56.5	1.7	5.7	0.080	0.213	31	29	27	27	31	30	28	27	this chapter
J1708-3508	+350.4	+3.1	146.8	2.8	3.1	0.165	2.534	34	32	30	29	35	33	31	29	(Bates et al., 2011)
J1731-1847	+6.9	+8.2	106.6	2.6	1.5	0.034	7.223	39	36	33	31	38	36	33	31	(Bates et al., 2011)
J1801-3210	+358.9	-3.4	176.7	3.7	44.6	0.141	0.687	36	34	31	31	34	32	30	29	(Bates et al., 2011)
J1811-2405	+7.1	-1.4	60.6	1.8	3.1	0.239	11.360	48	43	38	35	49	44	39	35	(Bates et al., 2011)
J1825-0319	+27.0	+4.1	119.5	3.1	10.6	0.181	9.210	49	44	39	36	48	43	38	35	(Burgay et al., 2013)
J2236-5527	+334.2	-51.3	20.0	0.8	11.4	0.229	0.063	31	29	26	26	29	28	26	25	(Burgay et al., 2013)

**Table 3.4** – Derived optical parameters for the companions for published pulsars, and those presented here, in binary systems with a likely WD companion discovered in the HTRU survey to date. Predicted apparent magnitudes for WDs with pure H, or He atmospheres are provided in the U, B, V, and R bands for a system ages of the spin-down age,  $\tau_c$ . PSR J1227-6208 is not included as its companion mass range indicates it is either a heavy ONeMg WD or another NS.

Name	U <sub>H</sub>	B <sub>H</sub>	V <sub>H</sub>	R <sub>H</sub>	U <sub>He</sub>	B <sub>He</sub>	V <sub>He</sub>	R <sub>He</sub>	Ref.
J1017–7156	27	27	26	26	26	26	26	25	(Keith et al., 2010)
J1125–5825	24	24	24	23	24	24	24	23	(Bates et al., 2011)
J1337–6423	27	27	27	26	28	28	27	26	(Keith et al., 2010)
J1405–4656	21	21	21	21	21	21	21	20	this chapter
J1431–4715	25	24	24	23	24	25	24	23	this chapter
J1431–5740	29	29	27	26	30	29	28	27	(Burgay et al., 2013)
J1446–4701	25	25	24	24	25	25	24	23	(Keith et al., 2010)
J1502–6752	24	24	24	24	24	24	24	24	(Keith et al., 2010)
J1543–5149	29	28	26	26	29	28	27	26	(Keith et al., 2010)
J1545–4550	25	25	24	23	24	25	24	23	(Burgay et al., 2013)
J1653–2054	23	24	23	23	23	23	23	23	this chapter
J1708–3508	27	26	25	25	26	26	25	25	(Bates et al., 2011)
J1731–1847	33	31	29	28	33	31	29	28	(Bates et al., 2011)
J1801–3210	33	31	29	28	34	32	30	29	(Bates et al., 2011)
J1811–2405	40	37	33	31	40	37	33	31	(Bates et al., 2011)
J1825–0319	41	38	35	33	41	38	34	32	(Burgay et al., 2013)
J2236–5527	23	23	23	22	23	23	22	22	(Burgay et al., 2013)

**Table 3.5** – The calculated apparent magnitudes for the WDs in the common U, B, V, and R filters. In this Table the age of the system, which is used to place the WD on a cooling curve, is taken to be  $\text{Age} = \tau_{c, 10}$ . This means that the WDs are younger, hotter, and more luminous. They would therefore have lower apparent magnitudes and be easier to detect. These values should be compared to those in Table 3.4.

It is unlikely that any of these MSP’s WD companions will be optically detected if  $\tau_c$  is an accurate approximation of a binary’s age. Calculations using  $\text{Age} = \tau_{c, 10}$  suggest that the best systems for an optical detection would be PSRs J1125–5825, J1405–4656, J1653–2056; and J2236–5527 may be detected and measured spectroscopically by an 8-m class ground based optical telescope.

### 3.5 Discussion

The discovery of five new MSPs from the High Time Resolution Universe survey has been presented. These pulsars represent members of a wide range of known recycled pulsar types, including possibly a DNS system with an unusually low-eccentricity orbit, an eclipsing reback system, and an isolated, mildly recycled pulsar, indicating it probably came from a HMXB, which disrupted during the second ccSN.

Tauris & Savonije (1999) derived a relationship between orbital period and companion mass for binary MSPs with WD companions which have formed via a LMXB phase (see Figure 3.7). This relationship is based on a predictable core mass for a main sequence star as a function of stellar radius. During spin-up in an LMXB, the edge of the star is at the position of the Roche lobe, which is a function of only the two masses and the orbital

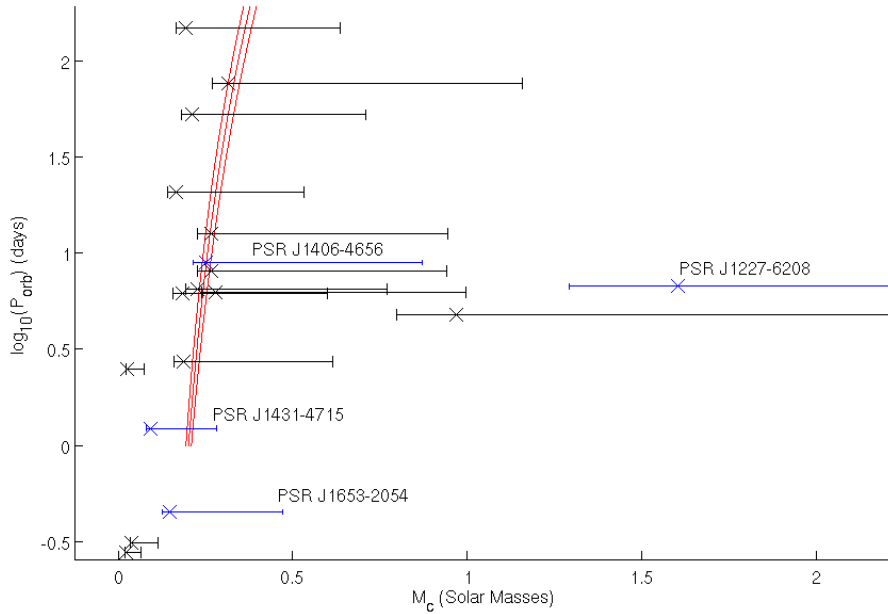


**Figure 3.7** – A plot of orbital period,  $P_{\text{orb}}$  against median companion mass. The left-most error bars correspond to the minimum companion mass,  $M_{\text{c, min}}$ , and the right-most error bars correspond to the maximum mass,  $M_{\text{c, max}}$ . The four new binary discoveries described in this chapter are in blue, while all other published HTRU pulsars are shown in black. The red lines indicate the relationship for HeWDs derived by Tauris & Savonije (1999) for 3 different companion progenitors.

separation (see Equation 3.5). After the companion star exhausts its fuel and the outer layers are blown off, the stellar core becomes a WD. The WD mass is therefore linked to the orbital period at cessation of mass transfer/spin-up.

Of the binary systems described here, PSR J1653–2054 has a shorter orbital period than those described by Tauris & Savonije (1999), who only considered  $P_{\text{orb}} \gtrsim 2$  days. PSRs J1405–4656 and J1431–4715 are in agreement with Tauris & Savonije (1999). PSR J1227–6208 did not form via the LMXB phase, which predicts this relationship; its minimum companion mass is considerably higher than a low-mass WD.

It would be interesting to attempt detections of some WDs in HTRU sample in order to test the reliability of MSP spin-down ages. PSRs J1125–5825, J1405–4656, and J1545–4550 are the most likely to result in positive detections. An optical observation of PSR J1431–4715 would also be informative: if it is a redback system then its companion may be non-degenerate and it instead could be at the end of the spin-up phase (Roberts, 2011). The companion may also be distinctly non-spheroidal, and measurements of an or-

---

bitally modulated light curve can constrain the inclination (Stappers et al., 2001; Reynolds et al., 2007). If spectroscopy as a function of orbital phase is possible for the companion then component masses can be constrained (van Kerkwijk, Breton & Kulkarni, 2011; Romani et al., 2012).

# Chapter 4

## Binary pulsars - two extreme cases

Pulsars are found with an enormous range of companion types with different mass ranges. These include other degenerate objects like neutron stars (NSs) and white dwarfs (WDs), main sequence stars, objects which are being ablated by the pulsar, and planetary mass bodies. The companion and the pulsar can each affect the evolution and properties of the other significantly; to understand binary systems fully therefore, all orbital components should be studied in detail.

One of the least common types of companion to a pulsar are also the least massive; these are the systems with a companion mass which is approximately planetary. The first case of such a system was PSR B1257+12, which is a pulsar with three orbiting planetary mass companions (Wolszczan & Frail, 1992; Wolszczan, 1994). Two of the companions have masses approximately 4 times the mass of the Earth in 66 and 98 day orbits, and the third, is an approximately lunar mass companion to the pulsar in a 25 day orbit. It is thought that these planets formed from a disk of material surrounding the pulsar (see Podsiadlowski 1993 and references therein). No other pulsars with planetary mass companions in bound orbits were discovered until PSR J1719–1438. This system contains a fully-recycled millisecond pulsar (MSP) in orbit with a very low mass companion,  $M_{c, \min} = 1.15 \times 10^{-3} M_{\odot}$  (Bailes et al., 2011). It is however quite different because it has an orbital period,  $P_{\text{orb}} = 2.17$  hrs that is considerably shorter than the orbits of the companions to PSR B1257+12. It is thought the “planet” in the PSR J1719–1438 system formed quite differently from those in the PSR B1257+12 system, and instead is the remnant core of a low mass WD which transferred mass via Roche lobe overflow to the pulsar during an Ultra-Compact X-ray Binary (UCXB) phase (van Haften et al., 2012b). The degenerate, low-mass, core of this WD then remains as the orbital companion to the recycled pulsar.

Another interesting type of pulsar binary system are those containing normal pulsars - that is those whose measured spin parameters indicate that they have not undergone a spin-up phase (see Chapter 1). As the pulsar is thought to have formed via a core-collapse supernova (ccSN) then this should cause an asymmetric kinematic kick (e.g. Chaurasia & Bailes 2005). This in turn is then likely to impart a significant eccentricity to the system, particularly for wide orbits (Tauris & Sennels, 2000). If the pulsar's companion then undergoes Roche lobe overflow, transferring material to the pulsar, tidal forces tend to circularise the orbit, this is the reason most recycled pulsar-WD binaries have small eccentricities (Bhattacharya & van den Heuvel, 1991).

In this chapter I present the discovery of two contrasting pulsar binary systems: a MSP with an ultra low mass companion - PSR J2322–2650; and a normal pulsar in a long period, wide binary with a white dwarf-mass companion - PSR J1837–0822. Both systems were discovered in data from the High Time Resolution Universe (HTRU) survey (Keith et al., 2010), the MSP in the high-latitude region and the normal pulsar in the mid-latitude region. The two systems are different in many interesting ways, and illustrate the extremes of pulsar types being discovered by the HTRU survey. The measured and derived parameters for both systems are given in Table 4.1.

## 4.1 PSR J2322–2650

PSR J2322–2650 is a pulsar with a spin period,  $P = 3.4$  ms and  $\dot{P} = 1.2 \times 10^{-21}$ . This places it in the region of the  $P - \dot{P}$  diagram populated by the fully recycled pulsars. Consequently it is a system which likely developed via a low mass x-ray binary (LMXB) phase with a long, stable period of mass transfer from the companion to the pulsar (see Chapter 1).

It is also possible that the system evolved through a UCXB phase (van Haften et al., 2012a). A UCXB is a periodically modulated x-ray source with millisecond periods (e.g. Markwardt et al. 2002; Galloway et al. 2002). The millisecond pulsations are caused by the rotating NS, which is accreting material from its WD orbital companion on to its surface. While the orbital periods of UCXBs are typically 10s of minutes, it is thought that the orbit widens as the companion loses mass, and that the final orbital periods at cessation of accretion may be around 1.5 hours (Deloye & Bildsten, 2003). It may be therefore that the orbital period of PSR J2322–2652 ( $P_{\text{orb}} = 0.322$  days) is too long for it to have formed via a UCXB phase unless there is some other form of orbital angular momentum loss (van

Parameter	PSR J2322–2650	J1837–0822
Right Ascension (J2000)	23:22:34.6334(2)	18:37:39.660(1)
Declination (J2000)	−26:50:58.301(1)	−08:22:12.2(1)
Galactic Longitude (°)	+28.6	23.9
Galactic Latitude (°)	−69.8	−0.8
Discovery S/N	9.5	9.7
Offset from survey beam centre (°)	0.04	0.04
TOA Range (MJD)	56129 – 56497	55956 – 56499
$P$ (ms)	3.463099125393(1)	1099.19593350(1)
$\dot{P}$	$1.22(2) \times 10^{-21}$	$1.16(3) \times 10^{-16}$
DM (cm <sup>−3</sup> pc)	6.18	506.6
DM Distance, $d$ (kpc)	0.321	6.7
$\tau_c$ (Gyr)	3.6	0.15
$B_{\text{surf}}$ (Gauss)	$2.3 \times 10^9$	$3.6 \times 10^{11}$
$B_{\text{lc}}$ (Gauss)	94	2.6
$\dot{E}$ (erg s <sup>−1</sup> )	$1.1 \times 10^{33}$	$3.5 \times 10^{30}$
Binary Model	BT	BT
$P_{\text{orb}}$ (d)	0.32296392(7)	98.368(4)
$a_p \sin(i)$ (ls)	0.002787(1)	40.8782(2)
$T_0$ (MJD)	56129.99(1)	55978.095(3)
$e$	< 0.0005	0.02430(1)
$\omega$ (°)	–	21.83(3)
$M_{c,\text{min}}$ ( $M_{\odot}$ )	$7 \times 10^{-4}$	0.22
$M_{c,\text{med}}$ ( $M_{\odot}$ )	$8 \times 10^{-4}$	0.32
$M_{c,\text{max}}$ ( $M_{\odot}$ )	$25 \times 10^{-4}$	1.21

**Table 4.1** – Astrometric, spin, and orbital parameters for two contrasting binary systems. In all calculations a pulsar mass,  $M_p = 1.4 M_{\odot}$  is assumed. The maximum companion mass,  $M_{c,\text{max}}$  is defined as being the companion mass that 95% of randomly inclined orbits would not exceed.

Haafte et al., 2012a).

### 4.1.1 Spin characteristics

A transverse pulsar velocity,  $v_T$ , causes an apparent period derivative of the pulsar spin period. This is called the Shklovskii effect and increases the apparent spin period derivative,  $\dot{P}$ , by an amount  $\dot{P}_{\text{Shk}} = Pv_T^2/cd$ , where  $d$  is the distance to the pulsar. Using a nominal MSP transverse velocity of  $v_T = 85 \text{ km s}^{-1}$  (Toscano et al., 1999) and the distance inferred from the NE2001 model for PSR J2322–2650,  $d = 0.321 \text{ kpc}$ , then  $\dot{P}_{\text{Shk}} = 8.3 \times 10^{-21}$ . This is a factor of 7 higher than the measured  $\dot{P}$ . In order that  $\dot{P}_{\text{Shk}} < \dot{P}$  either the system is either considerably further away than predicted, or the transverse velocity is considerably lower ( $v_T < 32 \text{ km s}^{-1}$ ). This velocity would not be that unusual for an MSP, where the mean MSP transverse velocity is  $\bar{v}_T = 85 \pm 13 \text{ km s}^{-1}$  (Toscano et al., 1999). If however the system did have a transverse velocity,  $v_T = \bar{v}_T$  then

$$d = \frac{P\bar{v}_T^2}{c\dot{P}}. \quad (4.1)$$

If the distance is incorrect, then in order that  $\dot{P}_{\text{Shk}} < \dot{P}$ ,  $d > 2.2 \text{ kpc}$ . This would equate to an underestimation of the distance by the NE2001 model by a factor of 6.8; the model is known to underestimate distances by at most a factor of around 2 (Chatterjee et al., 2009). It therefore seems likely that the system has a somewhat low transverse velocity for a MSP; of course it may also be the case that  $d$  is underestimated by a factor  $\lesssim 2$ . If  $\dot{P}$  is entirely due to  $\dot{P}_{\text{Shk}}$  then the intrinsic  $\dot{P}$  must be remarkably small ( $\lesssim 10^{-22}$ ). This would be lower than any other  $\dot{P}$  measurement for known pulsars, which also seems unlikely. If the pulsar is as close as the NE2001 model predicts, then a proper motion measurement should be possible, which would help in determining the intrinsic  $\dot{P}$ .

### 4.1.2 Orbital characteristics

The orbital period,  $P_{\text{orb}} = 7.75 \text{ hrs}$ , and projected semi-major axis of the pulsar orbit is  $a_p \sin(i) = 0.00278 \text{ ls}$ . For an orbital inclination  $i = 90^\circ$ , to the plane of the sky, the minimum companion mass  $M_{c, \text{min}} = 0.00076 M_\odot$ ;  $0.79 M_J^1$ .

<sup>1</sup>The mass of Jupiter,  $M_J = 1.898 \times 10^{27} \text{ kg}$

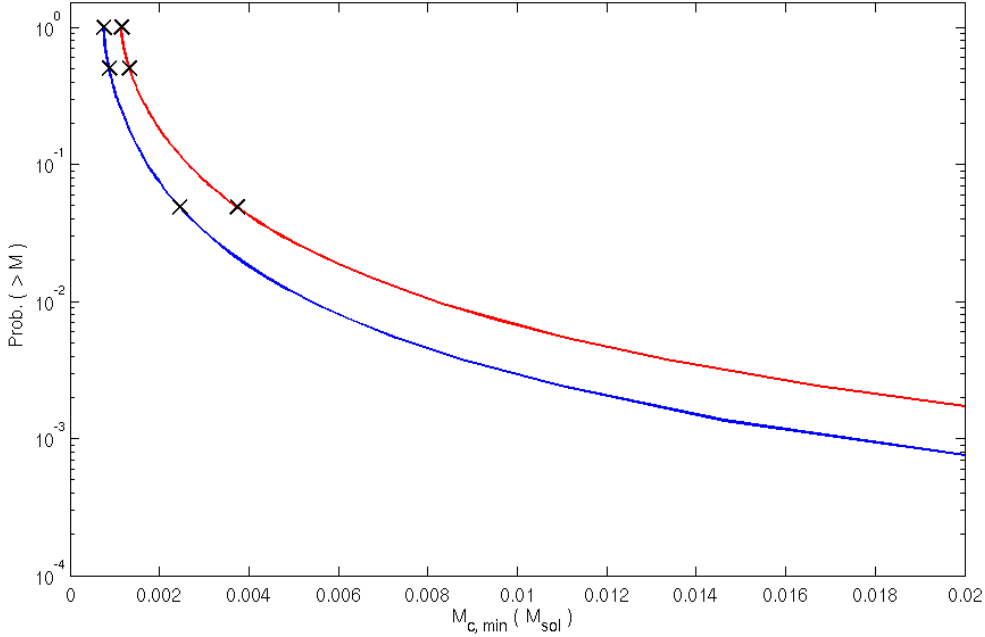


**Figure 4.1** – A plot showing the companion mass of PSRs J2322–2650 and J1719–1438 (Bailes et al., 2011) as the blue and red lines respectively. The minimum, median and 95% confidence interval masses are shown as black crosses.

PSR J2322–2650 is similar to PSR J1719–1438 ( $P = 5.79$  ms,  $P_{\text{orb}} = 2.17$  hrs  $a_p \sin(i) = 0.0018$  ls,  $e < 0.06$ ), also discovered in the High Time Resolution Universe (HTRU) survey (Bailes et al., 2011). Following the analysis of Bailes et al. (2011), I calculate the companion mass as a function of inclination (see Figure 4.1), enabling the calculation of the orbital separation,  $A$ , and Roche lobe distance,  $R_L$  from the companion (using a pulsar mass  $M_p = 1.4 M_{\odot}$ ) (see Equation 3.5). If the system is being viewed edge-on the orbital separation,  $A = 5.1$  ls and the Roche lobe is located  $R_L = 0.19$  ls from the companion.

The MSP is losing energy via the emission of magnetic dipole radiation, and as such it is slowing down. The inferred spin down energy of the pulsar is  $\dot{E} = 4\pi^2 I P \dot{P}^{-3} = 1.1 \times 10^{33}$  ergs  $s^{-1}$ , where  $I = 10^{45}$  g  $cm^3$  is commonly used as the neutron star moment of inertia. The spin-down dipole radiation  $\dot{E}$  of the pulsar at the distance of the companion is  $\dot{E}/A^2 = 1.1 \times 10^{33}$  ergs  $s^{-1}$  ls $^{-2}$ . The mass of the companion is somewhat lower than, but similar to, those of the black widow systems where eclipses are observed (Roberts, 2011). The value of  $\dot{E}/A^2$  is typical of redback and black widow systems and suggests that perhaps here we might also expect eclipses. To consider this, in Figure 4.2 I plot the

residuals from the best-fit timing model as a function of orbital phase.

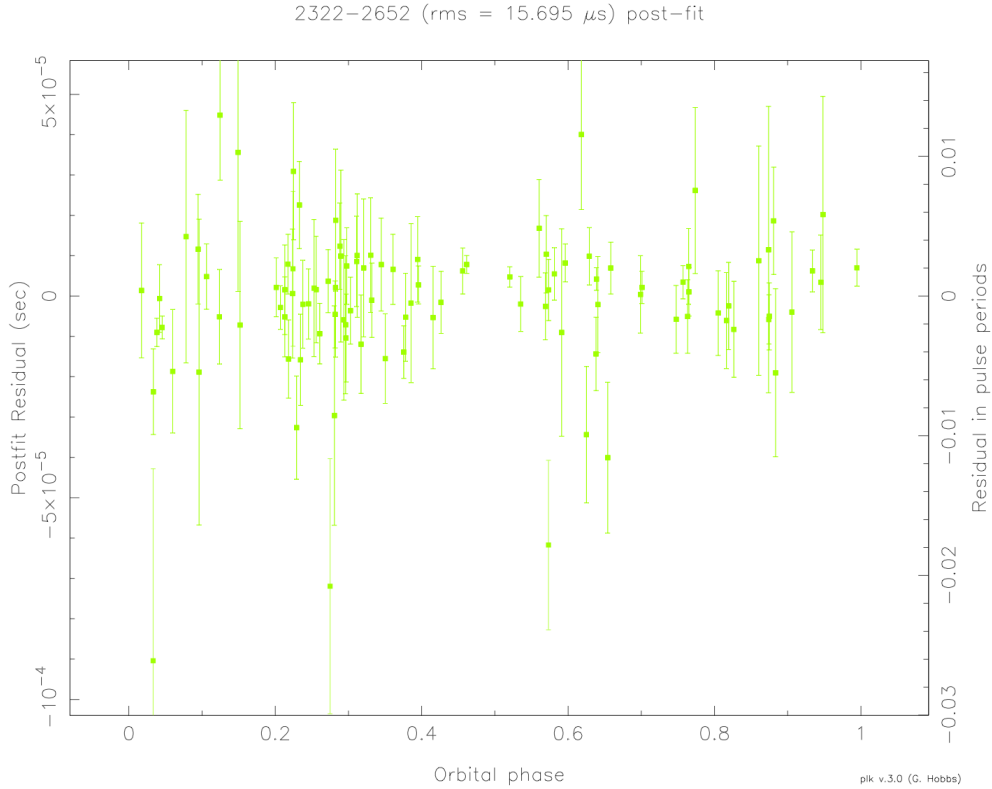


**Figure 4.2** – The orbital phase resolved TOAs for PSR J2322–2650. Orbital phase,  $\Phi = 0$  is the ascending node of the orbit. The corresponding superior conjunction in this plot occurs at  $\Phi = 0.25$ .

There are no excess delays visible in the timing residuals (see Figure 4.2), which would indicate an eclipse by ionised material surrounding the companion. PSR J2322–2652 is typically a weak pulsar, and so an integration time of approximately one hour is required to make a detection using the 76-m Lovell telescope at Jodrell Bank Observatory, corresponding to 12.9% of an orbit. This fundamentally limits the duration of a detectable eclipse; any delay in pulsar arrival time for pulses during an eclipse shorter than this integration time will be smeared out. For an eclipse to last longer than the observing time it must be larger than 2.7 ls in the dimension that passes in front of the pulsar. This is greater than the distance of the Roche lobe from the companion and so, if there was eclipsing material surrounding the companion then some may not be gravitationally bound to the companion (depending on the shape of the region). The likely companion mass of PSR J2322–2650 is significantly lower than any known Galactic field eclipsing system (Roberts, 2011).

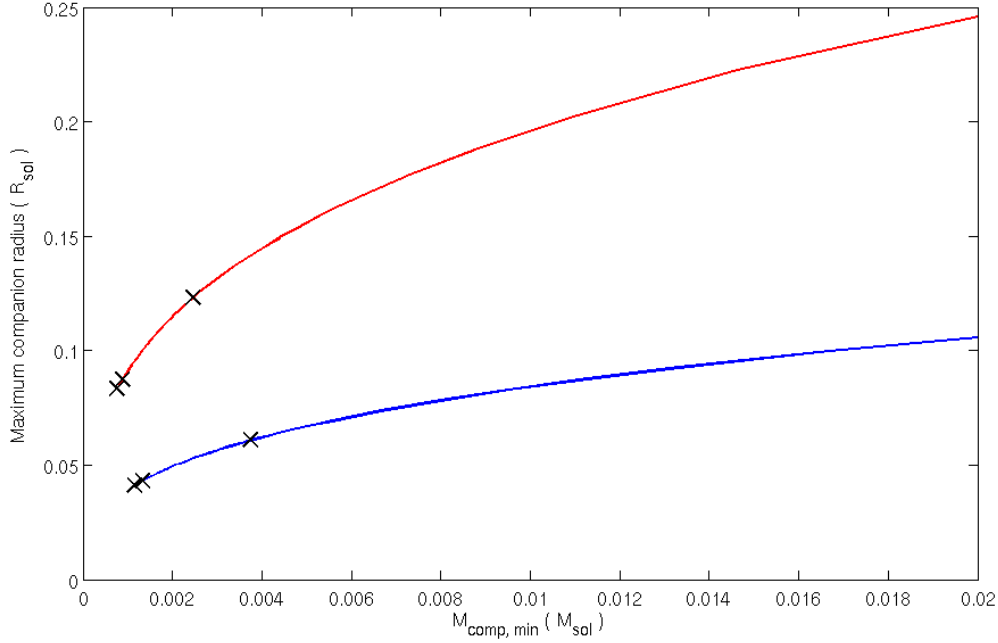


**Figure 4.3** – A plot showing the maximum companion radius as a function of companion mass of PSRs J2322–2650 and J1719–1438 (Bailes et al., 2011), shown as the blue and red lines respectively. The minimum, median and 95% confidence interval masses are shown as black crosses. The maximum radius is defined by the size of the Roche lobe. It is of course possible that the companion radius could be smaller than the Roche lobe radius.

The mass-radius plot shown in Figure 4.3 indicates that PSR J1749–1438 has a smaller lower limit on the radius for a given companion mass (and inclination). This is because PSR J2322–2650 is in a wider orbit and consequently, while the component masses are similar, the Roche lobe is larger and hence less constraining on the companion radius.

By assuming that the radius of the companion is no larger than the Roche lobe, and using companion masses calculated as a function of orbital inclination from pulsar timing, a lower limit on the mean density of the companion can be calculated (Bailes et al., 2011). The mean density of the companion to PSR J2322–2650,  $\rho_c > 1.9 \text{ g cm}^{-3}$ , this is considerably smaller than the lower limit from PSR J1719–1438 ( $\rho_c > 23 \text{ g cm}^{-3}$ ) which is due to the smaller orbital separation and consequently the smaller value for  $R_L$ . This constraint on  $\rho_c$  does not rule out a rocky planet, which in the Solar system have typical densities of  $6 \text{ g cm}^{-3}$ , nor does it rule out a gas giant planet, like Jupiter, which has a density of approximately  $2 \text{ g cm}^{-3}$ .

If we assume the incident  $\dot{E}$  at the companion ( $4.6 \times 10^{14} \text{ ergs s}^{-1} \text{ m}^{-2}$ ) is absorbed and

re-radiated according to Boltzmann's law it is possible to calculate the temperature of this re-radiated radiation from the MSP-facing side of the companion. This is at a maximum when the companion albedo,  $a = 1$ , and is found to be  $T_{c, \max} = 5350$  K, peaking at around 540 nm in visible light.

If PSR J1719–1438 has fundamentally the same type of companion as PSR J2322–2652, then the calculations of Bailes et al. (2011) provide a stronger constraint on the mean density. Using this density, and  $M_{c, \min}$  for the companion to PSR J2322–2650, we can estimate the absolute magnitude of the fully illuminated face of the companion at superior conjunction in the edge-on case. This indicates that the absolute magnitude would be  $M = 22$  and, using the distance from the NE2001 model, the apparent magnitude,  $m = 30$ , if this were the case this would render the companion optically undetectable. If  $R_L$  is used as the companion radius then  $M = 20$  and  $m = 28$ . In the SIMBAD catalog of sources<sup>2</sup> there is a magnitude 11 star located 170 arcseconds from the position of PSR J2322–2652. The measurement accuracy of both the pulsar and stellar position indicate that the two are not related.

An increasing number of pulsars, MSPs, and reback and black widow systems are being identified as pulsed gamma-ray sources by the Fermi mission (e.g. The Fermi-LAT collaboration 2013). Pulsars which have been detected, including MSPs, all have a measured value of  $\dot{E} > 10^{33}$  erg s<sup>-1</sup>. This suggests that PSR J2322–2650 is unlikely to be detected as a Fermi gamma-ray source. The Fermi second year source catalog has been checked for an unassociated point source coincident with the pulsar's position, but none is found (Nolan et al., 2012).

## 4.2 PSR J1837–0832

PSR J1837–0820 is a binary pulsar that has a measured spin period,  $P = 1.099$  s and  $\dot{P} = 1.16 \times 10^{-16}$ . This places it firmly amongst the normal pulsars in the  $P - \dot{P}$  diagram. Consequently, the inferred surface magnetic field strength,  $B_{\text{surf}} = 3.6 \times 10^{11}$  G and the characteristic age,  $\tau_c = 0.150$  Gy, which are both typical of normal pulsars. These values are very different from fully-recycled MSPs, or even partially recycled pulsars. It is therefore likely that PSR J1837–0822 has not undergone a period of spin-up during its evolution.

<sup>2</sup><http://simbad.u-strasbg.fr/simbad/>

There are a very few binary pulsars with similar  $P$  and  $\dot{P}$  values to PSR J1837–0832, these are PSRs B0820+02, B1718–19, and J1822–0848, and J0737–3029B. Two of these systems, PSRs B0820+02 and J1822–0848, have similar orbital parameters and minimum companion masses (Lorimer et al., 2006). PSR J0737–3039B is in an eccentric orbit with another pulsar and PSR B1718–19 is in a relatively tight ( $a_p \sin(i) = 0.35$  ls) and short orbit ( $P_{\text{orb}} = 0.25$  d), and might be associated with a globular cluster (Lyne et al., 1993). The companion to PSR B0820+02 has been detected optically and confirmed as a helium WD (Koester, Chanmugam & Reimers, 1992). PSR B0820+02 indicates that similar systems can be found with evolved degenerate companions. If the companion to PSR J1837–0832 is also a WD, then the relationship between orbital period and companion mass predicts a WD mass,  $M_c = 0.35 M_{\odot}$  for  $P_{\text{orb}} = 98$  d (Tauris & Savonije, 1999). For a pulsar mass of  $M_p = 1.4 M_{\odot}$  this companion mass corresponds to an inclination,  $i = 47^{\circ}$ .

The minimum companion mass would be typical of WD companions to fully recycled MSPs. For systems in which the neutron star has formed before the companion forms a WD, low eccentricities ( $e < 0.1$ ) are expected. These low values are expected because of circularisation of the orbit during the spin-up phase (Verbunt & Phinney, 1995). When the NS forms after the WD then the ccSN is expected to induce significant eccentricity, which persists because there is no Roche lobe overflow and no further orbital circularisation. The orbital eccentricity of PSR J1837–0822,  $e = 0.024$ , while small is significantly measured. It is too low for a system in which the pulsar formed after its companion as the kinematic kick provided by the ccSN would be expected to impart a much larger eccentricity, if not disrupt the binary totally (Tauris & Sennels, 2000). The population analysis of Tauris & Sennels also suggests that  $e = 0.024$  and  $P_{\text{orb}} = 98.368$  d is highly unlikely for a system in which the WD formed first. It is possible that the companion to PSR J1837–0822 is non-degenerate, its large implied distance from the NE2001 model (Cordes & Lazio, 2002) would suggest an optical detection is unlikely.

HTRU is discovering a range of pulsars in different evolutionary states, a number of which are very rare, and even unique. These systems highlight both the complexity of the binary evolution processes in which they are sometimes involved and the value of continued exploration for new systems.

## Chapter 5

# A Population of Fast Radio Bursts at Cosmological Distances

This chapter is based on paper published in *Science* entitled “A population of fast radio bursts at cosmological distances”

D. Thornton, B. Stappers, M. Bailes, B. Barsdell, S. Bates, N. D. R. Bhat, M. Burgay, S. Burke-Spolaor, D. J. Champion, P. Coster, N. D’Amico, A. Jameson, S. Johnston, M. Keith, M. Kramer, L. Levin, S. Milia, C. Ng, A. Possenti, W. van Straten.

5th July 2013

Searches for transient astrophysical sources often reveal unexpected classes of objects that are useful physical laboratories. In a recent survey for pulsars and fast transients, we have uncovered four millisecond-duration radio transients all more than  $40^\circ$  from the Galactic plane. The bursts properties indicate that they are of celestial rather than terrestrial origin. Host galaxy and intergalactic medium models suggest that they have cosmological redshifts of 0.5 to 1 and distances of up to 3 gigaparsecs. No temporally coincident x- or gamma-ray signature was identified in association with the bursts. Characterization of the source population and identification of host galaxies offers an opportunity to determine the baryonic content of the universe.

## 5.1 Introduction

The four fast radio bursts (FRBs) (see Figure 5.1 and Table 5.1) reported here were detected in the high Galactic-latitude region of the High Time Resolution Universe (HTRU) survey (Keith et al., 2010), which was designed to detect short-time-scale radio transients and pulsars (Galactic pulsed radio sources). The survey uses the 64-m Parkes radio telescope and its 13-beam receiver to acquire data across a bandwidth of 400 MHz centered at 1.382 GHz (see Chapter 2). These FRBs were found using the search methodology described in Chapter 2.

We measured minimum fluences for the FRBs of  $F = 0.6$  to  $8.0 \text{ Jy ms}^1$ . At cosmological distances, this indicates that they are more luminous than bursts from any known transient radio source (Cordes, 2009). Follow-up observations at the original beam positions have not detected any repeat events, indicating that the FRBs are likely cataclysmic in nature.

Candidate extragalactic bursts have previously been reported with varying degrees of plausibility (Lorimer et al., 2007; Keane et al., 2012; Bannister et al., 2012; Rubio-Herrera et al., 2012), along with a suggestion that FRB 010724 (the Lorimer burst) is similar to other signals that may be of local origin (Burke-Spolaor et al., 2011a; Bagchi, Nieves & McLaughlin, 2012). To be consistent with a celestial origin, FRBs should exhibit certain pulse properties. In particular, observations of radio pulsars in the Milky Way (MW) have confirmed that radio emission is delayed by propagation through the ionized interstellar medium (ISM), which can be considered a cold plasma. This delay has a power law dependence of  $\delta t \propto \text{DM} \times \nu^{-2}$  and a typical frequency dependent width of  $W \propto \nu^{-4}$  (see Figure 5.2). The dispersion measure (DM) is related to the integrated column density of free electrons along the line of sight to the source and is a proxy for distance. The frequency-dependent pulse broadening occurs as an astrophysical pulse is scattered by an inhomogeneous turbulent medium, causing a characteristic exponential tail.

## 5.2 Pulse fitting

In order to test the adherence of these FRBs to attributes expected for narrow astrophysical pulse shapes the full bandwidth was divided into a number of sub bands. Each sub band was

---

<sup>1</sup>  $1 \text{ Jy} \equiv 10^{26} \text{ Wm}^{-2}\text{Hz}^{-1}$

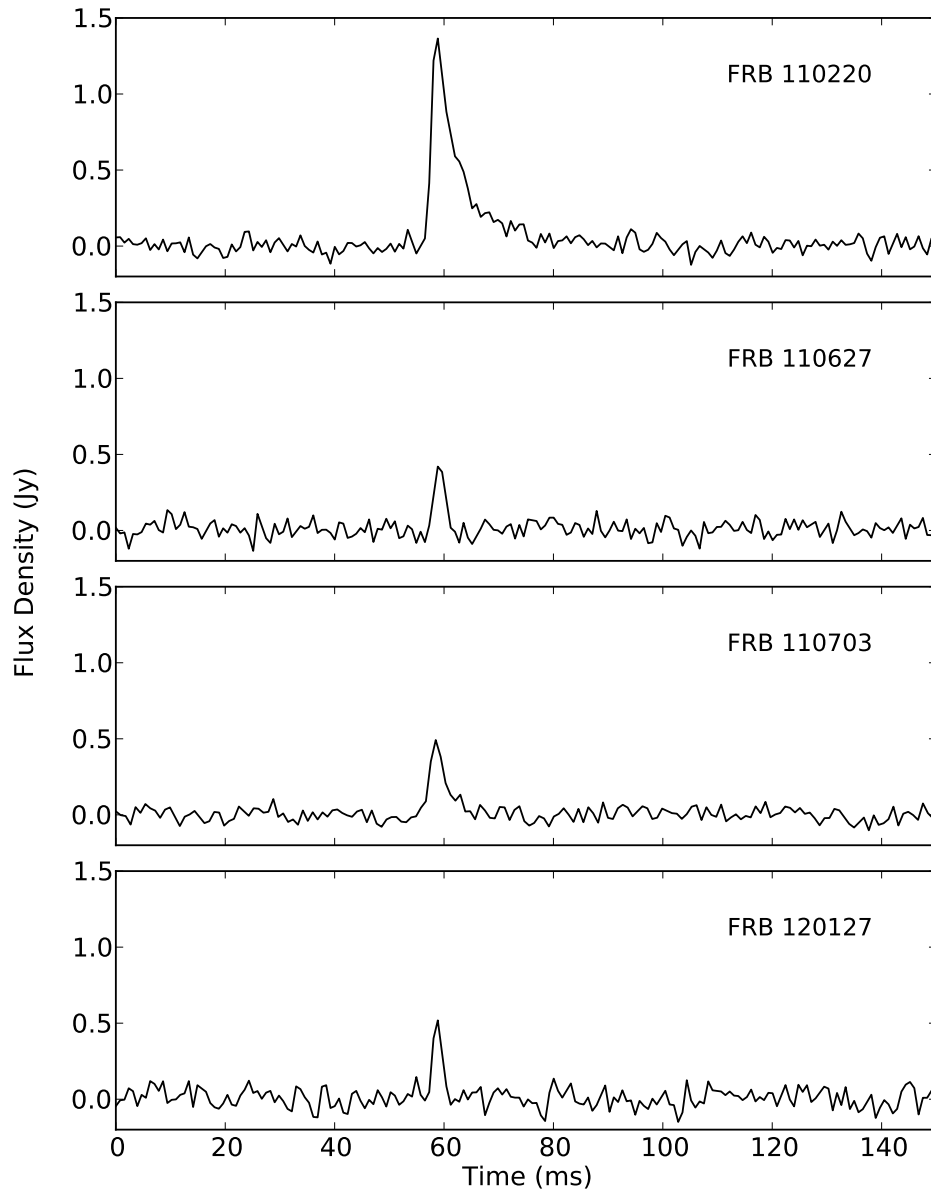


**Figure 5.1** – The frequency-integrated flux densities for the four FRBs. The time resolutions for each of the bursts are chosen to match the level of dispersive smearing in the central frequency channel (0.8, 0.6, 0.9, and 0.5 ms, respectively).

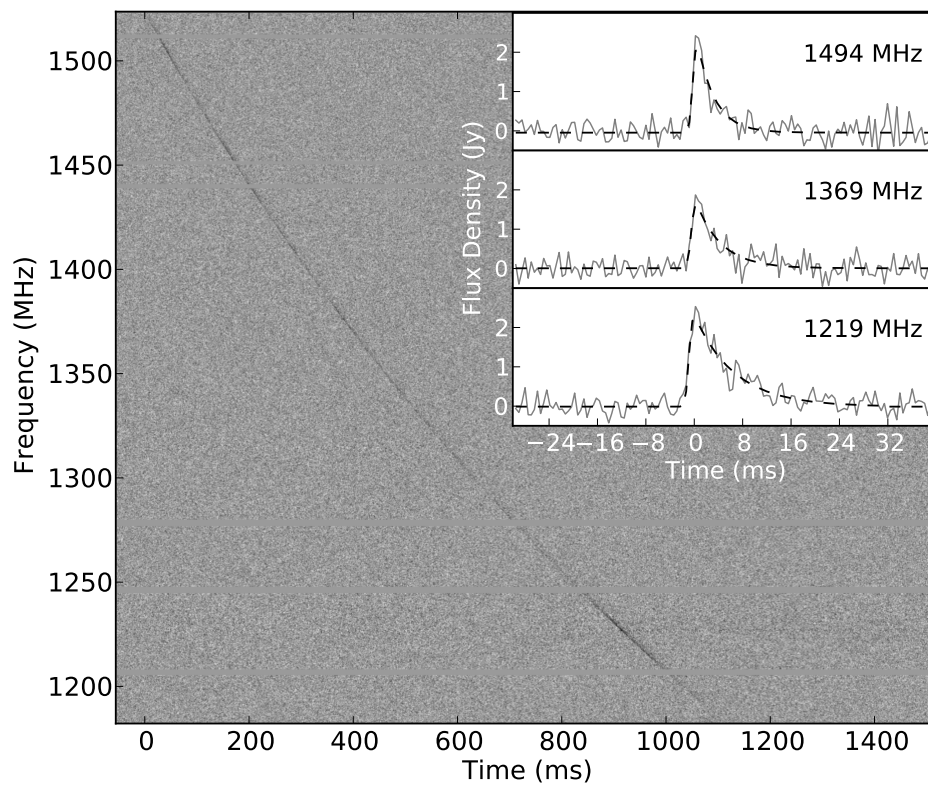


**Figure 5.2** – A dynamic spectrum showing the frequency-dependent delay of FRB 110220. Time is measured relative to the time of arrival in the highest frequency channel. For clarity we have integrated 30 time samples, corresponding to the dispersion smearing in the lowest frequency channel. (Inset) The top, middle, and bottom 25-MHz-wide dedispersed subband used in the pulse-fitting analysis; the peaks of the pulses are aligned to time = 0. The data are shown as solid gray lines and the best-fit profiles by dashed black lines.

convolved with a template with a scattering tail using a characteristic scattering time. This scattering time was determined from a value at a reference frequency of 1 GHz, which was scaled according to  $\tau \propto \nu^\beta$  to each sub-band center frequency. Note  $\tau$  is the broadening due to scattering, and is different from the measured width,  $W$ , which may include intrinsic and other broadening effects. Using the arrival time of the burst at reference frequency  $\nu_0$ , the arrival time at a frequency  $\nu$  was scaled according to a dispersion law  $\delta t \propto \text{DM} \times \nu^\alpha$ . The parameters  $\delta t(\nu_0)$ ,  $\tau(\nu_0)$ , DM,  $\alpha$ , and  $\beta$ , were determined in a least-square fit using the SIMPLEX and MIGRAD algorithms from CERN's MINUIT package (James, 2008). Uncertainties were derived using the MINUIT algorithm to explore the error matrix, which also attempts to account for correlations between parameters.

An overall baseline and amplitude of the scattered pulse of each sub band were also treated as free parameters to be fit. Before the final step, these parameters were kept fixed to the previous best fit value.

### 5.2.1 FRB 110220

FRB 110220 has the largest SNR and allows the determination of all the parameters as described above. The band was divided into 16 sub-bands, two sub-bands at the top and one at the bottom of the frequency range were excluded from the fit, as, due to an instrumental roll-over of the bandpass, SNR was low. The remaining 13 sub bands, with 25 MHz bandwidth each, are frequency-averaged versions of the original 0.39 MHz-wide channels in each sub-band. The time resolution was rebinned to 0.512 ms per sample. The fitting results are consistent with an unresolved pulse at infinite frequency, so a Gaussian pulse was used as a template. The width of the pulse was varied according to the dispersion smearing at each sub-band, ranging from 0.87 ms (1.7 samples) to 1.80 ms (3.5 samples). To take this variation of the width into account before convolving with the scattering tail, the fitting was performed for various widths in this range. In the case of  $\alpha$  these fits indicated a small spread of values about that given in Table 5.1 on page 127, the uncertainty specified is the spread of these values; the statistical uncertainty on each fit was significantly smaller, as indicated in Figure 5.3. For  $\beta$  the spread of values was of similar magnitude to the statistical uncertainty on a single fit; in this case the uncertainty of the value in Table 5.1 reflect the spread of  $\beta$  and the statistical uncertainty on a single fit which are of a similar magnitude.

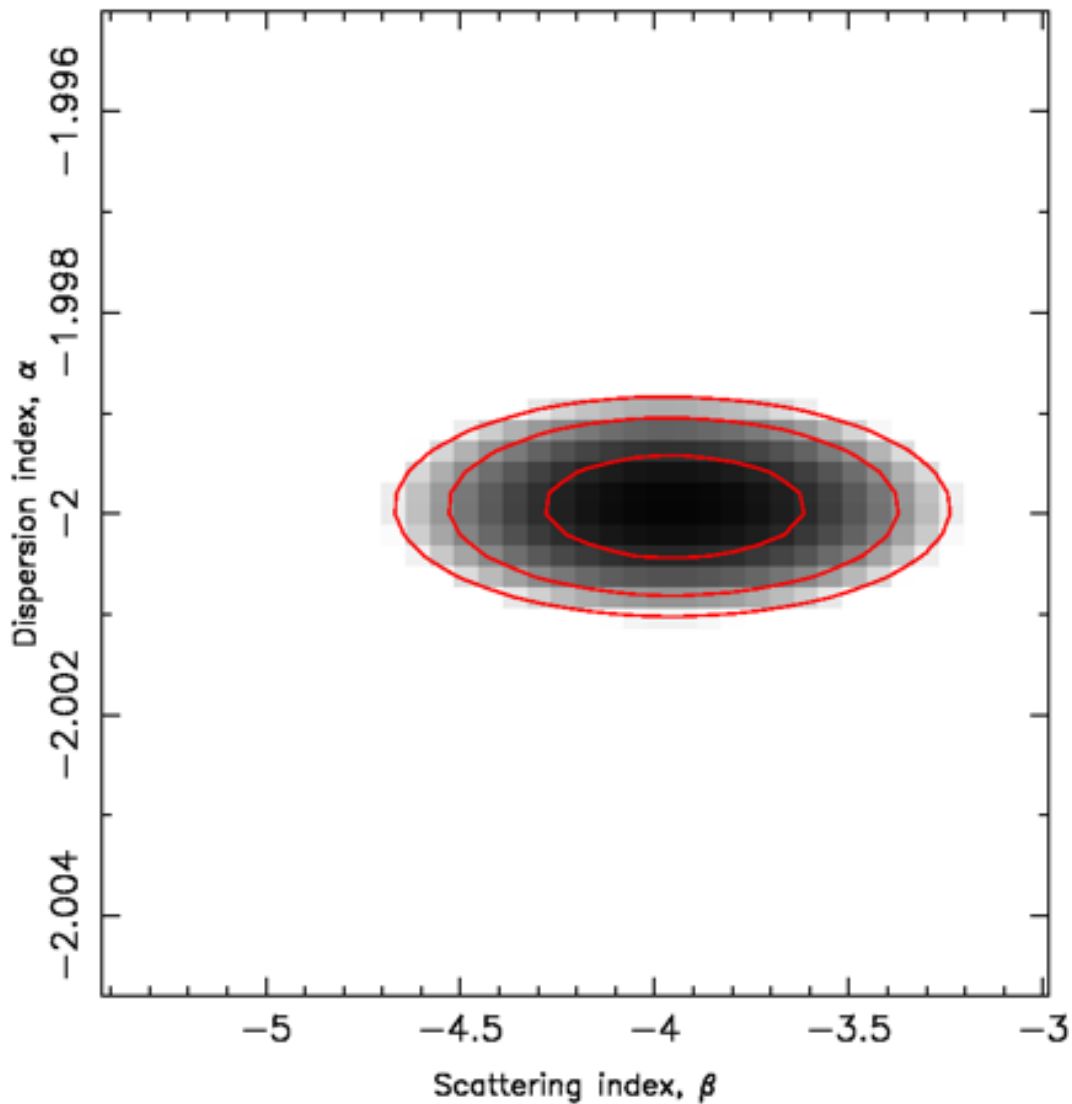


**Figure 5.3** – A grayscale plot showing the reduced  $\chi^2$  as a function of dispersion index,  $\alpha$ , and scattering index,  $\beta$  for FRB 110220. The concentric lines indicate the 1-, 2-, and 3- $\sigma$  confidence intervals about the best values (see Table 5.1). Note this figure corresponds to the fit with a smeared intrinsic width of 2 bins, 1.02 ms, not the ranges indicated in Table 5.1.

The template could have been spread by dispersion within each sub-band, but as the dispersion law was included in the fit, and as the true intrinsic shape of the pulse is not known, variation of the template width was used as a means to explore the dependence of our results on template width. All of the intrinsic pulse width fits indicated a similar  $\chi^2$  including unresolved (limited by the downsampled temporal resolution). The marginally best  $\chi^2$  was obtained for a dispersed (within the sub-bands) template width of 2 bins (1.02 ms), i.e.  $\chi^2 = 26316$  for 26605 degrees of freedom, corresponding to a reduced  $\chi^2$  of 0.989, indicating an excellent fit (see Figure 5.3). Taking the dispersion smearing into account, this

suggests an intrinsic width of less than 1.02 ms. Parameterizing the frequency dependence of  $\delta t$  and  $W$  as  $\alpha$  and  $\beta$ , respectively, we measured  $\alpha = 2.003 \pm 0.006$  and  $\beta = 4.0 \pm 0.4$  for FRB 110220 (see Table 5.1 on page 127 and Fig. 5.2), as expected for propagation through a cold plasma. Overall, the fit is consistent with the expectation from a cold plasma law and interstellar scattering, confirming the astrophysical nature of FRB 110220.

### 5.2.2 FRB 110703

FRB 110703 was weaker than FRB 110220 and had to be frequency collapsed to just eight sub-bands of 50 MHz bandwidth. Two sub-bands were excluded at the top and bottom of the band. The rebinning factor in time was also larger than for FRB 110220 in order to achieve sufficient SNR. We found, for the resulting 3.512 ms resolution, that the pulse was consistent with not having been scattered. Attempts to increase the time resolution in order to resolve the pulse resulted in an SNR too low to obtain reliable fit results. We therefore only adapted one template width, namely 0.57 bins (2.01 ms), which corresponds to the DM smearing at the lowest frequency channel, and fitted in the final step only for  $\delta t(\nu_0)$ , DM, and  $\alpha$ . Again, the results support the astrophysical nature of the pulse. Note in Table 5.1 the uncertainty on  $\alpha$  is taken to be the uncertainty for FRB 110220. We do this because we have not fit for  $\beta$  simply because there is insufficient SNR; there is likely some covariance between  $\alpha$  and  $\beta$  which is implicit in the value derived for  $\alpha$ .

Although FRB 110703 shows no evidence of scattering, we determined  $\alpha = 2.000 \pm 0.006$ . FRBs 110627 and 120127 do not have sufficient signal-to-noise ratios (SNRs) to yield astrophysically interesting constraints for either parameter and show no evidence of scattering.

## 5.3 Interpretation

In order to estimate a distance to the source of these FRBs we must understand the causes of the observed dispersion. The non-Galactic DM contribution,  $DM_E$ , is the sum of two components: the intergalactic medium (IGM;  $DM_{IGM}$ ) and a possible host galaxy ( $DM_{Host}$ ). The intervening medium could be purely intergalactic and could also include a contribution from an intervening galaxy. Two options are considered according to the proximity of the source to the center of a host galaxy. If located at the center of a galaxy, this may be a highly dispersive region; for example, lines of sight passing through the central regions of

Milky Way-like galaxies could lead to DMs in excess of  $700 \text{ cm}^{-3} \text{ pc}$  in the central  $\sim 100 \text{ pc}$  (Deneva, Cordes & Lazio, 2009), independent of the line-of-sight inclination. In this case,  $\text{DM}_E$  is dominated by  $\text{DM}_{\text{Host}}$  and requires FRBs to be emitted by an unknown mechanism in the central region, possibly associated with the supermassive black hole located there.

### 5.3.1 Combining dispersive regions

In order to combine dispersion from different sources or regions at different redshifts we must first understand simple dispersion, before generalising to the redshifted case. The propagation time of a pulse at a single frequency,  $\nu$ , over a distance  $L$  is given by

$$t = \frac{L}{c} + \frac{e^2}{2\pi m_e c} \frac{1}{\nu^2} \int_0^L n_e dl, \quad (5.1)$$

where  $e$  and  $m_e$  are the electronic charge and mass respectively,  $c$  is the speed of light and  $n_e$  is the free electron density. The DM is defined as

$$\text{DM} = \int_0^L n_e dl. \quad (5.2)$$

If all dispersion was taking place at a fixed frequency,  $\nu$ , then DMs may simply be summed. This is the case in the Milky Way where there is not significant redshift of the radio waves. However, when redshift is important and  $\nu(z)$  (the radiation which is dispersed is a function of redshift) then

$$\text{DM}_{\text{measured}} \neq \text{rest frame}(\text{DM}_{\text{MW}} + \text{DM}_{\text{IGM}} + \text{DM}_{\text{host}} + \text{DM}_{\text{inter}}), \quad (5.3)$$

because the frequencies are affected by redshift, and each dispersive region is at a different redshift,  $z$ .

By calculating the delay across the observing band as the difference in propagation time between a high ( $\nu_{\text{high}}$ ) and low ( $\nu_{\text{low}}$ ) frequency,  $\delta t$ , as

$$\delta t = \frac{e^2}{2\pi m_e c} \text{DM} \left( \frac{1}{\nu_{\text{low}}^2} - \frac{1}{\nu_{\text{high}}^2} \right), \quad (5.4)$$

in the non-redshifted case. Delays from different regions of propagation can be summed together, with each region taking place at a different redshift and frequency. The delay measured across the observing band at the telescope,  $\delta t_{\text{total}}$ , is therefore

$$\delta t_{\text{total}} = \delta t_{\text{Milky Way}}(l, b) + \delta t_{\text{Host}}(i, z) + \delta t_{\text{inter}}(i_{\text{inter}}, z_{\text{inter}}) + \delta t_{\text{IGM}}(z), \quad (5.5)$$

where  $\delta t_{\text{Milky Way}}(l, b)$  is the Milky Way delay contribution in the direction  $(l, b)$ ,  $\delta t_{\text{Host}}(i, z)$  is the host contribution for a galaxy at inclination,  $i$ , to the line of sight at a redshift  $z$ ,  $\delta t_{\text{inter}}(i_{\text{inter}}, z_{\text{inter}})$  is the contribution from an intervening galaxy at inclination,  $i_{\text{inter}}$  to the line of sight at redshift  $z_{\text{inter}}$ , and  $\delta t_{\text{IGM}}(z)$  is the IGM delay contribution for a source at redshift,  $z$ . The MW contribution,  $\delta t_{\text{Milky Way}}(l, b)$ , is simply defined by Equation 5.4 with a model  $\text{DM}(l, b)$  (Cordes & Lazio, 2002).

For delay contributions at a single non-zero redshift, like those of a host galaxy or an intervening galaxy, Equation 5.4 is refined as

$$\delta t_{\text{Host/inter}} = \frac{e^2}{2\pi m_e c} \text{DM}_{\text{Host/inter}} \left( \frac{1}{(\nu_{\text{low}}(1 + z_{\text{Host/inter}}))^2} - \frac{1}{(\nu_{\text{high}}(1 + z_{\text{Host/inter}}))^2} \right), \quad (5.6)$$

where the frequency of the radiation is higher through cosmological redshift,  $\nu_{\text{obs}} \rightarrow \nu_{\text{obs}}(1 + z)$ . This delay to the signal takes place at a single redshift and is fixed after the radiation leaves that region. It is clear from Equation 5.6 that summations of redshifted delays from multiple redshifts still sum to a delay across the observing band which is  $\propto \nu^{-2}$ . Equation 5.6 would be applicable to any contribution at a fixed redshift.

In the case of the IGM, dispersion takes place at a range of redshifts and is an integrated effect between source and host. Cosmological redshift for dispersion in the IGM affects the frequency,  $\nu$ , the free-electron density,  $n_e$ , and the line element,  $dl$ , from Equation 5.4. For the electron density in the IGM, we define  $n_{e,\text{IGM}}$  as

$$n_{e,\text{IGM}} = x(z)n_{e,0}(1 + z)^3, \quad (5.7)$$

where  $x(z)$  is the ionisation fraction as a function of redshift, and  $n_{e,0}$  is the local intergalactic electron density. Converting the  $dl$  to  $dz$  via

$$dl = c \frac{dt}{dz}, dz \quad (5.8)$$

and

$$\frac{dt}{dz} = \frac{1}{H(z)(1+z)}, \quad (5.9)$$

where  $H(z)$  is the Hubble constant which, in a  $\Lambda$ CDM model of cosmological expansion, is given by

$$H(z) = H_0(\Omega_M(1+z)^3 + \Omega_\Lambda)^{\frac{1}{2}}, \quad (5.10)$$

where  $H_0$  is the Hubble constant now, and  $\Omega_M$  and  $\Omega_\Lambda$  are the fractions of baryonic and dark matter of the critical density for a flat universe respectively.

Combining Equations 5.7, 5.8, 5.9, and 5.10 we derive the propagation time for a single *observing* frequency,  $\nu$ , due to the IGM as

$$t_{\text{IGM}}(\nu, z_{\text{Host}}) = \frac{e^2 n_{e,0}}{2\pi m_e \nu^2} \int_0^{z_{\text{Host}}} \frac{x(z) dz}{H_0(\Omega_M(1+z)^3 + \Omega_\Lambda)^{\frac{1}{2}}}. \quad (5.11)$$

Finally we integrate Equation 5.11 to find the delay across the observing band,  $\delta t_{\text{IGM}}(z) = t_{\text{IGM}}(\nu_{\text{low}}, z) - t_{\text{IGM}}(\nu_{\text{high}}, z)$  due to the IGM (see Figure 5.4). It has been shown that the universe is significantly ionised to  $z \lesssim 6$  (Gunn & Peterson, 1965). In this analysis the ionisation fraction  $x(z) = 1$  has been used throughout.

By equating the sum of delay contributions (Equation 5.5) to the measured delay across the observing band we can estimate the redshift (see Figure 5.4). An estimation of the DM, and therefore the delays, for the Milky Way and host galaxy are necessary to do this.

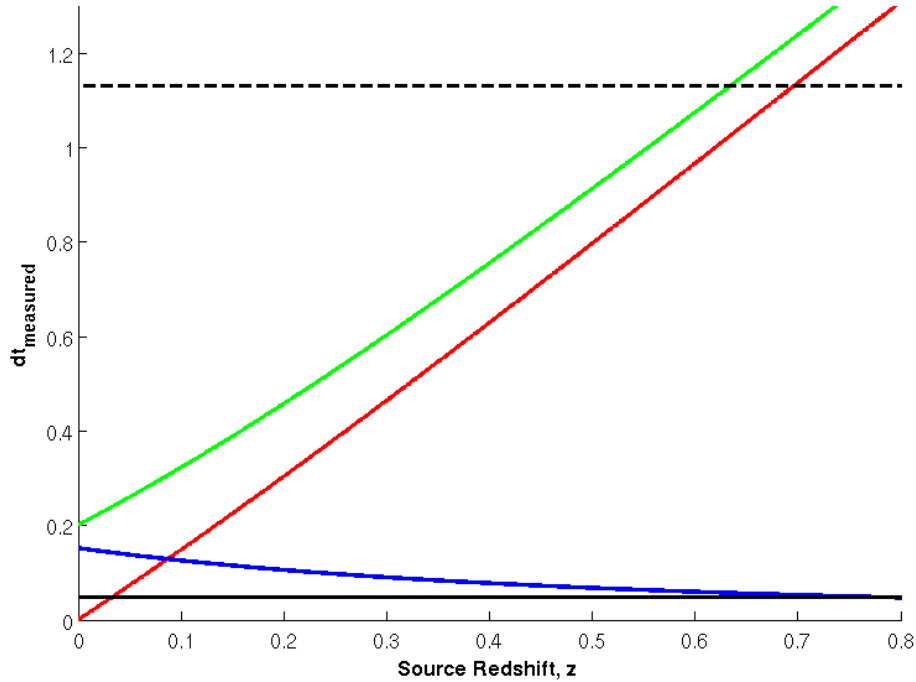


**Figure 5.4** – Modelled dispersive delay (in seconds) across the observing band of the HTRU survey is shown plotted against redshift. The flat dashed line indicates the delay across the observing band for FRB 110220. The solid black line is the MW contribution and is constant irrespective of the redshift of the source, the red line is the delay due to the IGM, the blue line is the delay contribution from a host galaxy with  $DM_{\text{Host}} = 100 \text{ cm}^{-3}\text{pc}$ , and the green line is the sum of the IGM, host and MW contributions. When the sum of contributions is equal to the measured delay the redshift is inferred.

### 5.3.2 Dispersion and scattering sources

The four FRBs were detected with DMs in the range from  $553$  to  $1103 \text{ cm}^{-3} \text{ pc}$ . Their high Galactic latitudes ( $|b| > 41^\circ$ , see Table 5.1) correspond to lines of sight through the low column density Galactic ISM (see Figure 5.5) corresponding to just 3 to 6% of the DM measured (Cordes & Lazio, 2002). These small Galactic DM contributions are highly supportive of an extragalactic origin and are substantially smaller fractions than those of previously reported bursts, which were 15% of  $DM = 375 \text{ cm}^{-3} \text{ pc}$  for FRB 010724 (Lorimer et al., 2007) and 70% of  $DM = 746 \text{ cm}^{-3} \text{ pc}$  for FRB 010621 (Keane et al., 2012).

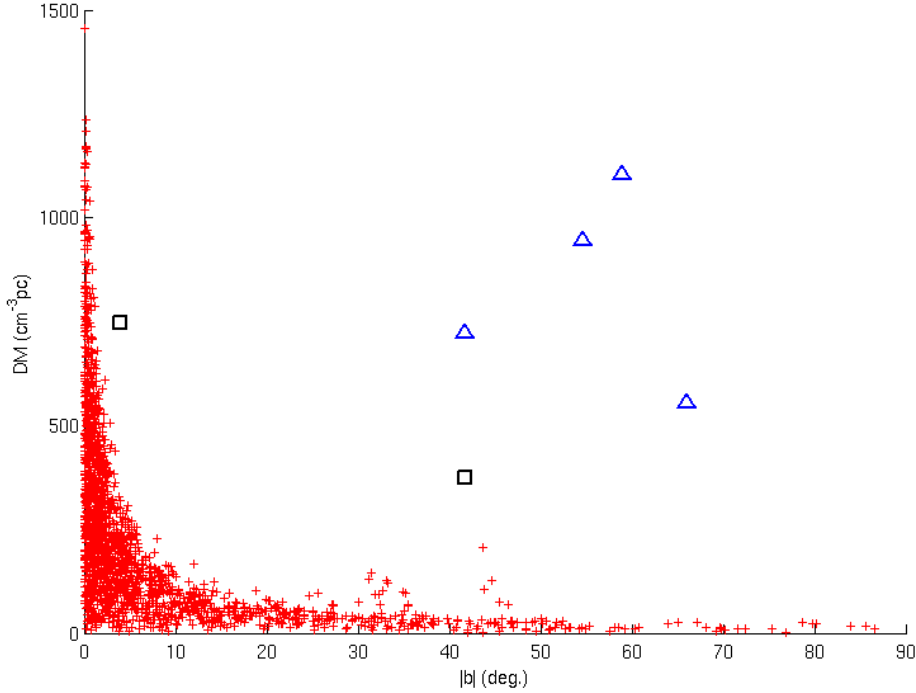


**Figure 5.5** – Measured DM for FRBs and known pulsars is plotted against the magnitude of their Galactic latitude,  $|b|$ . The FRBs from this paper are shown as blue triangles, FRB 010621 and 010724 are shown as black squares, pulsars are indicated by red + symbols. The FRBs exhibit significantly higher dispersion than pulsars at similar  $|b|$ . The pulsars with apparent dispersion excess located at  $30^\circ < |b| < 45^\circ$  are in the Magellanic clouds, which are an additional source of free electrons, and therefore, dispersion.

If outside a central region, then elliptical host galaxies (which are expected to have a low electron density) will not contribute to  $DM_E$  significantly, and  $DM_{\text{Host}}$  for a spiral galaxy will only contribute significantly to  $DM_E$  if viewed close to edge-on [inclination,  $i > 87^\circ$  for  $DM > 700 \text{ cm}^{-3} \text{ pc}$ ; probability( $i > 87^\circ$ )  $\approx 0.05$ ]. The chance of all four FRBs coming from edge-on spiral galaxies is therefore negligible ( $10^{-6}$ ). Consequently, if the sources are not located in a galactic center,  $DM_{\text{Host}}$  would likely be small, and  $DM_{\text{IGM}}$  dominates. Assuming an IGM free-electron distribution, which takes into account cosmological redshift and assumes a universal ionization fraction of 1 (Ioka, 2003; Inoue, 2004), the sources are inferred to be at redshifts  $z = 0.45$  to  $0.96$ , corresponding to co-moving distances of 1.7 to 3.2 Gpc (see Section 5.3.1 and Table 5.1).

In principle, pulse scatter-broadening measurements can constrain the location and strength of an intervening scattering screen (Williamson, 1972). FRBs 110627, 110703, and 120127 are too weak to enable the determination of any scattering; however, FRB

110220 exhibits an exponential scattering tail (see Figure 5.1). There are at least two possible sources and locations for the responsible scattering screens: a host galaxy or the IGM. It is possible that both contribute to varying degrees. For screen-source,  $D_{\text{src}}$ , and screen-observer,  $D_{\text{obs}}$ , distances, the magnitude of the pulse broadening resulting from scattering is multiplied by the factor  $D_{\text{src}}D_{\text{obs}}/(D_{\text{src}} + D_{\text{obs}})^2$ . For a screen and source located in a distant galaxy, this effect probably requires the source to be in a high-scattering region, for example, a galactic center.

The second possibility is scattering because of turbulence in the ionized IGM, unassociated with any galaxy. There is a weakly constrained empirical relationship between DM and measured scattering for pulsars in the MW. If applicable to the IGM, then the observed scattering implies  $\text{DM}_{\text{IGM}} > 100 \text{ cm}^{-3}\text{pc}$  (Bhat et al., 2004). With use of the aforementioned model of the ionized IGM, this DM equates to  $z > 0.11$  (see section 5.7; Ioka 2003; Inoue 2004). The probability of an intervening galaxy located along the line of sight within  $z \approx 1$  is  $\lesssim 0.05$  (Roeder & Verreault, 1969). Such a galaxy could be a source of scattering and dispersion, but the magnitude would be subject to the same inclination dependence as described for a source located in the disk of a spiral galaxy.

## 5.4 Non-dispersed origins

The FRBs are measured to obey astronomical dispersive delay and scattering to a high accuracy; it seems unlikely that a man-made source, especially emitting in a protected band, would so accurately reproduce this behaviour. The broadband nature of the bursts also rules out the majority of the RFI environment, which consists of short-duration non-dispersed narrowband pulses.

Observations at Parkes have previously shown swept frequency pulses of terrestrial origin, dubbed “peryttons” (Burke-Spolaor et al., 2011a). The  $\sim 25$  now-reported peryttons (Burke-Spolaor et al., 2011a; Bagchi, Nieves & McLaughlin, 2012; Kocz et al., 2012) are characterized by 20 - 50 ms wide, symmetric, swept-frequency pulses that imperfectly mimic a  $\delta t \propto \nu^{-2}$  dispersive sweep. Peryttons’ equivalent DM distribution has a peak near  $375 \text{ cm}^{-3}\text{pc}$  and a negative skew (the range is  $\sim 200 - 420 \text{ cm}^{-3}\text{pc}$ ). Peryttons are easily recognized by their appearance in all beams of the multibeam receiver, indicating a sidelobe detection. The similarity of these perytton properties with the sweep rate and duration of the FRB 010724 led to the suggestion it might be a perytton during which the telescope was directly pointed at the source, however its celestial or terrestrial origin cannot

yet be conclusively determined (Burke-Spolaor et al., 2011a). This is not the case for the four FRBs presented here, which have a much larger (and apparently random) DM range, adhere to a dispersive sweep to high precision, and three of which are a factor of  $> 3$  shorter duration than all known perytons. Furthermore, the fast-rise and exponential-tail profile of FRB 110220 makes a clear case for cold plasma propagation; FRB 010724, while displaying frequency-dependent pulse broadening, did not have clear asymmetry.

Because spatial filters are powerful discriminators of local RFI, the current search system rejects signals that are significantly detected in nine or more of the telescope's 13 beams. Therefore, we are likely filtering out a large number of perytons expected to appear in the HTRU survey. Thus far, two perytons (sufficiently weak to not be detected in all beams due to receiver gain variations) have been discovered in HTRU data from the year 2010. This indicates that perytons are still occurring at the telescope, however, it also confirms that perytons still exhibit the same imperfectly-dispersed, symmetric form, with  $\langle DM \rangle \sim 375 \text{ cm}^{-3} \text{ pc}$  and  $\langle W \rangle \sim 30 \text{ ms}$ . Like all previously-detected perytons, the new perytons are not obvious analogs to FRBs.

The Sun is known to emit frequency-swept radio bursts at 1 to 3 GHz [type III dm; (Isliker & Benz, 1994)]. These bursts have typical widths of 0.2 to 10 s and positive frequency sweeps, entirely inconsistent with measurements of  $W$  and  $\alpha$  for the FRBs. Whereas FRB 110220 was separated from the Sun by  $5.6^\circ$ , FRB 110703 was detected at night and the others so far from the Sun that any solar radiation should have appeared in multiple beams. These FRBs were only detected in a single beam; it is therefore unlikely they are of solar origin.

## 5.5 Energetics

Uncertainty in the true position of the FRBs within the frequency-dependent gain pattern of the telescope makes inferring a spectral index, and hence flux densities outside the observing band, difficult. A likely off-axis position changes the intrinsic spectral index significantly. The spectral energy distribution across the band in FRB 110220 is characterized by bright bands  $\sim 100 \text{ MHz}$  wide (see Figure 5.2); the SNRs are too low in the other three FRBs to quantify this behavior (see Section 5.5). Similar spectral characteristics are commonly observed in the emission of high- $|b|$  pulsars. The SNR in 4 sub-bands for each FRB is shown in Figure 5.6 for comparison.

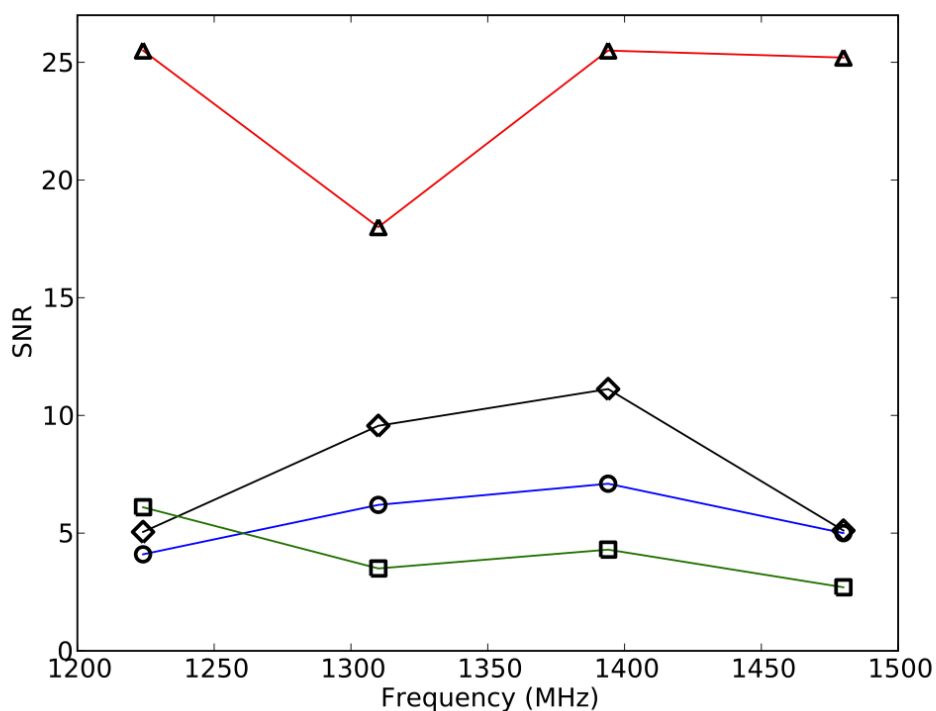


**Figure 5.6** – The SNRs of the FRBs (110220: triangles, 110627: circles, 110703: diamonds, 120127: squares). For each the total band has been split into four 100 MHz sub-bands and the SNR of the pulse in each measured.

The energy released,  $E$ , (see Table 5.1) is calculated as the total energy of the burst at the source. The energy released,  $E \sim F \cdot D^2 \cdot B$ , where  $F$  is the fluence,  $D$  is the cosmological luminosity distance, and  $B$  is the bandwidth at the source. Note that emission is not assumed isotropic, instead a beam of 1 steradian is used for simplicity. In the case of these FRBs the width (and therefore fluence), distance, and bandwidth must be corrected to account for cosmological redshift. These corrections have been made for the  $E$  values in Table 5.1. As the measurement of spectral index is inconclusive we have assumed it to be flat (see Figure 5.6) and do not extrapolate beyond the redshifted observing band.

## 5.6 Fast Radio Burst rate

With four FRBs it is possible to calculate an approximate event rate. The high-latitude HTRU survey region is 24% complete, resulting in 4500 square degrees observed for

270 seconds. This corresponds to an FRB rate of  $R_{\text{FRB}}(F \sim 3 \text{ Jy ms}) = 1.0_{-0.5}^{+0.6} \times 10^4 \text{ sky}^{-1} \text{ day}^{-1}$ , where the  $1 - \sigma$  uncertainty assumes Poissonian statistics. The MW foreground would reduce this rate, with increased sky temperature, scattering, and dispersion for surveys close to the Galactic plane. In the absence of these conditions, our rate implies that  $17_{-7}^{+9}$ ,  $7_{-3}^{+4}$ , and  $12_{-5}^{+6}$  FRBs should be found in the completed high- and medium-latitude parts of the HTRU (Keith et al., 2010) and Parkes multibeam pulsar (PMPS) surveys (Manchester et al., 2001).

One candidate FRB with  $\text{DM} > \text{DM}_{\text{MW}}$  has been detected in the PMPS [ $|b| < 5^\circ$ ; (Keane et al., 2012; Bagchi, Nieves & McLaughlin, 2012)]. This burst could be explained by neutron star emission, given a small scale height error in Galactic DM model (Gaensler et al., 2008); however, observations have not detected any repetition. No excess-DM FRBs were detected in a burst search of the first 23% of the medium-latitude ( $|b| < 15^\circ$ ) HTRU survey (Burke-Spolaor et al., 2011b).

The event rate originally suggested for FRB 010724,  $R_{010724} = 225 \text{ sky}^{-1} \text{ day}^{-1}$  (Lorimer et al., 2007), is consistent with our event rate given a Euclidean universe and a population with distance independent intrinsic luminosities (source count,  $N \propto F^{-\frac{3}{2}}$ ), yielding  $R_{\text{FRB}}(F \sim 3 \text{ Jy ms}) \sim 10^2 R_{\text{FRB}}(F_{010724} \sim 150 \text{ Jy ms})$ .

	<b>FRB 110220</b>	<b>FRB 110627</b>	<b>FRB 110703</b>	<b>FRB 120127</b>
Beam right ascension (J2000)	22 <sup>h</sup> 34 <sup>m</sup>	21 <sup>h</sup> 03 <sup>m</sup>	23 <sup>h</sup> 30 <sup>m</sup>	23 <sup>h</sup> 15 <sup>m</sup>
Beam declination (J2000)	-12°24′	-44°44′	-02°52′	-18°25′
Galactic latitude, $b$ (°)	-54.7	-41.7	-59.0	-66.2
Galactic longitude, $l$ (°)	+50.8	+355.8	+81.0	+49.2
UTC (dd/mm/yyyy)	20/02/2011	27/06/2011	03/07/2011	27/01/2012
hh:mm:ss.sss	01:55:48.947	21:33:48.957	18:59:40.591	08:11:21.723
DM (cm <sup>-3</sup> pc)	944.38 ± 0.05	723.0 ± 0.3	1103.6 ± 0.7	553.3 ± 0.3
DM <sub>E</sub> (cm <sup>-3</sup> pc)	910	677	1072	521
Redshift, $z$ (DM <sub>Host</sub> = 100 cm <sup>-3</sup> pc)	0.81	0.61	0.96	0.45
Co-moving distance, $D$ (Gpc) at $z$	2.8	2.2	3.2	1.7
Dispersion index, $\alpha$	-2.003 ± 0.006	-	-2.000 ± 0.006	-
Scattering index, $\beta$	-4.0 ± 0.4	-	-	-
Observed width at 1.3 GHz, $W$ (ms)	5.6 ± 0.1	< 1.4	< 4.3	< 1.1
SNR	49	11	16	11
Minimum peak flux density, $S_\nu$ (Jy)	1.3	0.4	0.5	0.5
Fluence at 1.3 GHz, $F$ (Jy ms)	8.0	0.7	1.8	0.6
$S_\nu D^2$ ( $\times 10^{12}$ Jy kpc <sup>2</sup> )	10.2	1.9	5.1	1.4
Energy released, $E$ (J)	$\sim 10^{33}$	$\sim 10^{31}$	$\sim 10^{32}$	$\sim 10^{31}$

Table 5.1 – see next page

**Table 1** Parameters for the four FRBs. The position given is the center of the gain pattern of the beam in which the FRB was detected (half-power beam width  $\sim 14$  arc min). The UTC corresponds to the arrival time at 1581.804688 MHz. The DM uncertainties depend not only on SNR but also on whether  $\alpha$  and  $\beta$  are assumed ( $\alpha = -2$ ; no scattering) or fit for; where fitted,  $\alpha$  and  $\beta$  are given. The co-moving distance was calculated by using  $DM_{\text{Host}} = 100 \text{ cm}^{-3}\text{pc}$  (in the rest frame of the host) and a standard, flat-universe  $\Lambda$ CDM cosmology which describes the expansion of the universe with baryonic and dark matter, and dark energy [ $H_0 = 71 \text{ km s}^{-1} \text{ Mpc}^{-1}$ ,  $\Omega_M = 0.27$ ,  $\Omega_\Lambda = 0.73$ ;  $H_0$  is the Hubble constant and  $\Omega_M$  and  $\Omega_\Lambda$  are fractions of the critical density of matter and dark energy respectively (Spergel et al., 2003)].  $\alpha$  and  $\beta$  are from a series of fits using intrinsic pulse widths of 0.87 to 3.5 ms; the uncertainties reflect the spread of values obtained. The observed widths are shown; FRBs 110627, 110703, and 120127 are limited by the temporal resolution due to dispersion smearing. The energy released is calculated for the observing band in the rest frame of the source.

## 5.7 FRB locations

Detailed attempts to constrain the position of FRB 110220 by using its non-detection in the other beams does not produce a better localization than the half-power beam-width (HPBW) and is not simply described by a single quantity. Positioning is further complicated because the beam shape is frequency dependent it is wider for lower frequencies. This imparts an apparent spectral index to a source located away from the beam center. Combining this with the unknown intrinsic spectral index there is little constraint on the location within the beam. For these reasons the HPBW is used while recognizing the difficulty in knowing the true position.

There are 15, 56, 30, and 54 catalogued galaxies within the HPBW for FRB 110220, 110627, 110703, and 120127 respectively. Some of these have measured redshifts of  $z = 0.02, 0.6$ . If located in one of these galaxies then  $DM_{\text{IGM}}$  would be either  $17 \text{ cm}^{-3}\text{pc}$  ( $z = 0.02$ ) or  $570 \text{ cm}^{-3}\text{pc}$  ( $z = 0.6$ ), as such a significant fraction of  $DM_E$  would be due to the host. In these directions there are almost certainly as yet undiscovered galaxies at other redshifts. The empirical relationship between DM and scattering (Bhat et al., 2004) may be used to constrain the redshift to  $z > 0.11$ . However, this relationship is based on measurements of pulsars in the MW, and may not be applicable to the IGM.

In addition to looking at galaxies in the field of view we also looked for temporally as-

sociated GRBs or x-ray transients. Gamma-ray and X-ray telescopes have all-sky monitors however we did not find any catalogued event (NASA HEASARC) which could be related to any of the FRBs in this paper. The Astronomers Telegram was also checked for possibly associated events; none were found.

## 5.8 Possible sources

There are no known transients detected at gamma-ray, x-ray, or optical wavelengths or publicly announced gravitational wave triggers that can be temporally associated with any FRBs. In particular there is no known gamma ray burst (GRB) with a coincident position on a time scale commensurate with previous tentative detections of short-duration radio emission (Bannister et al., 2012). GRBs have highly beamed gamma-ray emission (Frail et al., 2001), and, if FRBs are associated with them, the radio emission must be beamed differently. By using the distances in Table 5.1, we found that the comoving volume contains  $\sim 10^9$  late-type galaxies (Madgwick et al., 2002), and the FRB rate is therefore  $R_{\text{FRB}} = 10^{-3} \text{ galaxy}^{-1} \text{ year}^{-1}$ .  $R_{\text{FRB}}$  is thus inconsistent with  $R_{\text{GRB}} = 10^{-6} \text{ galaxy}^{-1} \text{ year}^{-1}$ , even when beaming of emission is accounted for (Frail et al., 2001).

Soft gamma-ray repeaters (SGRs) undergo giant bursts at a rate consistent with FRBs (Ofek, 2007), and the energy within our band is well within the budget of the few known SGR giant burst cases (Hurley et al., 2005). See Chapter 6 for more information.

Another postulated source class is the interaction of the magnetic fields of two coalescing neutron stars (Hansen & Lyutikov, 2001). However, the large implied FRB luminosities indicate that coalescing neutron stars may not be responsible for FRBs. Furthermore,  $R_{\text{FRB}}$  is significantly higher than the predicted rate for neutron star mergers. Black hole evaporation has also been postulated as a source of FRBs; however, the predicted luminosity within our observing band far exceeds the energy budget of an evaporation event (Rees, 1977).

The core-collapse supernova (ccSN) rate of  $R_{\text{ccSN}} = 10^{-2} \text{ galaxy}^{-1} \text{ year}^{-1}$  (Diehl et al., 2006) is consistent with  $R_{\text{FRB}}$ . There is no known mechanism to generate an FRB from a lone ccSN. It may, however, be possible that a ccSN with an orbiting neutron star can produce millisecond-duration radio bursts during the interaction of the ccSN explosion and the magnetic field of the neutron star (Egorov & Postnov, 2009), although the need for an orbiting neutron star will make these rarer.

As extragalactic sources, FRBs represent a probe of the ionized IGM. Real-time de-

tectons and immediate follow-up at other wavelengths may identify a host galaxy with an independent redshift measurement, thus enabling the IGM baryon content to be determined (Ioka, 2003). Even without host identifications, further bright FRB detections will be a unique probe of the magneto-ionic properties of the IGM.

# Chapter 6

## FRBs: burst profiles, population, and source

### 6.1 Introduction

Fast radio bursts (FRBs) are single, highly dispersed bursts of radio waves lasting just a few milliseconds. They are distinguished by anomalously high dispersion measures for their line of sight through the Milky Way (MW). The first case was discovered in data from a pulsar survey of the Magellanic clouds (the so-called “Lorimer burst”; Lorimer et al. 2007). For several years the veracity of the Lorimer burst as an astronomical source was in doubt. More recently, discoveries by Keane et al. (2012), and those presented in Chapter 5, have confirmed FRBs as being a real astronomical population. To-date there are five published examples which are highly likely to be of extragalactic origin (Lorimer et al., 2007; Thornton et al., 2013), and one which may be extragalactic (Keane et al., 2012). FRBs are a relatively newly discovered population of radio sources and, with only a handful of examples, little is known about their properties, both as individual sources and as a population.

The signal from an FRB that we measure corresponds to a short increase in the received power across the specific observing band. One way to study an FRB is to correct the data for the influence of ionised material along the line of sight to the source in order to measure its *profile* (dedispersion) (see Chapter 2), which is the received power as a function of time. A burst’s profile can be generated for the total bandwidth of the observation, or to investigate it as a function of observing frequency for a number of subbands. Four of the

six published examples of FRBs came from the HTRU survey, which like previous pulsar surveys (e.g. Parkes Multibeam Pulsar Survey in which FRB 110701 - the Keane Burst - was discovered) does not record separate data for each of the two polarisation signals from the receiver (Manchester et al., 2001; Keith et al., 2010). While polarisation data may provide more insight in to the emission mechanism there is still much that can be learnt from the total intensity burst profiles. For instance, in two cases FRBs have been observed to have a frequency dependent width, which has been attributed to interstellar or intergalactic scattering (Lorimer et al., 2007) and see Chapter 5.

While pulsars appear to be unrelated to FRBs, the two populations do share some common traits in their signal. They both have sufficiently high brightness temperatures that the emission mechanism must be coherent, and they both show similar burst or pulse widths. Both also exhibit similar propagation effects: all radio pulsars and FRBs show dispersive delays, while some show measurable scattering.

Pulsars exhibit an enormous range of pulse profiles that cannot be attributed to dispersion or scattering; for example, some have multiple peaks of different shapes and sizes - *pulse structure*. This structure is often interpreted as a linear sum of individual components which may come from different regions of the pulsar magnetosphere (e.g. Hassall et al. 2012). Previously no FRB profile had been observed to have any discernible structure, all have been either effectively unresolved, or have simple scattered Gaussian-like profiles. As is the case for pulsars, measurable structure in an FRB profile may provide a method to measure the emission region's size and frequency dependence. In Section 6.2 I present and describe the discovery of a fifth FRB from the HTRU survey, which is the first to exhibit structure in the burst profile.

As well as understanding individual FRBs it is important to consider the population and their distribution in the Universe. With an understanding of source locations, spectral characteristics, and luminosities, predictions could be made about how many FRBs may exist and how many of those may be detectable by different surveys and instruments.

Currently, our best understanding comes from just seven events; as such conclusions are dominated by small number statistics, and are consequently quite uncertain. The best estimate of the rate of FRBs is  $R_{\text{FRB}} \approx 10^4 \text{ sky}^{-1} \text{ day}^{-1}$  for bursts with redshift,  $z < 1$  (see Chapter 5). The known FRBs have a range of measured DM values ( $375 \lesssim \text{DM} \lesssim 1628 \text{ cm}^{-3} \text{ pc}$ ), but which are not evenly spread over the range of DM that is being searched. In particular, the HTRU survey, in which five FRBs have been discovered, is currently searched up to a maximum dispersion measure,  $\text{DM}_{\text{max}} = 2000 \text{ cm}^{-3} \text{ pc}$ . Why have more

FRBs not been found at higher DMs in this survey? Is the handful of cases consistent with simple models of source distribution in the Universe? In Section 6.3 I describe a population simulation of FRBs which begins to address these questions. In addition, I also speculate on what may be learnt by future detection of a statistically significant number of FRBs.

Recently, there have been some theoretical papers which aim to explain the source of FRBs. It has been postulated that merging double neutron star systems could in fact be responsible, and that rate is significantly uncertain that it may be reconcilable with the FRB rate (Totani, 2013). This however seems to be a mistake on the part of the authors in their calculation of the co-moving volume with  $z < 1$ , and the rate does apparently preclude merging double neutron star binaries as the source. The emission mechanism considered is coherent radio emission from two orbiting neutron stars when the rotation of the two magnetospheres synchronise just prior to merger. It has also been postulated that supramassive neutron stars, which only avoid collapse to a black hole because of their rotation, could be responsible for FRBs (Falcke & Rezzolla, 2013). The mechanism supposed is that such a neutron star will have an increasing rotation period through the emission of magnetic dipole radiation. When the rotation period is sufficiently long that rotation is no longer able to overcome gravitational forces the neutron star will collapse to a black hole. While the surface of the neutron star will be beyond the event horizon a large part of the magnetosphere would not, and the magnetic field lines would “snap” releasing a large amount of radio energy, consistent with FRB luminosities.

In Chapter 5 we conclude that Soft Gamma-ray Repeater (SGR) giant flares and FRBs may be associated with one another. They appear to occur at similar rates and the energy contained in an FRB is well within the apparent energy budget of an SGR giant flare. A simultaneous detection of an associated event to a FRB at a different energy, or even an associated gravitational wave signal, would be extremely useful in understanding the properties and the source of FRBs. For example an optical, x-ray, or gamma-ray associated event would likely be able to constrain the position to sufficient accuracy that a host galaxy could be identified. In Section 6.4 I take a further look at the possibility of SGR giant flares and FRBs being associated. I pay particular attention to the rotationally modulated emission after SGR giant flares.

## 6.2 FRB 121002

FRB 121002 was detected in the high-latitude region of the HTRU survey (see Chapter 2 for details). The FRB reached the telescope on 2nd October 2012 at 13:09:18.402 UTC; this corresponds to 23:09:18.402 local time on the same day. The FRB was discovered in archival data in May 2013. The SNR of the burst in the search pipeline was 12, which had been optimised by boxcar filtering. The dispersion measure of the burst is the highest yet measured for an FRB,  $DM = 1628.76 \text{ cm}^{-3} \text{ pc}$ . There is no published associated astronomical event detected at other wavelengths. Repeat observations at the beam positions of all FRB discoveries have not detected any repeat bursts. The detection of such a repeat event would indicate that the source is not cataclysmic in nature, and instead it would perhaps indicate a source which is either rotating or in orbit with another body.

In the single pulse search of the HTRU survey the test values of dispersion measure,  $DM_{\text{test}}$ , are not evenly distributed between the minimum and maximum values: the step sizes,  $DM_{\text{step}}$ , are larger for higher DMs (see Chapter 2). For an approximate  $DM = 1628 \text{ cm}^{-3} \text{ pc}$  these steps are relatively wide ( $DM_{\text{step}} \approx 4 \text{ cm}^{-3} \text{ pc}$ ). This means the DM from the search pipeline is relatively inaccurate. Once identified, however, the DM is refined by correcting the dispersion delays between channels with more finely and evenly spaced  $DM_{\text{test}}$  values, maximising the SNR of the burst in order to determine the best DM for this FRB (see Table 6.1).

Beam right ascension (J2000)	18 <sup>h</sup> 14 <sup>m</sup>
Beam declination (J2000)	−85°11′
Galactic longitude, $l$ (°)	+308
Galactic latitude, $b$ (°)	−26
UTC (dd/mm/yyyy)	02/10/2012
hh:mm:ss.sss)	13:09:18.402
DM ( $\text{cm}^{-3}$ pc)	$1628.76 \pm 0.05$
DM <sub>E</sub> ( $\text{cm}^{-3}$ pc)	1553
Redshift, $z$ (for DM <sub>Host</sub> = 100 $\text{cm}^{-3}$ pc)	1.45
Co-moving distance, $D$ (Gpc) at $z$	4.3
Width (component A) at 1.3 GHz, $W_A$ (ms)	$2.1 \pm 0.2$
Width (component B) at 1.3 GHz, $W_B$ (ms)	$3.7 \pm 0.2$
Component separation at 1.3 GHz, $\Delta$ (ms)	$5.1 \pm 0.2$
SNR	12
Minimum peak flux density, $S_\nu$ (Jy)	0.35
Fluence at 1.3 GHz, $F$ (Jy ms)	1.5
$S_\nu D^2$ ( $\times 10^{12}$ Jy kpc <sup>2</sup> )	6.4
Energy released, $E$ (J)	$\sim 10^{32}$

**Table 6.1** – Measured and inferred values for FRB 121002 including measurements of the two identified components, A and B (see Figure 6.1). DM<sub>E</sub> is the DM which can not be accounted for by the NE2001 model of Galactic ionised material in the direction of FRB 121002 (Cordes & Lazio, 2002).  $1 \text{ Jy} \equiv 10^{-26} \text{ J s}^{-1} \text{ Hz}^{-1}$

In order to discover FRB 121002 the number of searched observations from the high-latitude HTRU survey increased over the number used to derive the rate in Chapter 5. With five known FRBs so far discovered in this processing of the high-latitude survey the updated FRB rate is  $R_{\text{FRB}} = 8.7_{-3.5}^{+6.2} \times 10^3 \text{ sky}^{-1} \text{ day}^{-1}$ . This rate is not significantly different from the rate from provided in Chapter 5.

## 6.2.1 Distance

In order to infer the distance from the DM the different contributions to the observed DM must be determined or approximated. By using a model of the ionised intergalactic medium

(Ioka, 2003; Inoue, 2004) for the IGM contribution; the NE2001 model for the MW contribution; and by modelling a host galaxy as an inclined MW-type galaxy, it is possible to isolate the dispersive delay due to the IGM. From the IGM contribution a distance to the source can be inferred. Following the procedure described in Chapter 5, I calculate the source to be at a redshift,  $z = 1.45$ , corresponding to a co-moving distance of 4.3 Gigaparsecs using the  $\Lambda$ CDM model of universal expansion (Spergel et al., 2003). For the dispersion imparted by ionised material in a host galaxy I have used a host contribution to dispersion,  $DM_{\text{Host}} = 100 \text{ cm}^{-3} \text{ pc}$ . This  $DM_{\text{host}}$  corresponds to a source located in the disk of a MW-like galaxy at a median inclination angle,  $i$ , to the plane of the sky ( $i = 60^\circ$ ). Because the source and host are located at significant redshift,  $z$ , then the radio frequencies,  $\nu$ , in the rest frame of the host would be higher by a factor of  $(1 + z)$ . Because dispersive delay  $\delta t \propto DM\nu^{-2}$ , redshifted host contributions make a relatively smaller contribution, as the redshift increases, to the total dispersive delay across the observing band (see Chapter 5 and Section 6.3 for more information). For instance, for a significantly redshifted source,  $DM_{\text{Host}} > DM_{\text{obs}}$  is not impossible.

## 6.2.2 Burst profile

In order to measure a burst profile the dispersion delays between frequency channels are corrected for. This corresponds to ensuring that the burst appears to arrive in all channels simultaneously. Having corrected for these delays the channels are either all averaged together, or averaged into groups to form a number of subbands. In the case of FBR 121002 it appears that the burst profile is more complex than a single peak; it appears to have some distinct structure (see Figure 6.1).

In order to quantify this, I fit one and two Gaussian shapes to the profile data via a least-squares fitting routine to optimise the model parameters. Each Gaussian burst shape was described by a height, width, and centroid position, all of which were allowed to vary simultaneously (for both Gaussians in the double case). The reduced- $\chi^2$  for a fitted single Gaussian is  $\chi_{\text{red}}^2 = 1.99$  (see Figure 6.1). For a fit comprising two independent, simultaneously fitted Gaussians then  $\chi_{\text{red}}^2 = 1.37$ . This indicates that the measured burst profile data is significantly better modelled by two independent Gaussian profiles than by just one (see Figure 6.1).

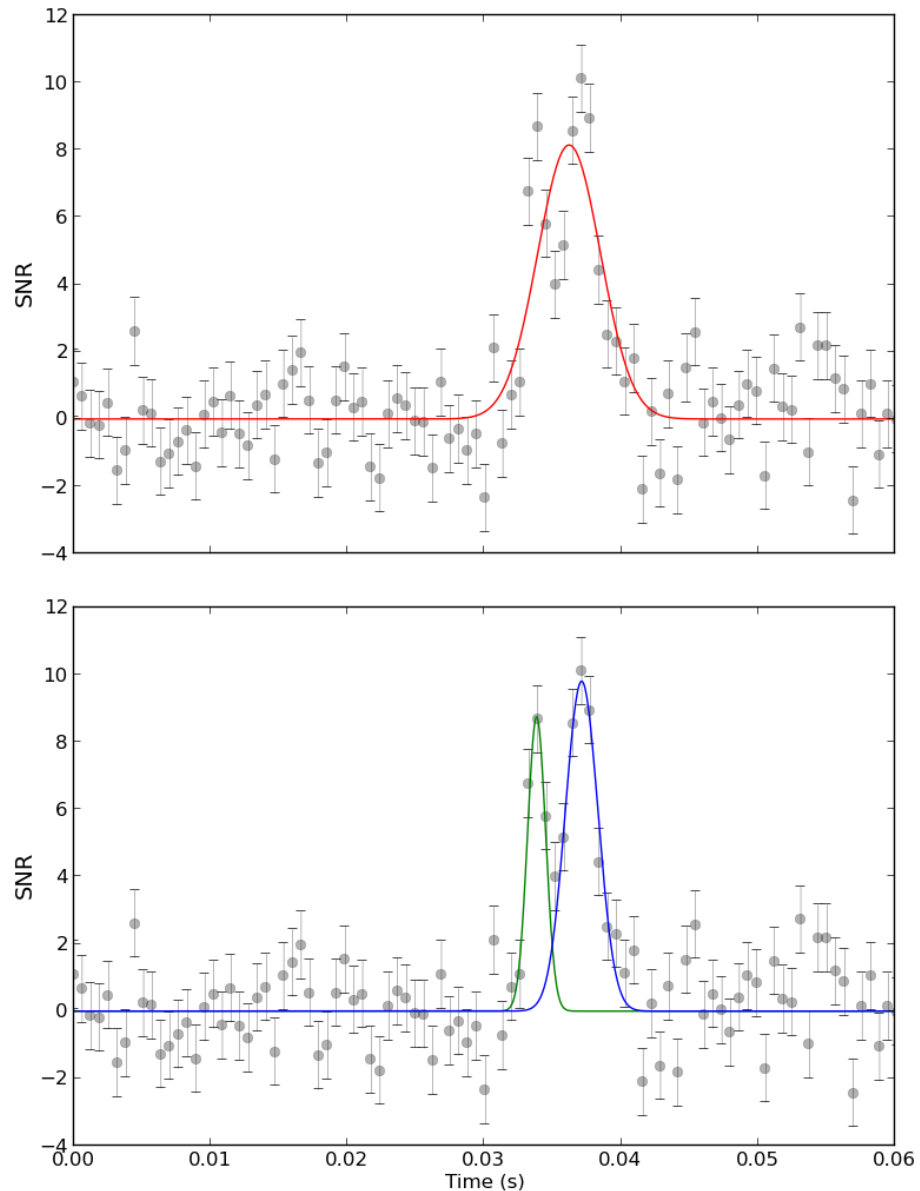


**Figure 6.1** – Single (top) and double (bottom) Gaussian components fitted to the fully frequency-averaged burst profile of FRB 121002 (points). The single Gaussian fit is shown by a red line; in the double Gaussian fit both components are shown, the leading component A (green) and the trailing component B (blue). Groups of 10 consecutive time samples of the raw data have been averaged in order to increase the SNR (giving a sampling time,  $t_{\text{samp}} = 640 \mu\text{s}$ ).

In the fit comprising two Gaussian components the parameters of the fit indicate that the

separation of the peaks of components A and B is  $\Delta = 5.1 \pm 0.4$  ms (see Figure 6.1). There are two possible interpretations of this result: either components A and B were emitted from the same location at different times; or they they were emitted from two different locations. In the former case the time between emission would be  $t_{\text{sep}} = (1 + z)^{-1} \Delta = 2.1$  ms (at  $z = 1.45$ ). Or, in the latter case the line-of-sight separation of the emission regions for components A and B would be  $d_{\text{sep}} = c(1 + z)^{-1} \Delta = 630$  km, also for  $z = 1.45$ . The factors of  $(1 + z)^{-1}$  are due to cosmological time-dilation: time periods in the rest frame of the source are a factor  $(1 + z)^{-1}$  shorter at the source than they are observed to be.

In the case of two emission events at different times,  $t_{\text{sep}}$  would be consistent with upper limits of intrinsic FRB widths  $\lesssim 2$  ms; as are the widths of both components. Because scattering and dispersive effects would affect the two components in identical ways,  $t_{\text{sep}}$  is a real timescale of emission at the source. The two peaks may either come from a single event, which has two emission stages or regions, or from two, non-cataclysmic events at a single source.

FRB 121002 is of sufficiently high SNR that it can be detected in a number of subbands. By splitting the band into four equal subbands the behaviour of the profile with frequency can be investigated. To do this the Gaussian profile components A and B were fitted to the data from each subband (see Figure 6.2).

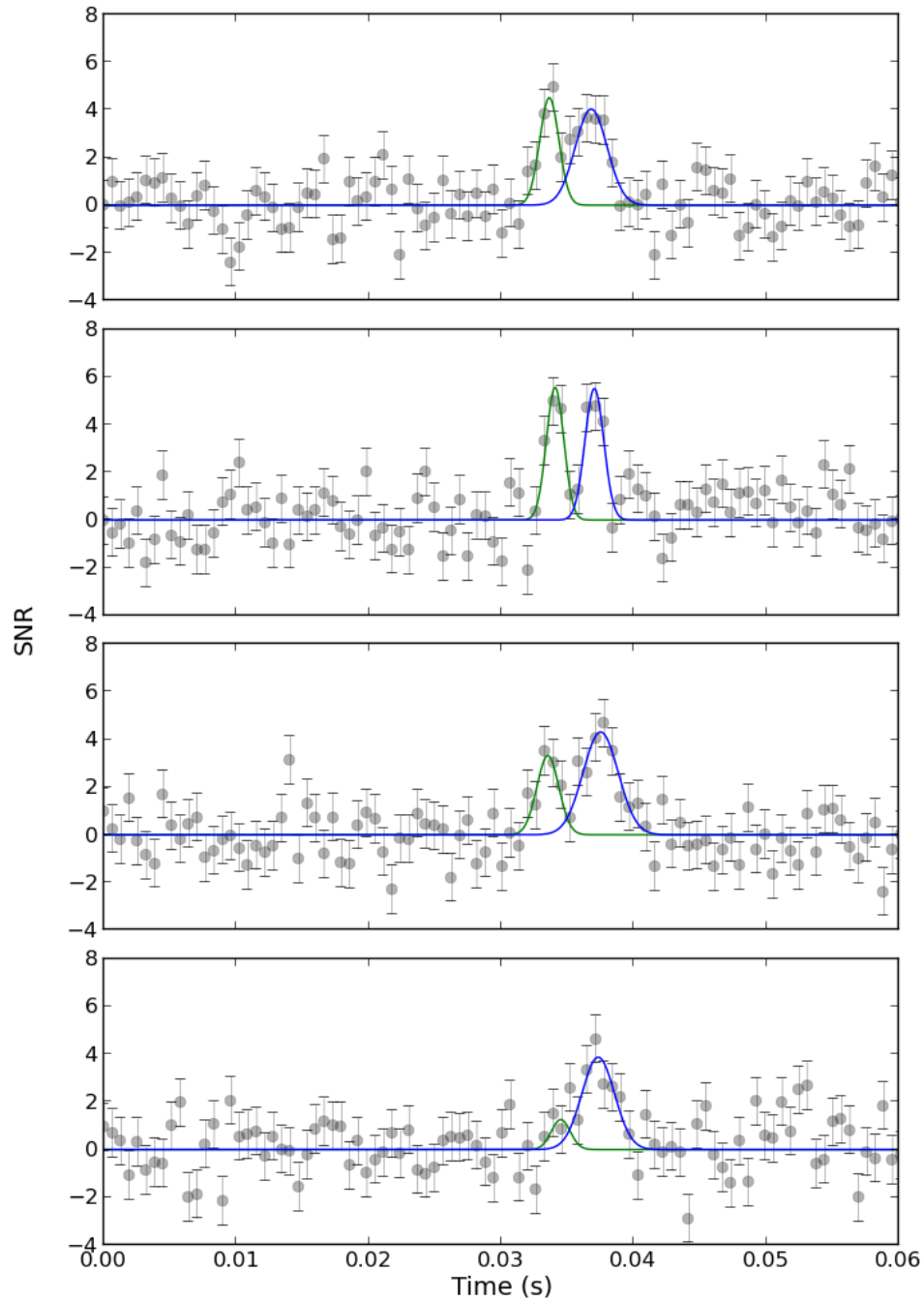


**Figure 6.2** – Four equal sub-bands of the observing band are shown. The central frequencies of the sub-bands are 1480, 1395, 1310, and 1225 MHz from top to bottom respectively. Each has been fit independently with two Gaussian components (A: green line, B: blue line; see Figure 6.1). The data has been temporally downsampled by a factor of 10 (resolution = 640  $\mu$ secs) in order to increase the SNR whilst retaining visibility of the two peaks. In the lowest frequency subband component A has not been significantly detected.

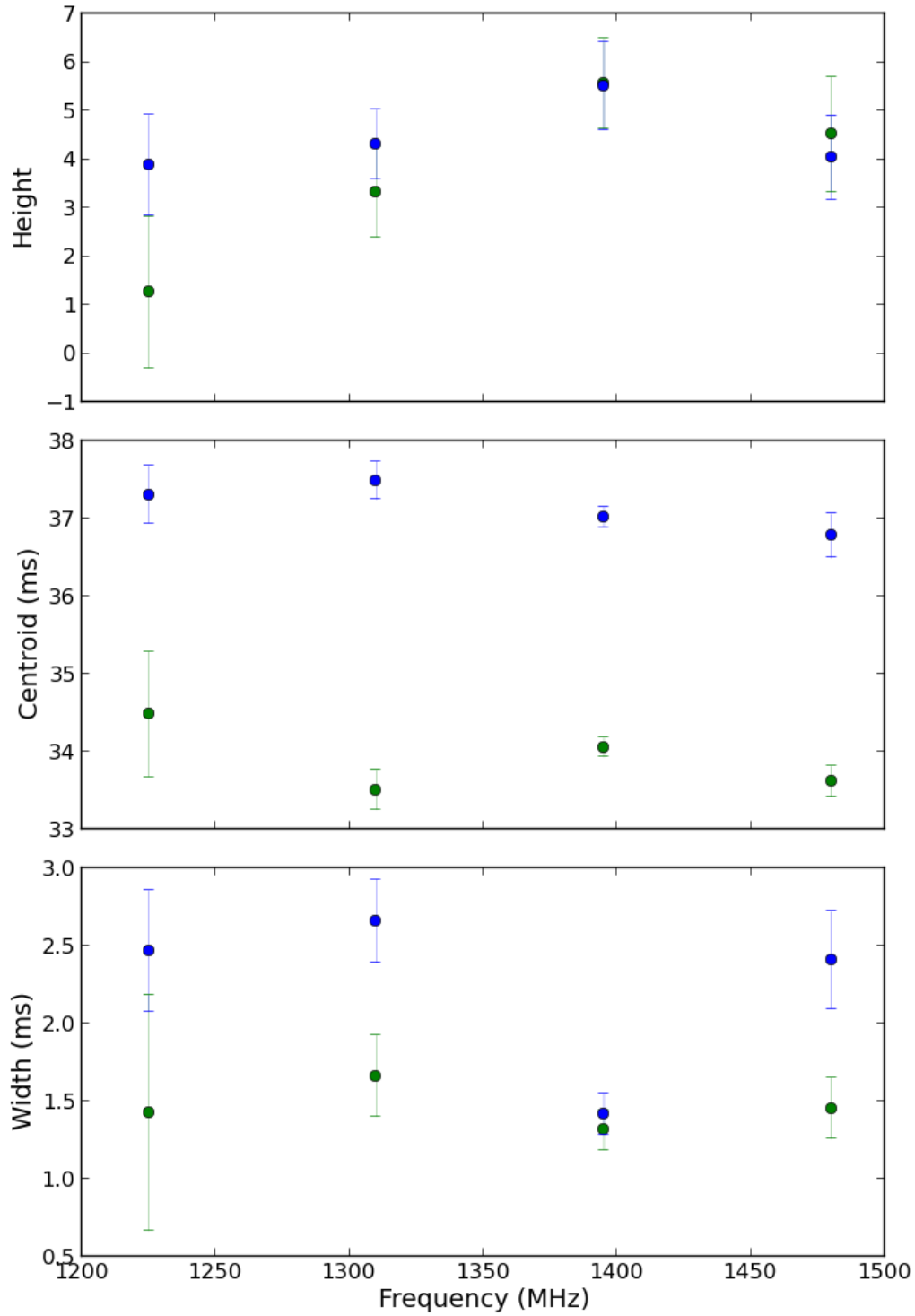


**Figure 6.3** – The frequency dependence of the parameters describing Gaussian-shape components A (green) and B (blue) (see Figure 6.1). The top panel shows the height of the Gaussians in arbitrary units; the middle panel shows the centroid on the scale of Figure 6.1; and the lower panel shows the half-height width.

---

From Figure 6.3 it is clear that there are no significant trends in the behaviour of the components across the band. Measurement of pulse profiles across observing bands similar to the HTRU band is difficult even for bright pulsars (T. Hassall, *private communication*) and to measure profile evolution usually requires multi-band observations. In addition, the low SNR of the profiles in each sub-band makes the detection of variation in the fitted Gaussian components extremely difficult. Measurement of higher-SNR FRBs exhibiting burst structure and detected across wider bandwidths should enable the measurement of any trends in the magnitude, width, and relative separation of substructure components.

## 6.3 An FRB population simulation

In order to gain some understanding of how many FRBs it may be possible to detect, and their DM and redshift distributions the sources and their detection can be simulated. The method is to simulate FRBs which are distributed through the universe to a maximum redshift,  $z_{\max}$ . The luminosity of each burst is calculated based on a redshift corrected energy of the known FRB cases. Each source therefore has a known redshift and luminosity. From this, the detectability of each FRB for a given observing setup is calculated.

FRB sources are thought to be located at cosmological distances because of their anomalously large DM measurements. There are several contributions to the dispersive delay which are quantified by the observed DM in the observing band. Each of these contributions are considered and included in the simulation.

We consider here the simulations for the detectability of FRBs by the HTRU survey. This is so we can compare the current rate of detection with model predictions. The rate of sources in the mid-latitude HTRU survey is also considered to illustrate how the Galactic plane may affect detectability, and to understand the lack of detections in the direction of the Galactic plane where many previous pulsar surveys with the spectral and temporal resolution necessary to detect FRBs have observed.

### 6.3.1 Spatial distribution

The measured rate of FRBs across the sky with fluences,  $F \sim 3 \text{ Jy ms}$ , is  $R_{\text{FRB}}(F \sim 3 \text{ Jy ms}) = 1.0 \times 10^4 \text{ sky}^{-1} \text{ day}^{-1}$  for sources located within redshift,  $z \lesssim 1$  (see Chapter 5). The inferred rate for the significantly higher fluence FRB 010724 is  $R_{\text{FRB}}(F \sim 150 \text{ Jy ms}) = 225 \text{ sky}^{-1} \text{ day}^{-1}$ . While the uncertainties on these inferred rates are significant, particularly for FRB 010724, it appears that  $R_{\text{FRB}} \propto F^{-3/2}$ , indicative of a source population with constant number density per unit co-moving volume, and with a luminosity distribution which is not a function of redshift (see Chapter 5). I therefore simulate a population of sources with a constant number density per unit co-moving volume. The number of sources within redshift,  $z$  is therefore

$$N(z) = N_0(1+z)^3, \quad (6.1)$$

where  $N_0 = 37.1 \text{ Gpc}^{-1}$  is the density of sources in the local universe ( $z = 0$ ). To convert to a rate,  $R(< z)$ , a further factor of  $(1 + z)$  is included to account for cosmological time dilation: that is, for a redshifted group of sources the time between FRBs appears to be shorter and consequently the rate is higher.  $R(< z)$  is therefore given by

$$R(z) = R_0(1 + z)^4, \quad (6.2)$$

where  $R_0$  is the local rate of FRBs. In order to calculate  $R_0$ , Equation 6.2 is integrated up to  $z = 1$ , and equated to  $R_{\text{FRB}}$ . Equation 6.2 is then used to calculate the rate of sources per co-moving density element as a function of redshift. A source population is then generated such that the redshift values are distributed according to Equation 6.2. While the measured rate is for  $z \leq 1$ , the distribution may be extrapolated to higher redshifts. With the assumptions discussed above, this simulation is extended to  $z_{\text{max}} = 2$ . I chose this value for  $z_{\text{max}}$  in order that FRBs with  $\text{DM}_{\text{obs}} > \text{DM}_{\text{max}}$  are generated, where  $\text{DM}_{\text{max}} = 2000 \text{ cm}^{-3} \text{ pc}$  is used because it is currently the maximum test value for dedispersion in the HTRU high-latitude survey. The simulation consists of 1 day's FRBs in the universe with  $z \leq 2$ , this corresponds to approximately 50000 FRBs.

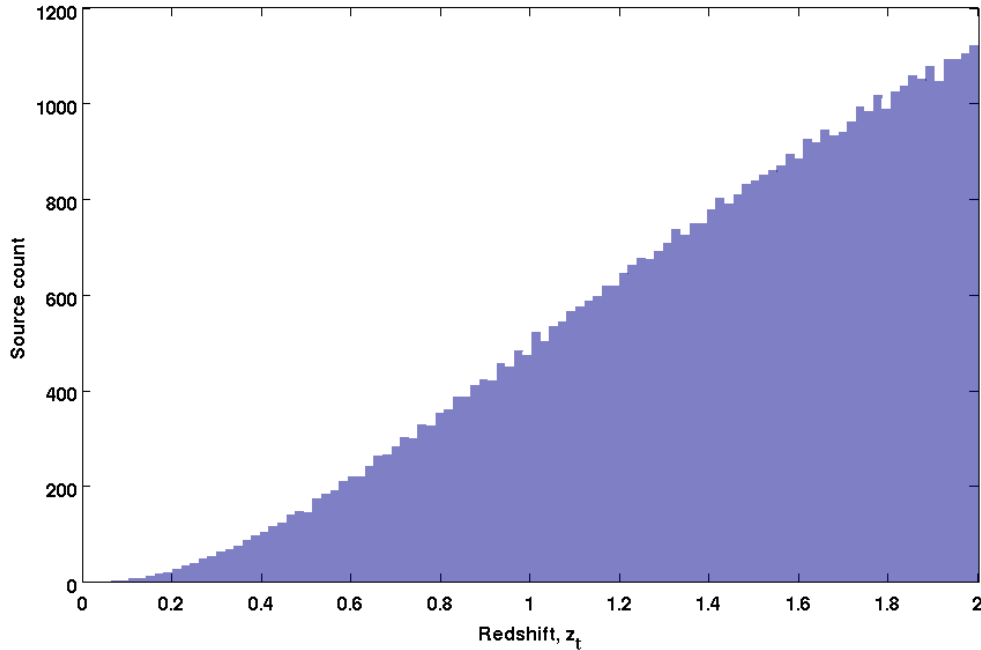


**Figure 6.4** – A histogram of the true redshifts (the redshifts assigned to the sources),  $z_t$ , for one days worth of FRBs. Note that this number of FRBs is the number that arrive at the Earth in a single day; a telescope has a relatively small field of view, and consequently could never detect them all.

### 6.3.2 Dispersive delay contributions

There are multiple contributions to the observed dispersive delay for an FRB; these include the ionised ISM in the MW foreground, the ionised IGM, any ionised material in a host galaxy, and a possible intervening galaxy along the line of sight. The probability of an intervening galaxy for a source at  $z = 1$  is thought to be 0.05 (Roeder & Verreault, 1969); this possibility is not included in this simulation.

#### The Milky Way contribution

The ionised material distribution in the Milky Way has been quite well measured using pulsar DMs and distances, among other methods. These measurements have enabled the development of a model of ionised material in the ISM (the NE2001 model; Cordes & Lazio 2002). This model can be used to infer the maximum DM,  $DM_{MW}$ , that may be imparted to a signal coming from beyond the MW.  $DM_{MW}$  is strongly dependent on direction through

the Galaxy, which can be described by a source's Galactic latitude and longitude ( $l, b$ ). Each FRB in the simulation is assigned a random  $l$  and  $b$ , which then dictates  $DM_{\text{MW}}$ ; resulting in the following range,  $19 < DM_{\text{MW}} < 1680 \text{ cm}^{-3} \text{ pc}$ .

### A host contribution

If the sources are located in host disk galaxies similar to the MW then the underlying distribution of ionised material for the MW, which defines the large scale behaviour of the NE2001 model, can be used to infer the  $DM_{\text{Host}}$  which may be expected. The thin and thick disk components of ionised material used in the NE2001 model are used to calculate  $DM_{\text{Host}}$  for a source located in the disk, viewed from outside the galaxy. The simulation assumes that the disk of the host galaxy is circularly symmetric and as such  $DM_{\text{Host}}$  only depends on the viewing angle,  $i$ . This angle is measured relative to the plane of the sky; so a disk galaxy viewed edge-on has  $i = 90^\circ$ . A host galaxy viewed edge-on therefore corresponds to the largest possible  $DM_{\text{Host}}$  contribution, when the observer sees the source through the most ionised disk material.

Of course it is possible that FRBs may be located in other host types, with differing  $DM_{\text{Host}}$  values to those of MW-type galaxies. Extremely low values of  $DM_{\text{Host}}$  are a behaviour which is replicated by the MW model for host galaxies. Very high values of  $DM_{\text{Host}}$  can result in a overestimation of redshift (see Section 6.3.10), although this becomes increasingly less important for sources at higher redshifts. FRB 010724 also provides an upper limit for any DM that may always be present in a FRB, with a measured value of  $DM_{\text{Host}}$  with  $DM_{\text{obs}} = 375 \text{ cm}^{-3} \text{ pc}$ .

While the orientations of disk galaxies is of course random in space, the probability of a given galaxy being viewed at an angle  $i$  is given by  $P = (1 - \cos(i))$ . Each FRB in the simulation is therefore assigned an inclination such that the values of  $P$  are evenly and randomly distributed between 0 and 1. This effectively means that host disk galaxies are more likely to be viewed at higher inclinations; the median inclination angle  $i_m = 60^\circ$ .

Because the electromagnetic radiation of sources located at a significant redshift are at higher frequency, the contribution to the dispersive delay,  $\delta t$ , from  $DM_{\text{Host}}$  falls with redshift ( $\delta t \propto \nu^{-2}$ ). This means that host galaxies make an increasingly small contribution to  $DM_{\text{obs}}$  with increasing redshift.

### The IGM contribution

In the case of the simulation the true redshift,  $z_t$ , of each source is known. This means that the dispersive delay contribution due to ionised material in the IGM can be calculated for each source. The ionised IGM is modelled in the same way as described in Chapter 5, which in turn is derived from Ioka (2003) and Inoue (2004). The effective frequency of the radio waves which will eventually be detected in the observing band of the telescope is higher at higher redshifts, and because the dispersive delays are imparted to the burst over a range of redshifts from the source to the observer, the delay caused by the IGM is an integrated effect.

### 6.3.3 Luminosity

The energy emitted during an FRB within the redshift corrected HTRU observing bandwidth is calculated for the known FRBs to be between  $10^{31} - 10^{33}$  J. With the unknown position of the known FRBs within the beam gain pattern of the telescope there is considerable uncertainty in the true flux density and therefore the inferred luminosity. The nominal value for the energy emitted in the radio by an FRB in the simulation is  $10^{32}$  J, which is then emitted over an intrinsic pulse width,  $W_{\text{int}} = 0.002$  s, for each simulated FRB. This value is assuming a beaming angle of 1 steradian, of course if the emission is not beamed the energy emitted would be  $4\pi$  times larger. The intrinsic luminosity makes a difference to the most distant FRBs which can be detected, it does not however change the underlying behaviour of the simulation or conclusions.  $W_{\text{int}}$  is an approximate value based on the limits on the intrinsic widths of known FRBs (see Chapter 5).

For each source  $z_t$  is known, so the frequency band of the emission is known. Sources at high redshift must be emitting in a band which is of higher frequency (and wider) than the observing band of the telescope in order to be detected in the HTRU observing band. This effectively means that a high redshift source will have higher or lower flux density at the telescope depending on the intrinsic spectrum of FRBs. In the case of the simulation this is described by a power law quantified by a spectral index,  $\gamma$ , such that the intrinsic flux density,  $S \propto \nu^\gamma$ . For  $\gamma < 0$  the measured flux density will fall with redshift, and vice-versa for  $\gamma > 0$ . An important consequence of  $\gamma \neq 0$  would be that distant sources would have either higher or lower flux densities at the Earth according to the sign of  $\gamma$ ; this would of course affect detectability.

The true spectral index of FRBs is not well constrained, predominantly because of the unknown position of known FRBs within the gain pattern of the telescope. Because this gain pattern is wider for lower frequencies, an off-axis position can alter the apparent spectral index considerably (Burke-Spolaor et al., 2011a). Burke-Spolaor et al. quantify this effect and find that FRB 010724 has an intrinsic spectral index of  $-2.5 \lesssim \gamma \lesssim -0.6$ . This calculation is possible for FRB 010724 because it was detected in three adjacent beams of the multibeam receiver, thus its true sky position and position in the gain pattern can be constrained. The simulation described below is performed with  $\gamma = 0$ , however in Section 6.3.9 I investigate how  $\gamma < 0$  would affect the results. This redshift dependence of the emission band for an FRB means that by observing FRBs at different redshifts we are effectively measuring different regions of the intrinsic spectrum. Consequently it may be possible to measure the intrinsic spectrum of FRBs without knowing the position of the FRBs in the telescope gain pattern. To be able to do this with any accuracy however will require the detection of a statistically significant number of FRBs.

### 6.3.4 Burst broadening effects

A broadened pulse has a reduced peak flux density, and consequently has a lower SNR in an observation and is more difficult to detect. The observed width,  $W_{\text{obs}}$ , of a burst is not simply the intrinsic width,  $W_{\text{int}}$ : there are multiple effects which may broaden a pulse in time. Scattering of the radio waves by turbulent ionised material along the line of sight to the source will broaden the burst. Scattering causes the radio waves to take slightly differing (longer) paths to the observer. Some of the burst energy is therefore delayed relative to the first radio waves to arrive at the telescope (those which have taken a straight line path from source to the telescope) and the burst profile is broadened. The empirical relation of Bhat et al. (2004) between DM and the magnitude of scatter-broadening for pulsars in the MW predicts a very large amount of scattering for high DMs. This would then spread a burst to be wider than any of the matched filters, making detection difficult.

It is apparent from Figure 6.5 that if the scattering relation of Bhat et al. was applicable to the IGM then it would have prevented the detection of known FRBs. Consequently it seems highly unlikely that the IGM follows this scattering relationship. For this reason scattering is not applied in this simulation.

There are also unavoidable instrumental effects which can broaden a pulse. The data capture hardware has a finite sampling time,  $t_{\text{samp}}$ ; consequently a burst which is narrower

than  $t_{\text{samp}}$  would at least be broadened to this width. This is however a small effect when compared to smearing by dispersive delays, some of which are uncorrectable in filterbank data. The first of these is the delay within a frequency channel (see Section 2.3.9),  $W_{\text{DM}} \propto \text{DM}$ , this is therefore detrimental to the detectability of high-DM bursts. In the HTRU survey the test values of dispersion measure,  $\text{DM}_{\text{test}}$ , are not evenly spaced between  $0 < \text{DM}_{\text{test}} < \text{DM}_{\text{max}}$ , and the spacing increases for higher  $\text{DM}_{\text{test}}$  values. This means there is residual dispersive smearing in the dedispersed time-series, this may be corrected in pulses which are detected in order to measure the best DM, but reduces the detectability of high-DM pulses in the time-series during searching.

The final effect is a broadening due to cosmological time dilation. A burst from a source at redshift  $z$  will appear a factor of  $(1 + z)$  times broader at the observer than it was at the source.

### 6.3.5 Detectability

In order to calculate the SNR a burst would be detected at in the HTRU survey, the peak flux density  $S_{\text{peak}}$  and  $W_{\text{obs}}$  must both be determined. Because  $z_t$  of each source is known, the luminosity distance,  $D_L$ , can be calculated (for a  $\Lambda$ CDM model of universal expansion). This is the distance measure which is used to determine flux densities of redshifted sources where  $S_{\text{peak}} \propto D_L^{-2}$ . Note that the SNR of a burst increases linearly with intrinsic luminosity. By increasing this luminosity more distant sources are detectable and vice-versa.

With  $S_{\text{peak}}$  and  $W_{\text{obs}}$ , determining the SNR of the burst in the time-series with  $\text{DM}_{\text{test}}$  closest to the true DM of the source is possible using the radiometer equation (see Section 2.3.9). This SNR can be further refined by calculating the SNR of the burst when a range of box-car matched filters are applied. The widths of the filters are  $W_{\text{filt}} = t_{\text{samp}} 2^n$  where  $0 \leq n \leq 9$  (as is currently performed in the HTRU single pulse search). For  $W_{\text{obs}}$  which fall in the range of  $W_{\text{filt}}$  the burst SNR is increased. The SNR for a given burst in the simulation is the maximum attainable given the limited boxcar filter widths.

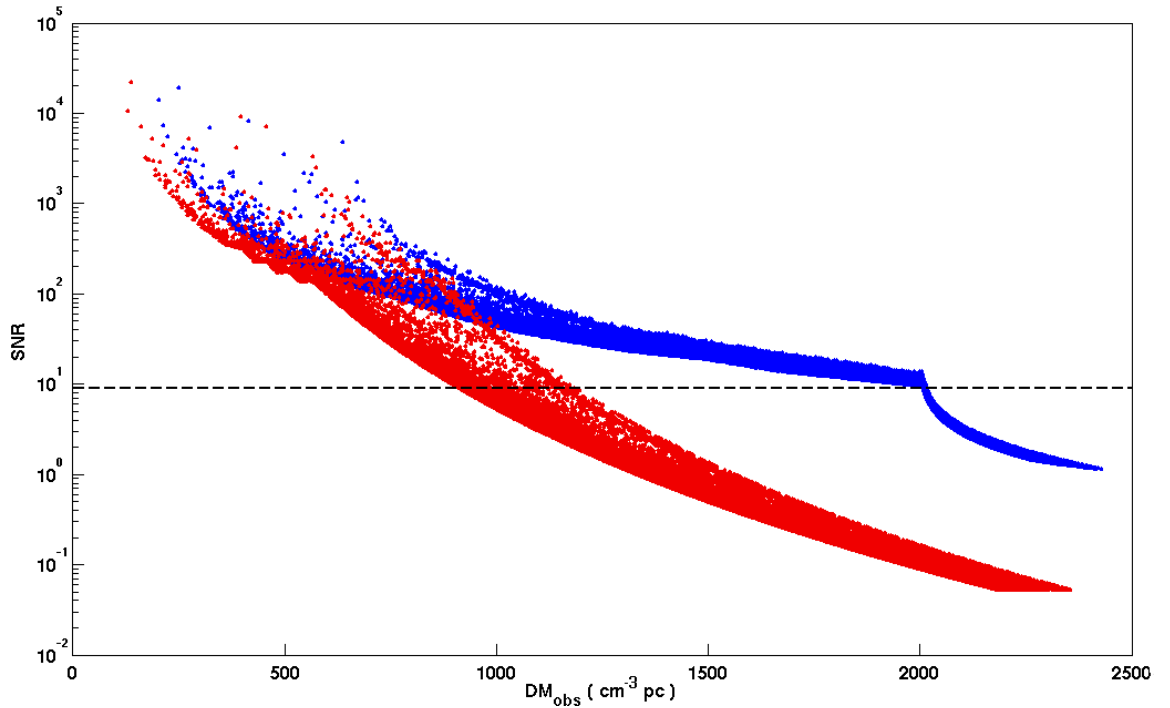


**Figure 6.5** – The simulated FRBs  $W_{\text{obs}}$  against  $DM_{\text{obs}}$  for FRBs with (red) and without (blue) scattering taken into account. The dotted black line indicates a limiting  $\text{SNR} = 9$ . Those FRBs with  $\text{SNR} < 9$  and  $DM_{\text{obs}} < 2000 \text{ cm}^{-3} \text{ pc}$  would be undetectable in the current HTRU search pipeline.

### 6.3.6 HTRU detectability and the Galactic plane

The current implementation of the HTRU high-latitude single pulse search filters out FRBs with  $\text{SNR} < 9$ . FRBs with  $DM_{\text{obs}} > 2000 \text{ cm}^{-3} \text{ pc}$  are unlikely to be detectable as they exceed  $DM_{\text{max}}$  and the difference between  $DM_{\text{test}}$  and  $DM_{\text{obs}}$  broadens the bursts significantly (see Figure 6.5). These same filtering criteria are applied to the bursts in the simulation. This filtering process indicates around 30% of the FRBs in the simulation would be undetectable by the Parkes HTRU survey hardware using current single pulse search parameters. For the assumed FRB luminosity there are FRBs detectable across the full range of  $DM_{\text{test}}$  in the no-scattering case (see Figure 6.5). All further simulations are carried out with no scattering applied to the FRBs.

### 6.3.7 The effect of the Galactic plane

To illustrate the effect of the Galactic plane the filtered FRBs are split in to two groups, those with  $|b| < 15^\circ$  and those with  $|b| > 15^\circ$ . The rate of detectable FRBs in the  $|b| > 15^\circ$  region,  $R(|b| > 15^\circ) \approx 1 \text{ deg}^{-2} \text{ day}^{-1}$  whereas in the  $|b| < 15^\circ$  the rate is  $R(|b| < 15^\circ) \approx 0.5 \text{ deg}^{-2} \text{ day}^{-1}$  (see Figure 6.6).

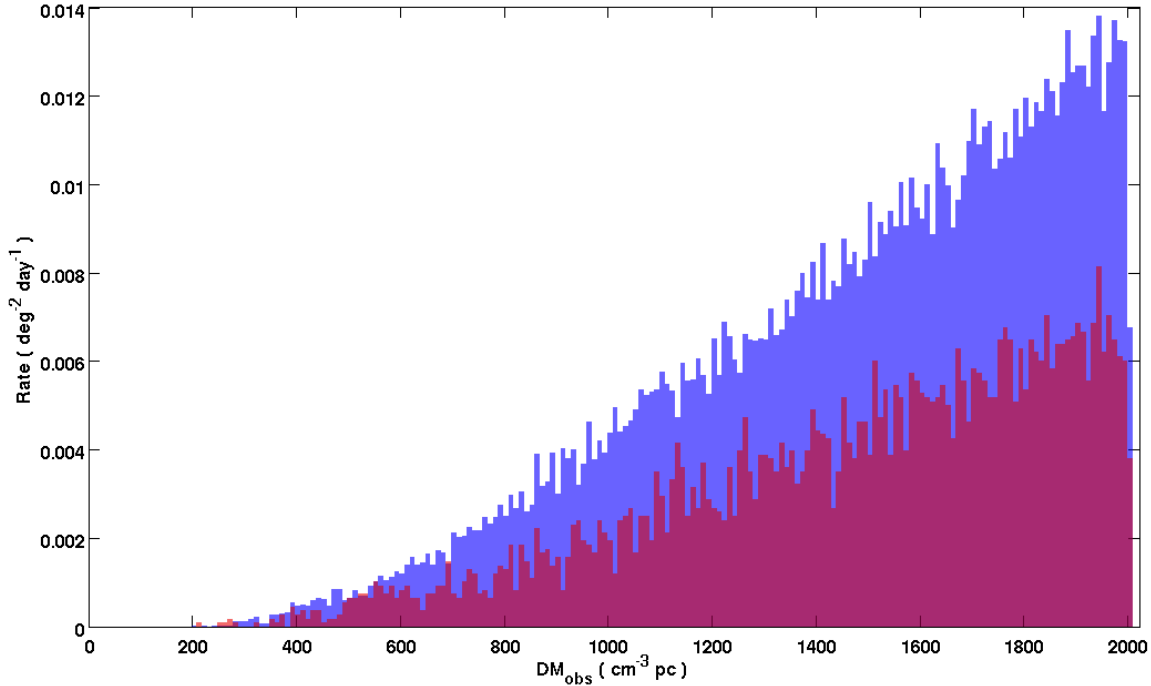


**Figure 6.6** – The FRB rate for  $DM_{\text{obs}}$  are shown for sources with  $|b| < 15^\circ$  (red) and  $|b| > 15^\circ$  (blue).

This discrepancy between FRB rates for the regions close to the Galactic plane when compared to high-latitude regions can be attributed to the dispersive effect of the MW foreground. For many FRBs which would otherwise be detected in the  $|b| < 15^\circ$  region this extra dispersion from the MW foreground means the  $DM_{\text{obs}} > 2000 \text{ cm}^{-3} \text{ pc}$  and the FRB is therefore undetectable. This may partially explain the lack of detections in previous pulsar surveys, which have often had survey regions centred on the Galactic plane (e.g. Manchester et al. 2001).

This means that the prediction for the number of FRBs in the HTRU medium latitude survey (from Chapter 5) may be somewhat overestimated (which covers a region with  $|b| < 15^\circ$ ). A revised prediction for the number of FRBs from  $z < 1$ , based on the detrimental

affect of the Galactic plane described above, is  $4_{-3}^{+4}$ , and  $6_{-5}^{+6}$  for the HTRU medium latitude survey and PMPS surveys respectively (compared to original predictions of  $7_{-3}^{+4}$ , and  $12_{-5}^{+6}$ ).

### 6.3.8 The simulation and the known FRB sample

With just five known FRBs in the HTRU high-latitude survey, the uncertainties on the rate are dominated by small number statistics and are consequently large. By comparing the known FRBs to the distributions generated in the simulation it is possible to begin to understand the underlying source distribution (see Figure 6.7).

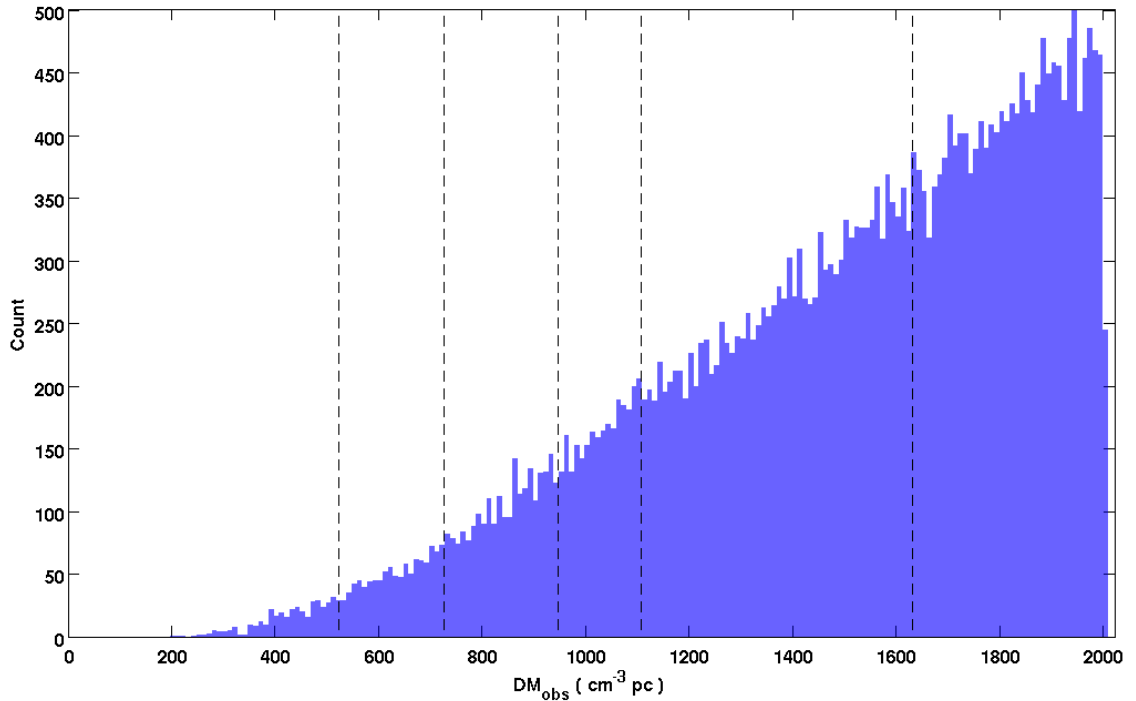


**Figure 6.7** – A histogram of  $DM_{\text{obs}}$  for detectable sources is shown for sources (blue).  $DM_{\text{obs}}$  for the five known FRBs from the HTRU survey are also shown (black dashed lines).

In order to understand if the five known FRBs are consistent with being drawn from the distribution of detectable sources shown in Figure 6.7 groups of five FRBs were randomly selected (from those detectable with  $|b| > 15^\circ$ ) and their mean DM,  $\overline{DM}_{\text{obs}}$ , was calculated. This was repeated for 10000 sets of five FRBs. The distribution of  $\overline{DM}_{\text{obs}}$  then indicates the expected value for a randomly selected group of five FRBs. The known FRBs from the HTRU survey have a  $\overline{DM}_{\text{obs, known}} = 983 \text{ cm}^{-3} \text{ pc}$  and a standard deviation of  $422 \text{ cm}^{-3} \text{ pc}$ . By comparing the distribution of  $\overline{DM}_{\text{obs}}$  from the simulation and  $\overline{DM}_{\text{obs, known}}$  it is possible

to see if the known FRBs are consistent with coming from the simulated population (see Figure 6.8).

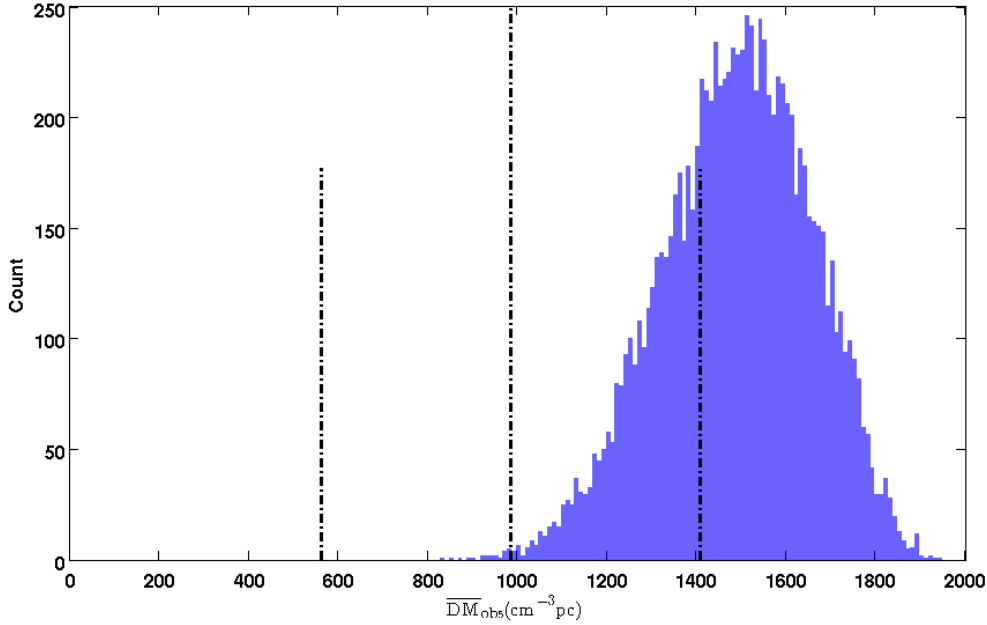


**Figure 6.8** – A histogram of  $\overline{DM}_{\text{obs}}$  is shown for groups of five sources with  $|b| > 15^\circ$  (blue).  $\overline{DM}_{\text{obs, known}}$  is indicated by the central black dotted-dashed line, while the dotted-dashed lines indicate  $\pm$  one standard deviation from  $\overline{DM}_{\text{obs, known}}$ .

With only five known FRBs in the HTRU  $|b| > 15^\circ$  region the spread in values is wide. While the uncertainties on  $\overline{DM}_{\text{obs, known}}$  are large it is within one standard deviation of the simulated values. It therefore seems that  $\overline{DM}_{\text{obs, known}}$  is consistent with being drawn from the simulated distribution. With more measurements of FRBs  $\overline{DM}_{\text{obs, known}}$  will become more reliable.

### 6.3.9 The effect of $\gamma < 0$

The emission band for a high redshift source is at a higher frequency than a low redshift source. By detecting sources at a range of redshifts therefore we are measuring the luminosity of the sources in a range of emission bands. A negative spectral index means that the luminosity is lower for high-redshift sources. This corresponds to a lower flux density at the telescope and therefore high-redshift ( $\sim$  high-DM) sources are harder to detect. As a direct consequence the expected value for  $\overline{DM}_{\text{obs}}$  decreases with decreasing  $\gamma$ . This effect

means that the distribution of the DMs of FRBs can provide an indication of the intrinsic spectrum. Note that this method of determining  $\gamma$  does not depend on knowing the position of the FRB in the telescope gain pattern.

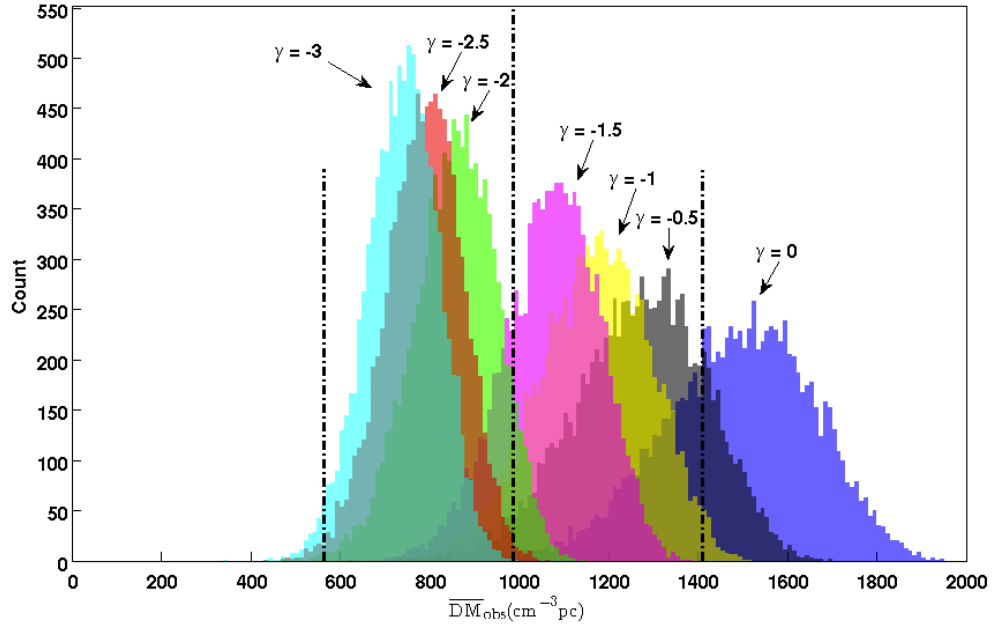


**Figure 6.9** – A histogram of  $\overline{DM}_{\text{obs}}$  is shown for groups of five sources with  $|b| > 15^\circ$ . Histograms are shown for  $\gamma = 0, -0.5, -1, -1.5, -2, -2.5,$  and  $-3$ .  $\overline{DM}_{\text{obs, known}}$  is indicated by the longer black dotted-dashed line, while the smaller dotted-dashed lines indicate  $\pm$  one standard deviation from  $\overline{DM}_{\text{obs, known}}$ .

With so few sources the DMs are widely spread, providing little indication of their true mean value. Consequently, no significant measurement of the intrinsic spectral index of FRBs can be made. All the values of  $\gamma$  shown in Figure 6.9 are consistent with the current DM measurements. If however the mean value of the five known FRBs is correct, then the measurements would indicate that FRBs have an intrinsic spectral index  $\gamma_{\text{int}} < 0$ , consistent with the measurements of FRB 010724; and  $-2 < \gamma_{\text{int}} < -1.5$  is apparently preferred.

### 6.3.10 Inferred redshift accuracy

For the known FRBs the redshift is inferred from the dispersive delay, and by assuming a host DM contribution from a MW-type host galaxy at a median inclination angle,  $i = 60^\circ$ . This is however an approximation as there is currently no way to know what the host

inclination angle or DM contribution may be. In the simulation however, both  $i$  and  $z_t$  are known, and the *implied* redshift,  $z_i$ , for a source located in a MW-type galaxy viewed at  $i = 60^\circ$  is calculated. This is the same calculation that was performed for the known FRBs to calculate the redshift values given in Chapter 5, and we can use the simulations to determine the accuracy of the inferred redshift by comparing the two redshifts,  $z_t$  and  $z_i$  (see Figure 6.10).

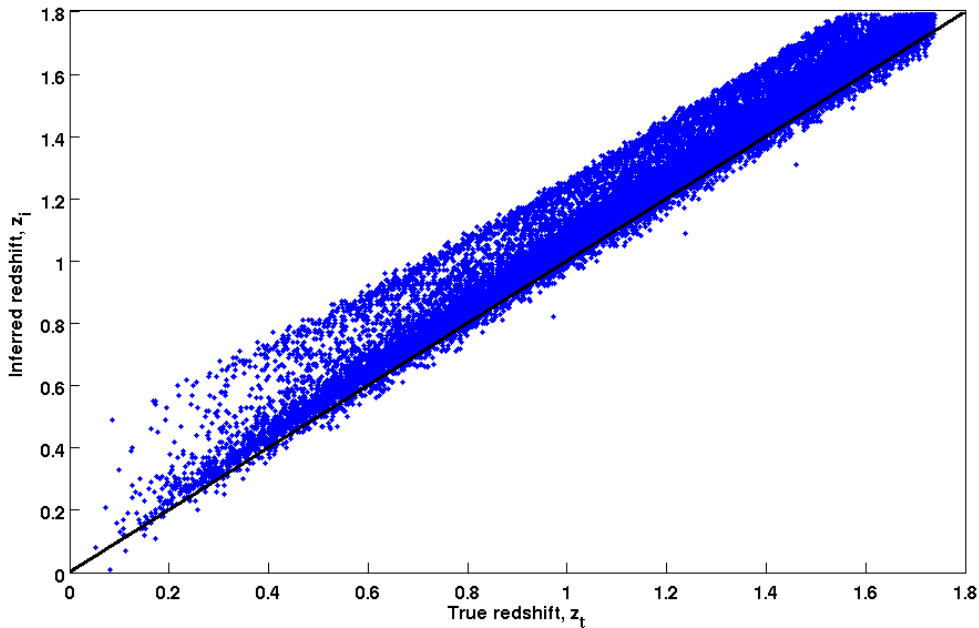


**Figure 6.10** – The inferred redshift of an FRB (for  $|b| > 15^\circ$ ) if it is assumed to be in a MW-like host galaxy viewed at a median inclination angle, as a function of true redshift,  $z_t$ . There is a strong positive correlation between the two values. The spread in values for  $z_i$  for a given  $z_t$  is due to the spread in  $DM_{\text{Host}}$  and  $DM_{\text{MW}}$  values. The black line indicates  $z_i = z_t$ .

Figure 6.10 shows that if the simulation is correct, then the inferred value of redshift is a good approximation to the true value. The distribution for a given value of  $z_t$  is however asymmetric. An overestimate of the redshift is more likely, with a representative standard deviation of  $\sigma_z = 0.15$ . As the redshift increases, the frequency of the radio waves that will be detected at the Earth at 1.4 GHz in the host galaxy also increases, this means that the host contribution to the total dispersive delays becomes less important. This is shown by the reducing spread in  $z_i$  values for increasing  $z_t$ .

In conclusion, firstly it seems that scattering can not have the same relationship to DM in the IGM as it does in the MW. If it did then it would have smeared out FRBs which have

already been detected. There is however measured scattering for two known FRBs. With scattering so important to the observed width of FRBs, it will be extremely important for the detectability of FRBs, particularly for low-frequency radio telescopes if  $W_{\text{scatt}} \propto \nu^{-4}$ .

The absolute luminosity will likely be difficult to measure with FRBs detected in an unknown location in a telescope's gain pattern. However I have shown that the intrinsic spectral slope of FRBs can be determined via detection of a statistically significant number of them, without having to measure spectral evolution across the observing band.

## 6.4 FRBs and SGR giant flares

### 6.4.1 SGRs, AXPs, and magnetars

There are two classes of magnetically-powered x-ray pulsar, the Anomalous X-ray Pulsar (AXP) and the Soft gamma repeater (SGR). The nomenclature of AXP and SGR is largely due to the method of discovery. SGRs were discovered via bursting behaviour in hard x-rays and gamma-rays (Mazets, Golenetskii & Gur'yan, 1979; Mazets et al., 1979), while AXPs were discovered via soft x-ray pulsations (e.g. Fahlman & Gregory 1981). From the timing of these pulsations the spin period,  $P$ , and its rate of change,  $\dot{P}$ , were measured and the surface magnetic field strength,  $B_{\text{surf}}$ , and the rate of energy loss due to the emission of magnetic dipole radiation,  $\dot{E}_{\text{dipole}}$ , calculated. This requires interpreting the pulsations as coming from a rotating dipole (see Chapter 1). The magnetic field strength is found to be extremely large ( $B_{\text{surf}} \sim 10^{14}$  G), several orders of magnitude higher than for typical pulsars (Duncan & Thompson, 1992) and the objects are now collectively called magnetars.

Under the assumption that the spin-down is dipole powered the calculated  $\dot{E}_{\text{dipole}}$  is too small in magnetars to account for the high-energy emission and there must be another energy source. The energy stored in the extremely high magnetic field of magnetars is thought to be responsible for the observed high-energy emission (Duncan & Thompson, 1992; Thompson & Duncan, 1996). A model in which magnetars are the underlying source of the high-energy emission was therefore developed to explain SGRs and AXPs (Thompson & Duncan, 1995; Thompson & Duncan, 1996).

While most SGRs and AXPs do not emit detectable pulsed radio emission, there are exceptions (Camilo et al., 2006; Levin et al., 2010). Where measured, this emission is pulsed similarly to pulsars, although there are many reasons to suggest that it is somewhat different from typical pulsar radio emission. The flux density of magnetar radio emission varies dramatically and apparently chaotically on timescales of around one day, not a characteristic for pulsars (when it is an intrinsic property of the pulsar not the pulse propagation). Magnetar pulse shapes also change on both long and short timescales (Camilo et al., 2007a; Kramer et al., 2007). The radio spectral index appears to be either flat or positive (Camilo et al., 2007b, 2008; Lazaridis et al., 2008; Levin et al., 2010), different from pulsars, which have a mean spectral index  $\alpha = -1.6$  (Lorimer et al., 1995b). The rate of spin-down of radio magnetars is also not constant (e.g. Thompson et al. 2000; Levin et al. 2010).

### 6.4.2 SGR giant flares

SGRs very occasionally emit bursts of gamma-rays; called *giant flares*. The initial gamma-ray burst usually lasts just a fraction of second, and is then followed by hard x-ray emission with power modulated at what is thought to be the spin period of the underlying neutron star (see Figure 6.11). There are several recorded cases of giant flares from three separate SGRs; SGR 0526–66 (Mazets et al., 1979), SGR 1806–20 (Hurley et al., 2005; Palmer et al., 2005), and SGR 1900+14 (Hurley et al., 1999).

A particularly well studied case is the brightest flare from SGR 1806–20 which was reported by the International Gamma-Ray Astrophysics Laboratory (INTEGRAL), on the 27th December 2004 (henceforth referred to as DEC04). It was also detected by the Reuven Ramaty High Energy Solar Spectroscopic Imager (RHESSI; Hurley et al. (2005), Swift (Palmer et al., 2005), and several other smaller instruments. The Burst Alert Telescope (BAT) instrument on the Swift satellite resolved the initial flare at gamma-ray energies at a temporal resolution of  $100\mu\text{secs}$ . With this resolution, the rise of the emission was apparent indicating the system is evolving significantly in just 1 ms.

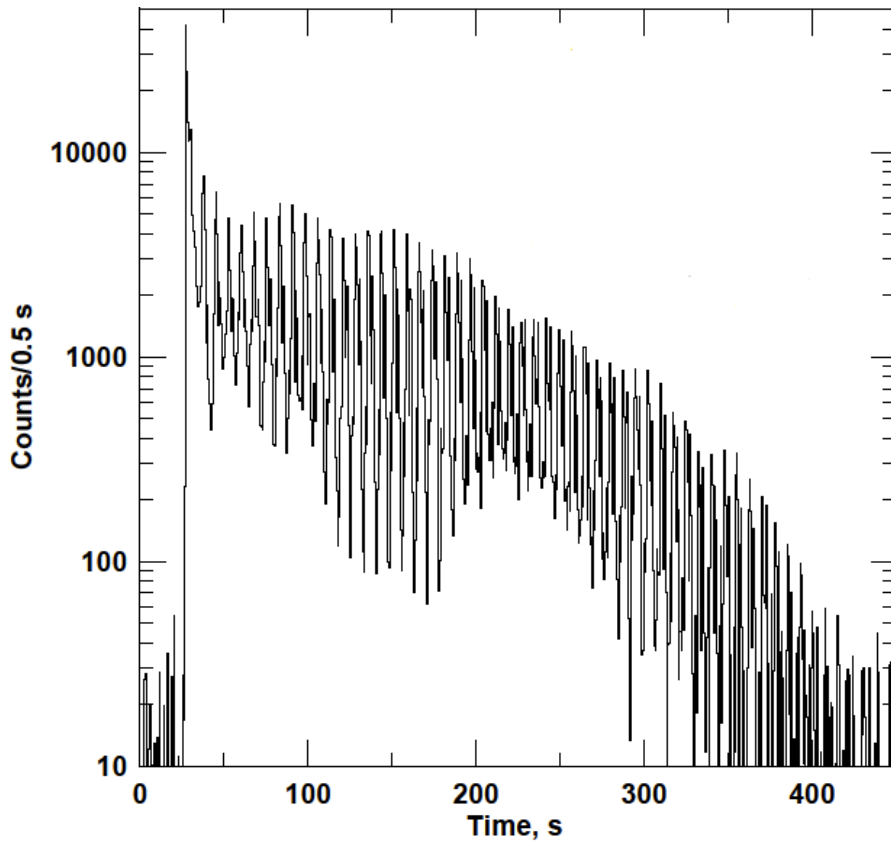


**Figure 6.11** – Gamma-ray counts are shown per 0.5 second sampling period during the DEC04 event. The flare began at 26.64 seconds and saturated the receiver in 1 millisecond. The spin period-modulated gamma-ray emission after the initial flare continues for  $\sim 400$  seconds. This is the gamma-ray emission as measured by the RHESSI satellite. Figure modified from Hurley et al. (2005).

### 6.4.3 Could FRBs be associated with SGR giant flares?

No associated emission from across the electromagnetic spectrum has been detected for the handful of known FRBs. Whilst there is no conclusive FRB-like radio emission associated with known SGR giant flares there are very tentative detections of radio bursts possibly associated with GRBs (Bannister et al., 2012). Supposing that FRBs *are* prompt radio emission from SGR giant flares that has not yet been observed, it is possible to investigate what we may expect to see. Prompt radio emission at 1.4 GHz would arrive  $2.1 \times \left( \frac{\text{DM}}{\text{cm}^{-3}\text{pc}} \right)$  ms after the high energy emission. Even for a DM of several thousand this is just a few seconds. It is therefore likely that, if it exists, FRB emission from a gamma-ray-detected giant flare has not yet been observed because no suitable radio telescope has been on source within this time.

The gamma-ray emission of a giant flare is formed of an initial spike, followed by intensity modulated emission for around 400 seconds (see Figure 6.11). The spin period of SGR 1806–20 is 7.5 s, so this corresponds to modulated emission detected by RHESSI for around 53 rotations of the magnetar. If an FRB corresponds to the initial spike in gamma-ray emission and the radio emission follows the same pattern indicated in the gamma-rays, then similar, weaker radio emission may follow, modulated at a typical magnetar rotation period. If this were the case then would it be possible to detect this modulated emission from the source after a giant flare event? Whilst this discussion supposes that radio emission from magnetars is similar in mechanism to pulsar emission it should be clear from Section 6.4.1 that there are significant differences in a lot of their properties, and could even switch on after periods of high-energy activity (Levin et al., 2010). The only radio emission from magnetars which has been studied in detail is seen well after the initial flare has occurred and the properties of this emission may be significantly different.

The gamma-ray flux during the DEC04 event fell by a factor of  $\frac{40000}{7500} = 5.3$  between the peak of the high-energy flare and the first subsequent intensity peak. Assuming that the radio flux, and therefore fluence, of an FRB fell by the same factor then the detected SNR would also fall by the same factor. With the detected FRB SNRs lying between 11 and 49 the SNRs of the first peak of the rotationally modulated emission would fall to between 2 and 9, these have not as yet been observed in inspection of the dedispersed time-series after the burst, however they lie at the edge of detectability. During the initial gamma-ray peak the receivers saturated and as such the ratio of gamma-ray flux between the initial and subsequent peak is considerably uncertain. The ratio could therefore be considerably higher than 5.3; indeed a ratio of 8.2 would result in a subsequent FRB peak with  $\text{SNR} < 6$  in the brightest FRB case which did not saturate the receiver. Any periodically modulation radio emission after the initial burst may be detectable via Fourier analysis, as discussed below.

For magnetars,  $\dot{E}_{\text{dipole}} \sim 10^{33} \text{ erg s}^{-1}$  and as discussed above it is insufficient to support the observed high-energy emission. As FRBs have an energy  $\sim 10^{30} - 10^{40}$  ergs released in, at most, a few milliseconds, the spin-down energy of a typical magnetar would also therefore be unable to account for the energy of an FRB.

It is possible however to measure pulsar-like spin parameters from the high-energy emission. Magnetars have typical spin-periods,  $P = 2 - 12$  secs and spin-down,  $\dot{P} \sim 10^{-11} - 10^{-10} \text{ s s}^{-1}$ . The spin-period can be used to calculate the largest radius at which the ionised plasma in the magnetosphere may co-rotate with the neutron star.

A light cylinder radius,  $R_{LC} = 1 \times 10^5 - 6 \times 10^6$  km, is calculated which defines the size of the co-rotating plasma around the magnetar. Because FRBs are from a coherent emission mechanism then the width at the source constrains the size of the emission region. With FRB widths,  $W = 1 - 6$  ms, the light cylinder radius,  $R_{LS}$  is 3 orders of magnitude larger than the FRB emission region ( $R_{LS} \sim 10^2 - 10^3$  km). Consequently the total magnetosphere can not be responsible and instead an FRB from a magnetar would originate from a sub-region. This is similar for pulsars, whose pulses imply an emission region much smaller than the light cylinder radius. For pulsars this region is located above the magnetic poles - the *polar cap*.

Pulsar pulse profile widths are often observed to decrease with observing frequency, indicating a larger emission region located further from the magnetic pole at lower frequencies. The last magnetic field line which closes within the light cylinder defines an opening angle of the (predominantly) dipolar field. This phenomenon is called *radius-to-frequency mapping*. An empirical relation between emission height and spin-period exists from which we may calculate the 10% opening angle of the beam in degrees,  $\rho$ , as

$$\rho = 5.4 \left( \frac{P}{\text{secs}} \right)^{-\frac{1}{2}} \text{ } ^\circ. \quad (6.3)$$

In turn it is possible to convert from  $\rho$  to emission height from the neutron star surface (Lorimer & Kramer, 2005),  $R_{em}$  as

$$\frac{R_{em}}{R_{LC}} = \left( \frac{\rho}{86^\circ} \right)^2. \quad (6.4)$$

Using Equation 6.4 and typical magnetar spin periods we can infer that the emission height is  $\frac{R_{em}}{R_{LC}} = 2 \times 10^{-3} - 2 \times 10^{-2}$ . This would mean that a typical emission height approximately agrees with FRB widths and their implied emission zone size.

If the polar cap of a magnetar was the source of FRBs then the radio emission region co-rotates with the magnetar, as the gamma- and x-ray emission appears to do. In order to see modulated radio emission following an FRB from a single source, radio emission must persist for multiple spin periods. With typical widths of  $\sim$  milliseconds and a typical magnetar spin-period of  $\sim$  seconds, then for each rotation the total energy released in the radio band would be  $\sim$  1000 times greater than for the single FRB.

The energy emitted in known SGR giant flares in x-rays and gamma-rays is between  $10^{44}$  and  $10^{46}$  ergs, with the energy in the modulated tail being around 1% of the total energy in the initial spike. The energy of the modulated tail of the DEC04 event was around  $\sim 10^{44}$  ergs and lasted around 400 seconds. To sustain FRB emission for one second appears to require  $\sim 10^{41} - 10^{43}$  ergs. Assuming that the total energy available for radio emission was of a similar magnitude then modulated emission may be sustainable for  $\sim 10^1 - 10^2$  spin periods if the radio luminosity was constant, if the radio luminosity fell, then modulated emission could persist for longer. If this were the case then it is possible that a Fourier analysis of the dedispersed time-series may detect pulsations with a period  $\sim$  seconds (magnetar-type spin periods). None of the known FRBs show a significant periodicity in the survey observations. The HTRU high-latitude survey observations are 270 s long, shorter than the detectable high-energy pulsations from the DEC04 event. The FRBs from the HTRU survey were also detected some time into the observation, particularly the brightest FRB 110220, which occurred 208 seconds into the observation. Both of these factors would reduce the detectability of emission modulated at a rotational period.

It is thought that SGR J1806–20 is located at a distance of 15 kpc based on its apparent association with a stellar cluster (Corbel & Eikenberry, 2004; Figer, Najarro & Kudritzki, 2004). Consequently, Hurley et al. (2005) estimate that a DEC04 event would be detected by the Swift BAT to a distance,  $D_{\text{Max}} = 70 \left( \frac{d_{\text{DEC04}}}{15 \text{ kpc}} \right)$  Mpc; corresponding to a redshift,  $z = 0.017$ . If, therefore, there was a gamma-ray signal similar to that of DEC04 associated with an FRB and the sources were located at a distance  $D > D_{\text{max}}$  it would not be detected by Swift.

Using the Swift observing logs we can determine the pointing direction of the BAT at the time of the FRBs. Only FRB 110627 was close, and was separated from the pointing direction of the BAT by  $\delta = 16.5^\circ$ , well within the approximately rectangular BAT Field Of View (FOV). The BAT is not equally sensitive to sources from all directions in its FOV; there is coding mask in front of the aperture which reduces the counts from sources in a off-axis direction. It is possible that  $\delta = 16.5^\circ$  would place the source in a "partially-coded" region, reducing absolute sensitivity slightly. If there were a DEC04 event associated with FRB 110627, however, then it is most likely that the source must be located at a distance  $D > 70$  Mpc.

Swift is sensitive to DEC04-type events within a volume of approximately  $1.4 \times 10^{-3} \text{ Gpc}^3$  around the Earth. With an FRB rate of  $R_{\text{FRB}} = 1.0 \times 10^4 \text{ sky}^{-1} \text{ day}^{-1}$  in a volume of  $\sim 150 \text{ Gpc}^3$  then the rate of FRBs with an associated, detectable DEC04 flare would be  $R_{\text{FRB/DEC04}} \sim 10^{-8} \text{ sky}^{-1} \text{ day}^{-1}$ . Consequently, this rate and the sensitivity of Swift to dis-

tant DEC04 flares means it is unlikely that an FRB will go off within the sensitive volume, even if they are associated.

## Chapter 7

# The High Time Resolution Universe Survey high Galactic-latitude survey - Status

The HTRU survey uses the 64-m Parkes radio telescope to survey the radio sky for pulsars and transients. The 13-beam multibeam receiver is used to enable relatively rapid coverage of the sky. The survey has an observing bandwidth between 1.118 and 1.518 GHz, of which around 340 MHz is RFI free and useful. The survey is split into three parts, the low-, medium- and high-latitude regions. See Chapter 2 for more details on the survey. My work has predominantly been on the high-latitude survey, with some pulsar discoveries in the medium latitude. The data is recorded in filterbank format using the compute cluster which forms a part of the digital back-end system, BPSR. The data are sent electronically to Swinburne University of Technology, and are written to tape, which are then sent to Jodrell Bank Centre for Astrophysics. The data are Fourier searched for pulsars using the *Hydra* computing cluster. In 2011 a single pulse searching pipeline was implemented to also run on the Hydra cluster (see Chapter 2).

Observing for the HTRU survey began in 2008 with the low- and medium-latitude regions being prioritised initially. At the time of writing the low- and medium-latitude survey regions have been completely observed, while the high-latitude survey is around 80% observed. The medium-latitude was completely Fourier searched at Jodrell Bank, and also at Swinburne University of Technology. Processing of the high-latitude survey is ongoing at Jodrell Bank Centre for Astrophysics. There is also a close-to real time single pulse search routine bring run on the data at the telescope in order to attempt to discover FRBs.

The high-latitude survey was designed to be a snapshot of the transient radio sky (Keith et al., 2010). The observing times are short (270 seconds) and as such the survey is not as sensitive as the medium- or low-latitude survey regions. However, the survey region is large, and most has not been surveyed with a comparable sensitivity at  $\nu \sim 1.4$  GHz before.

The high latitude survey consists of the sky which is visible to the 64-m Parkes radio telescope, excluding the areas covered by the medium- and low-latitude regions (see Table 2.1). It is expected to be sensitive to relatively bright pulsars. It will likely find a number of MSPs, which are expected to have a larger scale height above the Galactic plane than normal pulsars ().

## 7.1 Survey status

The total high-latitude survey consists of 443'287 telescope beams. This corresponds to a total of  $1.2 \times 10^8$  s of total data duration, or  $9.2 \times 10^6$  s of telescope time (13 beams are observed simultaneously). Of the total survey area approximately 80% has been observed, 58.0% has been Fourier searched for pulsars, and 47.2% has been searched for single pulses, all percentages are of the total survey area, including both observed and as yet unobserved.

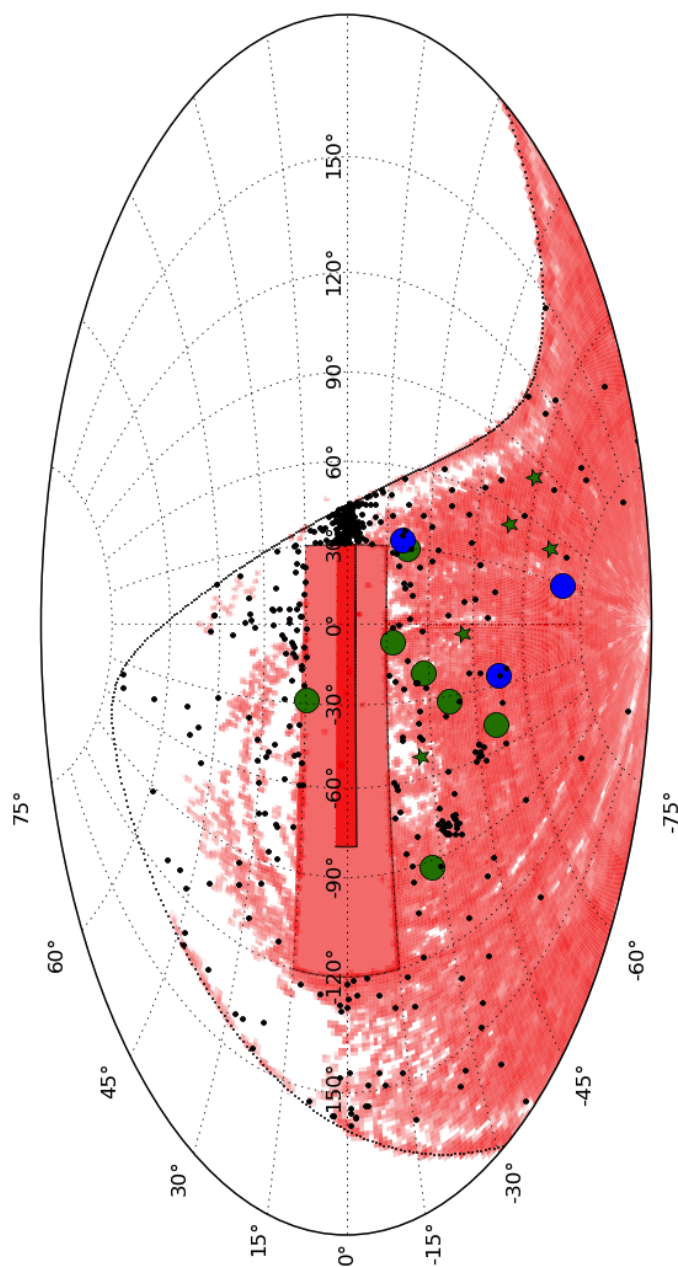


**Figure 7.1** – An Aitoff projection showing the status of the high-latitude HTRU survey in Galactic coordinates (the Galactic plane runs across the centre of the plot, with  $l, b = 0, 0$  in the centre). Newly discovered pulsars (green circles) and recycled pulsars (blue circles) are indicated, along with FRBs (green stars). Pulsars known prior to the commencement of the HTRU survey are indicated by the black points. The survey Fourier processing status is indicated by the red background, where dark red indicates fully processed. The limit of the survey region is indicated the black line, which defines the northerly declination limit of the 64-m Parkes radio telescope ( $\delta < +10^\circ$ ). The medium- and low-latitude survey regions are also indicated by the rectangular red shaded regions centred on the Galactic plane.

## 7.2 Pulsars

In Figure 7.2 I show the spin periods and DMs for the new discoveries in the high-latitude survey region. The discovery SNR of the pulsars is indicated by the size of the plot point, ranging from 12 to 38. As expected, in this region of the Galaxy in the direction of most high-latitude observations to give rise high DM values. The DM of the pulsar just below the Galactic center is still low, indicating it is nearby.

### 7.2.1 Normal pulsars

Seven normal pulsars have so far been confirmed from the high-latitude survey. They have periods between 0.338 and 2.273 s, and DMs between 13.1 and 101  $\text{cm}^{-3}$  pc. Five are isolated, while two have not been observed sufficiently yet to determine the presence of any possible orbital companion.

Only seven normal pulsars have been discovered to-date, this number is consistent with the prediction of Keith et al. (2010), who predicted 11 discoveries in the completed high-latitude survey. An updated prediction for the total number of discoveries in the high-latitude survey region is 12. This is based simply on the amount of the survey which has been Fourier searched.

This is somewhat lower than the predictions of Keith et al. who predicted 11 new normal pulsars and 13 new MSPs, even extrapolating to the completed survey. The reasons for this are unclear, although it is possible that the remaining, unprocessed survey contains more pulsars than that already processed.

### 7.2.2 Recycled pulsars

To-date three new fully recycled pulsars have been discovered in the high-latitude survey. These have measured spin periods between 3.2 and 6.9 ms, indicating they have all evolved through a low-mass x-ray binary (see Chapter 1), which spun them up to the observed pulse periods. Two are known to be in orbital systems, the third is a relatively unusual isolated MSP. PSR J2322–2650 has an ultra-low mass companion, and is described in detail in Chapter 4.

Extrapolating from the number of discoveries to the completed survey indicates that 5

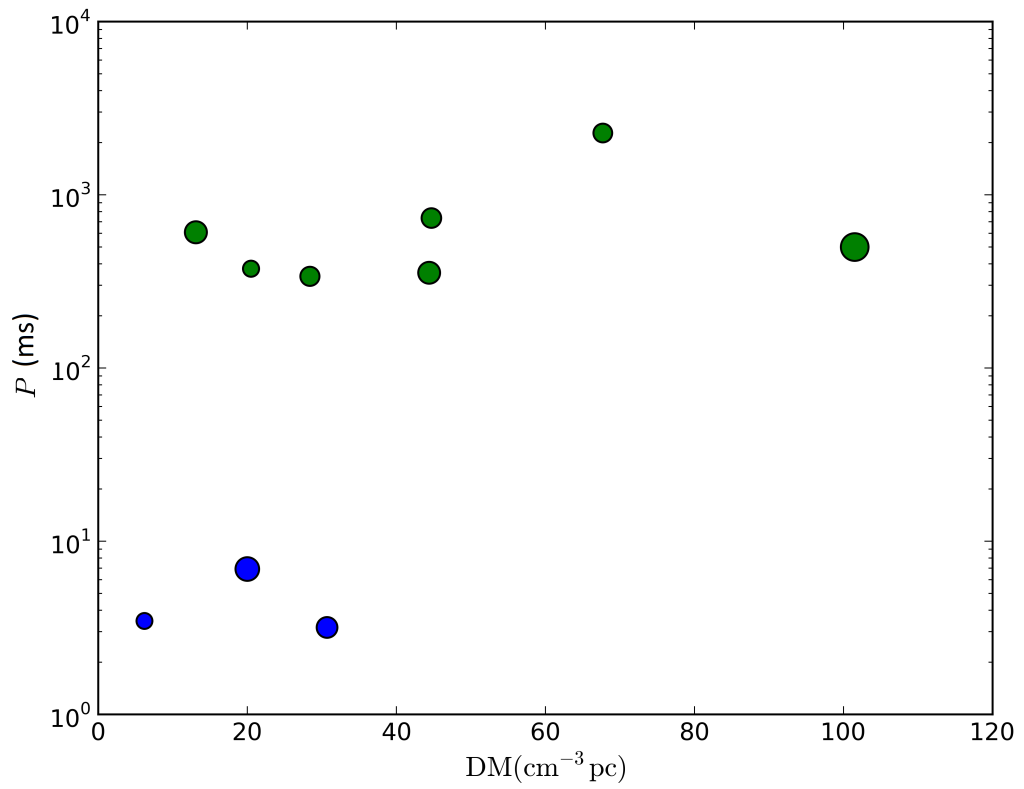


**Figure 7.2** – Plots of new normal pulsars (green) and recycled pulsar (blue) are shown. The size of the points is proportional to the signal to noise ratio (SNR) of the pulsar in the search observation.

recycled pulsars will be found in total. This is somewhat lower than the prediction of Keith et al. (2010), who predicted that 13 MSPs would be discovered. One possible reason for this discrepancy is the distribution of processed pointings. The majority of unobserved and unsearched pointings are relatively close to the Galactic plane (see Figure 7.1). This is due to the medium- and low-latitude regions taking priority when available. This resulted in high-latitude telescope pointings which are at similar RAs being left until the end of the survey (the medium- and low-latitude survey regions have now been completely observed). Because the distributions of all types of pulsar are centred on the Galactic plane, it may be that there is proportionally more pulsars in the high-latitude pointings which are as yet unsearched.

### 7.3 Fast Radio Bursts

In this processing of the high-latitude data five Fast Radio Bursts (FRBs) have been discovered, in the archival data (see Chapters 5 and 6). They have measured DM values between 521 and 1628  $\text{cm}^{-3}$  pc, none of which are consistent with being due to the Milky Way. All have been detected in only a single beam, with SNRs in the search pipeline between 11 and 49.

If the host galaxy dispersion measure is approximated as being due to a Milky Way-type galaxy inclined to the line of sight at a median inclination angle, then the sources of these FRBs could be at redshifts between 0.45 and 1.45. With 47.2% of the high-latitude survey searched for single pulses, the rate for bursts with fluence,  $F \sim 3$  Jy ms is  $R_{\text{FRB}} = 7.3_{-3.0}^{+3.5} \times 10^3 \text{ sky}^{-1} \text{ day}^{-1}$ . The prediction for the total number of FRBs which will be found in the high-latitude survey is  $11_{-4}^{+5}$ . A discussion of the number of FRBs that may be found in survey regions close to the Galactic plane is provided in Chapter 6.

# Chapter 8

## Conclusions

### 8.1 The High Time Resolution Universe survey

The High Time Resolution Universe survey is a 1.4 GHz survey for pulsars and transients, which uses the 64-m Parkes radio telescope. My work has focused on the high-latitude survey region which aims to discover bright recycled pulsars, normal pulsars, and millisecond timescale radio transients. In particular Millisecond Pulsars (MSPs) which are in exotic binaries, and those which are suitable for Pulsar Timing Array (PTA) projects would be interesting and useful discoveries. In addition to pulsars, the high latitude region aims to provide a snapshot of the radio transient sky. In particular the sheer size of the survey region, and quantity of data acquired, makes detection of relatively rare events possible (for the size of the telescope field-of-view).

Finally, the HTRU survey, when complete, will form an enormous legacy dataset for further, more detailed searches for extreme pulsar systems. For instance, it is possible to make corrections for a putative acceleration of unknown pulsars in the raw data (Ransom, Eikenberry & Middleditch, 2002), this kind of *acceleration searching* will be an inevitable further search of the same data for pulsars in extreme binary systems. Better candidate filtration and sorting algorithms may also be able to identify pulsars which have, as yet, been missed. These algorithms could be applied to the derived dataset formed of the candidates, without having to re-search the raw filterbank data.

### 8.1.1 Pulsars

In Chapter 3 I presented the discovery of five recycled pulsars from the HTRU survey. Four are in binary systems, while one is isolated. They have spin periods between 2.01 and 66.2 ms. The binary systems have a range of measured properties from which minimum companion masses between 0.08 and  $1.29 M_{\odot}$  are calculated. This spans a large range of the known binary pulsar populations.

Orbitally modulated timing residuals are measured for PSR J1431–4715, indicating it is a redback system. The companion is surrounded by ionised material, which around superior conjunction causes unmodelled delays of the radio pulses. It is thought that this eclipsing material is being ablated from the companion by the spin-down energy of the pulsar. The delays are attributed to extra dispersion with a maximum free electron column density of  $10^{18} \text{ cm}^{-2}$ , in good agreement with other eclipsing systems. The cloud of ionised material possibly extends beyond the Roche lobe of the orbit, meaning that it is not gravitationally bound to the companion and must be continually replenished.

PSR J1227–6208 is a mildly recycled pulsar with a spin period of 34.5 ms. This system likely evolved via mass transfer in a high mass x-ray binary. This is in agreement with the properties of the companion, which has a relatively high minimum mass of  $1.29 M_{\odot}$ . This system shares a lot of common traits with double neutron star systems, except for its small orbital eccentricity. We performed a  $\chi^2$  analysis of the residuals to constrain the inclination and companion mass via a possible measurement of the Shapiro delay. We conclude that an edge-on configuration with a  $1.29 M_{\odot}$  companion is not favoured, and it is possible that the orbit is somewhat inclined, the companion is more massive, and therefore closer to a canonical neutron star mass of  $1.4 M_{\odot}$ . With an improvement of about a factor of two in timing precision, and more intense campaigns during periastron passage should reveal the true nature of the companion.

PSR J1729–2117 is also a mildly recycled pulsar with a spin period of 66.2 ms, although this pulsar is isolated. We conclude it was likely spun-up in a high mass x-ray binary before the companion underwent core collapse supernova, disrupting the orbit completely. We attempted to measure the proper motion for this system via pulsar timing, which we expect to be large, however its location close to the ecliptic makes this impossible at the moment.

PSRs J1405–4656 and J1653–2054 are typical fully recycled pulsars with spin periods of 7.6 and 4.1 ms respectively. Both these systems have likely WD companions and the or-

bital parameters are in good agreement with the predicted relationship between companion mass and orbital period for systems which evolved via a low mass x-ray binary.

In Chapter 4 I present two further exotic binary pulsar systems from the HTRU survey. The two systems are at opposite ends of the spectrum of binary pulsars, one being a normal pulsar with a measured spin period of 1.09 s, and the other a fully recycled MSP with an observed spin period of 3.46 ms.

The MSP, PSR J2322–2650, is in a very tight orbit, with a projected radius of just 0.0027 ls. Along with the orbital period of 0.322 d this corresponds to a minimum companion mass of  $7 \times 10^{-4} M_{\odot}$ , just less than the mass of Jupiter. As such, this system is a member of the extremely rare planet pulsar category. By using the Roche lobe as the maximum radius of the companion we are able to place a lower limit on the mean density of the companion of  $1.9g \text{ g cm}^{-3}$ .

The normal pulsar PSR J1837–0832 is in a wide, long orbit with an orbital period and projected size of 98.3 d and 40.8 ls respectively. The spin parameters of this system indicate it is an old normal pulsar, and has not been recycled. This is an interesting situation because these systems are expected to have significant orbital eccentricity induced by the core collapse supernova in which the pulsar was born. This system however has a low orbital eccentricity of 0.024.

## 8.1.2 Fast Radio Bursts

In Chapter 5 I presented the discovery of four non-repeating radio bursts. The dispersion measures of these are entirely inconsistent with being due to the ionised material associated with the Milky Way. Named Fast Radio Bursts (FRBs), they were discovered in the high-latitude survey and confirm a real astronomical source population. These discoveries also confirm the Lorimer burst as the first example of an FRB, itself a revolutionary discovery. In the brightest case, FRB 110220, we are able to fit for the effect of dispersion and scattering simultaneously. The results,  $\delta t \propto \nu^{-2.003 \pm 0.006}$  and  $W_{\text{obs}} \propto \nu^{-4.0 \pm 0.4}$ , show remarkable adherence to the expectations for astrophysical propagation and scattering. The second brightest case, FRB 110703, is also fit for the dispersion index, where  $\delta t \propto \nu^{-2.000 \pm 0.006}$ , again confirming its astrophysical origin.

The FRBs presented in Chapter 5 have dispersion measures between 944 and 1103  $\text{cm}^{-3}\text{pc}$ . Using models for the Milky Way, intergalactic material, and host galaxy we infer redshifts

of the sources from 0.45 to 0.96, making them a cosmologically significant population.

At a fluence of around 3 Jy ms FRBs have a high rate of approximately  $10^4 \text{ sky}^{-1} \text{ day}^{-1}$  inferred from the high-latitude survey. This is in agreement with the rate of the much brighter Lorimer burst, and indicates that the sources may be distributed with a constant density per unit co-moving distance and have a luminosity which does not evolve with redshift.

So far FRBs have only been detected with the Parkes radio telescope, which has, and continues to, dedicate large amounts of time to surveys with the necessary resolution to identify FRBs. All FRBs have also been discovered at 1.4 GHz at an unknown location in the gain pattern of the receiver. This makes a meaningful spectral measurement impossible, and thus the intrinsic spectrum is currently not well constrained. In Chapter 6 I demonstrate, using a simulation of FRBs, that it may be possible to measure the spectrum of redshifted FRBs with a statistically significant number of detections, even without knowing the positions of the FRBs in the gain pattern.

In Chapter 6 I also present the discovery of FRB 121002, which has a very high dispersion measure of  $1628 \text{ cm}^{-3} \text{ pc}$ , indicating a redshift for its source of 1.45, when the Universe was less than half as old as it is now. This FRB has some complexity in the burst shape which has been measured. The burst shape indicates there is either two different sites for radio emission, or two distinct emission events during this FRB. A connection between SGR giant flares and FRBs would be extremely interesting. It is conceivable that the double peak of FRB 121002 may be two radio “radio flashes” from a rapidly rotating magnetar. This may be possible as it is possible that magnetars form with  $\sim \text{ms}$  spin periods, followed by rapid decay to their observed, slower spin periods (Duncan & Thompson, 1992). Future discovery of high signal-to-noise ratio FRBs that also exhibit burst structure may provide direct measurement of the emission region, and in turn help in understanding their sources.

The future study of FRBs will depend on the detection of many more, and the identification of host galaxies. Low frequency radio telescopes such as LOFAR hold a lot of promise for FRB detection with large fields of view and the possibility of retrospectively imaging the sky in which an FRB is detected. There are of course at least two important considerations for low frequency telescopes, a) the spectral index of FRBs, and b) the detrimental effect of scattering in FRB detectability. In the former case there is some indication from the Lorimer burst and from the HTRU FRBs that the spectral index is negative, which would help detectability of FRBs at low frequencies. The magnitude of scattering may be a problem at low radio frequencies, although the lack of detection of scattering in the

majority of FRB cases indicates it is almost certainly not as great as scattering of pulsars by the turbulent ionised interstellar medium. Indeed, recent consideration of scattering by turbulent ionised material at cosmological redshifts indicates it will not be as detrimental as Galactic measurements may suggest (Macquart & Koay, 2013).

One way which will definitely help to understand the sources of FRBs will be associated events at other wavelengths. Optical or high-energy detections could provide the positional accuracy to identify a host galaxy, with a consequent true redshift measurement. The distribution of FRBs within their host galaxies, and the types of the host galaxies themselves, will also help to determine the sources. The relative spectral energy distribution across all energies will also be important in the development of emission models.

A final important aspect of the future of FRB astronomy will be their identification as soon as possible after the observation. Once identified it will be necessary to make available the FRB details to the astronomy community as a whole as quickly as possible. The field around an FRB then forms a target for multi-wavelength follow-up. While it is not clear what may be detected or on what timescale, it is apparent that FRBs are dynamic events lasting, at most, a few milliseconds. FRBs should be followed up for both short timescale emission and possible longer timescale afterglows.

FRB 121002 is one of the most highly dispersed millisecond radio sources ever observed. There is currently little reason to suggest that FRBs could not be detected at significantly higher dispersion measures than this. Future surveys and processings of old survey data should extend the maximum test value of DM to the point that detectability of FRBs would be dominated by instrumental effects. FRBs may prove to be an excellent tool for understanding the magneto-ionic properties of the IGM to significant redshifts.

# Bibliography

- Abbott B. P. et al., 2009, Reports on Progress in Physics, 72, 076901
- Abdo A. A. et al., 2009, Science, 325, 848
- Abdo A. A. et al., 2010, ApJS, 187, 460
- Ables J. G., Manchester R. N., 1976, A&A, 50, 177
- Acernese F. et al., 2006, Classical and Quantum Gravity, 23, 635
- Alpar M. A., Anderson P. W., Pines D., Shaham J., 1981, ApJ, 249, L29
- Alpar M. A., Anderson P. W., Pines D., Shaham J., 1984, ApJ, 276, 325
- Alpar M. A., Cheng A. F., Ruderman M. A., Shaham J., 1982, Nature, 300, 728
- Amôres E. B., Lépine J. R. D., 2005, AJ, 130, 659
- Anderson P. W., Itoh N., 1975, Nature, 256, 25
- Antoniadis J. et al., 2013, Science, 340, 448
- Archibald A. M., Kaspi V. M., Bogdanov S., Hessels J. W. T., Stairs I. H., Ransom S. M.,  
McLaughlin M. A., 2010, ApJ, 722, 88
- Baade W., Zwicky F., 1934, Proc. Nat. Acad. Sci., 20, 254
- Bagchi M., Nieves A. C., McLaughlin M., 2012, MNRAS, 425, 2501
- Bailes M., 1989, ApJ, 342, 917
- Bailes M. et al., 2011, Science, 333, 1717
- Bannister K. W., Murphy T., Gaensler B. M., Reynolds J. E., 2012, ApJ, 757, 38
- Bassa C. G., van Kerkwijk M. H., Kulkarni S. R., 2003, A&A, 403, 1067

- Bassa C. G., van Kerkwijk M. H., Kulkarni S. R., 2006, *A&A*, 450, 295
- Bates S. D. et al., 2012, *MNRAS*, 427, 1052
- Bates S. D. et al., 2011, *MNRAS*, 416, 2455
- Baym G., Pines D., 1971, *Ann. Phys. (U.S.A.)*, 66, 816
- Bergeron P. et al., 2011, *ApJ*, 737, 28
- Bhat N. D. R., Cordes J. M., Camilo F., Nice D. J., Lorimer D. R., 2004, *ApJ*, 605, 759
- Bhattacharya D., van den Heuvel E. P. J., 1991, *Phys. Rep.*, 203, 1
- Boyles J. et al., 2013, *ApJ*, 763, 80
- Breton R. P. et al., 2013, *ApJ*, 769, 108
- Burgay M. et al., 2013, *MNRAS*, 433, 259
- Burgay M. et al., 2003, *Nature*, 426, 531
- Burgay M. et al., 2006, *MNRAS*, 368, 283
- Burke-Spolaor S., Bailes M., Ekers R., Macquart J.-P., Crawford, III F., 2011a, *ApJ*, 727, 18
- Burke-Spolaor S. et al., 2011b, *ArXiv e-prints*
- Camilo F. et al., 2007a, *ApJ*, 663, 497
- Camilo F. et al., 2001, *ApJ*, 548, L187
- Camilo F., Nice D. J., Taylor J. H., 1993, *ApJ*, 412, L37
- Camilo F., Ransom S. M., Halpern J. P., Reynolds J., 2007b, *ApJ*, 666, L93
- Camilo F., Ransom S. M., Halpern J. P., Reynolds J., Helfand D. J., Zimmerman N., Sarkissian J., 2006, *Nature*, 442, 892
- Camilo F., Reynolds J., Johnston S., Halpern J. P., Ransom S. M., 2008, *ApJ*, 679, 681
- Champion D. J., Lorimer D. R., McLaughlin M. A., Cordes J. M., Arzoumanian Z., Weisberg J. M., Taylor J. H., 2004, *MNRAS*, 350, L61
- Chandrasekhar S., 1931, *ApJ*, 74, 81

- Chatterjee S. et al., 2009, *ApJ*, 698, 250
- Chaurasia H. K., Bailes M., 2005, *ApJ*, 632, 1054
- Cheng K. S., Ho C., Ruderman M., 1986, *ApJ*, 300, 500
- Cocke W. J., Disney M. J., Taylor D. J., 1969, *Nature*, 221, 525
- Cooley J. W., Tukey J. W., 1965, *Math. Comput.*, 19, 297
- Corbel S., Eikenberry S. S., 2004, *A&A*, 419, 191
- Cordes J. M., 2009, *SKA Memo Series*, 1
- Cordes J. M., Lazio T. J. W., 2002, *ArXiv Astrophysics e-prints*, preprint (arXiv:astro-ph/0207156)
- Deller A. T., Tingay S. J., Bailes M., Reynolds J. E., 2009, *ApJ*, 701, 1243
- Deloye C. J., Bildsten L., 2003, *ApJ*, 598, 1217
- Demorest P. B., Pennucci T., Ransom S. M., Roberts M. S. E., Hessels J. W. T., 2010, *Nature*, 467, 1081
- Deneva J. S., Cordes J. M., Lazio T. J. W., 2009, *ApJ*, 702, L177
- Dewi J. D. M., Podsiadlowski P., Pols O. R., 2005, *MNRAS*, 363, L71
- Diehl R. et al., 2006, *Nature*, 439, 45
- Duncan R. C., Thompson C., 1992, *ApJ*, 392, L9
- Eatough R. et al., 2013, *The Astronomer's Telegram*, 5058, 1
- Eatough R. P., Molkenhain N., Kramer M., Noutsos A., Keith M. J., Stappers B. W., Lyne A. G., 2010, *mnras*, 407, 2443
- Edwards R. T., Bailes M., van Straten W., Britton M. C., 2001a, *MNRAS*, 326, 358
- Edwards R. T., Bailes M., van Straten W., Britton M. C., 2001b, *MNRAS*, 326, 358
- Eggleton P. P., 1983, *ApJ*, 268, 368
- Egorov A. E., Postnov K. A., 2009, *Astronomy Letters*, 35, 241
- Eichler D., Levinson A., 1988, *ApJ*, 335, L67

- Espinoza C. M. et al., 2013, MNRAS, 430, 571
- Espinoza C. M., Lyne A. G., Stappers B. W., Kramer M., 2011, MNRAS, 414, 1679
- Fahlman G. G., Gregory P. C., 1981, Nature, 293, 202
- Falcke H., Rezzolla L., 2013, ArXiv e-prints
- Faucher-Giguère C.-A., Loeb A., 2011, MNRAS, 415, 3951
- Faulkner A. J. et al., 2005, ApJ, 618, L119
- Faulkner A. J. et al., 2004, MNRAS, 355, 147
- Figer D. F., Najarro F., Kudritzki R. P., 2004, ApJ, 610, L109
- Foster R. S., 1990, PhD thesis, University of California, Berkeley
- Frail D. A., Goss W. M., Whiteoak J. B. Z., 1994, ApJ, 437, 781
- Frail D. A. et al., 2001, ApJ, 562, L55
- Freire P. C. C. et al., 2012, MNRAS, 423, 3328
- Frigo M., Johnson S. G., 2005, Proceedings of the IEEE, 93, 216, special issue on “Program Generation, Optimization, and Platform Adaptation”
- Fruchter A. S., Stinebring D. R., Taylor J. H., 1988, Nature, 333, 237
- Gaensler B. M., Madsen G. J., Chatterjee S., Mao S. A., 2008, PASA, 25, 184
- Galloway D. K., Chakrabarty D., Morgan E. H., Remillard R. A., 2002, ApJ, 576, L137
- Goldreich P., Julian W. H., 1969, ApJ, 157, 869
- Gunn J. E., Peterson B. A., 1965, ApJ, 142, 1633
- Hansen B. M. S., Lyutikov M., 2001, MNRAS, 322, 695
- Hassall T. E. et al., 2012, AAP, 543, A66
- Hellings R. W., Downs G. S., 1983, ApJ, 265, L39
- Hessels J. W. T., Ransom S. M., Stairs I. H., Freire P. C. C., Kaspi V. M., Camilo F., 2006, Science, 311, 1901

- Hessels J. W. T. et al., 2011, in American Institute of Physics Conference Series, Vol. 1357, American Institute of Physics Conference Series, Burgay M., D'Amico N., Esposito P., Pellizzoni A., Possenti A., eds., pp. 40–43
- Hewish A., Bell S. J., Pilkington J. D. H., Scott P. F., Collins R. A., 1968, *Nature*, 217, 709
- Hills J. G., 1983, *ApJ*, 267, 322
- Hobbs G. et al., 2010, *Classical and Quantum Gravity*, 27, 084013
- Hobbs G. et al., 2004, *MNRAS*, 352, 1439
- Hobbs G. B., Edwards R. T., Manchester R. N., 2006, *MNRAS*, 369, 655
- Holberg J. B., Bergeron P., 2006, *AJ*, 132, 1221
- Hotan A. W., van Straten W., Manchester R. N., 2004, *PASA*, 21, 302
- Hulse R. A., Taylor J. H., 1975, *ApJ*, 195, L51
- Hurley K. et al., 2005, *Nature*, 434, 1098
- Hurley K. et al., 1999, *Nature*, 397, 41
- Inoue S., 2004, *MNRAS*, 348, 999
- Ioka K., 2003, *ApJ*, 598, L79
- Islaker H., Benz A. O., 1994, *AAPS*, 104, 145
- Jacoby B. A., Bailes M., Ord S., Knight H., Hotan A., Edwards R. T., Kulkarni S. R., 2006, *ApJ*, in preparation
- Jacoby B. A., Hotan A., Bailes M., Ord S., Kulkarni S. R., 2005, *ApJ*, 629, L113
- James F., 2008, *Minuit*
- Jenet F. et al., 2009, *ArXiv e-prints*
- Johnston S. et al., 2007, *PASA*, 24, 174
- Keane E. F., Kramer M., 2008, *MNRAS*, 391, 2009
- Keane E. F., Kramer M., Lyne A. G., Stappers B. W., McLaughlin M. A., .., 2011, *ArXiv e-prints*
- Keane E. F., Stappers B. W., Kramer M., Lyne A. G., 2012, *MNRAS*, L491

- Keith M. J. et al., 2010, MNRAS, 1356
- Knispel B. et al., 2013, ArXiv e-prints
- Kocz J., Bailes M., Barnes D., Burke-Spolaor S., Levin L., 2012, MNRAS, 420, 271
- Koester D., Chanmugam G., Reimers D., 1992, ApJ, 395, L107
- Kouwenhoven M. L. A., Voûte J. L. L., 2001, AAP, 378, 700
- Kowalski P. M., Saumon D., 2006, ApJ, 651, L137
- Kramer M. et al., 2003a, MNRAS, 342, 1299
- Kramer M., Lyne A. G., Hobbs G., Löhmer O., Carr P., Jordan C., Wolszczan A., 2003b, ApJ, 593, L31
- Kramer M., Lyne A. G., O'Brien J. T., Jordan C. A., Lorimer D. R., 2006a, Science, 312, 549
- Kramer M. et al., 2006b, Science, 314, 97
- Kramer M., Stappers B. W., Jessner A., Lyne A. G., Jordan C. A., 2007, MNRAS, 377, 107
- Lada C. J., 2006, ApJ, 640, L63
- Lange C., Camilo F., Wex N., Kramer M., Backer D., Lyne A., Doroshenko O., 2001, MNRAS, 326, 274
- Lattimer J. H., Prakash M., 2004, Science, 304, 536
- Lattimer J. M., Prakash M., 2001, ApJ, 550, 426
- Lazaridis K., Jessner A., Kramer M., Stappers B. W., Lyne A. G., Jordan C. A., Serylak M., Zensus J. A., 2008, MNRAS, 390, 839
- Levin L. et al., 2010, ApJ, 721, L33
- Lorimer D. R., 2010, ArXiv e-prints
- Lorimer D. R., Bailes M., McLaughlin M. A., Narkevic D. J., Crawford F., 2007, Science, 318, 777
- Lorimer D. R. et al., 2006, MNRAS, 372, 777
- Lorimer D. R., Festin L., Lyne A. G., Nicastro L., 1995a, Nature, 376, 393

- Lorimer D. R., Kramer M., 2005, *Handbook of Pulsar Astronomy*. Cambridge University Press
- Lorimer D. R. et al., 2004, *MNRAS*, 347, L21
- Lorimer D. R., Yates J. A., Lyne A. G., Gould D. M., 1995b, *MNRAS*, 273, 411
- Lyne A. G., Biggs J. D., Harrison P. A., Bailes M., 1993, *Nature*, 361, 47
- Lyne A. G. et al., 2004, *Science*, 303, 1153
- Lyne A. G. et al., 2000, *MNRAS*, 312, 698
- Lyne A. G., Lorimer D. R., 1994, *Nature*, 369, 127
- Madgwick D. S. et al., 2002, *MNRAS*, 333, 133
- Manchester R. N., Fan G., Lyne A. G., Kaspi V. M., Crawford F., 2006, *ApJ*, 649, 235
- Manchester R. N. et al., 2013, *PASA*, 30, 17
- Manchester R. N., Hobbs G. B., Teoh A., Hobbs M., 2005, *AJ*, 129, 1993
- Manchester R. N. et al., 2001, *MNRAS*, 328, 17
- Markwardt C. B., Swank J. H., Strohmayer T. E., Zand J. J. M. i., Marshall F. E., 2002, *ApJ*, 575, L21
- Mazets E. P., Golenetskii S. V., Gur'yan Y. A., 1979, *Sov. Astron. Lett.*, 5, 343
- Mazets E. P., Golenetskii S. V., Ilinskii V. N., Apetkar R. L., Guryan Y. A., 1979, *Nature*, 282, 587
- McLaughlin M. A., Cordes J. M., 2003, *ApJ*, 596, 982
- McLaughlin M. A. et al., 2006, *Nature*, 439, 817
- Mickaliger M. B. et al., 2012, *ApJ*, 759, 127
- Morris D. J. et al., 2002, *MNRAS*, 335, 275
- Nolan P. L. et al., 2012, *ApJS*, 199, 31
- Ofek E. O., 2007, *ApJ*, 659, 339
- Oppenheimer J. R., Volkoff G., 1939, *Phys. Rev.*, 55, 374

- Pacini F., 1967, *Nature*, 216, 567
- Palmer D. M. et al., 2005, *Nature*, 434, 1107
- Phinney E. S., 1992, *Philos. Trans. Roy. Soc. London A*, 341, 39
- Pilkington J. D. H., Hewish A., Bell S. J., Cole T. W., 1968, *Nature*, 218, 126
- Podsiadlowski P., 1993, in *Planets Around Pulsars*, Phillips J. A., Thorsett S. E., Kulkarni S. R., eds., *Astronomical Society of the Pacific Conference Series*, pp. 149–165
- Ransom S. M., Eikenberry S. S., Middleditch J., 2002, *AJ*, 124, 1788
- Rees M. J., 1977, *Nature*, 266, 333
- Reynolds M. T., Callanan P. J., Fruchter A. S., Torres M. A. P., Beer M. E., Gibbons R. A., 2007, *MNRAS*, 379, 1117
- Roberts M. S. E., 2011, in *American Institute of Physics Conference Series*, Vol. 1357, *American Institute of Physics Conference Series*, Burgay M., D’Amico N., Esposito P., Pellizzoni A., Possenti A., eds., pp. 127–130
- Roeder R. C., Verreault R. T., 1969, *ApJ*, 155, 1047
- Romani R. W., 1989, in *Timing Neutron Stars*, Ögelman H., van den Heuvel E. P. J., eds., pp. 113–117
- Romani R. W., Filippenko A. V., Silverman J. M., Cenko S. B., Greiner J., Rau A., Elliott J., Pletsch H. J., 2012, *ApJ*, 760, L36
- Rubio-Herrera E., Stappers B. W., Hessels J. W. T., Braun R., 2012, *ArXiv e-prints*
- Ruderman M., Shaham J., Tavani M., 1989, *ApJ*, 336, 507
- Sanidas S. A., Battye R. A., Stappers B. W., 2012, *prd*, 85, 122003
- Schlegel D. J., Finkbeiner D. P., Davis M., 1998, *ApJ*, 500, 525
- Sesana A., 2013, *ArXiv e-prints*
- Sesana A., Vecchio A., Volonteri M., 2009, *MNRAS*, 394, 2255
- Shannon R. M., Johnston S., 2013, *ArXiv e-prints*
- Shapiro I. I., 1964, *Phys. Rev. Lett.*, 13, 789

- Smits R., Kramer M., Stappers B., Lorimer D. R., Cordes J., Faulkner A., 2009, *AAP*, 493, 1161
- Spergel D. N. et al., 2003, *ApJS*, 148, 175
- Stairs I. H. et al., 2011, in *American Institute of Physics Conference Series*, Vol. 1357, American Institute of Physics Conference Series, Burgay M., D'Amico N., Esposito P., Pellizzoni A., Possenti A., eds., pp. 335–340
- Stappers B. W. et al., 1996, *ApJ*, 465, L119
- Stappers B. W., van Kerkwijk M. H., Bell J. F., Kulkarni S. R., 2001, *ApJ*, 548, L183
- Staveley-Smith L. et al., 1996, *PASA*, 13, 243
- Stinebring D. R., Smirnova T. V., Hankins T. H., Hovis J., Kaspi V., Kempner J., Meyers E., Nice D. J., 2000, *ApJ*, 539, 300
- Tauris T. M., 2012, *Science*, 335, 561
- Tauris T. M., Langer N., Kramer M., 2012, *MNRAS*, 425, 1601
- Tauris T. M., Savonije G. J., 1999, *A&A*, 350, 928
- Tauris T. M., Sennels T., 2000, *A&A*, 355, 236
- Tauris T. M., van den Heuvel E. P. J., 2003, *ArXiv Astrophysics e-prints*
- Taylor J. H., Weisberg J. M., 1982, *ApJ*, 253, 908
- The Fermi-LAT collaboration, 2013, *ArXiv e-prints*
- Thompson C., Duncan R. C., 1995, *MNRAS*, 275, 255
- Thompson C., Duncan R. C., 1996, *ApJ*, 473, 322
- Thompson C., Duncan R. C., Woods P. M., Kouveliotou C., Finger M. H., van Paradijs J., 2000, *ApJ*, 543, 340
- Thornton D. et al., 2013, *ArXiv e-prints*
- Toscano M., Sandhu J. S., Bailes M., Manchester R. N., Britton M. C., Kulkarni S. R., Anderson S. B., Stappers B. W., 1999, *MNRAS*, 307, 925
- Totani T., 2013, *ArXiv e-prints*

- Tremblay P.-E., Bergeron P., Gianninas A., 2011, *ApJ*, 730, 128
- van Haaften L. M., Nelemans G., Voss R., Jonker P. G., 2012a, *AAP*, 541, A22
- van Haaften L. M., Nelemans G., Voss R., Wood M. A., Kuijpers J., 2012b, *AAP*, 537, A104
- van Haasteren R. et al., 2011, *MNRAS*, 414, 3117
- van Kerkwijk M. H., Bergeron P., Kulkarni S. R., 1996, *ApJ*, 467, L89
- van Kerkwijk M. H., Breton R. P., Kulkarni S. R., 2011, *ApJ*, 728, 95
- van Leeuwen J., Stappers B. W., 2010, *aap*, 509, A7+
- Verbiest J. P. W. et al., 2009, *MNRAS*, 400, 951
- Verbunt F., Phinney E. S., 1995, *AAP*, 296, 709
- Weisberg J. M., Nice D. J., Taylor J. H., 2010, *ApJ*, 722, 1030
- Wijnands R., van der Klis M., 1998, *Nature*, 394, 344
- Williamson I. P., 1972, *MNRAS*, 157, 55+
- Wolszczan A., 1994, *Science*, 264, 538
- Wolszczan A., Frail D. A., 1992, *Nature*, 355, 145
- Young M. D., Manchester R. N., Johnston S., 1999, *Nature*, 400, 848